Geochronological constraints on the formation, setting and evolution of the Olympic Dam IOCG deposit and the Olympic IOCG Province, South Australia

Alexander R. Cherry

BAdvSci(Hons) University of New South Wales

ARC Centre of Excellence in Ore Deposits (CODES)
School of Natural Sciences (Earth Sciences)

Submitted in fulfilment of the requirements for the degree of
Doctor of Philosophy
University of Tasmania

April 2018

Table of contents

List of Figures and Tables

List of Appendices

Abstract

The Olympic Dam Cu-U-Au-Ag deposit in the Olympic Cu-Au Province (Gawler Craton, South Australia) is unique in the iron oxide-copper-gold (IOCG) deposit class for its polymetallic tenor and size; it is one of the largest economic accumulations of metals in the world. The deposit is hosted within the Olympic Dam Breccia Complex (ODBC) within the Roxby Downs Granite. The breccia complex also contains clasts and domains of other lithologies, including surficial lithologies (bedded clastic facies and felsic volcanic rocks). The Olympic Dam deposit, along with the other deposits and prospects in the Olympic Province, was originally suggested to have developed entirely within a geologically brief magmatic-hydrothermal event at ca. 1590 Ma. However, recent work has suggested Olympic Dam has been episodically modified after 1590 Ma. This thesis aims to clarify aspects of the architecture and timing of events at Olympic Dam as well as the nearby Olympic Province primarily through application of geochronology as well as mineral chemistry and textural analyses. This aim is addressed through: (1) determining the timing and relationships of the surficial lithologies in the ODBC with the Roxby Downs Granite, (2) demonstrating that Olympic Dam was originally overlain by the U-prospective Pandurra Formation and (3) exploring the complex history of hydrothermal mineralisation in the nearby Acropolis prospect.

New high-precision CA-TIMS geochronology has constrained the Roxby Downs Granite (1593.87 ± 0.21 Ma) to be slightly younger than felsic volcanic clasts (Gawler Range Volcanics -1594.73 ± 0.30 Ma) in the ODBC. The absence of older country rock fragments in the ODBC and shallow emplacement textures in the Roxby Downs Granite suggest the granite intruded already-present Gawler Range Volcanics. The age of tuffaceous mudstone intervals (1590.97 ± 0.58 Ma) in the bedded clastic facies indicates a basin was present at Olympic Dam and the bedded clastic facies were being deposited ca. 3 myr after emplacement of the Roxby Downs Granite. The provenance of the bedded clastic facies is suggested to have changed from initially volcanic-dominated to granitoid-dominated as Hiltaba Suite granitoids within the vicinity of Olympic Dam were unroofed. The onset of formation of the breccia complex and the hydrothermal system is therefore constrained by the age of the Roxby Downs Granite; the breccia complex and the hydrothermal system were active after deposition of the bedded clastic facies. These age constraints and data from other workers are used to propose a model for the deposition and incorporation of the bedded clastic facies involving faults being responsible for their segmentation and entrainment into the breccia complex.

A quartz-rich sandstone facies association recently discovered in the ODBC is entirely brecciated and has characteristics distinct from, and is not interbedded with, the other facies associations of the bedded clastic facies. In addition to the ca. 1590 Ma detrital zircon population present in all of the bedded clastic facies, the quartz-rich sandstone contains significant Palaeoproterozoic and Archaean age detrital zircon populations. The detrital and cement mineralogy, sedimentary textures, diagenetic age, and detrital zircon age populations match most closely sandstones of the ca. 1440 Ma Pandurra Formation which was originally deposited in the regionally extensive intracratonic Cariewerloo Basin. This correlation indicates the Cariewerloo Basin originally extended over the ODBC and that it was incorporated by tectonic activity at least 150 myr after the breccia complex first formed at ca. 1590 Ma. The Cariewerloo Basin is also speculated to have been a source of or conduit for oxidised U-bearing fluids that may have interacted with, and possibly added to, the Olympic Dam U resource long after 1590 Ma.

Further evidence of post-1590 Ma events affecting the Olympic Province was obtained from a study of apatite in the hydrothermal mineral assemblage (comprising an initial magnetite-apatite assemblage and a later hematite-dominated assemblage) of the nearby Acropolis prospect. The prospect is structurally simpler and less brecciated than Olympic Dam, and the initial magnetite-dominated assemblage is well preserved. The apatite grains contain zones with abundant inclusions of REE-phosphate minerals (xenotime and monazite) as well as inclusion-free zones. The inclusion-rich zones are interpreted to have formed from the fluid-aided recrystallisation of original, inclusion-free apatite, resulting in the remobilisation of REE, U and Th from apatite into REE-phosphate inclusions. U-Th-Pb geochronology of apatite, xenotime and monazite revealed multiple ages; both inclusion-free and inclusion-rich zones of apatite yield ages coincident with the age of the host volcanic units (ca. 1590 Ma). The xenotime and monazite inclusions have ages that indicate alteration events at ca. 1370 Ma and possibly at ca. 500 Ma. Although the ca. 500 Ma age corresponds to the Delamerian Orogeny in the Adelaide Fold Belt adjacent to the Gawler Craton, the ca. 1370 Ma age does not correspond to any known event in or near the Gawler Craton but instead corresponds best with an event in Laurentia. Challenges in the interpretation of the monazite data imply xenotime is a more robust geochronometer in this setting.

This thesis establishes a precise geochronological framework for the setting of significant lithologies at Olympic Dam and constrains the maximum age of the ODBC and the Olympic Dam deposit. Furthermore, the presence of the significantly younger Pandurra Formation in the ODBC

implies that tectonic activity affected Olympic Dam long after 1590 Ma and has raised the potential for a late contribution of U to the deposit resource. The identification of multiple post-1590 Ma tectonothermal events affecting the Acropolis prospect suggests the wider Olympic Province has also experienced episodic modification. These findings contribute to the theory that the endowment of the Olympic Dam deposit and the Olympic Province did not occur within a single geologically brief event and may be due to episodic modification. The formation of such well-endowed deposits and metallogenic provinces may, in fact, require prolonged or episodic processes and offers the potential to assist in future exploration targeting for large IOCG deposits (i.e. in regions with a complex and long-lived geological history).

Statements and Declarations

Declaration of originality

This thesis contains no material which has been accepted for a degree or diploma by the University or any other institution, except by way of background information and duly acknowledged in the thesis, and to the best of my knowledge and belief no material previously published or written by another person except where due acknowledgement is made in the text of the thesis, nor does the thesis contain any material that infringes copyright.

Signed: **Dated:** 04/04/2018

Authority of access

This thesis may be made available for loan and limited copying and communication in accordance with the Copyright Act 1968.

Signed: **Dated:** 04/04/2018

Statement regarding published work contained in this thesis

The publishers of the papers comprising Chapters 2, 3 and 4 hold the copyright for that content and access to the material should be sought from the corresponding journals. The remaining non-published content of the thesis may be made available for loan and limited copying and communication in accordance with the Copyright Act 1968.

Signed: **Dated:** 10/11/2018

Statement of authorship – List of authors

The following people contributed to the publication and submission of work undertaken as a part of this thesis:

Candidate, Author 1: Alexander Cherry, ARC Centre of Excellence in Ore Deposits (CODES), School of Natural Sciences, University of Tasmania

Author 2: Kathy Ehrig, Co-Supervisor, BHP Olympic Dam

Author 3: Vadim S. Kamenetsky, Primary Supervisor, CODES, School of Natural Sciences, University of Tasmania

Author 4: Jocelyn McPhie, Co-Supervisor, CODES, School of Natural Sciences, University of Tasmania

Author 5: James L. Crowley, Department of Geosciences, Boise State University

Author 6: Maya B. Kamenetsky, CODES, School of Natural Sciences, University of Tasmania

Author 7: John L. Keeling, Geological Survey of South Australia

Author 8: Sebastien Meffre, CODES, School of Natural Sciences, University of Tasmania

Author 9: Olga B. Apukhtina, CODES, School of Natural Sciences, University of Tasmania

Author 10: Jay M. Thompson, CODES, School of Natural Sciences, University of Tasmania

Author 11: Sasha Krneta, School of Physical Sciences, University of Adelaide

Proportion of work undertaken towards papers

Paper 1 - Precise geochronological constraints on the origin, setting and incorporation of ca. 1.59 Ga surficial facies into the Olympic Dam Breccia Complex, South Australia

Located in Chapter 2 (published in *Precambrian Research*)

Candidate was the primary author and with authors 2, 3 and 4 contributed to the conception and design of the research. Along with authors 5 and 6, the candidate collected data and contributed to its interpretation. The majority of revisions were provided by authors 3 and 4.

Candidate contributed approximately 85% to the planning, execution, and preparation of the paper.

Paper 2 - Linking Olympic Dam and the Cariewerloo Basin: Was a sedimentary basin involved in formation of the world's largest uranium deposit?

Located in Chapter 3 (published in *Precambrian Research*)

Candidate was the primary author and with authors 2, 3 and 4 contributed to the conception and design of the research. Along with authors 4, 6 and 8, the candidate collected data and contributed to its interpretation. The revisions were provided by authors 3, 4 and 9.

Candidate contributed approximately 90% to the planning, execution, and preparation of the paper.

Paper 3 - Tectonothermal events in the Olympic IOCG Province constrained by apatite and REE-phosphate geochronology

Located in Chapter 4 (published in the *Australian Journal of Earth Sciences*)

Candidate was the primary author and with author 10 contributed to the conception and design of the research. Along with authors 8 and 10, the candidate collected data and contributed to its interpretation. The revisions were provided by authors 2, 3, 4, 10 and 11.

Candidate contributed approximately 95% to the planning, execution, and preparation of the paper.

We the undersigned agree with the above stated "proportion of work undertaken" for each of the above published or submitted peer-reviewed papers contributing to the thesis:

Signed: _____

Vadim Kamenetsky

Supervisor

School of Natural Sciences

University of Tasmania

Leonid Danyushevsky

Head of Discipline (Earth Sciences)

School of Natural Sciences

University of Tasmania

Date: 04/04/2018 04/04/2018

Publications during course of thesis

Journal articles

Cherry, A.R., Ehrig, K., Kamenetsky, V.S., McPhie, J., Crowley, J.L. and Kamenetsky, M.B., 2018, Precise geochronological constraints on the origin, setting and incorporation of ca. 1.59 Ga surficial facies into the Olympic Dam Breccia Complex, South Australia: Precambrian Research, v. 315, p. 162-178.

Cherry, A.R., Kamenetsky, V.S., McPhie, J., Thompson, J.M., Ehrig, K., Meffre, S., Kamenetsky, M.B. and Krneta, S., 2018, Tectonothermal events in the Olympic IOCG Province constrained by apatite and REE-phosphate geochronology: Australian Journal of Earth Sciences, v. 65, p. 643-659.

Cherry, A.R., McPhie, J., Kamenetsky, V.S., Ehrig, K., Keeling, J.L., Kamenetsky, M.B., Meffre, S. and Apukhtina, O.B., 2017, Linking Olympic Dam and the Cariewerloo Basin: Was a sedimentary basin involved in formation of the world's largest uranium deposit?: Precambrian Research, v. 300, p. 168 –180.

Conference presentations

Cherry, A.R., Kamenetsky, V.S., McPhie, J., Ehrig, K., 2017, Constraints on the setting, timing and incorporation of surficial lithologies into the Olympic Dam Breccia Complex, in GSA Earth Sciences Student Symposium - Tasmania, 16 November 2017, Hobart, Australia.

Cherry, A.R., Kamenetsky, V.S., McPhie, J., Ehrig, K. and Keeling, J.L., 2017, Post-1590 Ma modification of the supergiant Olympic Dam deposit: links with regional tectonothermal events, in Proceedings of the 14th SGA Biennial Meeting, 20-23 August 2017, Québec City, Canada, v. 3, p. 847-850.

Cherry, A.R., Kamenetsky, V.S., Ehrig, K., McPhie, J., Kamenetsky, M. and Apukhtina, O., 2016, Sedimentary facies within the Olympic Dam Breccia Complex: a potential metal source, in AESC 2016 – Australian Earth Sciences Convention abstracts, 26-30 June 2016, Adelaide, Australia, p. 76.

Cherry, A.R., Kamenetsky, V.S., Ehrig, K., McPhie, J., Kamenetsky, M., Ciobanu, C.L. and Cook, N.J., 2015, Petrography and provenance of bedded sedimentary units within the Olympic Dam deposit, in SEG 2015 – Society of Economic Geologists Conference, 27-30 September 2015, Hobart, Australia, p. 186.

Acknowledgements

Dima Kamenetsky, my primary supervisor, made this project possible and gave guidance throughout.
My two co-supervisors, Kathy Ehrig provided support both knowledgeable and financial,
And Jocelyn McPhie offered semantic rigour and engagement that I could not do without,
And who thought my writing was 'almost exceptional'. Their support was essential.

Sebastien Meffre and Jay Thompson provided critical insight to geochronology interpretation.
Maya Kamenetsky aided with data analysis and taught me how to prepare samples with success.
John Keeling and Liz Jagodzinski from the GSSA are appreciated for their collaboration,
And Jim Crowley from Boise facilitated hands-on exposure to the CA-TIMS process.

Karsten Goemann and Sandrin Feig of the CSL assisted with data collection.
Fellow PhD candidates of the Olympic Dam team (Matt, Nathan, Olga, and Qiuyue), along with my
Other UTas PhD friends (Brian, Cassady, Laura, Naomi, Adam, and Dave) helped give me direction
Their camaraderie and constructive discussion enabled me to scrape by.

My family in Sydney are thanked for their assistance.
Final thanks go to Emily, for your supreme patience with the long distance.

Chapter 1 - Introduction

1.1 Preamble

The supergiant Olympic Dam Cu-U-Au-Ag deposit (located in the Gawler Craton of South Australia, Fig. 1.1) is one of the largest economic accumulations of Cu, U, Au and Ag in the world (10.1 Gt at 0.78% Cu, 0.25 kg/t U_3O_8, 0.33 g/t Au, 1 g/t Ag; BHP, 2017). Olympic Dam is part of the Olympic Cu-Au(-U) Province along the eastern margin of the Gawler Craton (Skirrow et al., 2007). The Olympic Province includes numerous deposits and prospects (including the Acropolis prospect) that have been suggested to be temporally related to the Olympic Dam deposit (e.g. Bastrakov et al., 2007; Skirrow et al., 2007; Hayward and Skirrow, 2010) as well as the voluminous Gawler Range Volcanics and Hiltaba Suite granitoids that occur over much of the Gawler Craton (Fig. 1.1). Olympic Dam was one of the deposits used to define the Iron Oxide-Copper-Gold (IOCG) deposit class (Hitzman et al., 1992), but is unique for its size and polymetallic endowment. The size and significance of the Olympic Dam deposit to the IOCG class emphasises the importance of understanding the architecture and genesis of the deposit. Genetic interpretation depends on a good understanding of the architecture and timing of events, both of which have been challenging in the context of Olympic Dam. Prior study of the deposit has been impeded by over 300 m of cover; initial studies were limited by sparse drill holes from surface (Roberts and Hudson, 1983) or relatively limited underground exposures (Oreskes and Einaudi, 1990; Reeve et al., 1990). This thesis is devoted to advancing knowledge of both the architecture and timing of the Olympic Dam deposit as well as contributing to the temporal evolution of the Olympic Province as a whole using integrated textural, mineralogical and geochronological data.

1.2 Significance and aims

The Olympic Dam deposit is hosted by an Fe-oxide-rich breccia complex (the Olympic Dam Breccia Complex – ODBC) which is, in turn, hosted entirely within the ca. 1590 Ma Roxby Downs Granite (RDG). The majority of the ODBC is comprised of variably brecciated, altered RDG and also contains clasts and domains of other lithologies (Fig. 1.2 and 1.3), including surficial facies. The surficial facies (which include bedded clastic facies such as mudstones, sandstones and conglomerates of varying provenances and tuffaceous mudstones, as well as felsic volcanic rocks) are also brecciated and have been affected by the OD hydrothermal system. These surficial facies were used by various workers to underpin models of the genesis and setting of the ODBC and deposit (e.g. Roberts and Hudson, 1983; Oreskes and Einaudi, 1990; Reeve et al., 1990; Johnson and Cross, 1995; McPhie et al., 2011b; McPhie

et al., 2016). However, the temporal relationship and setting of the surficial facies with each other, the RDG and the ODBC have not been adequately constrained. None of the prior geochronology at Olympic Dam has had sufficient precision to discriminate amongst the different host lithologies, which has, in part, contributed to the interpretation that the ODBC and deposit developed entirely within a geologically brief magmatic-hydrothermal event at ca. 1590 Ma (e.g. Johnson and Cross, 1995).

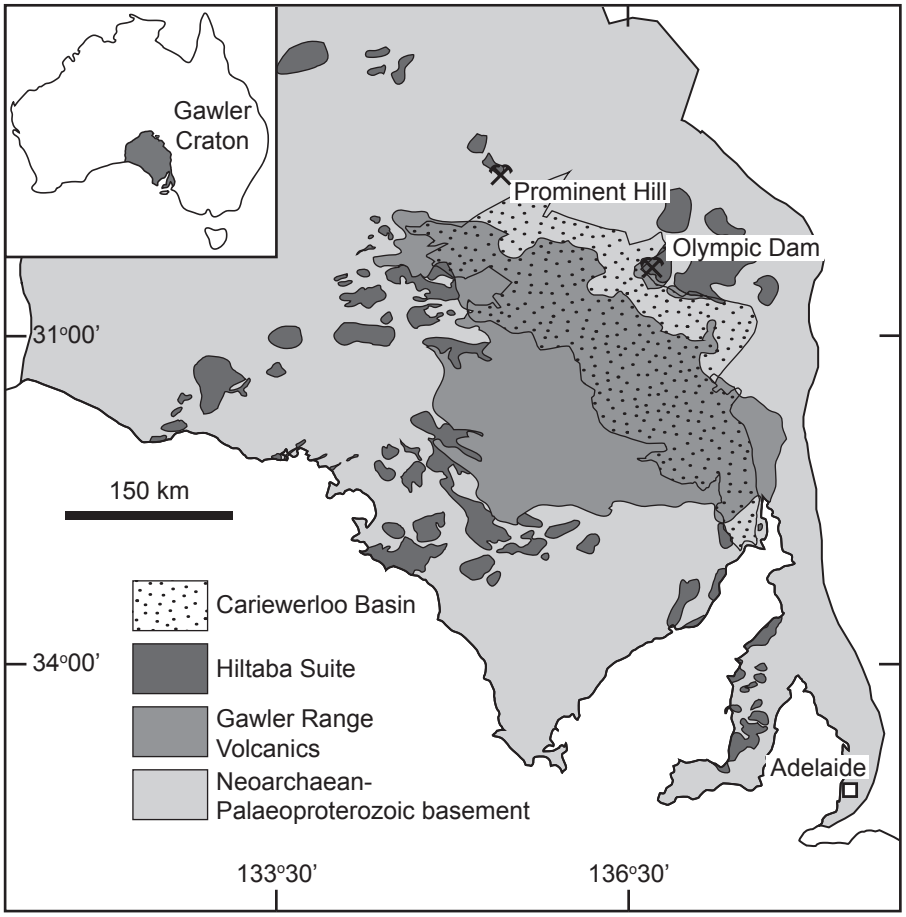

Figure 1.1 Simplified pre-Neoproterozoic crystalline basement of the Gawler Craton in South Australia (after Hand et al., 2007). The extent of the Mesoproterozoic Cariewerloo Basin is also shown.

Hydrothermal assemblages in the ODBC exhibit a deposit-wide zonation (Reeve et al., 1990; Ehrig et al., 2012). A gross zonation is apparent in Cu-Fe sulfides from S- and Fe-rich species (pyrite and chalcopyrite) in the margins of the deposit to S- and Fe-poor species (bornite and chalcocite) towards the centre. Uranium minerals (uraninite, coffinite, brannerite) are complexly zoned throughout the deposit. A reduced Fe-oxide assemblage (magnetite + apatite + siderite + chlorite + quartz) occurs toward the periphery (outward and at depth) of the deposit and grades inward to a more oxidised Fe-oxide assemblage (hematite + sericite + fluorite) and then a strongly oxidised assemblage (hematite + quartz + barite) in the central parts of the deposit. The consensus among prior workers is that the reduced Fe-oxide assemblage was replaced by the oxidised Fe-oxide assemblage (e.g. Oreskes and Einaudi, 1990; Reeve et al., 1990; Hayward and Skirrow, 2010; Ehrig et al., 2012; Ciobanu et

al., 2013; Krneta et al., 2016; Apukhtina et al., 2017). Geochronology on components of the reduced and oxidised Fe-oxide assemblages at Olympic Dam has indicated both assemblages were formed at ca. 1590 Ma, shortly after emplacement of the RDG (Ciobanu et al., 2013; Courtney-Davies et al., 2016; Apukhtina et al., 2017). However, some workers have proposed that there has been episodic modification, and potentially even upgrade, of the Olympic Dam resource long after 1590 Ma (e.g. Trueman, 1986; McInnes et al., 2008; Meffre et al., 2010; Maas et al., 2011; Kamenetsky et al., 2015; Ehrig, 2016). In addition, it is unclear whether the regionally significant red-bed Pandurra Formation

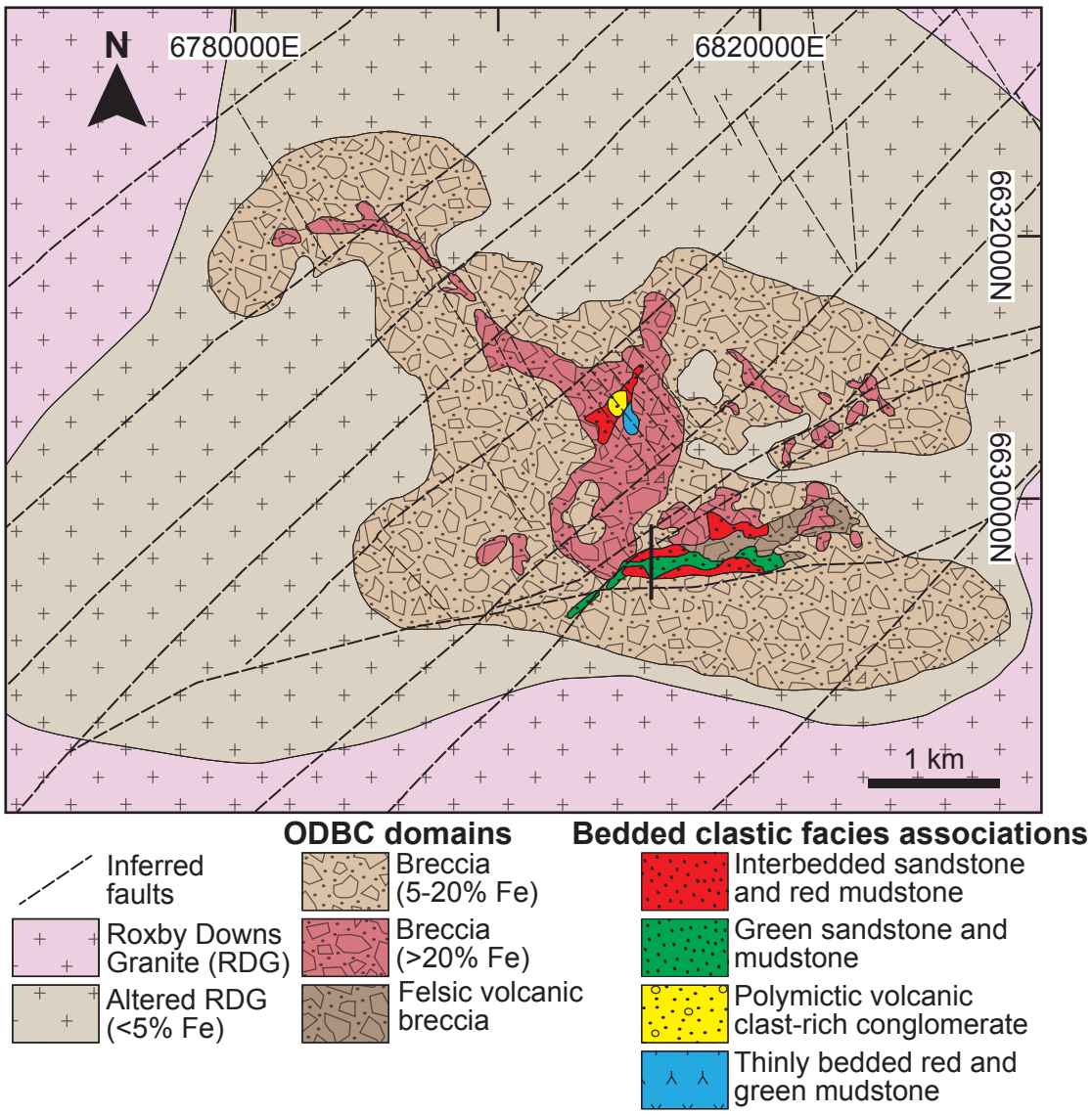

Figure 1.2 Plan view of the Olympic Dam Breccia Complex immediately below the unconformity with younger, unmineralised sedimentary successions of the Stuart Shelf. Simplified geology is shown, including the main Olympic Dam Breccia Complex (ODBC) zones and domains of bedded clastic facies associations. Inferred structure is based on underground mapping, oriented drillcore, acoustic televiewer logging and regional geophysical datasets. Deposit location is -30°26'25.225", 136°53'21.702", grid coordinates on the figure are referenced to GDA94/MGA zone 53 (after Ehrig et al., 2012).

sandstones of the Cariewerloo Basin that unconformably overlie much of the crystalline basement of the Olympic Province (Fig. 1.1) (Cowley, 1991) is related to the bedded clastic facies in the ODBC or played a role in the formation of the deposit (Johnson and McCulloch, 1995).

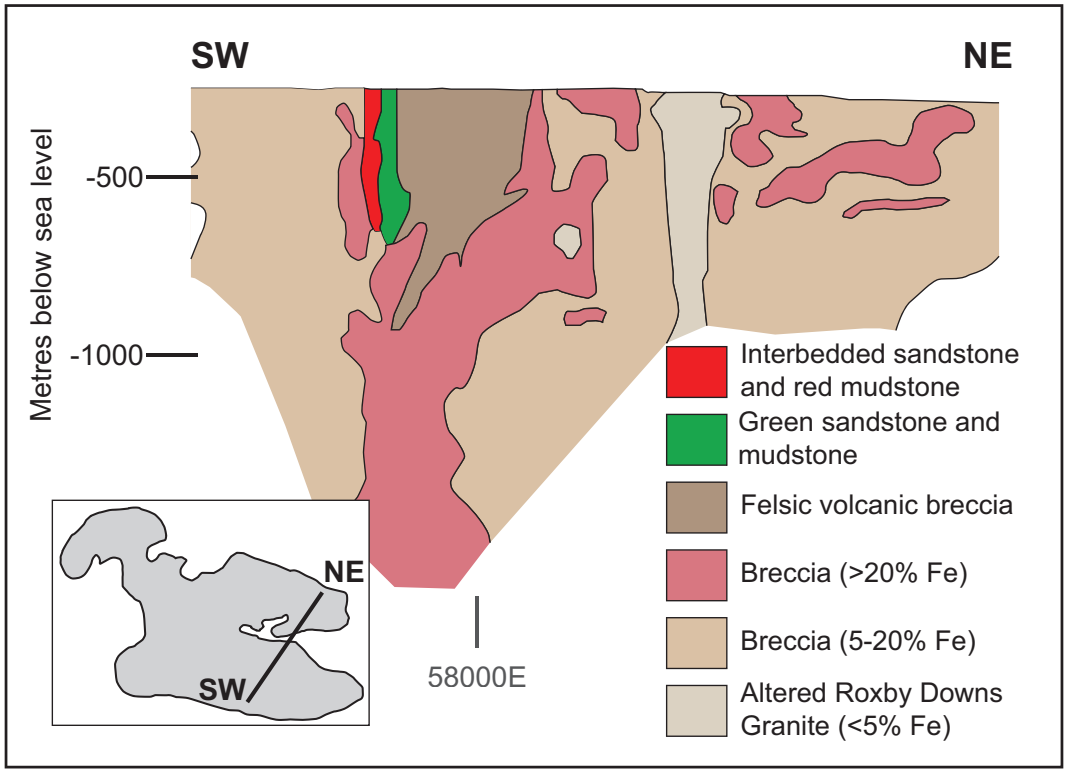

Figure 1.3 Cross-section of the Olympic Dam Breccia Complex showing distribution of the domains of surficial facies and breccia according to total Fe content, after Ehrig et al. (2012). The inset shows the location of the cross-section relative to the 5% Fe outline of the ODBC.

The Acropolis prospect, located approximately 20 km SW of Olympic Dam (Fig. 1.4), preserves a similar textural relationship between relatively reduced and oxidised Fe oxide assemblages as previously described at Olympic Dam (Paterson, 1986; Krneta et al., 2017). However, the only geochronology at Acropolis has been on apatite (ca. 1600-1590 Ma; Mortimer et al., 1988; Thompson et al., 2016), which is associated with the reduced Fe-oxide assemblage and is typically altered or recrystallised where hematite is present (Krneta et al., 2017); no attempt has been made to constrain the timing of alteration of the initial magnetite-rich assemblage in the prospect.

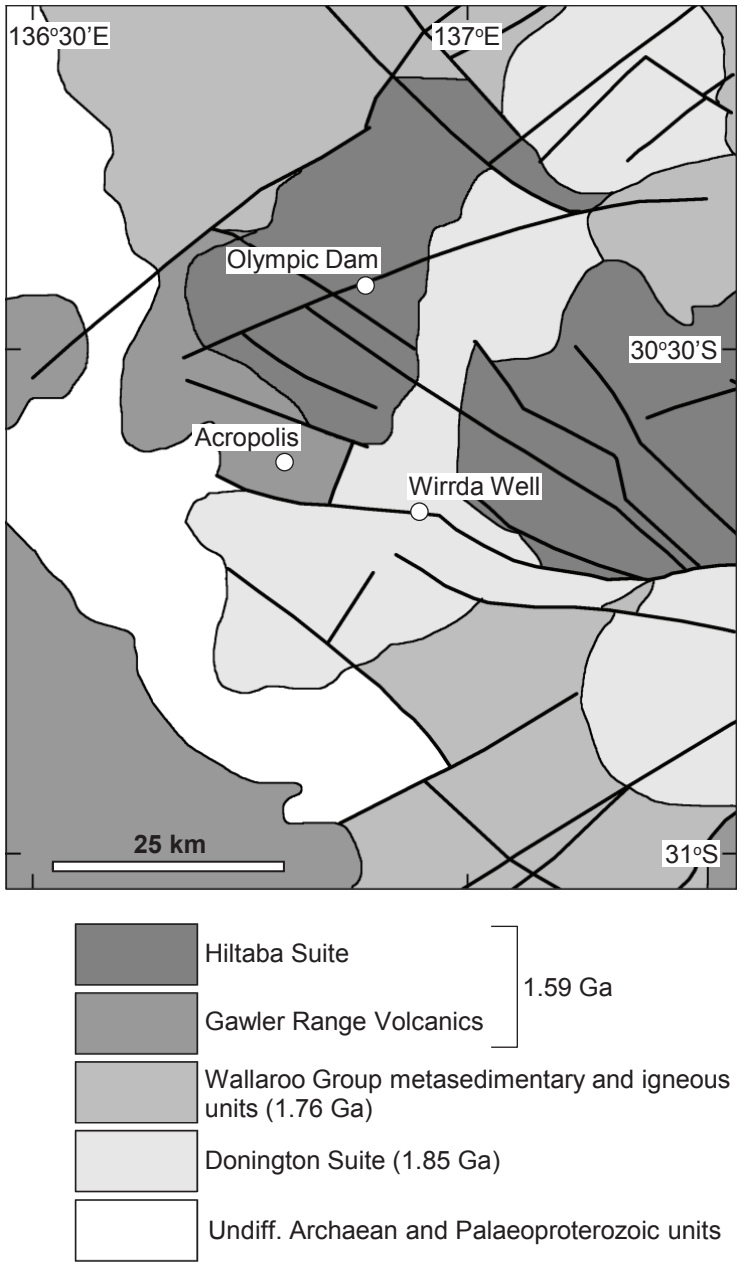

Figure 1.4 Regional geology of pre-Neoproterozoic crystalline basement in the vicinity of the Olympic Dam deposit and Acropolis prospect. Heavy black lines represent faults (after Skirrow et al., 2007).

This thesis contributes to the development of a geochronological framework to understand the formation and evolution of the Olympic Dam deposit and the Olympic Province. The specific aims of this study are to:

1. Determine the temporal relationship and setting of the surficial facies (bedded clastic facies and felsic volcanic rocks) in the ODBC with the host RDG and propose an incorporation model for the surficial facies into the ODBC

2. Determine if a specific clastic facies association (quartz-rich sandstone) in the ODBC is related Cariewerloo Basin sandstones and describe the implications for post-1590 Ma modification of Olympic Dam

3. Constrain the timing of alteration of the Acropolis prospect and discuss the implications of the impact of distal tectonothermal events on the wider Olympic Province

Resolving the relative setting and age of the host rocks to the Olympic Dam deposit and modelling the incorporation of the surficial facies into the ODBC contributes to constraining the maximum age and initial architecture of the deposit and the ODBC. Identifying the origin of the various lithologies that have been entrained into the ODBC will provide a clearer picture of the evolution of Olympic Dam and contribute to understanding of the role these lithologies may have had in the development of the ODBC and deposit. Identifying other tectonothermal events that affected Olympic Dam or elsewhere in the Olympic Province contributes to understanding the temporal evolution of the deposits and prospects in this metallogenic province. The prolonged, episodic history of modification of the ODBC and deposit may be what is required to form other polymetallic supergiant ore deposits.

1.3 Methods and approach

The aims of this study are addressed mainly through the application of precise geochronology to refine timing of emplacement or deposition of igneous or clastic host rocks, determine provenance of clastic facies in the ODBC and potential correlative successions present regionally, and determine the timing of formation of diagenetic, hydrothermal or secondary mineral phases. Mineral chemistry and textural analyses are employed to supplement the geochronological results and interpretations.

This study was conducted primarily on samples collected from drill core, the majority of which were from the drill core collection at BHP Olympic Dam in South Australia. A number of drill holes were logged on site at Olympic Dam prior to sample collection. Geochronology was conducted on mineral grain separates or in-situ with laser ablation-inductively coupled mass spectrometry (LA-ICPMS) as well as chemical abrasion-thermal ionisation mass spectrometry (CA-TIMS). Sample examination and imaging were conducted by optical and electron microscopy methods. Geochemical analyses of minerals were conducted by LA-ICPMS and electron microscopy methods (e.g. scanning electron microscopy and electron microprobe). The majority of analytical work was conducted at

the University of Tasmania (including at the Central Science Laboratory); the CA-TIMS analyses were conducted at Boise State University (Idaho, United States of America). Detailed descriptions of the methods of sample preparation and analytical techniques are presented in chapters 2, 3 and 5.

1.4 Thesis structure

The results of this thesis are presented in three research chapters following this introductory chapter. Each chapter focuses on a specific aim raised in the previous section of this chapter. The research chapters are presented in the structure of manuscripts that have been published or are currently under review for publication in peer-reviewed scientific journals. The content of the research chapters is unchanged but has been reformatted to fit into the thesis. The research chapters are briefly summarised and listed below:

Chapter 2, submitted to *Precambrian Research*, presents precise zircon geochronology of felsic volcanic rocks (GRV) and bedded clastic facies in the ODBC as well as the host RDG to constrain the timing and setting of those lithologies. This study also discusses the provenance, setting and incorporation of the bedded clastic facies into the ODBC.

Chapter 3, published in *Precambrian Research* (vol. 300, 2017), describes the quartz-rich sandstone facies association in the ODBC and identifies the Pandurra Formation as the best regional correlate. The implications of this correlation are discussed in the context of post-1590 Ma tectonic activity and potential introduction of U.

Chapter 4, submitted to the *Australian Journal of Earth Sciences*, describes the U-Th-Pb systematics of apatite, monazite and xenotime in the hydrothermal assemblage at the Acropolis prospect. This study also identifies multiple tectonothermal events affecting the Acropolis prospect, including two post-1590 Ma events.

The final chapter (**Chapter 5**) presents a summary of the findings and explores the significance of the research chapters. Potential future research questions that have become apparent as a result of this study are suggested at the end of the chapter.

Chapter 2 - Precise geochronological constraints on the origin, setting and incorporation of ca. 1.59 Ga surficial facies into the Olympic Dam Breccia Complex, South Australia

Precambrian Research, v. 315, p. 162-178

Alexander R. Cherry[1,*], Kathy Ehrig[2], Vadim S. Kamenetsky[1], Jocelyn McPhie[1], James L. Crowley[3], and Maya B. Kamenetsky[1]

[1]ARC Centre of Excellence in Ore Deposits (CODES), School of Natural Sciences, University of Tasmania, Hobart, Tasmania 7005, Australia

[2]BHP Olympic Dam, 55 Grenfell Street, Adelaide, South Australia 5000, Australia

[3]Department of Geosciences, Boise State University, 1910 University Drive, Boise, Idaho 83725, United States

2.0 Abstract

The Olympic Dam Breccia Complex (host to the Olympic Dam Cu-U-Au-Ag deposit) is derived largely from granite (Roxby Downs Granite) but includes clasts and domains derived from surficial facies (felsic volcanic rocks and bedded clastic facies). New high-precision CA-TIMS geochronology is used to constrain the ages of the granite, the volcanic rocks and bedded clastic facies. The felsic volcanic rocks (1594.73 Ma ± 0.30 Ma) are slightly older than the granite (1593.87 Ma ± 0.21 Ma). These ages, together with the absence of any older country rock in the breccia complex, suggest the felsic volcanic rocks that were originally present at Olympic Dam were intruded by the granite. The deposition of the bedded clastic facies (tuffaceous mudstone) has been constrained to 1590.97 ± 0.58 Ma, indicating the presence of a basin around 3 myr after emplacement of the granite and felsic volcanic rocks. Extrusive correlatives of mafic-ultramafic dykes intruding the breccia complex are proposed as a local source of detrital Cr-spinel in the bedded clastic facies. The granitoid-dominated provenance of some of the bedded clastic facies implies that ca. 1593 Ma granitoids were exposed when the bedded clastic facies were accumulating; the absence of ≥1740 Ma detrital zircons indicates the provenance did not extend beyond granitoids of the Burgoyne Batholith in the vicinity of Olympic Dam. An initial stratigraphic sequence is proposed for the BCF involving a transition in provenance from volcanic-dominated to granitoid-dominated. Faults are proposed to have been responsible for the segmentation and incorporation of the bedded clastic facies into the Olympic Dam Breccia Complex. The formation of the Olympic Dam Breccia Complex and Olympic Dam hydrothermal system

post-dated the emplacement of the Roxby Downs Granite (at 1593.87 ± 0.21 Ma). The bedded clastic facies (1590.97 ± 0.58 Ma) have been altered and mineralised.

2.1 Introduction

The Olympic Dam (OD) Cu-U-Au-Ag deposit is one of the largest in the world; current total resources have been estimated at over 10.1 Gt (0.78% Cu, 0.25 kg/t U_3O_8, 0.33 g/t Au, 1 g/t Ag) (BHP, 2017). Based on limited drill-hole information, OD was first described as a type of "sediment-hosted ore deposit" (Roberts and Hudson, 1983; p. 799). Successive studies following additional drilling and underground development reinterpreted the deposit to be hosted within a breccia complex (Olympic Dam Breccia Complex - ODBC) inside a granite pluton (Roxby Downs Granite - RDG) and suggested a "hydrothermal-tectonic" origin for the breccia complex (Oreskes and Einaudi, 1990; Reeve et al., 1990). The ODBC mainly comprises clasts of variably hematite-altered granite; clasts of mafic-ultramafic, felsic volcanic (correlated with the Gawler Range Volcanics - GRV) and various bedded clastic facies are locally the dominant clast-type (Reeve et al., 1990). Domains of bedded clastic facies have gradational or faulted contacts with the ODBC and are internally deformed (McPhie et al., 2011b; Ehrig et al., 2012).

The bedded clastic facies (BCF) are well bedded and overall relatively fine-grained (McPhie et al., 2011b). The origin of the BCF is a major aspect of two contrasting models of the architecture, early setting and relative timing of formation of the ODBC and deposit (Oreskes and Einaudi, 1990; Reeve et al., 1990; Johnson and Cross, 1995; McPhie et al., 2011b; Ehrig et al., 2012; McPhie et al., 2016). Reeve et al. (1990) suggested the BCF occurred within "localised diatreme structures" and represented deposits from explosive venting of the OD hydrothermal system (p. 1017). This model proposed that the BCF were derived from the ODBC as "reworked hydrothermal eruption breccias" and locally from the GRV (Reeve et al., 1990; p. 1033). Johnson and Cross (1995) dated samples thought to be from the diatreme structures and felsic dykes that post-dated mineralisation with the intent of determining a minimum age of the OD orebody. The diatreme model has had a significant influence on work on the age, and fluid and metal sources of OD, as well as on strategies of exploration for similar deposits (e.g. Oreskes and Einaudi, 1992; Haynes et al., 1995; Johnson and Cross, 1995; Johnson and McCulloch, 1995; Skirrow et al., 2007; Hayward and Skirrow, 2010). The alternative model proposed the BCF were remnants of a sedimentary basin that overlay the ODBC (Oreskes and Einaudi, 1990; McPhie et al., 2011b) and that the OD hydrothermal system may have interacted with the overlying basin (McPhie et al., 2011b; McPhie et al., 2016).

This study reports precise zircon chemical abrasion-thermal ionisation mass spectrometry (CA-TIMS) geochronology to constrain the ages and relationships of the BCF, the RDG and volcanic rocks (GRV) in the ODBC. The new ages indicate the RDG probably intruded the GRV at OD and that the BCF were deposited around 3 myr after emplacement of the GRV and RDG. The earliest timing of formation of the ODBC and OD hydrothermal system is constrained by the age of the RDG. The BCF are brecciated and contain hydrothermal minerals, implying that tectonic and hydrothermal activity was occurring after ca. 1591 Ma. Additional insights into the provenance of the BCF are provided, based on Cr-spinel compositional data, LA-ICPMS geochronology, and descriptions and interpretations of previous workers. The above data and interpretations (including those of previous workers) are used to propose an original stratigraphy of the surficial facies (BCF and GRV) and a model of their incorporation into the ODBC.

2.2 Geological setting

The Gawler Craton is dominated by late Archaean, Palaeoproterozoic and early Mesoproterozoic successions (Fig. 2.1a) (Drexel et al., 1993; Hand et al., 2007). The late Archaean Mulgathing and Sleaford Complexes (~2500 Ma) occupy the central-northern and southern portions of the craton, respectively (Hand et al., 2007). The Palaeoproterozoic Hutchison Group (~2000-1866 Ma) and Donington Suite (~1850 Ma) occur in the south and east, whereas the metasedimentary Wallaroo Group (~1760-1740 Ma) occurs along the eastern margin of the craton (Hand et al., 2007). These units were deformed in the Kimban orogeny (~1730-1690 Ma); the Archaean units were also affected by the earlier Sleafordian (~2480-2420 Ma) orogeny (Hand et al., 2007).

The granitoid Hiltaba Suite and co-magmatic GRV constitute an early Mesoproterozoic (~1590 Ma) silicic large igneous province (the Gawler SLIP; Allen et al., 2008; McPhie et al., 2008). The GRV are widespread over the central and eastern Gawler Craton and are subdivided into the upper GRV (thick, voluminous felsic lavas, ca. 1587 Ma) and lower GRV (very thick but spatially restricted felsic and subordinate mafic volcanic units, 1595-1587 Ma) (Blissett et al., 1993). The contemporaneous Benagerie Volcanic Suite in the Curnamona Province to the west of the Gawler Craton (Wade et al., 2012) indicates earliest Mesoproterozoic magmatism also extended beyond the Gawler Craton. Sedimentary successions of GRV age or related to GRV volcanism occur at Roopena (~270 km S of Olympic Dam; Curtis et al., 2018), Prominent Hill (~150 km NW of Olympic Dam; Bull et al., 2015) and OD (Reeve et al., 1990). The Hiltaba Suite comprises predominantly granitic batholiths and plutons, though there

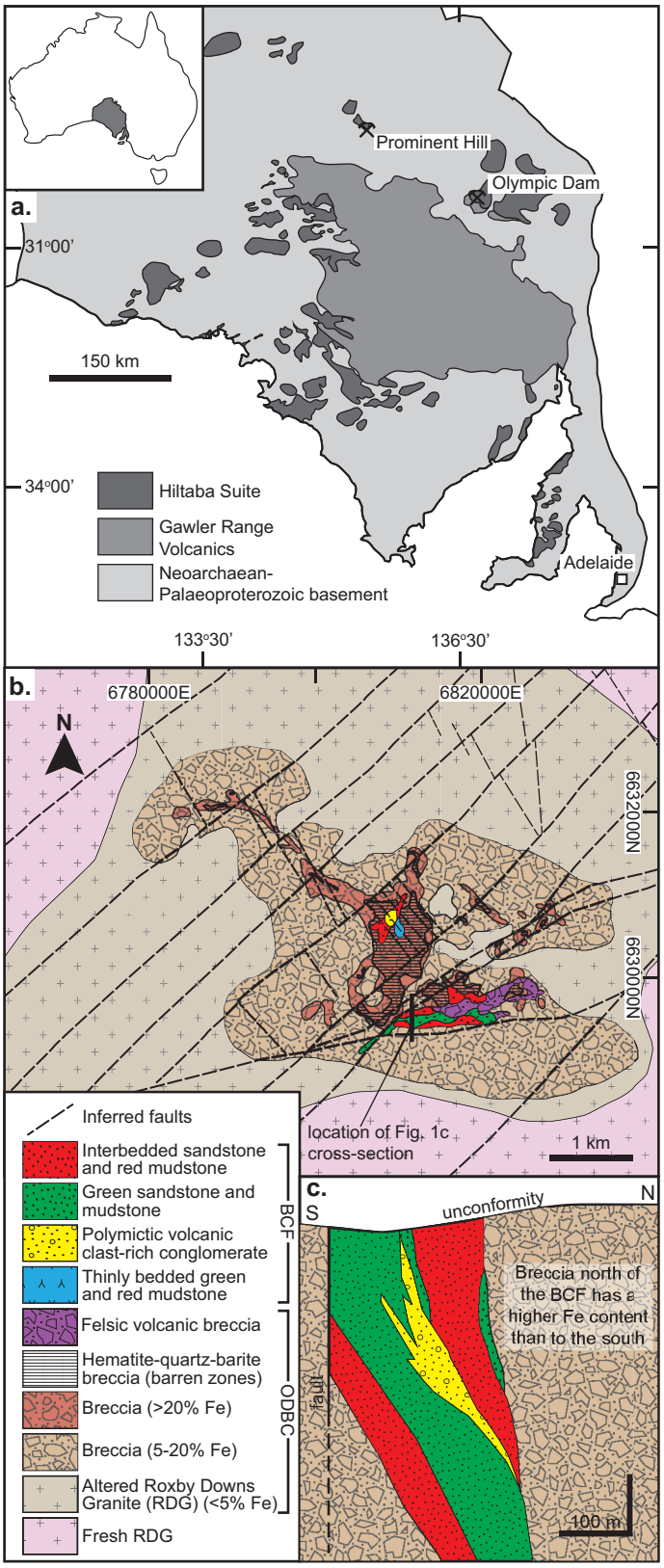

Figure 2.1 a. Simplified pre-Neoproterozoic crystalline basement geology of the Gawler craton (after Hand et al., 2007). **b.** Plan view of the Olympic Dam deposit immediately below the unconformity showing simplified geology, including BCF and main ODBC zones/domains. Deposit location is -30°26'25.225", 136°53'21.702", grid coordinates on the figure are referenced to GDA94/MGA zone 53 (after Ehrig et al., 2012). **c.** North-south cross-section of the western part of the southern BCF domain from McPhie et al. (2016) showing the multiple intervals of the different facies associations. RD2766, RD2767, RD2768, RD896, RU38-2625, RU38-2626 were the drill holes used by McPhie et al. (2016) to generate the cross-section.

is considerable compositional variation including the presence of minor mafic plutons (Flint, 1993). Evidence of deformation associated with emplacement of the Hiltaba Suite is summarised by Hand et al. (2007), who suggested it was restricted to contractional shear zones striking northwest-southeast in the western part of the Gawler Craton.

The eastern Gawler Craton and Gawler SLIP are unconformably overlain by the Mesoproterozoic (ca. 1.4 Ga) red-bed Pandurra Formation (Fanning et al., 1983; Preiss, 1987b; Cowley, 1991; Cherry et al., 2017). The Pandurra Formation is, in turn, unconformably overlain by the Neoproterozoic to Cambrian Stuart Shelf sedimentary formations (Preiss, 1993b, 2000). Mafic dykes of the Gairdner Dolerite dyke swarm intruded the northern and eastern Gawler Craton during the Neoproterozoic (ca. 830 Ma; Wingate et al., 1998).

2.3 Geology of Olympic Dam

The OD deposit is entirely contained within the ODBC, which is enclosed by the RDG (Fig. 2.1b), a member of the Hiltaba Suite (Reeve et al., 1990; Johnson and Cross, 1995). The main components in the ODBC are derived from the surrounding RDG and hydrothermal sources (Reeve et al., 1990). Brecciated felsic and mafic/ultramafic GRV (Reeve et al., 1990; Huang et al., 2016) and BCF (McPhie et al., 2011b) are also present and are locally significant in the ODBC. Gairdner Dolerite dykes intrude the ODBC (Huang et al., 2015).

The ODBC-RDG boundary is gradational and marked by progressively altered and brecciated granite (Reeve et al., 1990). The margin of the ODBC is defined by Ehrig et al. (2012) as the altered envelope where igneous biotite is not preserved in the granite (1 to 5 km from the deposit centre). In detail, the ODBC comprises numerous, irregularly shaped breccia bodies that consist of differing proportions of hematite and altered granite protolith (Oreskes and Einaudi, 1990; Reeve et al., 1990). However, there is a systematic increase in intensity of brecciation and hydrothermal alteration (mainly in the form of hematite addition) from the margins inward (Reeve et al., 1990; Ehrig et al., 2012). The intensity of brecciation and alteration can be such that identification of many of the protolith lithologies in the ODBC (such as granite, BCF and felsic and mafic-ultramafic GRV correlatives) is difficult (Ehrig et al., 2012). The hematite (or Fe) content is used to subdivide the breccias within the ODBC (Reeve et al., 1990). Granite-rich breccia largely consists of angular granite clasts, a relatively minor hydrothermal component (e.g. hematite) and low proportion of matrix (Reeve et al., 1990).

Hematite-rich breccia contains a much higher hydrothermal component relative to the granite component and matrix abundance increases with increasing hematite content (Reeve et al., 1990; Ehrig et al., 2012). Some domains in the hematite-rich breccia contain abundant felsic volcanic clasts (felsic volcanic breccia), particularly in the vicinity of the large (up to 300 m across/thick) domains of BCF in the southern portion of the ODBC (McPhie et al., 2011b; Ehrig et al., 2012). The felsic volcanic clasts in the felsic volcanic breccia are feldspar-phyric and have been suggested to be the incorporated remnants of felsic GRV unit(s) that were originally present above the RDG (Reeve et al., 1990; McPhie et al., 2011b).

Sericite (muscovite, illite, phengite and minor paragonite) is widespread throughout the ODBC and is the dominant alteration phase in the outer portions of the ODBC (e.g. granite-rich breccia). Sericite has been replaced by hematite towards the centre of the deposit (Ehrig et al., 2012), where the breccias contain little other than hematite, quartz and barite (Fig. 2.1b) (Reeve et al., 1990). Magnetite is present around the margins and at depth in the deposit (Ehrig et al., 2012). Significant hydrothermal fluorite, barite, pyrite, quartz, siderite, apatite and chlorite also occur, amongst numerous other phases (Ehrig et al., 2012). The main ore minerals include Cu-Fe sulfides (chalcopyrite, bornite, and chalcocite-like group minerals (i.e. chalcocite, digenite, djurleite, roxbyite, anilite), U minerals (uraninite, coffinite and brannerite), electrum and many minor phases (Ehrig et al., 2012). The majority of the ore occurs in hematite-rich breccia, although significant ore may be associated with granite-rich breccia; the central hematite-quartz-barite breccia (Fig. 2.1b) is largely devoid of Cu and U minerals but locally contains important amounts of Au (Reeve et al., 1990; Ehrig et al., 2012). The deposit-wide zonation of Cu-Fe sulfides involves chalcopyrite-pyrite at depth and towards the margins of the deposit, and an overall transition to bornite-chalcocite at shallower levels and towards the centre of the deposit (Reeve et al., 1990).

The host granite, breccia complex and ore deposit are all unconformably overlain by 300 m of Stuart Shelf sedimentary formations, including the Tregolana Shale and a thin layer of Nuccaleena Dolomite immediately above the unconformity (Roberts and Hudson, 1983). The Pandurra Formation once overlay OD but is no longer preserved (Cherry et al., 2017).

2.4 Bedded clastic facies (BCF)

The general characteristics of the BCF are here summarised from previous authors; their main characteristics are most recently described by McPhie et al. (2016). The majority of the BCF within the ODBC are contained within two domains (Fig. 2.1b, c) that extend several hundred metres below the unconformity with Stuart Shelf formations; bedded clasts thought to be fragments of the BCF have been intersected in the ODBC over 1300 m below the unconformity (e.g. RD2786a, ~1900 m down hole). The southern domain is the largest and has an E-W extent of ~1300 m and a vertical extent of over 700 m (Fig. 2.1c) (McPhie et al., 2011b). The northern domain is over 500 m long and its vertical extent is over 200 m. Both domains are over 300 m across (McPhie et al., 2016). Margins of the domains of BCF are faulted, obscured by hematite alteration or are gradational into the surrounding hematite breccia (McPhie et al., 2011b). Some faults crosscutting the BCF are occupied by mafic dykes and intervals of hematite-rich breccia (McPhie et al., 2011b). Soft-sediment deformation of the BCF has resulted in locally disrupted beds and disharmonic folds and faults. Faults, contorted beds and broken drill-core commonly obscure the stratigraphic relationships within the BCF.

The facies associations discussed here are equivalent to those presented by McPhie et al. (2016): (1) green sandstone and mudstone, (2) interbedded sandstone and red mudstone, (3) polymictic volcanic-clast conglomerate, (4) thinly bedded green and red mudstone, and (5) quartz-rich sandstone. A description of the detrital and secondary components of the BCF based on Ehrig et al. (2012), McPhie et al. (2011b), (2016) and observed in this study is presented in Appendix 2.1 and in Figures 2.2 to 2.5.

1. The green sandstone and mudstone facies association (Fig. 2.2) is a significant component of the southern domain of the BCF and consists of interlaminated sandstone and mudstone, and some thicker (1-10 m) sandstone beds, many of which contain intraformational mudstone clasts (McPhie et al., 2016).

2. The interbedded sandstone and red mudstone (Fig. 2.3) is a significant component of both the southern and northern domains of the BCF (McPhie et al., 2016). This facies association consists of red mudstone interbedded with pale sandstone and minor granule/pebble conglomerate or breccia beds (Ehrig et al., 2012; McPhie et al., 2016). The sandstone beds are internally massive, laminated, graded or cross-laminated; the cross laminae may be defined by

heavy minerals.

3. The polymictic volcanic-clast conglomerate facies (Fig. 2.4) is present in both the northern and southern domains of the BCF (McPhie et al., 2016). The conglomerate beds are poorly sorted and internally massive, vary from clast- to matrix-supported, and are intersected as 3-70 m thick intervals in drill holes (Ehrig et al., 2012; McPhie et al., 2016). The majority of clasts in the conglomerate are rounded although some are angular and irregular (McPhie et al., 2016). The conglomerate matrix is referred to by Oreskes and Einaudi (1990), Reeve et al. (1990) and, Johnson and Cross (1995) as pale, sericite-altered "volcanic lapilli and ash". In contrast, McPhie et al. (2016) described the conglomerate matrix as composed of polymictic volcanic sand-sized grains and also noted thin intervals of sandstone of similar composition intercalated with the conglomerate.

4. The thinly bedded green and red mudstone facies (Fig. 2.5) is a volumetrically minor component of the BCF (McPhie et al., 2016). This facies association consists mostly of laminated, red, hematite-rich mudstone that resembles banded iron formation (ironstone) (Fig. 2.5a) (Ehrig et al., 2012), and pale green tuffaceous mudstone that is internally massive or laminated and includes hematite-rich laminae (Fig. 2.5e) (Oreskes and Einaudi, 1990; Reeve et al., 1990; Johnson and Cross, 1995; McPhie et al., 2016). McPhie et al. (2016) reported the presence of altered bubble-wall glass shards in the tuffaceous mudstone. Laminated barite (Oreskes and Einaudi, 1990), interlaminated green and red mudstone, and beds of pale grey, brown and purple fine-grained sandstone are also included in this facies association (McPhie et al., 2016).

5. The quartz-rich sandstone facies was first reported by McPhie et al. (2016). Cherry et al. (2017) expanded description of the facies and correlated it with the ca. 1.4 Ga Pandurra Formation (on the basis of matching detrital zircon age populations, diagenetic age and mineralogy; see Chapter 3). This facies has been identified in only a few drill holes, near the southern domain of BCF. Contacts (where observed) between the quartz-rich sandstone and other BCF are always faulted. The intervals of this facies are strongly brecciated and comprise fragments of coarse-grained, quartz-rich sandstone suspended in a red-brown matrix of disaggregated sandstone. The sandstone fragments and red-brown matrix are dominated by quartz with granitoid and metamorphic characteristics, and also contain detrital muscovite, tourmaline,

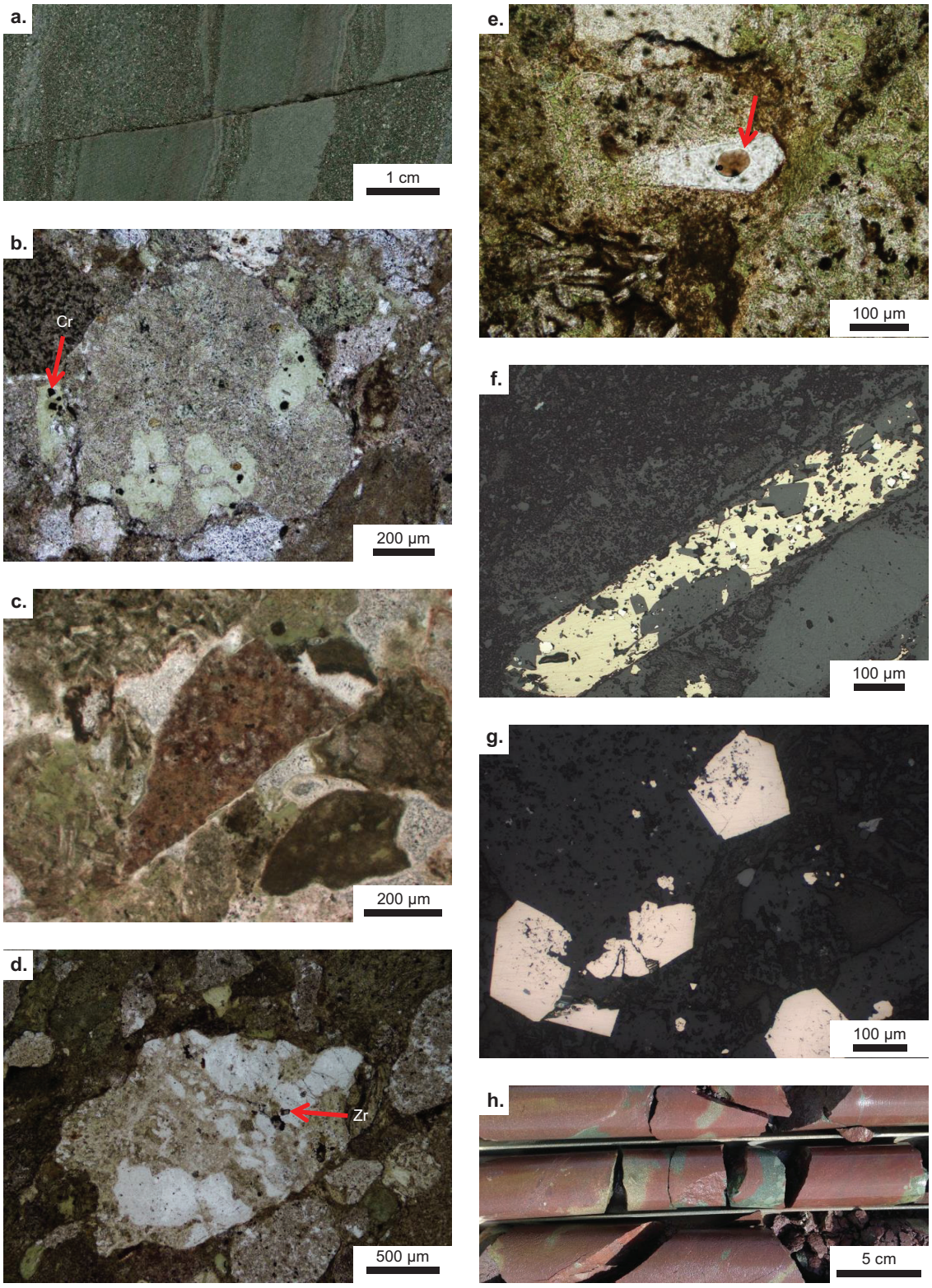

Figure 2.2 (right) Green sandstone and mudstone. **a.** Interbedded sandstone and mudstone (RD896, 607.15 m). **b.** Olivine-phyric lithic clast with fine Cr-spinel inclusions (fine opaque grains in chlorite-altered olivine, arrow) (Plane polarised light - PPL, RD1627, 522.3 m). **c.** Angular felsic volcanic clast with reddish hematite discolouration (PPL, RU38-2625, 434.5 m). **d.** Granite clast with contained zircon grain (arrow) (PPL, RD1627, 522.3 m). **e.** Volcanic-derived quartz grain with large melt inclusion (arrow) (PPL, RU38-2626, 399 m). **f.** Chalcopyrite and pyrite replacement of an elongate clast (Reflected light - RL, RD1624, 538.8 m). **g.** Large euhedral pyrite crystals, commonly with porous/spongy cores. Minor associated chalcopyrite (RL, RD1627, 738.4 m). **h.** Hematite altered originally green sandstone that is now red (RD1628, ~430 m).

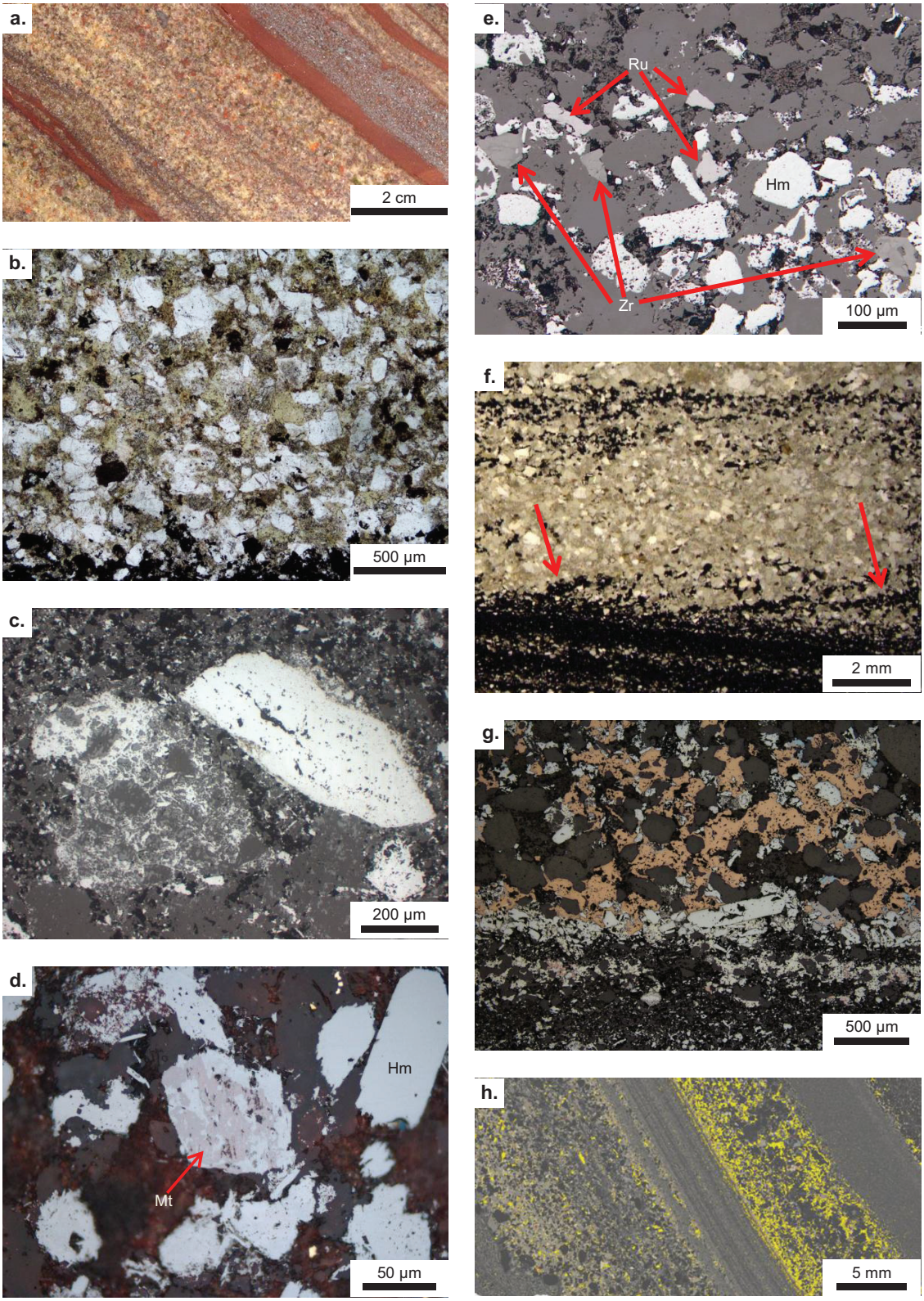

Figure 2.3 Interbedded sandstone and red mudstone. **a.** Interbedded sandstone and mudstone, the grey bed to the upper right contains significant specular hematite (RD1989, 601.5 m). **b.** Fine-grained sandstone with abundant quartz grains (white), sericite-altered clasts (yellow-brown) and some opaque hematite grains (PPL, RD1625, 685.4 m). **c.** Large elongate grains and hematite-quartz aggregate (RL, RU38-2626, 338.3 m). **d.** Hematite grain with patches of remnant magnetite (arrow) (RL, RD1625, 636.8 m). **e.** Heavy mineral band of hematite, zircon (arrows, Zr) and rutile (arrows, Ru) (RL, RD1625, 685.4 m). **f.** Quartz sandstone with opaque, hematite-rich beds and cross-beds (arrows) (PPL, RU38-2625, 345.7 m). **g.** Sandstone bed with hematite-rich layer adjacent to mudstone. Abundant bornite ± chalcocite (orange and blue) in the sandstone bed interstitial

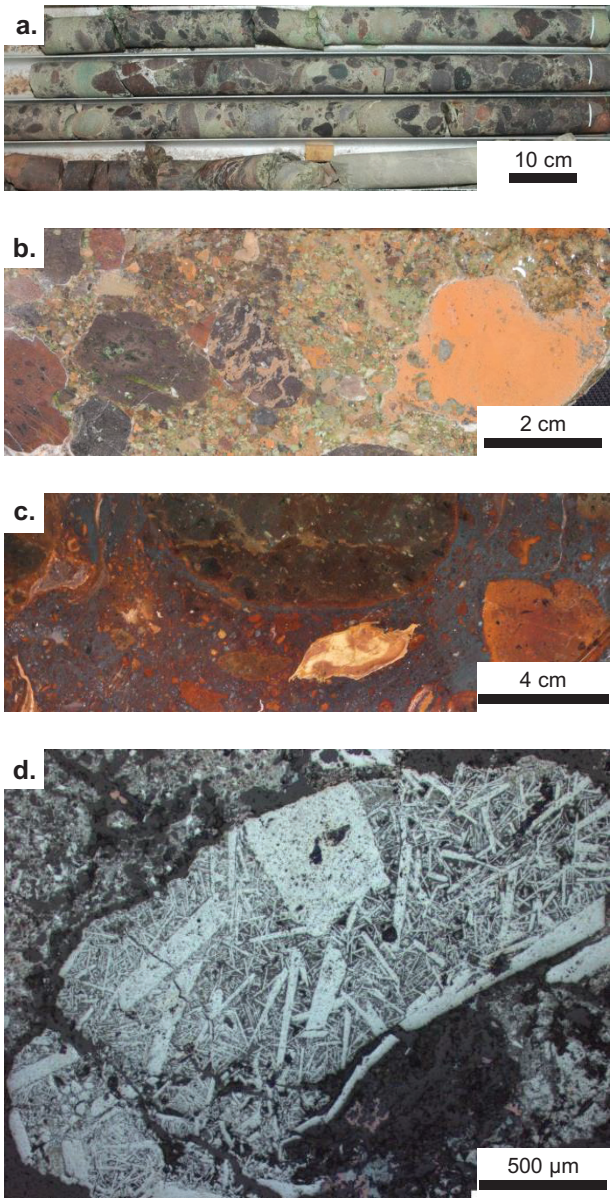

Figure 2.4 Polymictic volcanic-clast conglomerate **a.** Conglomerate with pale, tuff-like matrix. A hematite-rich interval at the bottom of the image grades into tuffaceous mudstone (RD3449, 403-406 m). **b.** Conglomerate with equivalent sand-sized matrix assemblage (RU31-6018, 103.8 m). **c.** Hematite-altered conglomerate with very hematite-rich matrix (RD3449, 405.5 m). **d.** Hematite-altered clast with preserved feldspar-phyric igneous texture (RL, RD2821, 668 m).

[continued from left] to detrital grains (RL, RD1625, 679 m). **h.** False colour back scattered electron image of the same sample as (g) showing the concentration of sulfide (yellow) in the sandstone beds relative to the mudstone beds (RL, RD1625, 679 m).

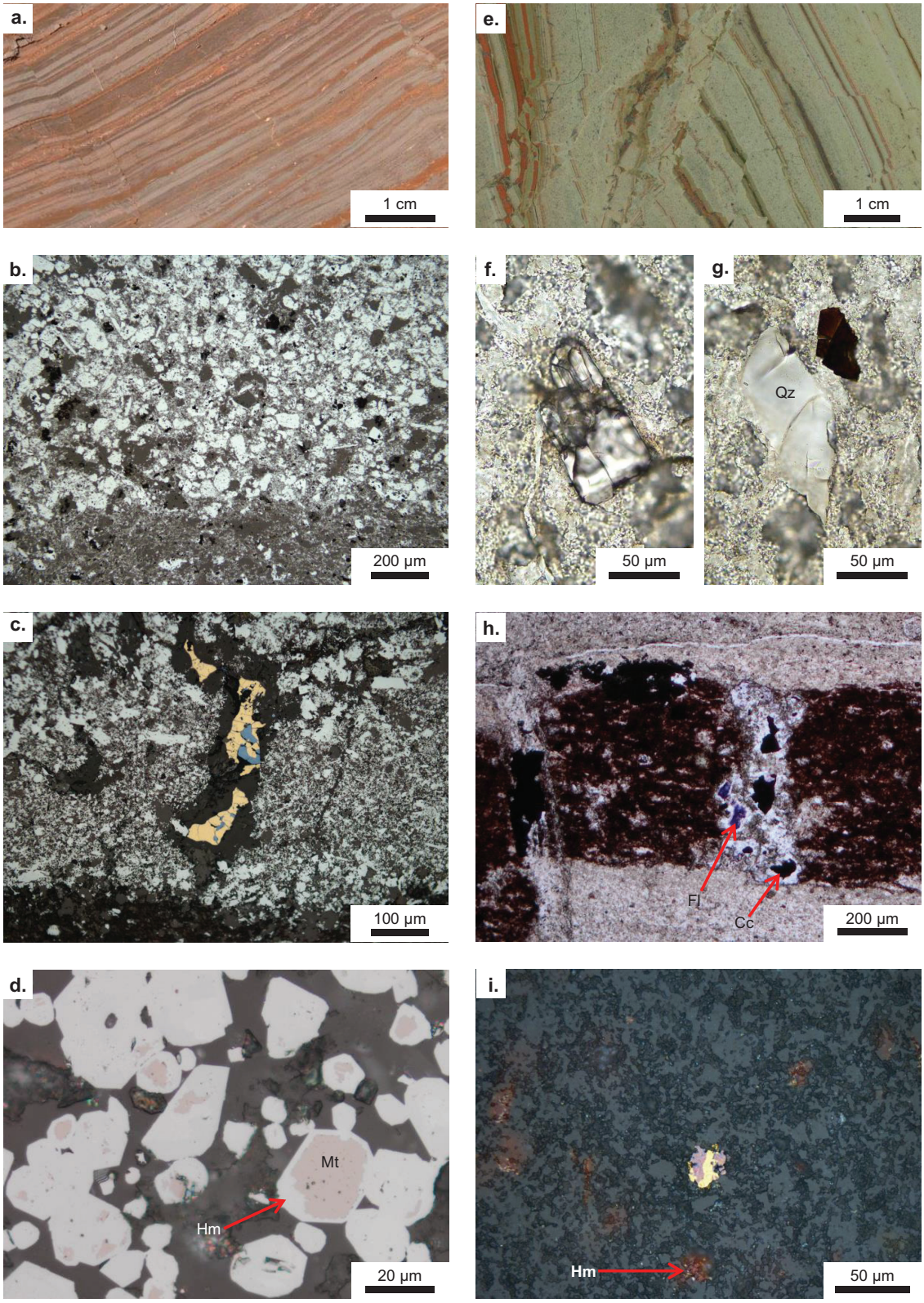

Figure 2.5 Tuffaceous mudstone and ironstone facies **a.** Finely laminated ironstone comprising alternating red and grey hematite-rich beds and sub-cm scale offsets (RD3449, 462.1 m). **b.** Bed of relatively coarse-grained hematite adjacent to a very fine-grained mudstone bed (RL, RD3449, 409.3 m). **c.** Veinlet of bornite, chalcocite and barite in a brittle fracture of a hematite-rich bed (RL, RD3449, 462.5 m). **d.** Hematite grains (arrow, Hm) with remnant magnetite cores (Mt); note the euhedral shaped grains (RL, RD3449, 486.4 m). **e.** Pale green tuffaceous mudstone with fine-grained, hematite-rich laminae (RD3449, 431.4 m). **f.** Euhedral, fractured zircon grain in tuffaceous mudstone (PPL, RD3449, 427.2 m). **g.** Angular quartz (Qz) and Cr-spinel (dark brown grain) in tuffaceous mudstone (PPL, RD3449, 427.2 m). **h.** Veinlet of opaque chalcocite (arrow, Cc) and fluorite (arrow,Fl)

zircon, hematite, ilmenite, and rutile. The sandstone fragments are cemented by quartz, illite and some hematite whereas the red-brown matrix contains abundant fine-grained hematite. The correlation of this facies with the Pandurra Formation indicates it is not related to the other BCF (Cherry et al., 2017) and so is not discussed further.

2.5 Zircon geochronology

The first zircon geochronology on the BCF at OD was conducted by Johnson and Cross (1995) on a sample of 'diatreme tuff' (probably equivalent to the tuffaceous mudstone component of the thinly bedded green and red mudstone) using the sensitive high-resolution ion microprobe (SHRIMP), which resulted in a $^{207}Pb/^{206}Pb$ weighted average age of 1597 ± 8 Ma (n = 26). Jagodzinski (2005) analysed zircon in 'volcaniclastic sandstone' (correlated with the green sandstone and mudstone association), producing a SHRIMP $^{207}Pb/^{206}Pb$ weighted average age of 1594.5 ± 3.3 Ma (n = 20). McPhie et al. (2016) reported laser ablation inductively coupled plasma mass spectrometry (LA-ICPMS) U-Pb ages of 1590.6 ± 3.2 Ma (n = 139, combined interbedded sandstone and red mudstone and green sandstone and mudstone facies associations) and 1603 ± 10 (n = 24, felsic volcanic clasts in polymictic volcanic-clast conglomerate facies) from three samples of the BCF. Johnson and Cross (1995) also analysed clasts from two units of "autobrecciated felsic dykes" (interpreted here to be conglomeratic intervals in the BCF or domains of felsic volcanic breccia), yielding respective SHRIMP $^{207}Pb/^{206}Pb$ weighted average ages of 1592 ± 8 Ma (n = 19) and 1584 ± 20 Ma (n = 13). Jagodzinski (2014) analysed zircon from the felsic volcanic breccia as well, producing a SHRIMP $^{207}Pb/^{206}Pb$ weighted average age of 1593 ± 6 Ma (n = 15). Jagodzinski (2014) also analysed the RDG (two sessions) and reported SHRIMP $^{207}Pb/^{206}Pb$ weighted average ages of 1594 ± 5 Ma (n = 27, session 1) and 1594 ± 7 Ma (n = 20, session 2).

2.5.1 Method overview

Detailed descriptions of the geochronology methods used in this study are provided in the Appendix 2.2 and 2.3. Samples were crushed, sieved and panned; zircons were handpicked from the resulting heavy mineral concentrate and mounted on 1-inch epoxy resin disks and polished. LA-ICPMS analysis was conducted at the University of Tasmania for single spot U-Pb zircon geochronology on

[continued from left] occupying a brittle fracture in a hematite-rich lamina in tuffaceous mudstone (PPL, RD3449, 431.4 m). **i.** Disseminated chalcopyrite (yellow) and bornite (purple) and patches of very fine-grained hematite (reddish discoloration, arrow, Hm) in massive tuffaceous mudstone (RL, RD3449, 429.8 m).

samples of the BCF. The resulting ages were determined using Isoplot (Ludwig, 2008). The dataset of McPhie et al. (2016) was reprocessed with additional samples, including tuffaceous mudstone. Zircon grains were selected for chemical abrasion-thermal ionisation mass spectrometry (CA-TIMS) conducted at the Isotope Geology Laboratory at Boise State University, Idaho, from samples of RDG, tuffaceous mudstone, and felsic volcanic fragments from the polymictic volcanic-clast conglomerate, a conglomerate interval in the interbedded sandstone and red mudstone and from the domain of felsic volcanic breccia (e.g. Fig. 2.6) adjacent to the southern domain of the BCF. The samples are described in more detail in Appendix 2.4. Care was taken to avoid contamination from the matrix of BCF or breccia samples by crushing only the volcanic fragments. The RDG samples were selected from drill holes far from the ODBC to minimise the potential alteration of zircons by the OD hydrothermal system. The high precision dates from CA-TIMS analysis were used to interpret and distinguish igneous crystallisation ages of the RDG and the GRV source(s) of the analysed samples. A one-way analysis of variance (ANOVA) was conducted on the CA-TIMS sample data to determine if any heterogeneity between the mean ages is statistically significant and was followed by Tukey-Kramer pairwise comparisons to determine which samples differed.

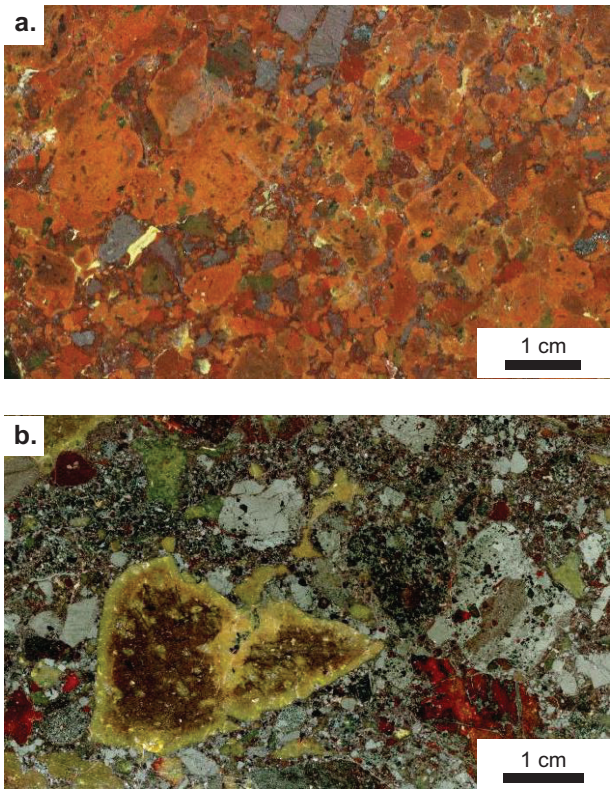

Figure 2.6 Felsic volcanic clast-rich breccia **a.** Samples with relatively little hematite alteration of clasts, some specular hematite grains (grey) (RD2899, 409.7 m). **b.** Abundant grey hematite clasts. Felsic volcanic clasts are variably sericite- (pale, yellowish margins) or hematite-altered (reddish clasts) (RD647, 488.4 m).

2.5.2 Results

2.5.2.1 LA-ICPMS geochronology

Detrital zircons in the BCF are euhedral to subhedral grains (up to 200 μm in length) and angular fragments; oscillatory zonation is common. Many grains are internally fractured, particularly in the tuffaceous mudstone (Fig. 2.5f). Single spot analyses were conducted on 460 zircon grains from the BCF. The number and drill holes of the analysed samples are presented in Table S2.4 of Appendix 2.2. Filtering for analyses that were highly discordant (metamict) and/or with elevated ^{204}Pb (indicative of the presence of common Pb) resulted in 346 grains being considered suitable for age interpretation. Data are presented in Appendix 2.5. The vast majority of the zircons in each of the BCF associations have ca. 1.59 Ga ages, as was noted by the prior studies listed above. The intercept dates for the BCF associations are (reporting random and total, including systematic, uncertainties (2s); Horstwood et al., 2016): 1592.3 ± 6.9 ± 17.6 Ma for the interbedded sandstone and red mudstone (n = 143/219, MSWD = 1.3, probability of fit – p.o.f = 0.018, Fig. 2.7a), 1590.3 ± 7.4 ± 17.8 Ma for the green sandstone and mudstone (n = 89/108, MSWD = 0.77, p.o.f = 0.94, Fig. 2.7b), 1588.2 ± 11 ± 19.5 Ma for the tuffaceous mudstone (n = 62/79, MSWD = 2.5, p.o.f = 0.000, Fig. 2.7c), and 1603.7 ± 11 ± 19.6 Ma for felsic volcanic clasts in the polymictic volcanic-clast conglomerate facies (n = 41/47, MSWD = 1.6, p.o.f = 0.010, Fig. 2.7d). Most of the intercept dates have mean square weighted deviations (MSWD) close to 1, which implies that the majority of the analyses in each facies association are within error (within the resolution of the LA-ICPMS technique). The higher MSWD of the tuffaceous mudstone is likely to be due to the zircons from that facies being fractured and altered. A small population of analyses (n = 11) comprising zircons from all facies associations except the polymictic volcanic-clast conglomerate recorded apparent older ages; 9 of the 11 analyses define a ca. 1700 Ma age (Fig. 2.7e).

2.5.2.2 CA-TIMS geochronology

The zircons were analysed from the samples listed in Table 2.1 and data are presented in Appendix 2.6. The results are summarised by lithology (and by sample where variation occurs) and include description of zircon texture (Fig. 2.8) and U-Pb dates. Isoplot 3.7 (Ludwig, 2008) was used to calculate weighted mean $^{207}Pb/^{206}Pb$ dates from 5-8 equivalent dates per samples (i.e. p.o.f >0.05). The igneous crystallization ages are based on the weighted mean $^{207}Pb/^{206}Pb$ dates rather than $^{206}Pb/^{238}U$

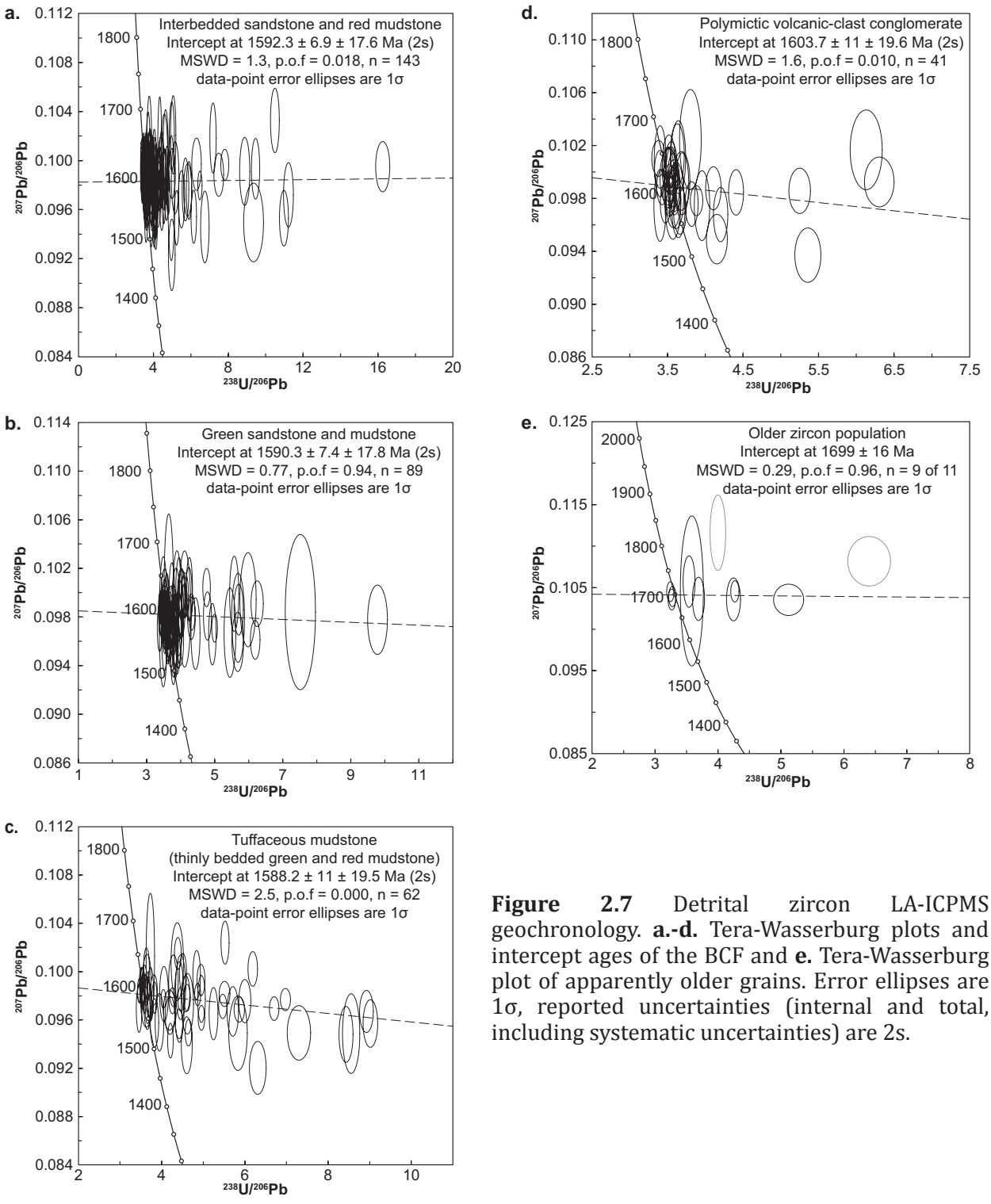

Figure 2.7 Detrital zircon LA-ICPMS geochronology. **a.-d.** Tera-Wasserburg plots and intercept ages of the BCF and **e.** Tera-Wasserburg plot of apparently older grains. Error ellipses are 1σ, reported uncertainties (internal and total, including systematic uncertainties) are 2s.

dates due to some $^{206}Pb/^{238}U$ dates being slightly to moderately younger, presumably due to Pb loss. Results are presented in Figs. 2.9 and 2.10. All analyses except for two are <1.9% discordant; 69 of the 73 analyses are <0.6% discordant. Errors on the weighted mean dates are given at 2σ and are the internal errors based on analytical uncertainties only, including counting statistics, subtraction of tracer solution, and blank and initial common Pb subtraction. The reported dates utilize the U decay constants recommended by Steiger and Jager (1977), including a $^{238}U/^{235}U$ of 137.88. If a more recently

determined $^{238}U/^{235}U$ of 137.818 were used (Hiess et al., 2012), $^{207}Pb/^{206}Pb$ dates would be younger by ~0.84 Ma.; though this would not change the overall results or interpretations presented here.

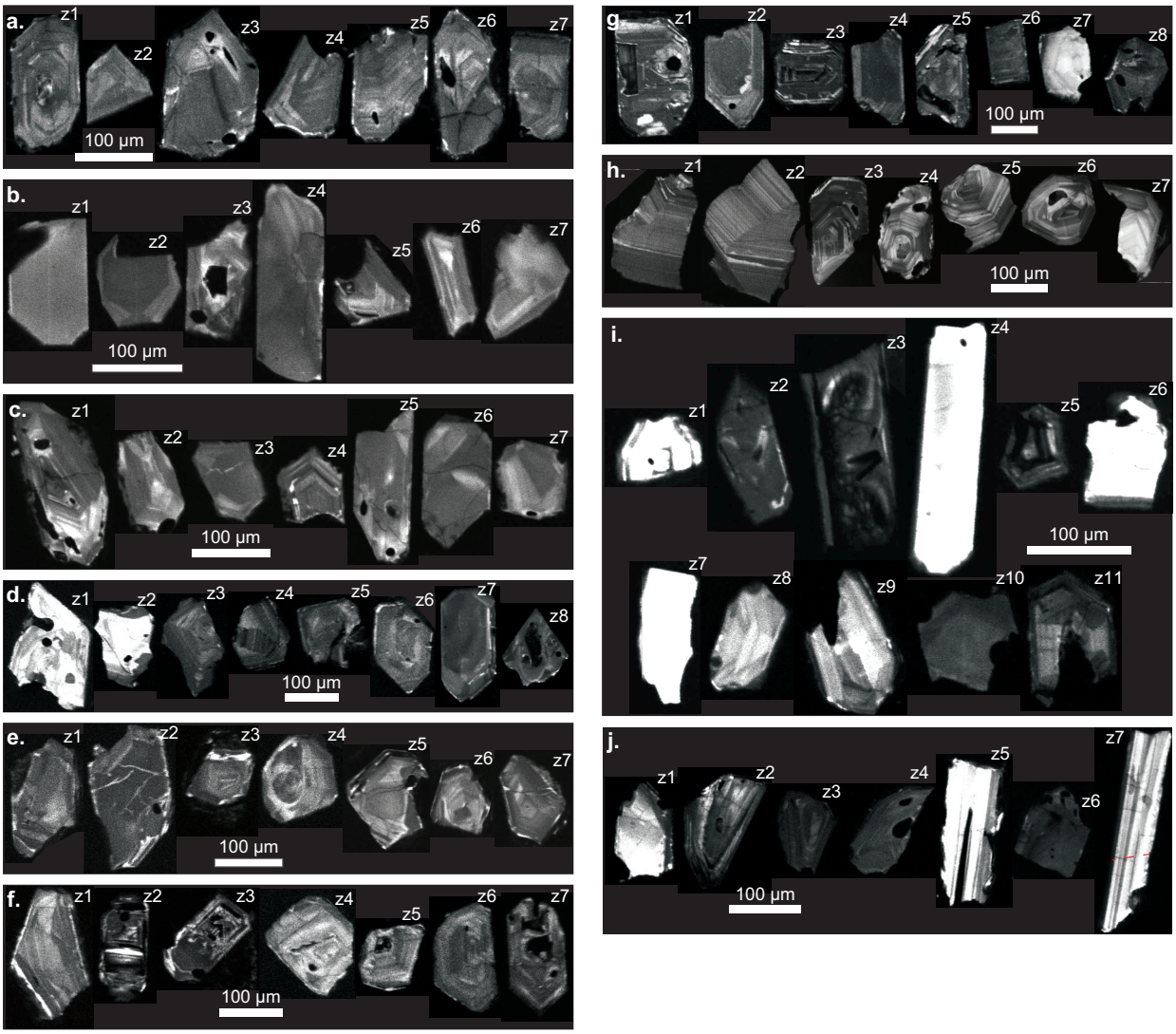

Figure 2.8 Cathodoluminescence (CL) images of zircons used for CA-TIMS analysis, collected by a scanning electron microscope at Boise State University. Grain labels (e.g. z1, z2) correspond to analysis number in the CA-TIMS dataset in the supplement (Table D2). Brightness of CL images are comparable within, but not between samples. **a.** OD1207 (SSH255, 426.4 m) – felsic volcanic breccia. **b.** OD55 (underground drive MJ54WEST grab sample) – polymictic volcanic clast-rich conglomerate. **c.** OD487 (RD1624, 602.5 m) – conglomerate interval in interbedded sandstone and red mudstone. **d.** OD1201 (RD2488, 681.9 m) – RDG. **e.** OD1202 (RD2499, 814.1 m) – RDG. **f.** OD1214 (RD2284, 352.8 m) – RDG. **g.** OD1215 (RD2499, 529.7 m) – RDG. **h.** 200036 6176 (RD575, 531 m) – RDG. **i.** OD239 (RD3449, 427.2 m) – tuffaceous mudstone. **j.** OD41 (RD3449, 429.8 m) – tuffaceous mudstone.

Table 2.1 Samples used for CA-TIMS analysis and their corresponding drill hole and depth. Note: the CA-TIMS results for sample 200036 6176 were first reported in (Jagodzinski et al., 2016).

Sample ID	Drill hole	Depth (m)	Lithology
OD1207	SSH255	426.4	GRV clast in felsic volcanic breccia
OD55	Grab sample from underground drive MJ54WEST		Large GRV clast in polymictic volcanic-clast conglomerate
OD487	RD1624	602.5	Large GRV clast in interbedded sandstone and red mudstone
OD1201	RD2488	681.9	RDG
OD1202	RD2499	814.1	RDG
OD1214	RD2284	352.8	RDG
OD1215	RD2499	529.7	RDG
200036 6176	RD575	531	RDG
OD239	RD3449	427.2	Tuffaceous mudstone
OD41	RD3449	429.8	Tuffaceous mudstone

Gawler Range Volcanics (GRV)

Sample OD55 is a felsic volcanic cobble collected from an underground drive in the polymictic volcanic-clast conglomerate association in the northern domain of the BCF. Sample OD487 is a cobble from conglomerate within an interval of interbedded sandstone and red mudstone in the southern domain of the BCF. Sample OD1207 consists of a coarse felsic clast from the domain of felsic volcanic breccia (inferred to be the incorporated remnants of felsic GRV originally present above the RDG) adjacent to the southern domain of the BCF; the felsic volcanic fragments are surrounded by hematite-rich matrix. A single cobble was crushed separately for CA-TIMS analysis, after first removing the outer surface and any attached matrix. Zircons from the three felsic volcanic samples have simple cores with rims that show oscillatory and/or sector zones (Fig. 2.8a-c). More complex oscillatory zonation appears to be more common in the zircons from the felsic volcanic breccia sample (OD1207). Inclusions and patchy zonation are evident in some grains in all three samples. Analysis of 7 zircons from each of the felsic volcanic samples resulted in weighted mean $^{207}Pb/^{206}Pb$ dates that agree within analytical uncertainty (Figs. 2.9 and 2.10): OD55 = 1594.87 ± 0.80 Ma (n = 6/7, MSWD = 1.5, p.o.f = 0.18); OD487 = 1594.52 ± 0.52 Ma (n = 7, MSWD = 0.49, p.o.f = 0.81); OD1207 = 1594.78 ± 0.56 Ma (n = 7, MSWD = 0.50, p.o.f = 0.81). The oldest 6 zircons were used to produce the weighted mean date of OD55; one analysis has a young date (1591.2 ± 1.2 Ma) which is attributed to ancient Pb loss. These

Figure 2.9 *[right]* Wetherill concordia plots of CA-TIMS analyses for the zircons in Figure 2.8. Plots constructed using Isoplot 3.7 (Ludwig, 2008). The grey bands behind the concordia lines represent the decay constant uncertainty (to 2σ) of the concordia lines. Error ellipses are also 2σ. Red ellipses in plots for OD55 and OD239 are excluded from age interpretation. Dashed lines separate each sample.

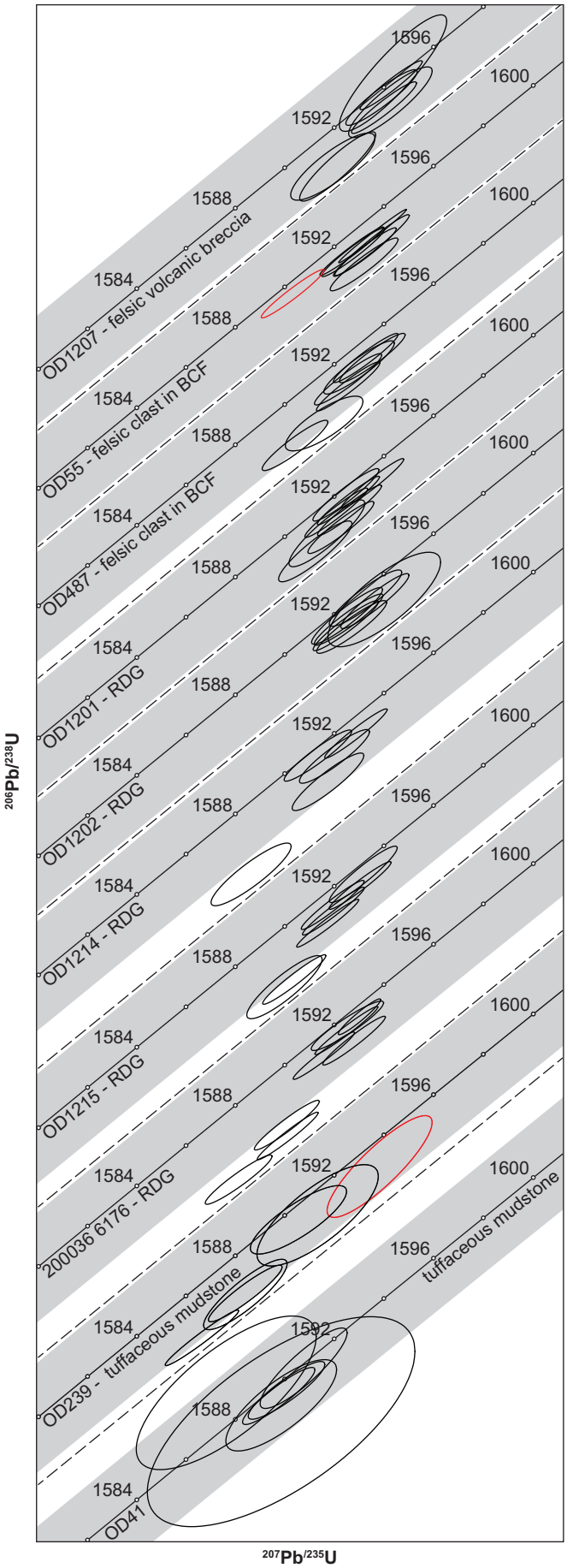
1596
1600
1592
1588
1584
OD1207 - felsic volcanic breccia
OD55 - felsic clast in BCF
OD487 - felsic clast in BCF
OD1201 - RDG
OD1202 - RDG
OD1214 - RDG
OD1215 - RDG
200036 6176 - RDG
OD239 - tuffaceous mudstone
tuffaceous mudstone
OD41
206Pb/238U
207Pb/235U

weighted mean dates are interpreted to represent the igneous crystallisation ages of the source GRV. Combining the analyses of all three samples produces a weighted mean age of 1594.73 ± 0.30 Ma (n = 20, MSWD = 0.76, p.o.f = 0.75). The low MSWD and high probability of fit indicate the three samples are statistically very similar and likely to be of the same age population.

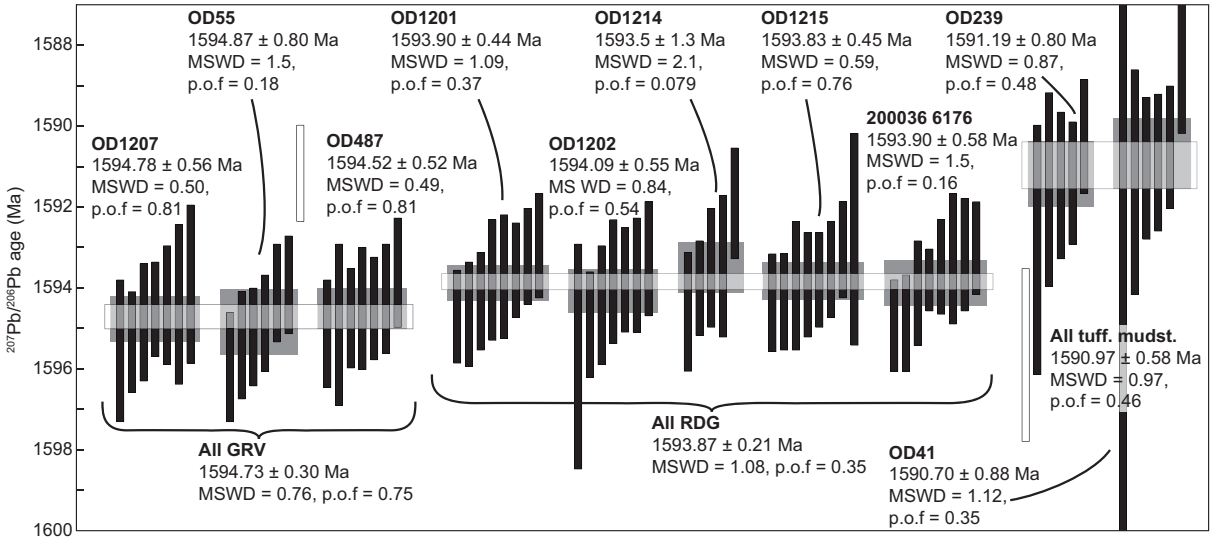

Figure 2.10 Ranked box plot of $^{207}Pb/^{206}Pb$ dates (Ma) of the zircon CA-TIMS analyses. Black bars are single analyses, white bars are excluded analyses. Grey boxes behind bars are the weighted mean dates of each sample. Light grey boxes in front of the bars are combined weighted mean dates. Error bar and box height are 2σ. Weighted mean dates determined using Isoplot 3.7 (Ludwig, 2008).

Roxby Downs Granite (RDG)

Many zircons from the five samples of RDG are fragments and most exhibit oscillatory zones; some grains have patchy and sector zones (Fig. 2.8d-h). Inclusions exist in many of the zircon grains. Grains with a bright CL response are inferred to be lower in U and consequently less damaged by decay of U and its unstable daughters. Analysis of up to 8 grains from each of the RDG samples resulted in weighted mean $^{207}Pb/^{206}Pb$ dates that agree within analytical uncertainty (Figs. 2.9 and 2.10): OD1201 = 1593.90 ± 0.44 Ma (n = 8, MSWD = 1.09, p.o.f = 0.37); OD1202 = 1594.09 ± 0.56 Ma (n = 7, MSWD = 0.84, p.o.f = 0.54); OD1214 = 1593.52 ± 0.63 Ma (n = 5/7, MSWD = 2.09, p.o.f = 0.079); OD1215 = 1593.83 ± 0.46 Ma (n = 8, MSWD = 0.59, p.o.f = 0.76); 200036 6176 = 1593.90 ± 0.58 Ma (n = 8, MSWD = 1.5, p.o.f = 0.16). Two analyses from OD1214 were not used in the weighted mean date: one is significantly older (1636.04 ± 1.22 Ma) indicating an inherited component and the other is highly discordant due to ancient Pb loss. Combining the analyses of all five samples yields a weighted mean of 1593.87 ± 0.21 Ma (n = 36, MSWD = 1.08, p.o.f = 0.35) and is interpreted to be the igneous crystallisation age of the RDG. The good agreement among all of the samples (shown by the MSWD and probability of fit of the combined weighted mean age) suggests the RDG was not emplaced incrementally over a long period of time, at least not beyond the resolution afforded by the CA-TIMS method.

Tuffaceous mudstone in the thinly bedded green and red mudstone facies association

Samples OD41 and OD239 are from tuffaceous mudstone from the northern domain of the BCF. Both samples retain the bubble-wall shard texture identified by McPhie et al. (2016), despite being altered largely to sericite. Zircons are commonly fractured or fragmented; many intact grains are elongate (relative to those from the RDG and felsic volcanic samples). CL images revealed two distinct populations (those with a strong CL response and those with a suppressed response, Fig. 2.8i, j) which are inversely correlated with U concentration. Oscillatory, sector and patchy zonation are variably apparent. Analysis of 6 grains from sample OD41 and 11 grains from sample OD239 yielded similar weighted mean dates (Figs. 2.9 and 2.10): OD41 = 1590.70 ± 0.88 Ma (n = 6, MSWD = 1.12, p.o.f = 0.35); OD239 = 1591.19 ± 0.80 Ma (n = 5/8, MSWD = 0.87, p.o.f = 0.48). Combining the analyses of the two samples yields a weighted mean of 1590.97 ± 0.58 Ma (n = 11, MSWD = 0.97, p.o.f = 0.46). A number of analyses from OD239 were not used for age interpretation: three were of poor quality (chemically abraded fragments too small to have sufficient radiogenic Pb for precise dates) and were not considered, two others are highly discordant and gave significantly younger dates (1582.02 ± 1.79 and 1575.84 ± 1.63 Ma) that are attributed to ancient Pb loss, and one had an older date (1595.67 ± 2.13 Ma) that is interpreted to indicate the presence of an inherited component or detrital zircon from reworking of the tuff or contamination of the sample. The increased number of rejected analyses is consistent with the higher MSWD of the weighted mean of the LA-ICPMS analyses.

2.6 Chromian spinel composition

Analyses of Cr-spinel grains from three samples of the green sandstone and mudstone were first reported by McPhie et al. (2011b), and showed a wide scatter in trace element abundance. The scatter was interpreted by those authors as well as McPhie et al. (2016) to reflect the green sandstone and mudstone having a broad provenance that received Cr-spinel generated in multiple tectonic settings. The data presented here expand upon that dataset, providing additional Cr-spinel analyses from seven samples of the green sandstone and mudstone as well as from five samples of tuffaceous mudstone. Chromian spinel occurs as free detrital grains (e.g. Fig. 2.5g) in both facies and as inclusions in olivine-phyric clasts (e.g. Fig. 2.2b) in the green sandstone and mudstone.

Chromian spinel grains were extracted from samples and mounted on epoxy resin disks in the same manner as the zircon grains. Compositions of Cr-spinel grains were determined with a Cameca SX100 electron microprobe (see Appendix 2.7 for details of the method). Multiple Cr-spinel grains in

the additional samples of green sandstone and mudstone and tuffaceous mudstone were analysed. The geochemical filter (ZnO < 0.3 wt.% and MnO < 0.6 wt.%) used by Huang et al. (2016) to select for least-altered grains excluded only 4 of the total 273 analysed grains.

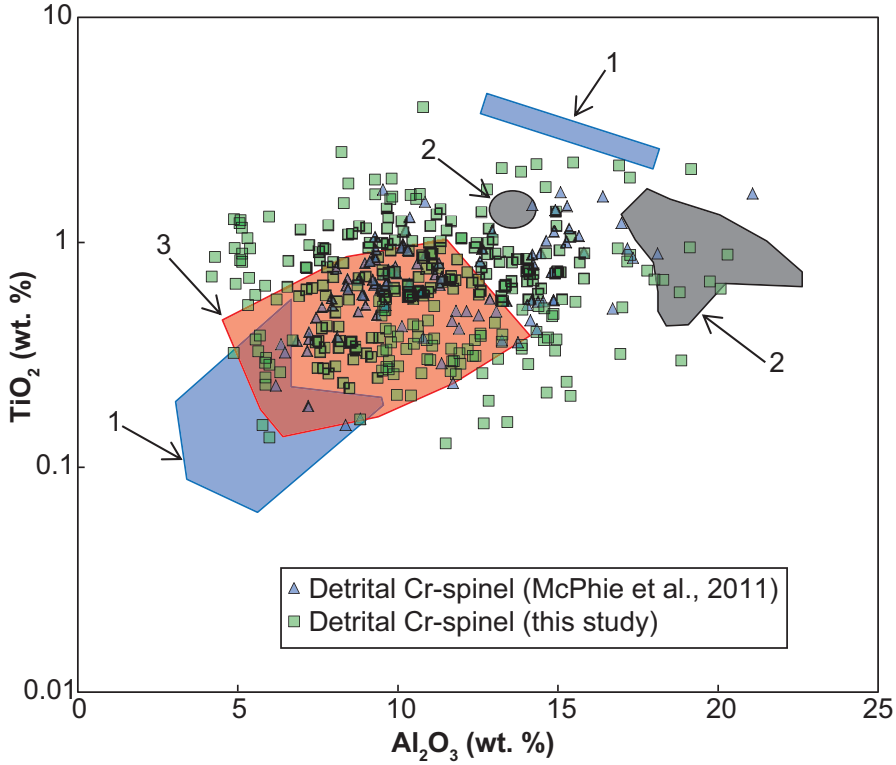

Figure 2.11 Bivariate TiO_2 and Al_2O_3 plot of Cr-spinel grains (n = 223) from the BCF. The fields represent Cr-spinel compositions from the altered mafic units in the ODBC presented by Huang et al. (2016): 1. Olivine-phyric lava/sill. 2. Olivine-phyric basaltic dykes. 3. Olivine-phyric dykes and other samples originally collected by K. Cross.

The analysed Cr-spinel grains from the green sandstone and mudstone have highly variable TiO_2 and Al_2O_3 compositions, on par with those previously reported by McPhie et al. (2011b) (Fig. 2.11). Analyses of Cr-spinel from the tuffaceous mudstone have a more restricted composition range than those from the green sandstone and mudstone (Appendix 2.8). High compositional variability is shown by multiple grains in single samples and between samples. The compositional ranges of most samples overlap, whereas some samples have relatively restricted ranges (Fig. 2.11).

2.7 Discussion

2.7.1 Provenance of the bedded clastic facies

2.7.1.1 Felsic GRV

The ca. 1590 Ma age of nearly all detrital zircon in the BCF corresponds to the age of the Gawler SLIP (Fanning et al., 1988; Creaser and Cooper, 1993; Jagodzinski et al., 2016), which suggests the GRV and/or Hiltaba Suite granitoids were the primary or most significant sources of material/detritus for the BCF. A GRV/Hiltaba Suite-dominated provenance for the BCF has been suggested by a number of prior workers (Oreskes and Einaudi, 1990; Reeve et al., 1990; McPhie et al., 2016).

The felsic volcanic clasts in the BCF are described as "texturally, mineralogically and compositionally identical to … the GRV" by McPhie et al. (2011b; p. 796), consistent with the LA-ICPMS and CA-TIMS geochronology of the BCF presented in this study. The domains of breccia composed primarily of felsic, feldspar-phyric volcanic clasts (e.g. Fig. 2.6) within the ODBC have been suggested to be the incorporated remnants of felsic GRV that was originally present above the RDG (Reeve et al., 1990; McPhie et al., 2011b). Indeed, the nearest intact felsic GRV known occur at the Acropolis prospect, approximately 20 km SW of OD (Creaser and Cooper, 1993). The CA-TIMS age of the felsic volcanic clast from the breccia (OD1207) is indistinguishable from the CA-TIMS ages of the felsic volcanic cobbles in the BCF (OD55 and OD487), as shown by the low MSWD and high probability of fit when analyses from all of the samples are combined (Fig. 2.10). The presence of felsic volcanic clasts in the BCF that are the same age as the felsic volcanic clast from the breccia suggests the GRV that was once present above the RDG (and probably present regionally) predated deposition of the BCF.

Comparison of CA-TIMS ages of the felsic volcanic samples with recent high-precision geochronology of the GRV throughout the Gawler Craton (Jagodzinski et al., 2016) has revealed that the GRV at OD was part of the lower GRV (1595-1587 Ma) as opposed to the upper GRV (ca. 1587 Ma). A number of the lower GRV samples from the Gawler Ranges dated by Jagodzinski et al. (2016) have CA-TIMS ages that correspond closely with the age of the tuffaceous mudstone (ca. 1591 Ma). A lower GRV source is also consistent with the presence of quartz in the tuffaceous mudstone, as the upper GRV is primarily feldspar-phyric (Allen et al., 2008).

2.7.1.2 Mafic GRV

A GRV origin or timing for the mafic volcanic clasts in the green sandstone and mudstone and the polymictic volcanic-clast conglomerate facies have been proposed by prior authors (Johnson and Cross, 1995; McPhie et al., 2011b; McPhie et al., 2016) but direct dating of the mafic volcanic clasts has not been possible to confirm their age. The mafic volcanic clasts with pseudomorphed olivine phenocrysts are texturally similar to olivine-phyric mafic dykes in the ODBC described by Huang et al. (2016). These dykes have been dated, by LA-ICPMS U-Pb geochronology of magmatic apatite, at ca. 1590 Ma and have been correlated with mafic lower GRV elsewhere in the Gawler Craton (Huang et al., 2016). The extrusive equivalents of these and similar mafic dykes may have been the source of the corresponding mafic volcanic clasts in the green sandstone and mudstone and the polymictic volcanic-clast conglomerate facies.

The highly variable compositions of the Cr-spinel in the green sandstone and mudstone were interpreted by McPhie et al. (2011b) and (2016) to reflect contribution from multiple volcanic sources because Cr-spinel compositions have been shown to be sensitive indicators of different tectonic settings. In particular, TiO_2 and Al_2O_3 composition of Cr-spinel varies with parental melt composition (Kamenetsky et al., 2001). The absence of any recognised local sources of Cr-spinel at the time also supported this interpretation. Huang et al. (2016) has since recognised GRV-age mafic dykes intruding the ODBC that contain pseudomorphed olivine phenocrysts with Cr-spinel inclusions. The presence of these dykes in the ODBC suggests these and similar dykes may have fed mafic volcanism in the vicinity of OD.

Analyses by Huang et al. (2016) of Cr-spinel from mafic units in the ODBC encompass significant compositional variation. A number of distinct compositional populations are present (Fig. 2.11) (see Appendix 2.8) that may each correspond to distinct parental melts. This variation in parental melt implies the presence of multiple magma sources in the vicinity of OD or the changing of parental melt composition of a single source over a relatively short period of time (e.g. Cr-spinel in Mt Etna; Kamenetsky and Clocchiatti, 1996). The compositions of Cr-spinel from mafic units that have thus far been identified within the ODBC have a broadly similar range to the detrital Cr-spinel in the BCF (Fig. 2.11). However, they do not account for all of the Cr-spinel variation in the BCF. This relationship suggests that, if the Cr-spinel in the BCF was locally derived, the volcanic source(s) had a greater compositional variation than indicated by the known GRV-age mafic units in the ODBC. Alternatively,

the Cr-spinel population in the BCF could be a mixture from local and remote sources.

The presence of quartz, zircon and bubble-wall shards in the tuffaceous mudstone suggests the source magma was felsic (McPhie et al., 2016). The sparse Cr-spinel grains in the tuffaceous mudstone were probably added via mixing with locally derived mafic components during waterlain deposition. The Cr-spinel in the tuffaceous mudstone has a more restricted compositional range relative to the green sandstone and mudstone.

2.7.1.3 Hiltaba Suite

A Hiltaba Suite contribution (e.g. granite clasts, granitoid quartz, feldspar, and zircon) to the BCF has been proposed by numerous prior authors (Reeve et al., 1990; Johnson and Cross, 1995; McPhie et al., 2011b; McPhie et al., 2016), in particular for the interbedded sandstone and red mudstone, although granite-derived quartz and granitic fragments are also present in other facies associations (e.g. green sandstone and mudstone, Fig. 2.2d). Much of the componentry of the interbedded sandstone and red mudstone (e.g. quartz, feldspar, Fe oxide, accessory zircon, tourmaline, fluorite, apatite and rutile) is present in the Hiltaba Suite granitoids in the vicinity of OD (including the RDG) (Creaser, 1996). The granitic components were probably contributed from Hiltaba Suite granitoids within the Burgoyne Batholith surrounding due to the absence of Palaeoproterozoic-age detrital zircons from basement rocks surrounding the Burgoyne Batholith (i.e. ≥1740 Ma).

The occurrence of detrital hematite grains in the interbedded sandstone and red mudstone with remnant magnetite cores/patches (e.g. Fig. 2.3d) suggests that an unknown proportion of the hematite may have originally been magnetite. Magnetite is present as a primary accessory phase in the Hiltaba Suite granitoids in the vicinity of OD (Creaser, 1996) and Fe oxide may have also been present in the form of magnetite-hematite veins in exposed Hiltaba Suite (such as in the RDG; Ehrig et al., 2012) or Gawler Range Volcanics in the vicinity of OD (cf. the nearby Acropolis prospect).

2.7.1.4 The ODBC?

Previous workers have suggested the ODBC was a source of clasts in the BCF (Oreskes and

Einaudi, 1990; Reeve et al., 1990). Hematite in the laminated, hematite-rich mudstone (ironstone) of the thinly bedded green and red mudstone facies association has characteristics consistent with formation through detrital deposition (e.g. Fig. 2.5b, c), chemical precipitation (e.g. Fig. 5d) or hydrothermal replacement of tuffaceous material (Oreskes and Einaudi, 1990). Erosion of exposed hematite-altered RDG or hematite-rich breccia (which has an RDG protolith) could produce many of the detrital components observed in the interbedded sandstone and red mudstone facies association. However, no components have been identified that uniquely indicate the ODBC was a source of detritus to the BCF. Further work is required to narrow the range of probable source(s) of detrital components (particularly Fe-oxide) in the interbedded sandstone and red mudstone facies association.

2.7.1.5 Palaeoproterozoic sources?

A very small population of zircons from three of the BCF associations defines an older age of ca. 1700 Ma (Fig. 2.7e). This older age population may indicate that some zircons (from the GRV or Hiltaba Suite) had inherited components or that a Palaeoproterozoic source contributed to the BCF. However, the ca. 1700 Ma age does not correlate with known zircon populations in the Wallaroo Group (≥1740 Ma) and Donington Suite (ca. 1850 Ma) that surround the Hiltaba Suite granitoids in the vicinity of OD (e.g. at Snake Gully, 10 km ENE of OD; Creaser, 1989; Jagodzinski, 2005). An inherited component (within the zircon population of the source rocks) or the presence of common Pb is suggested to be the probable cause of this ca. 1700 Ma population.

2.7.2 Age of the BCF

The preservation of bubble-wall shard texture in the tuffaceous mudstone suggests its deposition was contemporaneous with or shortly after eruption of the GRV; this texture would not survive significant reworking (Fisher and Schmincke, 1984). Polymictic volcanic-clast conglomerate facies adjacent to the tuffaceous mudstone has a tuff-like matrix (identification limited by intense sericite and/or hematite alteration of the matrix), which suggests the conglomerate may have been deposited at the same time as the tuffaceous mudstone or while the tuffaceous mudstone was still unconsolidated. The CA-TIMS age of zircon in the tuffaceous mudstone (1590.97 ± 0.58 Ma) is therefore taken to represent the timing of deposition of this facies and the other closely associated facies of the BCF. This result indicates that not only was a basin present above the GRV and RDG at this time but that the BCF are significantly younger than the GRV that underlay the basin.

2.7.3 Sulfides in the BCF

The same single or paired sulfide assemblages are present in all of the BCF associations, regardless of the detrital mineralogy of the facies being distinct, and in the ODBC (Fig. 2.2f-g, 2.3g-h, 2.5c, h-j) (e.g. pyrite-chalcopyrite, chalcopyrite-bornite, bornite-chalcocite; Ehrig et al., 2012). An exception is covellite which has replaced chalcocite (paired with bornite) in some BCF samples. Sulfides and associated hydrothermal phases (e.g. barite, fluorite and hematite) have morphologies and textures indicative of replacement and cavity-fill (e.g. Fig. 2.2f, 2.5c, h). The continuance of the same sulfide assemblage across facies and the ODBC as well as non-detrital textures indicate that sulfide deposition post-dates the deposition of the BCF (i.e. after 1591 Ma). The occurrence of sulfides occupying fractures/offsets of beds (e.g. Fig. 2.5c, h) suggests sulfide deposition took place after brittle deformation (i.e. potentially after lithification of the BCF).

2.7.4 Ages and relative relationships of the RDG and GRV at Olympic Dam

The timing of emplacement of the GRV at OD relative to the intrusion of the RDG has been a source of speculation (Oreskes and Einaudi, 1990; Reeve et al., 1990; McPhie et al., 2011b; McPhie et al., 2016). The CA-TIMS ages of the GRV and RDG samples overlap (Fig. 2.10), and thus ages from single samples cannot determine which is older. Combining all of the analyses to produce single weighted mean ages for the GRV (1594.73 ± 0.30 Ma, MSWD = 0.76, p.o.f = 0.75, n = 20) and RDG (1593.87 ± 0.21 Ma, MSWD = 1.08, p.o.f = 0.35, n = 5) reduces the 2σ uncertainties of each sufficiently and suggests the RDG is distinguishably younger than the GRV (Fig. 2.10). Combining the analyses in this manner assumes that the RDG and the GRV supplying the clasts are both single entities (pluton and emplacement unit, respectively), a reasonable presumption given that the sample ages for each unit are statistically indistinguishable (though the very small uncertainties of the combined ages are of uncertain statistical significance). The ANOVA also indicated the mean ages of the GRV and RDG samples are significantly heterogeneous, and the Tukey-Kramer pairwise comparison identified significant difference between the oldest GRV and youngest RDG samples (see Appendix 2.9).

Whether there was a contact (e.g. intrusive or unconformable) between the GRV and the RDG, or whether they were separated by older country rock is unknown. An unconformable contact implies the RDG would be significantly older than the GRV (to permit unroofing of the RDG prior to deposition of the GRV), which is precluded by the (potentially) older age of the GRV. Pre-1590 Ma (i.e. Palaeoproterozoic or earlier) zircons in the ODBC (as evidence of incorporation of older country rock)

have not yet been recorded, aside from within fragments of the younger Pandurra Formation (Cherry et al., 2017) and potentially in the BCF (Fig. 2.7e, section 2.7.1.5). The absence of evidence (thus far) of pre-1590 Ma components in the ODBC is consistent with the RDG intruding already-present GRV. An intrusive contact was first suggested by Reeve et al. (1990) and intrusive contacts between Hiltaba Suite granites and the GRV occur elsewhere in the Gawler Craton (e.g. Flint, 1993; Agangi, 2011). Intrusion of the RDG into the GRV would require the RDG to have been shallowly emplaced (the thickest known preserved sections of lower GRV are up to 3 km thick, e.g. Chitanilga Volcanic Complex; Allen et al., 2008). Various textures indicative of shallow emplacement (e.g. miarolitic cavities, aplitic dikes, granophyric zones; Candela, 1997) were reported in the RDG by Creaser (1989). Kontonikas-Charos et al. (2017) suggested crystallisation pressures of ~2.2 kbar for the RDG, which corresponds to a depth of 6-8 km. However, the Al-in-hornblende barometer and thermometer used by Kontonikas-Charos et al. (2017) (i.e. Blundy and Holland, 1990; Anderson and Smith, 1995) have significant associated uncertainties (the barometer is highly temperature sensitive and the calculated temperatures have a 2σ uncertainty of 75 °C, which imparts an uncertainty of up to 1.6 kbar to the calculated pressure) and the textural evidence for shallow emplacement is therefore considered more reliable.

2.7.5 Setting and stratigraphy of the BCF

The elongate, east-west, steeply dipping geometry of the southern BCF domain and of the separate facies associations (see Fig. 2 of McPhie et al., 2016) has been influenced by northeast- and northwest-striking fault sets (Hayward and Skirrow, 2010; McPhie et al., 2016). The original basin was proposed by McPhie et al. (2016) to have been defined by those same fault sets, partially on the basis of bedding measurements consistent with soft-sediment slumping down a palaeoslope with a northeasterly strike (dipping to the northwest or southeast).

Hematite-rich breccia, including domains of felsic volcanic breccia and hematite-quartz-barite breccia (characterised by intense, texturally destructive alteration of the protolith) occurs to the north of the main mass of the southern BCF domain (Fig. 2.1b) (Ehrig et al., 2012; McPhie et al., 2016). Juxtaposed to the south of the southern BCF domain is more granite-rich breccia, which then grades into unaltered RDG over a very short distance compared to elsewhere around the ODBC (Fig. 2.1b). Hayward and Skirrow (2010) noted the southern boundary of hematite-rich breccia, along which the southern BCF domain occurs, to be relatively planar and suggested it was influenced by a large, early northeast-striking fault zone. Significant vertical movement (i.e. north side up relative to the

south) along this fault zone could account for the narrow transition to unaltered RDG. The northern BCF domain was influenced by the same fault sets and has similar soft-sediment deformed bedding orientations as the southern BCF domain (McPhie et al., 2016), which suggests that it was originally part of the same basin. The northern BCF domain is also surrounded by a domain of hematite-quartz-barite breccia (Ehrig et al., 2012).

The southern BCF domain comprises multiple intervals of the different facies associations (Fig. 2.1c) (McPhie et al., 2016). Green sandstone and mudstone occurs in a thin northernmost interval that is adjacent to a segmented interval of interbedded sandstone and red mudstone (Fig. 2.1b, c). Portions of this interval (of interbedded sandstone and red mudstone) form an outlier separated by felsic volcanic breccia (Fig. 2.1b). Juxtaposed to the south of the interbedded sandstone and red mudstone is a second interval of green sandstone and mudstone; this interval is interbedded with polymictic volcanic-clast conglomerate and sandwiched to the south by a second interval of interbedded sandstone and red mudstone (Fig. 2.1c). The two intervals of the interbedded sandstone and red mudstone have been speculated by McPhie et al. (2016) to be either two distinct units or the result of fault repetition of a single unit. The presence of the northernmost interval of green sandstone and mudstone (also see Fig. 2C of McPhie et al., 2016) suggests that fault repetition is more likely, particularly considering the influence of faults on the geometry and segmentation of the BCF domains.

The presence of the felsic volcanic breccia domain immediately adjacent to the southern BCF domain (Fig. 2.1b) implies these surficial units were incorporated together. The significantly younger depositional timing of the BCF indicates the GRV (now felsic volcanic breccia) underlay the bedded clastic facies and suggests the north-to-south sequence of felsic volcanic breccia, to green sandstone and mudstone and then interbedded sandstone and red mudstone may reflect the original stratigraphic sequence. Such a stratigraphy is consistent with initial emplacement of the GRV, followed by deposition of clastic facies with a GRV-dominated provenance and changing to clastic facies with a granitoid-dominated provenance (as Hiltaba Suite granite was exposed). Further work (e.g. a comprehensive study of younging directions) is required to unequivocally resolve the stratigraphy of the BCF.

2.7.6 Incorporation of BCF and GRV into the ODBC

The incorporation of the BCF has been discussed in only limited detail by prior workers; most attributed incorporation simply to downfaulting of the BCF as blocks into the ODBC (Oreskes and

Einaudi, 1990; Hayward and Skirrow, 2010). McPhie et al. (2011b) speculated that hydrothermal-tectonic brecciation was focussed on faults, and began in the RDG and propagated upward into the overlying GRV and BCF. The steeply dipping orientation of the southern domain of BCF and relationship to significant faults are features that, until now, have not been considered. The interpreted deposition and incorporation of the BCF and the GRV (felsic volcanic breccia) (Fig. 2.12) is constrained by the new geochronological and facies data and is summarised below.

1. The GRV and the RDG were emplaced at 1594.73 ± 0.30 Ma and 1593.87 ± 0.21 Ma, respectively. As indicated above (section 2.7.4.), the nature of the contact (if present) of the GRV and RDG is uncertain, although an intrusive contact is suggested to be the most likely scenario. The ODBC started to form after emplacement of the RDG and GRV, brecciation being focussed along early faults, and possibly propagating up towards the GRV.

2. Northeast- and northwest-striking faults are inferred to have been responsible for causing local subsidence above the RDG and GRV, defining a basin in which the BCF began to accumulate (e.g. McPhie et al., 2016). The presence of brecciated mafic-ultramafic GRV dykes in the ODBC indicates igneous activity continued after emplacement of the RDG; the dykes may have fed mafic volcanism in the vicinity of OD.

A felsic eruptive centre (that could have been distal) produced a volcanic ash cloud that deposited tuffaceous mudstone in the basin at 1590.97 ± 0.58 Ma. The low preservation potential of glass shards (and tuffaceous mudstone as a whole) in active sedimentary environments suggests the tuffaceous mudstone would have been best preserved in the central portions of the basin (away from the margins). The initial sediment input is suggested to have been dominated by felsic and mafic GRV sources and comprised a series of low- (green sandstone and mudstone) and high-energy (polymictic volcanic-clast conglomerate facies) depositional events. The sediments were likely deposited as fans or lobes near the margins of the basin, although some of the high-energy depositional events were of sufficient scale to deposit conglomerate with the tuffaceous mudstone farther out in the basin.

3. The erosion of the GRV exposed Hiltaba Suite (and possibly the RDG) in the BCF source area and led to a shift from a GRV-dominated provenance to a granitoid-dominated provenance (interbedded sandstone and red mudstone). The ca. 3 myr between the emplacement of the GRV and

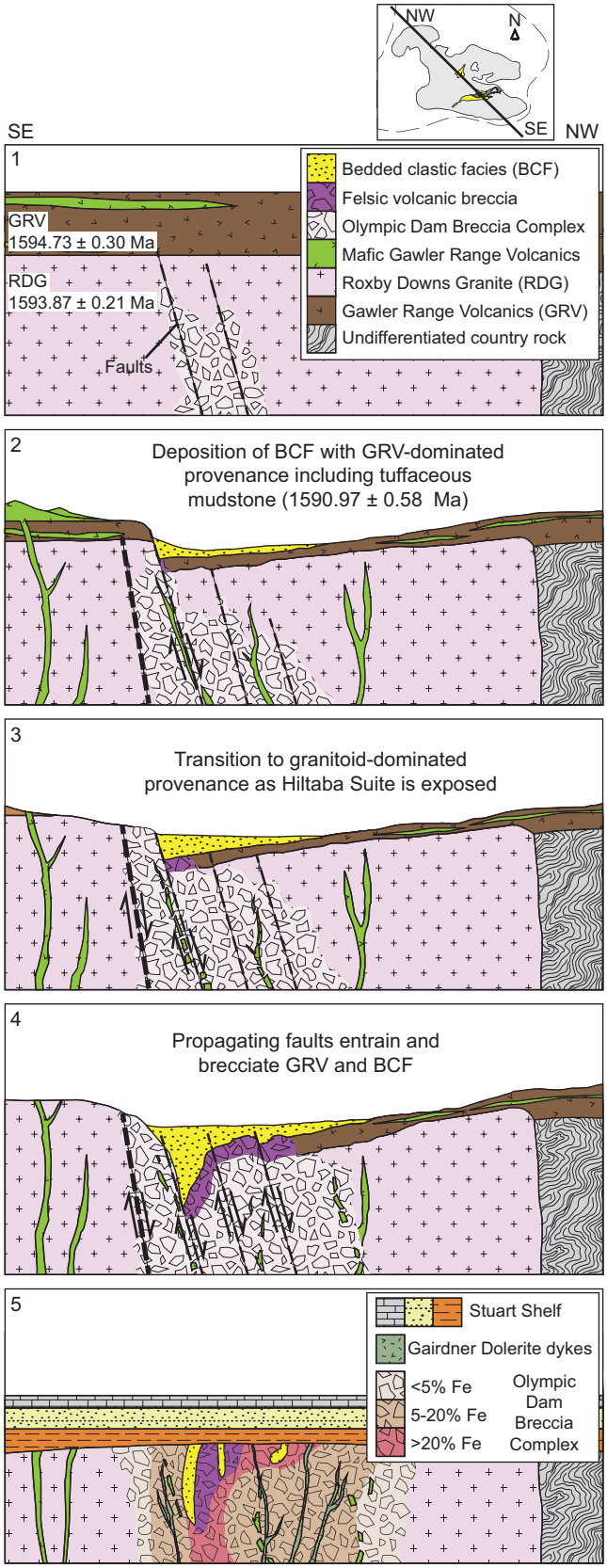

Figure 2.12 Schematic of proposed model of incorporation of the BCF and felsic volcanic breccia into the ODBC, refer to Section 2.7.6 for explanation of each panel. The approximate location of the cross-section is shown overlain on the plan view of the ODBC. Only faults inferred to be relevant to incorporation of the BCF and GRV into the ODBC are shown. The extent of Fe oxide development (after Ehrig et al., 2012) is shown only on panel 5 as the timing and distribution of Fe oxide in the ODBC is unknown relative to the deposition and incorporation of the BCF, save that the surficial units are variably altered and mineralised.

RDG, and the deposition of the BCF is likely to have been sufficient time to unroof Hiltaba Suite/RDG in the vicinity of OD. Detrital Fe oxide in the interbedded sandstone and red mudstone may have been derived from primary igneous Fe oxide and/or magnetite-hematite veins. It is unknown whether exposed portions of the ODBC were available to contribute to the BCF due to uncertainty of the timing of the initiation of the ODBC.

4. The faults that originally defined the basin are here inferred to also be responsible for initiating incorporation of the BCF and underlying GRV into the ODBC. Orientation measurements on soft-sediment folds are consistent with slumping down a northeast-striking palaeoslope (McPhie et al., 2016); more pronounced vertical movement the large, northeast-striking fault zone that defines the current southern margin of the BCF and hematite-rich breccia would be consistent with generating such a palaeoslope.

The progressive incorporation of the GRV and the BCF involved propagation of faults which led to brecciation and gradual segmentation into domains. The domains of the BCF were rotated by fault movement during incorporation, which steepened the dip of bedding in the BCF, particularly in the southern domain. The segmentation of the BCF led to the repetition of stratigraphy in the southern domain.

5. The RDG, ODBC and contained surficial lithologies (BCF and felsic volcanic rocks) were eroded and truncated by an unconformity overlain by the ca. 1440 Ma Pandurra Formation (Cherry et al., 2017). The Pandurra Formation was subsequently eroded and a second unconformity surface formed. This surface was overlain by post-glacial (Cryogenian?) sedimentary units of the Stuart Shelf, initially represented by facies indicative of a marine transgression (Nuccaleena Dolomite cap carbonate and Tregolana Shale; Williams, 1979; Reeve et al., 1990).

The timing of incorporation of the surficial units (BCF and felsic GRV) relative to hydrothermal alteration and mineralisation of the ODBC is not clear, save that the surficial units are variably altered, mineralised and brecciated, which indicates there was tectonic and hydrothermal activity occurring after ca. 1591 Ma. Any tectonic and hydrothermal activity that may have occurred prior to the BCF is currently constrained only by the emplacement of the RDG (at 1593.87 ± 0.20 Ma).

2.8 Conclusions

Precise CA-TIMS zircon geochronology has shown that the GRV at OD (1594.73 ± 0.30 Ma) is slightly older than the RDG (1593.87 ± 0.21 Ma). The ODBC apparently lacks components older than either the RDG or the GRV, and textures in the RDG suggest that it was shallowly emplaced (Creaser, 1989). It is therefore most likely that at OD, the RDG intruded the GRV. The new age data support previous interpretations (McPhie et al., 2011b) that the GRV at OD was originally overlain by the BCF; the GRV pre-dated deposition of the BCF (1590.97 ± 0.58 Ma) by about 3 myr. Hence, a basin was present at OD at least 3 myr after the RDG and GRV were emplaced. The initiation of brecciation and the hydrothermal system at OD post-dated the emplacement of the RDG. Because the BCF domains are partly brecciated and contain hydrothermal minerals (including sulfides), tectonic and hydrothermal activity took place after ca. 1591 Ma, but could have also occurred as early as ca. 1593 Ma (i.e. following emplacement of the RDG).

Cr-spinel in the BCF had previously been thought to indicate a regional provenance for lack of known local sources. Potential local sources of Cr-spinel with similar compositions are now known (e.g. extrusive correlates of mafic-ultramafic dykes intruding the ODBC). The Hiltaba Suite contribution to the BCF indicates that granite was unroofed somewhere in the source area by ca. 1591 Ma. Also, the absence of detrital Palaeoproterozoic zircons implies that the source was likely to have been from granitoids within the Burgoyne Batholith (i.e. within a 40 x 80 km^2 area around OD). The detrital Fe oxide in the BCF was also probably derived from within the Burgoyne Batholith; possible sources include primary igneous Fe oxide and magnetite-hematite veins in granite. Because the timing of initiation of the ODBC has not been determined, it is not known whether exposed portions of the ODBC could have contributed Fe oxide to the BCF. An original stratigraphy is proposed as part of a model for the incorporation of the BCF into the ODBC, where a transition from a volcanic-dominated provenance to a granitoid-dominated provenance is inferred. Faults subsequently segmented and entrained the BCF into the ODBC.

2.9 Acknowledgements

This paper represents part of the PhD project undertaken by A.R. Cherry while supported by an Australia Postgraduate Award scholarship. This project was funded by the Australian Research Council and BHP Olympic Dam. Discussions with M. Ferguson, N. Chapman, E. Jagodzinski, O. Apukhtina and Q. Huang are gratefully acknowledged. LA-ICPMS geochronology analysis and interpretation were assisted by S. Meffre and J. Thompson. Preparation of zircon for CA-TIMS was assisted by A. Edwards.

Appendix 2.1 Detrital and secondary componentry of the BCF

Table S2.1 Description of componentry of the bedded clastic facies associations, as observed in this study and by Ehrig et al. (2012), McPhie et al. (2011b) and McPhie et al. (2016).

Facies association	Description
Green sandstone and mudstone	
Sandstone	Detrital grains include altered mafic volcanic fragments with porphyritic (chlorite-pseudomorphed olivine phenocrysts with Cr-spinel inclusions; Fig. 2.2b), doleritic and vesicular textures, as well as felsic volcanic (Fig. 2.2c) and granite fragments (Fig. 2.2d), quartz (granite- and volcanic-derived; Fig. 2.2e), feldspar (orthoclase and albite), zircon, Cr-spinel and tourmaline. Cement and secondary minerals include quartz, carbonate, sericite, chlorite and sulfides (pyrite, chalcopyrite, bornite and chalcocite; Fig. 2.2f, g) which are accompanied by siderite, barite, fluorite and apatite. Secondary covellite, Ti oxide (rutile or anatase) and hematite are also observed in this study. Hydrothermal hematite in particular (e.g. Fig. 2.2h), ranges from almost non-existent to the major mineral in clasts and cement.
Mudstone	Contains chlorite, sericite, quartz, feldspar and accessory zircon and titanite.
Interbedded sandstone and red mudstone	
Sandstone	Detrital grains include granitoid-derived quartz, hematite, granite fragments, feldspar, zircon, tourmaline, rutile, fluorite and titanite. Felsic volcanic fragments and volcanic-derived quartz have been reported as well. Although the majority of quartz is granitoid-derived, some grains were noted in this study to be polycrystalline and contained zircon and tourmaline inclusions and sericite or chlorite at triple points. Variably sericite-altered feldspar and muscovite grains also occur. Hematite grains were noted in this study to range from angular to subrounded and have several different morphologies including elongate laths, tabular grains, zoned grains, and hematite-quartz aggregates (Fig. 2.3c); some hematite grains were noted to have magnetite cores (Fig. 2.3d). Rutile and tourmaline were noted by this study to also be concentrated in cross-beds (Fig. 2.3e). Cement and secondary minerals include quartz, sericite, hematite and the same sulfide assemblage and the green sandstone and mudstone (Fig. 2.3f). Barite, fluorite and Ti oxide were also noted in this study.
Mudstone	Dominated by hematite, minor magnetite, dispersed quartz, sericite and Fe-chlorite. Hematite grains were noted to usually occur as elongate laths.
Conglomerate	Hematite, feldspar-phyric (felsic) and mafic volcanic fragments and granitic clasts were reported.
Polymictic volcanic-clast conglomerate	

Conglomerate	Majority of clasts are granule- to cobble-sized felsic and mafic volcanic fragments (Fig. 2.4 a-c). Minor granite and hematite clasts were recorded by other workers. Hematite clasts were noted in this study to exhibit igneous textures (Fig. 2.4d) or comprise fine-grained aggregates of hematite and quartz. The pale matrix (e.g. Fig. 2.4a) was noted in this study to occur where the conglomerate was adjacent to sericite-altered tuffaceous mudstone in the northern BCF domain. The clasts and matrix are variably altered to hematite, chlorite and sericite. Other secondary minerals in the matrix include Ti oxide, carbonate, barite and the same sulfide assemblage as the other BCF. Some intervals of polymictic volcanic-clast conglomerate are strongly hematite-altered (Fig. 2.4c).
Thinly bedded sandstone and red mudstone	
Fe-rich mudstone	Reported to consist mainly of fine-grained hematite and sericite. Hematite grains are noted in this study to be angular to subrounded and have tabular, elongate lath and rare 'oolithic' morphologies. Grain size was commonly bedding controlled (Fig. 2.5b, c). Magnetite occurs as cores to hematite grains in some samples (Fig. 2.5d). Angular to subangular quartz grains and rare zircon were also noted by this study. Secondary minerals noted in this study include very fine-grained hematite occurring interstitially and as bladed/irregular overgrowths on larger grains. Minor barite, fluorite, apatite and sulfides (same assemblage as the rest of the BCF) are most apparent in fractures (Fig. 2.5c).
Sandstone	The detrital componentry is reported to consist mainly of angular to subangular fine-grained quartz, feldspar and felsic volcanic fragments.
Tuffaceous mudstone	Fine-grained, angular quartz and zircon have been previously reported; this study also noted minor tourmaline and Cr-spinel grains (Fig. 2.5f, g). Hematite can define very fine laminae (Fig. 2.5e, h). Secondary minerals noted by this study include sericite, very fine-grained hematite, barite, fluorite, sulfide and apatite (Fig. 2.5h, i).

Appendix 2.2 LA-ICPMS U-Pb geochronology methodology

The instrumentation used for zircon U-Pb geochronology varied over multiple analytical sessions (Table S2.2). All sessions employed an Agilent quadrupole ICPMS coupled to a Coherent COMPex Pro 193nm ArF Excimer laser system with a RESOlution/Laurin Technic constant geometry ablation cell. The data from all sessions were reprocessed to eliminate any errors that may have occurred over time. Downhole fractionation, instrument drift and mass bias correction factors for Pb/U ratios on zircons were calculated using 2 analyses of the primary zircon standard and checked on 1 analysis each of the secondary zircon standards analysed at the beginning of the session and 1 of each of the primary and secondary standards approximately every 15 unknown zircons (roughly every half hour) using the same spot size and analytical conditions as used on the samples. The correction factor for the $^{207}Pb/^{206}Pb$ ratio was calculated using large spots of the NIST610 reference glass analysed every 30 unknowns and corrected using the values recommended by Baker et al. (2004).

Each analysis of the zircon began with a 10-30 second analysis of the blank gas measurement followed by a further 20-30 seconds of analysis time when the laser was switched on. Zircons were sampled on 29-32μm spots using the laser at 5 Hz and a density of approximately 2 J/cm^2. The measurement time of the background and unknown as well as spot size were varied between analytical sessions over the several years of data collection but was consistent within sessions. A flow of He carrier gas at a rate of 0.35 litres/minute carried particles ablated by the laser out of the ablation cell to be mixed with Ar gas and carried to the plasma torch. Isotopes measured were ^{49}Ti, ^{56}Fe, ^{90}Zr, ^{178}Hf, ^{202}Hg, ^{204}Pb, ^{206}Pb, ^{207}Pb, ^{208}Pb, ^{232}Th, ^{235}U and ^{238}U with each isotope being measured every 0.17s with longer counting time on the Pb isotopes compared to the other isotopes. The data reduction used was based on the method outlined in Halpin et al. (2014) and is similar to that outlined in Black et al. (2004) and Paton et al. (2010). The program Isoplot 3.7 (Ludwig, 2008) was used for concordia plots and age calculations. The reference zircon 91500 ($^{207}Pb/^{206}Pb$ age = 1065.4 ± 0.3 Ma; Wiedenbeck et al., 1995) was used as a primary reference material for all analyses, which were further verified by secondary reference zircons Temora 2 ($^{206}Pb/^{238}U$ age = 416.8 ± 1.1 Ma; Black et al., 2003), GJ1 ($^{207}Pb/^{206}Pb$ age = 608.5 ± 0.4 Ma; Jackson et al., 2004) and Mud Tank (U/Pb age = 732 ± 5 Ma; Black and Gulson, 1978). The data were reduced using an in-house excel-based spreadsheet, with error propagation following the recommendations of Horstwood et al. (2016) (i.e. random uncertainties as well as total uncertainties including systematic uncertainties). Measured ages of reference materials are in Table S2.3.

Element abundances on zircons were calculated using the method outlined by Košler (2001) using Zr as the internal standard element, assuming stoichiometric proportions and using the NIST610 to standard correct for mass bias and drift.

Table S2.2 Summary of instrumentation and configuration for LA-ICPMS U-Pb geochronology

Session ID	Acquisition date	ICPMS (*Agilent*)	Cell model (*RESOlution*)	Spot size (μm)	Rep. rate (Hz)	Fluence (Jcm^{-2})	Background (ablation) time (s)
FE07	2011-02-07	7500cs	M50	34	5	2	15 (20)
MA04	2011-03-04	7500cs	M50	32	5	2	15 (20)
MY20	2011-05-20	7500cs	M50	32	5	2	15 (20)
SE01	2011-09-01	7500cs	M50	32	5	2	15 (25)
SE07	2011-09-07	7500cs	M50	32	5	1.95	30 (30)
MY16	2012-05-16	7500cs	S155	32	5	2.1	30 (30)
JN25	2013-06-25	7500cs	S155	32	5	2.15	20 (40)
MY13	2014-05-13	7500cs	S155	26	5	2	10 (30)
JL01	2015-07-01	7900	S155	29	5	1.8	30 (30)
AP19	2016-04-19	7900	S155	29	5	1.72	10 (25)
MY25	2016-05-25	7900	S155	29	5	2	10 (20)

Table S2.3 Reported and measured ages of reference materials for LA-ICPMS U-Pb geochronology

Reference material	Age type	Age ± 2*s* (Ma)	n	LA-ICPMS Age type	Age ± 2*s* ± $2s_{total}$ (Ma)	MSWD (p.o.f)
91500	ID-TIMS $^{207}Pb/^{206}Pb$	1065.4 ± 0.3	103	$^{206}Pb/^{238}U$	1063.6 ± 3.0 ± 11.2	0.20 (1.00)
Temora 2	ID-TIMS $^{206}Pb/^{238}U$	416.8 ± 1.1	45	$^{206}Pb/^{238}U$	417.5 ± 2.1 ± 4.7	0.72 (0.92)
GJ1	ID-TIMS $^{207}Pb/^{206}Pb$	608.53 ± 0.37	39	$^{206}Pb/^{238}U$	605.2 ± 2.6 ± 6.7	0.40 (1.00)
Mud Tank	ID-TIMS U-Pb	732 ± 5	20	U-Pb concordia	723 ± 15 ± 16.7	0.40 (0.99)

Table S2.4 List of samples from which detrital zircons were analysed

Sample ID	No. zircons (kept)	Drill hole	Depth (m)	BCF location (domain)	Date analysed
Green sandstone and mudstone					
OD032	14 (9)	RD1989	416.2	Southern	2011
OD033	13 (12)	RD1989	422.1	Southern	2011
OD130	6 (5)	RD1627	559.1	Southern	2011
OD131	12 (10)	RD1627	650.4	Southern	2011
OD138	12 (11)	RD1624	578.9	Southern	2011
OD506	5 (5)	RD1625	613.5	Southern	2012
OD521	33 (25)	RU38-2626	343.8	Southern	2014
OD525	4 (4)	RU38-2626	459.5	Southern	2012
OD758	9 (8)	RD896	637.2	Southern	2012
Interbedded sandstone and red mudstone					
OD036	29 (11)	RD1989	541.8	Southern	2014
OD037	10 (8)	RD1989	548.2	Southern	2011
OD051	14 (9)	RD3287	375.6	Southern	2011
OD123	12 (12)	RD1627	350.4	Southern	2011
OD509	45 (23)	RD1625	668.5	Southern	2014
OD517	32 (25)	RU38-2626	307.4	Southern	2014
OD620	39 (22)	RD2821	454.1	Southern	2014
OD749	8 (7)	RD896	353.6	Southern	2012
OD750	10 (10)	RD896	406.7	Southern	2012
OD760	10 (8)	RD916	380	Southern	2012
OD765	10 (8)	RD1988	337	Southern	2012
Polymictic volcanic-clast conglomerate					
OD055	16 (15)	MJ54WEST drive grab sample		Northern	2011
OD492	7 (7)	RD3449	375	Northern	2011
OD493	14 (12)	RD3449	378.8	Northern	2011
OD542	5 (4)	RD2765	345.8	Northern	2011
OD548	5 (3)	RD2765	408.4	Northern	2011
Thinly bedded red and green mudstone					
OD239	61 (51)	RD3449	427.2	Northern	2015
OD614	5 (5)	RD3449	451-451.5	Northern	2011
OD615	4 (2)	RD3449	337.5-338	Northern	2011
OD616	9 (4)	RD3449	376.5-377	Northern	2011

Single spot analyses were conducted on zircon grains collected from the BCF, including those by McPhie et al. (2016). When the analyses of McPhie et al. (2016) were reprocessed it was noted that some samples of a locally derived cross-bedded sandstone (that overlies the ODBC) and tuffaceous mudstone were included in the dataset "combined interbedded sandstone and red mudstone and green sandstone and mudstone". These samples were removed or reclassified to the appropriate facies association.

Analyses were filtered by removing metamict grains with significant Pb loss and those grains with elevated concentrations of ^{204}Pb. Analyses which produced anomalous ages (non-1.59 Ga) were excluded from interpretation of the dominant ca. 1.59 Ga age population.

Appendix 2.3 CA-TIMS U-Pb geochronology methodology

U-Pb dates were obtained by the chemical abrasion isotope dilution thermal ionization mass spectrometry (CA-TIMS) method from analyses composed of single zircon grains or fragments of grains (Appendix 2.6), modified after Mattinson (2005). Zircon was separated from rocks using standard techniques, placed in a muffle furnace at 900°C for 60 hours in quartz beakers, mounted in epoxy, and polished until the centers of the grains were exposed. Cathodoluminescence (CL) images were obtained with a JEOL JSM-1300 scanning electron microscope and Gatan MiniCL. Zircon was removed from the epoxy mounts for dating based on CL images.

Single grains or fragments were put into 3 ml Teflon PFA beakers and loaded into 300 µl Teflon PFA microcapsules. Fifteen microcapsules were placed in a large-capacity Parr vessel and the grains partially dissolved in 120 µl of 29 M HF for 12 hours at 180°C. The contents of the microcapsules were returned to 3 ml Teflon PFA beakers, HF removed, and the residual grains immersed in 3.5 M HNO_3, ultrasonically cleaned for an hour, and fluxed on a hotplate at 80°C for an hour. The HNO_3 was removed and grains or fragments were rinsed twice in ultrapure H_2O before being reloaded into the 300 µl Teflon PFA microcapsules (rinsed and fluxed in 6 M HCl during sonication and washing of the grains) and spiked with the Boise State University mixed ^{233}U-^{235}U-^{205}Pb tracer solution. Zircon was dissolved in Parr vessels in 120 µl of 29 M HF with a trace of 3.5 M HNO_3 at 220°C for 48 hours, dried to fluorides, and re-dissolved in 6 M HCl at 180°C overnight. U and Pb were separated from the zircon matrix using an HCl-based anion-exchange chromatographic procedure (Krogh, 1973), eluted together and dried with 2 µl of 0.05 N H_3PO_4.

Pb and U were loaded on a single outgassed Re filament in 5 µl of a silica-gel/phosphoric acid mixture (Gerstenberger and Haase, 1997), and U and Pb isotopic measurements made on a GV Isoprobe-T multicollector thermal ionization mass spectrometer equipped with an ion-counting Daly detector. Pb isotopes were measured by peak-jumping all isotopes on the Daly detector for 100 to 160 cycles, and corrected for 0.16 ± 0.03%/a.m.u. (1 sigma error) mass fractionation. Transitory isobaric interferences due to high-molecular weight organics, particularly on ^{204}Pb and ^{207}Pb, disappeared within approximately 60 cycles, while ionization efficiency averaged 10^4 cps/pg of each Pb isotope. Linearity (to ≥1.4 x 10^6 cps) and the associated deadtime correction of the Daly detector were monitored by repeated analyses of NBS982, and have been constant since installation. Uranium was analysed as UO_2^+ ions in static Faraday mode on 10^{12} ohm resistors for 300 cycles, and corrected

for isobaric interference of $^{233}U^{18}O^{16}O$ on $^{235}U^{16}O^{16}O$ with an $^{18}O/^{16}O$ of 0.00206. Ionization efficiency averaged 20 mV/ng of each U isotope. U mass fractionation was corrected using the known $^{233}U/^{235}U$ ratio of the Boise State University tracer solution.

U-Pb dates and uncertainties were calculated using the algorithms of Schmitz and Schoene (2007), $^{235}U/^{205}Pb$ of 77.93 and $^{233}U/^{235}U$ of 1.007066 for the Boise State University tracer solution, and U decay constants recommended by Jaffey et al. (1971). Dates utilize a $^{238}U/^{235}U$ of 137.88 (Steiger and Jager, 1977). If a more recently determined $^{238}U/^{235}U$ of 137.818 were used (Hiess et al., 2012), $^{207}Pb/^{206}Pb$ dates would be younger by 0.84 Ma. Dates were corrected for initial ^{230}Th disequilibrium using a $D_{Th/U}$ = 0.20 ± 0.05 (1σ) using the algorithms of Crowley et al. (2007), resulting in an increase in the $^{206}Pb/^{238}U$ dates of ~0.09 Ma. All common Pb in analyses was attributed to laboratory blank and subtracted based on the measured laboratory Pb isotopic composition and associated uncertainty. U blanks are estimated at 0.013 ± 0.009 pg (1σ).

Isoplot 3.7 Ludwig (2008) was used to calculate weighted mean $^{207}Pb/^{206}Pb$ dates from 5-8 equivalent dates per samples (i.e., probability of fit >0.05). The igneous crystallization ages are based on the weighted mean dates. The $^{207}Pb/^{206}Pb$ dates are used rather than $^{206}Pb/^{238}U$ dates due to some $^{206}Pb/^{238}U$ dates being slightly to moderately younger, presumably due to Pb loss; many of the grains are U-rich, cracked, and metamict. All analyses except for two are <1.9% discordant, with 69 of the 73 being <0.6% discordant. Errors on the weighted mean dates are given at 2σ and are the internal errors based on analytical uncertainties only, including counting statistics, subtraction of tracer solution, and blank and initial common Pb subtraction. These errors are ± 0.4-1.0 Ma. Including the U decay constant uncertainties propagated in quadrature increases the errors to ± 2.4-2.6 Ma. Seven aliquots of the 2000 Ma EARTHTIME synthetic age solution were analysed within a few months after the unknowns were analysed. These have radiogenic Pb ranging from 20 to 80 pg, similar the amounts in the unknowns. The weighted mean $^{207}Pb/^{206}Pb$ date is 2000.78 ± 0.47 Ma (MSWD = 0.8, pof = 0.59).

Appendix 2.4 Descriptions of CA-TIMS samples

Figure S2.1

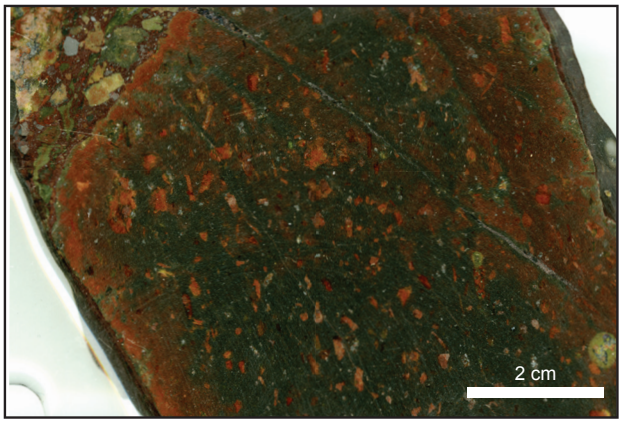

OD1207 (Fig. S2.1)

This sample of felsic volcanic breccia comprises a large felsic volcanic fragment in a reddish hematite-rich matrix. The volcanic clast has a dark grey groundmass that is reddish along the margins of the clast and along fractures. Abundant elongate, reddish laths in the groundmass are soft and are inferred to be former feldspar phenocrysts that have been replaced with sericite and hematite.

Figure S2.2

OD55 (Fig. S2.2, S2.3)

This sample comprises several large, rounded cobbles of felsic volcanic material with dark red groundmasses. Elongate and irregularly-shaped laths of sericite (and chlorite?) are inferred to have been feldspar phenocrysts. Pale grey, round or irregular quartz phenocrysts are subordinate to the feldspar phenocrysts.

Figure S2.3

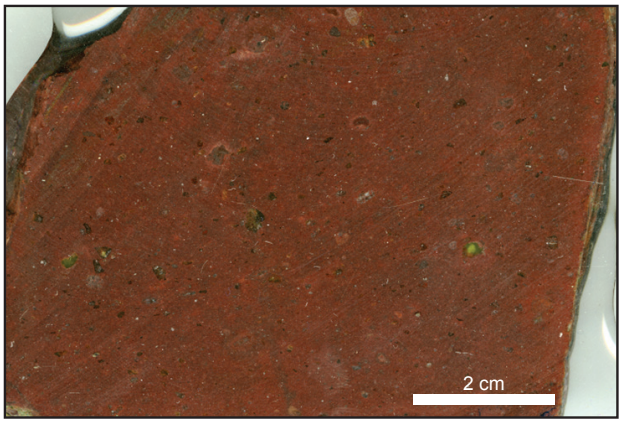

OD487 (Fig. S2.4)

This sample comprises rounded to angular fragments of felsic volcanic (and potentially some granitic) material from sub-mm to over 5 cm in size that define a couple of coarse-grained beds within an interval dominated by siltstone/sandstone. The felsic volcanic fragments appear to be largely feldspar-phyric (feldspars replaced by greenish sericite) and have a reddish-orange groundmass. The matrix surrounding the felsic volcanic fragments is a reddish-brown fine sandstone or

Figure S2.4

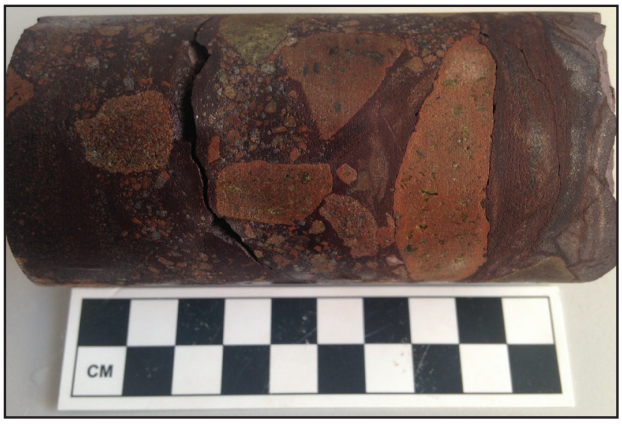

siltstone with dark heavy mineral bands (right of the image).

OD1201 (Fig. S2.5)

This sample of Roxby Downs Granite is coarse-grained, equigranular and has reddish coloured feldspars (hematite discolouration). Textural variation within the feldspars includes darker euhedral grains with beige zones and paler, anhedral feldspar that envelops quartz grains and the euhedral feldspar. Clusters of small black (magnetite, pyroxene and biotite) and pale cream grains (altered titanite) occur interstitial to the feldspar and quartz grains. Rare pyrite grains are observed.

OD1202 (Fig. S2.6)

This sample of Roxby Downs Granite is dominated by very reddish feldspar (hematite discoloured) that appears to have replaced much of the original assemblage. Rims of red feldspar are observed around subhedral sericite- (and/or chlorite) pseudomorphed feldspar grains. Quartz grains have much more variation in grain size and appear, in places, to be rimmed or even replaced by reddish feldspar. Black masses dispersed throughout the sample are inferred to be mafic microgranular enclaves. Pale beige grains are altered titanite and very fine pyrite grains are also present. Fractures through the sample are filled with sericite.

Figure S2.5

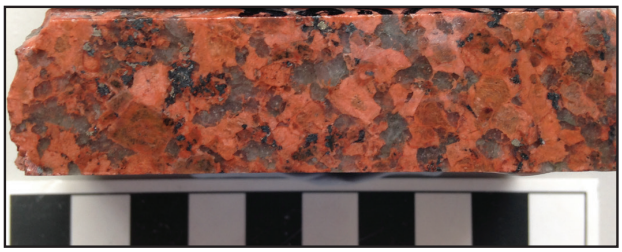

Figure S2.6

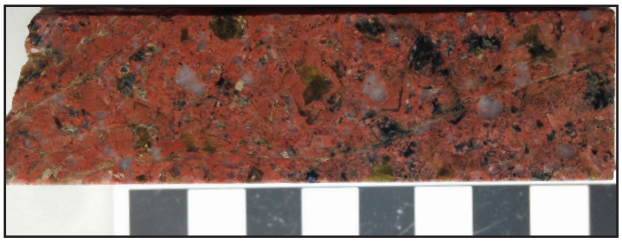

OD1214 (Fig. S2.7)

The feldspars in this sample of Roxby Downs Granite are less reddish and grains (feldspars and quartz) are less equigranular than sample OD1201. Abundant scattered dark grains and masses are aggregates of magnetite, pyroxenes and biotite or mafic microgranular enclaves. Fine-grained feldspars in the enclaves are more reddish than the big feldspars. Fine fractures through the sample are filled with hematite.

Figure S2.7

OD1215 (Fig. S2.8)

Figure S2.8

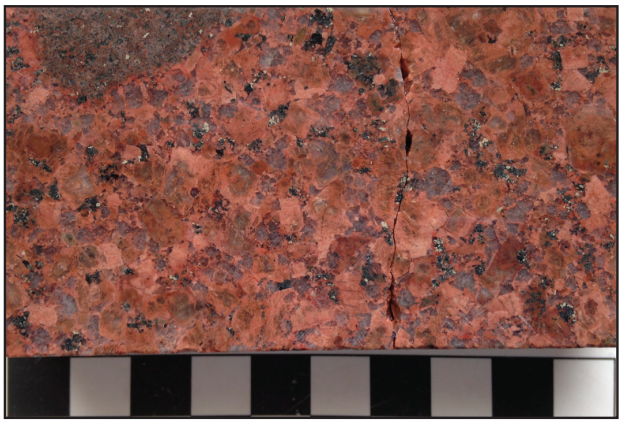

This sample of Roxby Downs Granite is coarse-grained, equigranular and has reddish feldspars. Many euhedral feldspar grains have beige, translucent cores rimmed by reddish feldspar. Quartz grains are also rimmed with reddish feldspar. Aggregates of dark grains are dispersed throughout the sample and comprise magnetite, biotite and pyroxene. Pale cream coloured grains associated with the aggregates are altered titanite. The sample contains a mafic microgranular enclave that contains feldspar, pyroxene, magnetite and altered titanite.

Figure S2.9

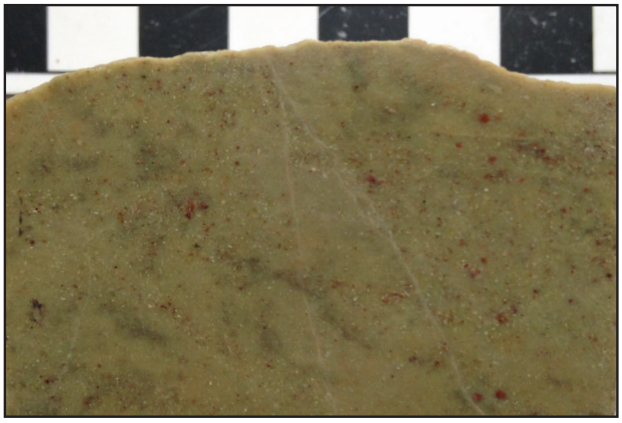

OD239 (Fig. S2.9)

This sample of tuffaceous mudstone is totally replaced with sericite; minor hematite is present as red speckles. Copper-bearing sulfides occur as darker spots.

Figure S2.10

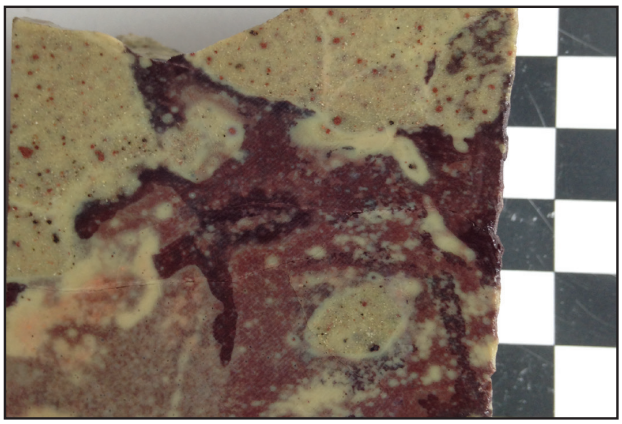

OD41 (Fig. S2.10)

This sample of tuffaceous mudstone is also completely sericitised but is also much more strongly altered with hematite (red to purple discolouration). Black/blue spots indicate the presence of Cu-bearing sulfides.

Appendix 2.5 Zircon LA-ICPMS geochronology data [digital appendix]

Appendix 2.6 Zircon CA-TIMS geochronology data [digital appendix]

Appendix 2.7 EPMA method - Cr-spinel

The major elements in Cr-spinel were analysed using a Cameca SX100 electron probe microanalyser (EPMA) at the Central Science Laboratory, University of Tasmania and the method is identical to that described in Huang et al. (2016). Table S2.5 comprises the list of analysed samples. Operating conditions of the EPMA included a 40 degrees take-off angle, beam energy of 15kV, beam current of 30 nA and beam diameter of 2 μm. Element concentrations were determined using the crystals LIF (large lithium fluoride) for Fe, Mn, Ti, Cr and Zn; LPET (large pentaerythritol) for P, K and Ca; and TAP (thallium acid phthalate) for Al, Si, Na and Mg. The following standards were used: Mn - Bustamite (Astimex block); Fe - Hematite (Astimex block); Ti - Rutile (Astimex block); Ca and Si - Clinopyroxene, Delegate (UTAS1 block); Mg - Olivine, San Carlos, USNM111312/444 (UTAS1 block); Al - Plagioclase, Labradorite, USNM115900 (UTAS1 block); Cr - Tiebaghi USNM117075 (UTAS2 block); Zn - Gahnite Brazil USNM145883 (UTAS2 block); Na - (K-) Anorthoclase, USNM133868 (UTAS3 block); K - Microcline (UTAS3 block); P - Apatite Durango (Apatites block). The counting time was 10 s for Na, Mn, Ti, K, Ca, P, 20 s for Zn, 30 s for Si, and 40 s for Al, Fe, Cr, Mg. The off peak counting time was 10 s for Na, Mn, Ti, K, Ca, P, and 20 s for Fe, Mg, Al, Si, Cr, Zn. Off-peak correction method was Linear for Na, Mg, Fe, Ti, K, Ca, Al, Si, Cr, Zn, and Slope (Hi) for Mn and P. Unknown and standard intensities were corrected for deadtime. Standard intensities were corrected for standard drift over time. Interference corrections were applied to Mn for interference by Cr. Oxygen was calculated by cation stoichiometry and included in the matrix correction. Further details can be found in Armstrong (1988).

Table S2.5. Samples and their drill-hole locations from which detrital Cr-spinel were analysed.

Sample ID	Cr-spinel analysed	Drill hole	Depth (m)	BCF domain
Green sandstone and mudstone (McPhie et al. 2011)				
ODX6867	20	RD2697	780-797	Southern
ODX6868	38	RD2697	797-814	Southern
ODX6869	48	RD2697	814-831	Southern
Green sandstone and mudstone (this study)				
OD034	34	RD1989	453.2	Southern
OD052	28	RD3287	465.8	Southern
OD129	47	RD1627	522.3	Southern
OD132	14	RD1627	738.4	Southern
OD136	2	RD1624	538.8	Southern
OD138	51	RD1624	578.9	Southern
OD499	13	RD1625	389.5	Southern
Thinly bedded red and green mudstone (this study)				
OD042	12	RD3449	431.5	Northern
OD239	12	RD3449	427.2	Northern
OD613	25	RD3449	491-492	Northern
OD614	25	RD3449	451-451.5	Northern
OD616	6	RD3449	376.5-377	Northern

Appendix 2.8 Cr-spinel EPMA chemistry data [digital appendix]

Appendix 2.9 Pairwise ANOVA and Tukey-Kramer test of CA-TIMS data [digital appendix]

Chapter 3 - Linking Olympic Dam and the Cariewerloo Basin: Was a sedimentary basin involved in formation of the world's largest uranium deposit?

Precambrian Research, v. 300, 168-180

Alexander R. Cherry[1], Jocelyn McPhie[1], Vadim S. Kamenetsky[1], Kathy Ehrig[2], John L. Keeling[3], Maya B. Kamenetsky[1], Sebastien Meffre[1], and Olga B. Apukhtina[1]

[1]ARC Centre of Excellence in Ore Deposits (CODES), School of Physical Sciences, University of Tasmania, Hobart, Tasmania 7001, Australia

[2]BHP Olympic Dam, 55 Grenfell Street, Adelaide, South Australia 5000, Australia

[3]Geological Survey of South Australia, Department of State Development, Adelaide, South Australia 5000, Australia

3.0 Abstract

The supergiant Olympic Dam Cu-U-Au-Ag deposit is hosted by the Olympic Dam Breccia Complex within a ca. 1.59 Ga granite. The breccia complex is largely granite-derived but also includes volcanic clasts and domains of bedded clastic facies. Recently discovered quartz-rich sandstone has a provenance that included Palaeoproterozoic and Archaean units represented by zircon populations centred at ca. 2.4 Ga and ca. 1.7 Ga. The texture, detrital and cement mineralogy, and distribution of detrital zircon ages in the quartz-rich sandstone closely match those in sandstone of the Pandurra Formation deposited in the regionally extensive intracratonic Cariewerloo Basin (ca. 1.44 Ga). The age of authigenic apatite (1.44 ± 0.02 Ga) in the brecciated quartz-rich sandstone is equivalent to the minimum depositional age of the Pandurra Formation. We conclude that the quartz-rich sandstone is a remnant of the Pandurra Formation, that the Pandurra Formation originally extended across the Olympic Dam Breccia Complex, and that it was incorporated by tectonic activity at least 150 myr after initial formation of the breccia complex. Furthermore, we speculate that oxidised U-bearing fluids from the overlying Cariewerloo Basin may have interacted with the Olympic Dam U resource, consistent with mounting evidence for substantial post-1.59 Ga remobilization and probable addition of U.

3.1 Introduction

The supergiant Olympic Dam (OD) Cu-U-Au-Ag deposit (10.1 Gt @ 0.78% Cu, 0.25kg/t U_3O_8, 0.3g/t Au, 1g/t Ag; BHP Billiton, 2016) is one of the largest known accumulations of metals, particularly U (Reeve et al., 1990; Ehrig et al., 2012). Olympic Dam is regarded as the flagship of the IOCG (iron-oxide-copper-gold) deposit class (Hitzman et al., 1992), although OD is distinct by virtue of its size and being the only deposit of this class to have economic quantities of U (Hitzman and Valenta, 2005).

The OD deposit is hosted by a breccia complex (Olympic Dam Breccia Complex, ODBC) within the ca. 1.59 Ga Roxby Downs Granite (RDG). Although early research concluded that OD was an unusual type of sediment-hosted Cu deposit (Roberts and Hudson, 1983), later research has favoured a hydrothermal origin and close link to a regional magmatic event at ~1.59 Ga (Oreskes and Einaudi, 1990; Reeve et al., 1990; Johnson and Cross, 1995; Skirrow et al., 2007). In addition, the ODBC is now recognized to be multi-stage and hydrothermal-tectonic in origin (Oreskes and Einaudi, 1990; Reeve et al., 1990; McPhie et al., 2011b).

The timing of formation of the ODBC is of paramount importance in constraining the timing of OD ore deposition and processes of ore genesis. Until recently, all of the lithological components of the ODBC (granite clasts, volcanic clasts, bedded clastic facies) have returned ages of ca. 1.59 Ga (Johnson and Cross, 1995; Jagodzinski, 2014) and the brecciation that generated the ODBC has been considered to have taken place at around the same time (Reeve et al., 1990; Johnson and Cross, 1995). However, McPhie et al. (2016) reported the presence of a brecciated quartz-rich sandstone in the ODBC that has a distinctive detrital zircon age population and provenance. Here we present additional data on the context, texture, mineralogy, petrography, detrital zircon population and diagenetic age of the quartz-rich sandstone. We test the hypothesis that the quartz-rich sandstone is not the same age as the other lithological components of the ODBC (i.e. ca. 1.59 Ga), but is related to other, potentially younger sedimentary formations in the vicinity of OD. The close correlation demonstrated with one of these successions indicates that it once directly overlay the ODBC and that tectonic activity affected the ODBC ~150 myr after initial formation. Furthermore, we speculate that this allowed access (into the ODBC) of basinal fluids that had the capacity to modify and even upgrade the OD U resource after 1.59 Ga.

3.2 Regional setting

Olympic Dam is one of several IOCG deposits and prospects in the Olympic IOCG Province along the eastern margin of the Gawler Craton (Skirrow et al., 2007) (Fig. 3.1). The Gawler Craton comprises Mesoarchaean to Palaeoproterozoic deformed and metamorphosed lithologies overlain by largely undeformed and unmetamorphosed Mesoproterozoic igneous rocks (Hand et al., 2007). The Mesoproterozoic igneous rocks include the Gawler Range Volcanics (GRV; ca. 1.595-1.587 Ga) (Jagodzinski et al., 2016) and the Hiltaba Suite granitoids, which together constitute the voluminous Gawler Silicic Large Igneous Province (Gawler SLIP) (Allen et al., 2008). The RDG (ca. 1593 Ma; Jagodzinski, 2014), which hosts the ODBC, is a member of the Hiltaba Suite (Fig. 3.1).

The eastern side of the Gawler Craton is unconformably overlain by the mostly flat-lying Mesoproterozoic Pandurra Formation (mainly quartz sandstone) (Cowley, 1993). The Pandurra Formation occurs to the north, west and south of OD (including at Acropolis, Emmie Bluff, Oak Dam and Wirrda Well IOCG prospects; Fig. 3.1b) but not at OD (Cowley, 1993). The Pandurra Formation and OD are unconformably overlain by flat-lying Neoproterozoic to Cambrian sedimentary formations (~350 m thick over the ODBC) of the Stuart Shelf (Roberts and Hudson, 1983; Preiss, 1993b). The Stuart Shelf succession includes the extensive Neoproterozoic Whyalla Sandstone (Preiss, 1987a), which is not preserved, or was not deposited, over the ODBC, but is present over the Acropolis and Emmie Bluff IOCG prospects (Fig. 3.1b). The Gairdner Dyke Swarm (ca. 0.83 Ga) (Wingate et al., 1998) intruded the Pandurra Formation (Cowley, 1993) and older units in the northeastern Gawler Craton, including the ODBC (Huang et al., 2015).

3.3 Olympic Dam deposit geology

The ODBC is surrounded by unbrecciated, weakly sericite-altered to fresh RDG and mainly consists of variably altered clasts of the RDG. Hydrothermally altered, brecciated GRV, bedded clastic facies and mafic dykes are locally abundant (Reeve et al., 1990; McPhie et al., 2011b; Ehrig et al., 2012). The brecciated GRV records the presence of GRV lavas above the RDG at OD prior to formation of the ODBC (McPhie et al., 2011b; Ehrig et al., 2012). The bedded clastic facies occur in large domains with faulted and/or brecciated contacts and as dispersed clasts. The domains and clasts consist of well-bedded mudstone, sandstone and conglomerate, and laminated ironstone (McPhie et al., 2016).

The intensity of hydrothermal alteration and brecciation increases towards the centre of the

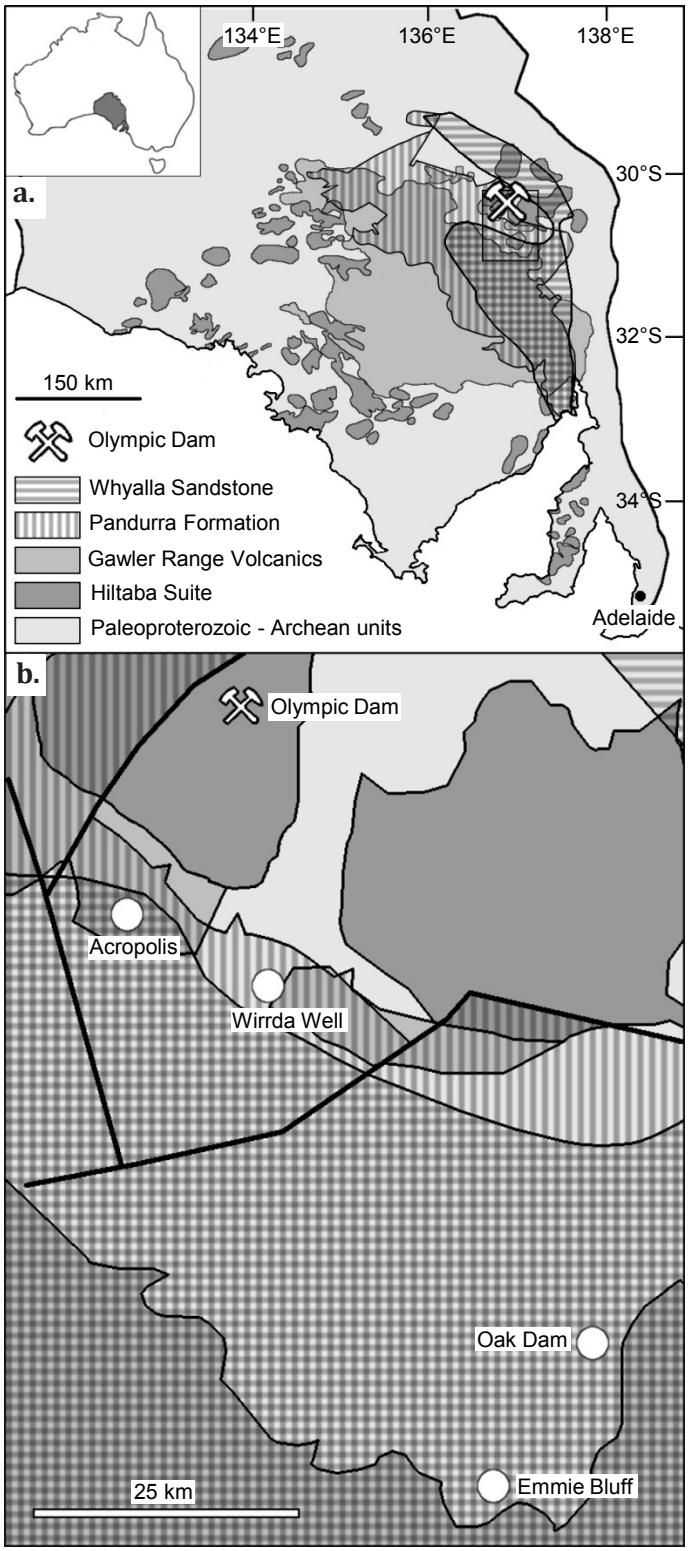

Figure 3.1 a. Location of Olympic Dam in the Gawler Craton (after Drexel et al., 1993; McPhie et al., 2011). The map also shows the distribution of the Mesoproterozoic Pandurra Formation and the Neoproterozoic Whyalla Sandstone. Shaded area on the inset map shows the Gawler Craton in South Australia. **b.** Location of Acropolis, Emmie Bluff, Oak Dam and Wirrda Well IOCG prospects.

ODBC resulting in a continuum in breccia texture and composition from peripheral sericite-altered, granite-rich breccia to hematite-rich breccia in the centre (Reeve et al., 1990; Ehrig et al., 2012). Several sets of steeply dipping brittle faults have been identified in the ODBC; these faults were in place pre- and syn-mineralization and locally show signs of post-mineralization reactivation (Fig. 3.2) (Ehrig et al., 2012).

The majority of the OD ore minerals are disseminated and show a strong association with the hematite-rich breccia. Copper sulfide minerals (chalcopyrite, bornite and chalcocite-group) are broadly zoned from S-poor sulfides (bornite + chalcocite) to Fe-rich sulfides (pyrite + chalcopyrite) with increasing depth (Reeve et al., 1990). The distribution of U minerals (uraninite + coffinite + brannerite) in the deposit is complex and not obviously zoned (Ehrig et al., 2012). Textures of the U minerals suggest there have been multiple episodes of precipitation and dissolution of U phases (Macmillan et al., 2016).

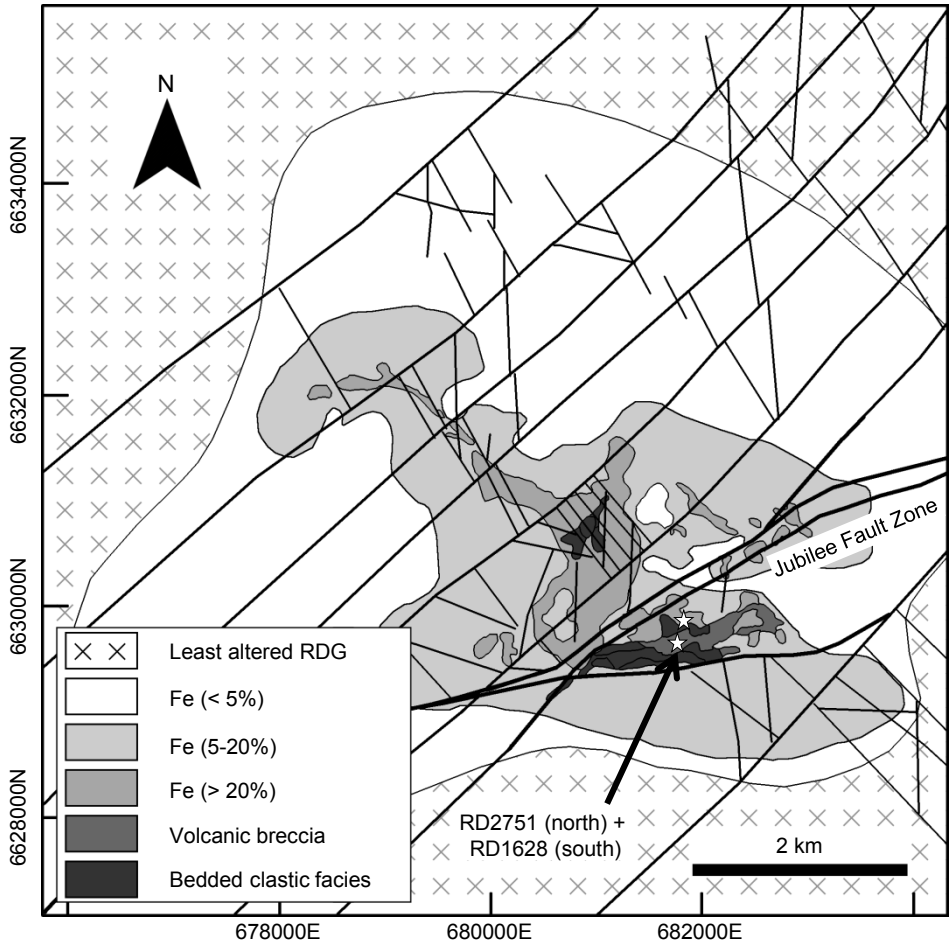

Figure 3.2 Map of Olympic Dam Breccia Complex (ODBC) at -350 mRL (after Hayward and Skirrow, 2010; Ehrig et al., 2012; Clark et al., 2016) and collars of RD1628 and RD2751 (stars). Granite breccia in the ODBC is shaded gray relative to Fe content (<5 wt.%, 5-20 wt.%, >20 wt.%), volcanic breccia and bedded clastic facies are shaded darker gray. Fault traces are shown as black lines, including the eastnortheast striking Jubilee Fault Zone.

3.4 Quartz-rich sandstone in the ODBC

Brecciated quartz-rich sandstone is a very minor component of the ODBC and has been identified in only two drill holes (Fig. 3.2) (McPhie et al., 2016). In both drill holes, the ~80-m-thick intervals of brecciated quartz-rich sandstone comprise mm- to decimetre-sized fragments of sandstone dispersed in red-brown, hematite-rich sandy matrix (Fig. 3.3a-c). In vertical drill hole RD1628, the interval of brecciated quartz-rich sandstone is immediately below the unconformity with the overlying Neoproterozoic succession and has a lower faulted contact with bedded clastic facies (Fig. 3.4). In inclined drill hole RD2751, the interval of brecciated quartz-rich sandstone is over 400 m below the unconformity surface and has upper and lower faulted contacts with hematite-rich breccia of the ODBC (Fig. 3.4). The interval of brecciated quartz-rich sandstone in RD2751 is situated below and ~100 m to the east of the interval in RD1628.

The quartz-rich sandstone fragments are angular to rounded (Fig. 3.3a-c). They are either internally massive or show well-defined internal bedding; the beds are planar or cross-stratified. The sandstone is poorly sorted, and mostly composed of fine- to very coarse-grained, angular to sub-rounded quartz grains with abundant syntaxial quartz overgrowths (Fig. 3.5a, b). Quartz grains are monocrystalline and polycrystalline; many grains show undulose extinction and contain abundant fluid and mineral inclusions. Minor clastic components include lithic fragments, muscovite, zircon, tourmaline, Ti-oxide (rutile/anatase), hematite and ilmenite. Some samples have abundant lithic clasts. The sandstone is cemented by the quartz overgrowths, and the intraclast pore space is filled mostly by illite/muscovite, and rarely by chlorite (clay speciation determined using reflectance spectroscopy, see Appendix 3.2 and 3.3) and late-stage quartz. Very fine-grained (ca. 10 μm), bladed hematite coats both detrital grains and quartz overgrowths, and is disseminated throughout the cement. Apatite is a minor component observed in the pore cement of a few sandstone fragments as isolated grains that are between 10-100 μm and commonly euhedral or clusters of grains that can be over 200 μm (Fig. 3.6a). The distribution and grain shape of the apatite suggests it is an authigenic phase. The intergrowth of apatite with the bladed hematite and quartz overgrowths further supports an authigenic origin (see Appendix 3.4).

The red-brown matrix surrounding the sandstone fragments comprises very poorly sorted, very fine- to coarse-grained quartz grains that are generally more angular and irregular (in some cases, embayed) than quartz grains in the sandstone fragments (Fig. 3.5c). Quartz overgrowths are

less common and in many cases have been truncated at grain boundaries. Minor clastic components in the matrix include lithic particles, muscovite, tourmaline and Ti-oxide, similar to those observed in the sandstone fragments. The cement is primarily illite; disseminated very fine-grained, bladed hematite and Ti-oxide are also present. There are small patches of matrix and haloes around sandstone fragments where the cement in the matrix is devoid of hematite (Fig. 3.5d).

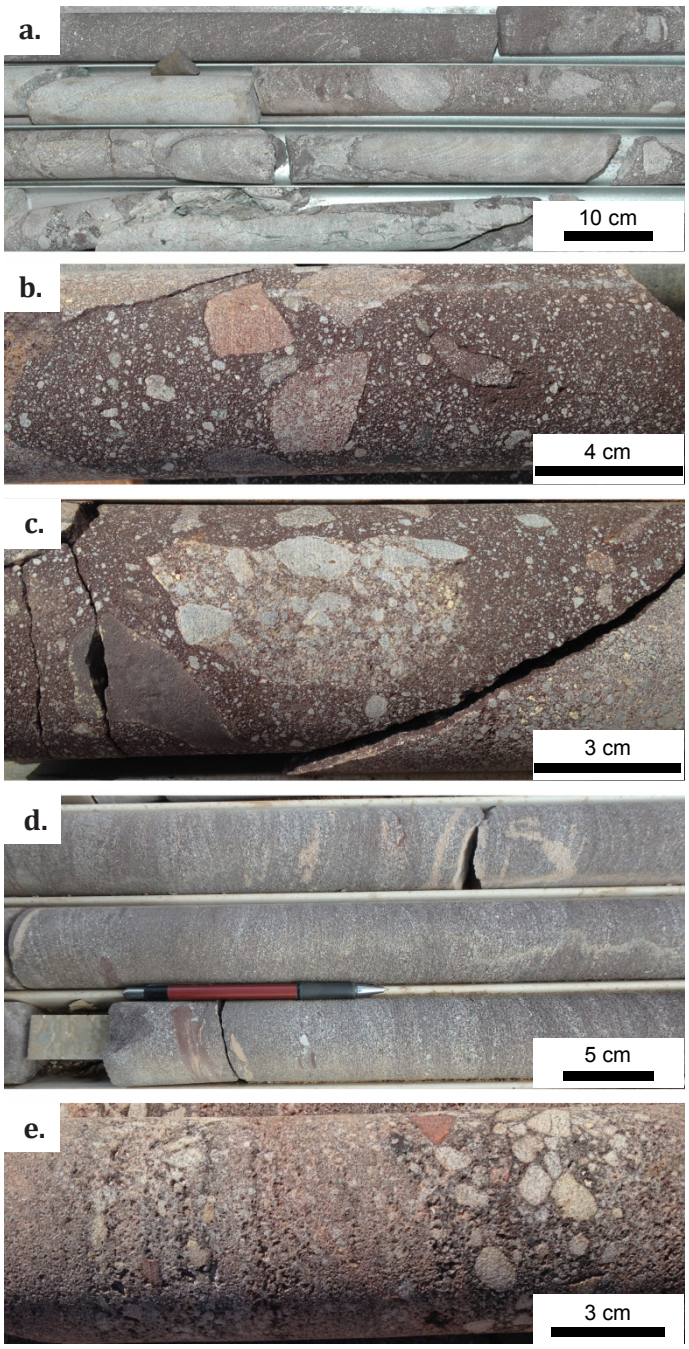

Figure 3.3 a. Interval of quartz-rich sandstone fragments in red-brown matrix, RD2751, ~890 m. **b, c.** Clasts of coarse-grained and pebbly quartz-rich sandstone in red-brown matrix, RD1628, 346.6 m, 352.3 m. **d.** Interval of Pandurra Formation quartz sandstone above the Acropolis prospect, ACD15, ~480 m. **e.** Pandurra Formation pebbly coarse sandstone above the Oak Dam prospect, AD3, 537.5 m.

Sulfides, and U and rare earth element (REE) minerals are rare in the brecciated quartz-rich sandstone, as indicated also in drill hole assays which show that economic elements (e.g. U) are mostly below detection (Fig. 3.4, see Appendix 3.5). Rare chalcopyrite occurs with chlorite in some sandstone fragments; xenotime, thorite, monazite, bastnäsite and synchysite are present only in trace abundances. In contrast, adjacent lithologies have elevated concentrations of Cu, U and REE, characteristic of the OD orebody (Fig. 3.4).

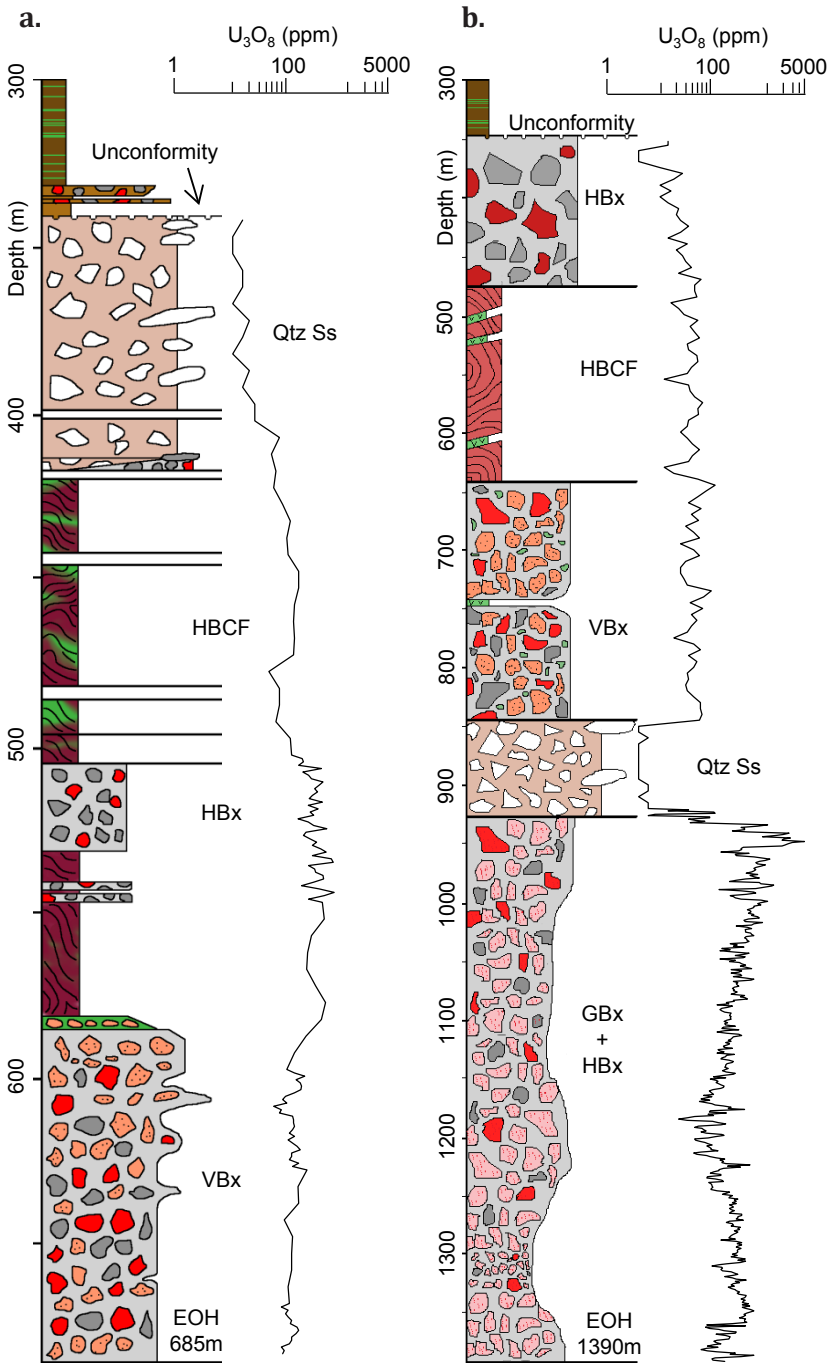

Figure 3.4 Lithology logs of drill core. **a.** RD1628 and **b.** RD2751 and corresponding assay of U_3O_8 grade (detection limit = 4-6 ppm). Note the different vertical scales of the two logs. The interval of quartz-rich sandstone in RD1628 is at ~340-420 m and in RD2751 is at ~840-925 m. The different lithologies and breccia types are juxtaposed by faults (black lines).The trend of U_3O_8 grade reflects that of Cu, Au, Ag and Fe. HBx - Hematite-rich breccia, VBx - Volcanic breccia, GBx - Granite-rich breccia, HBCF - Hematite-rich bedded clastic facies, Qtz Ss - brecciated quartz-rich sandstone.

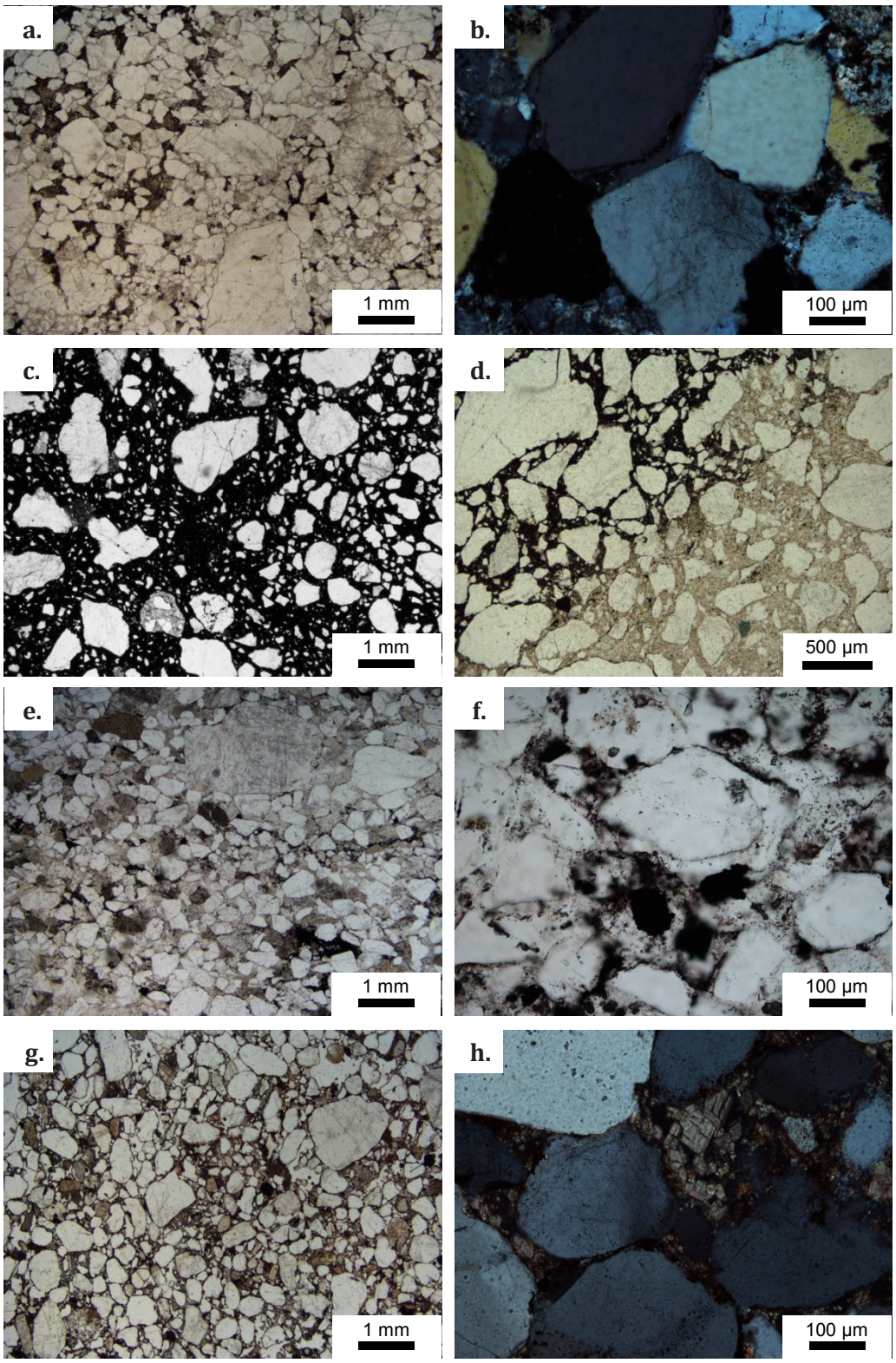

Figure 3.5 a-d. Quartz-rich sandstone (Olympic Dam). **a.** Poorly sorted sandstone from a sandstone fragment (plane polarised light - PPL, RD2751, 900.7 m). **b.** Syntaxial quartz overgrowths on detrital quartz in a sandstone fragment (cross polarised light - CPL, RD1628, 370 m). **c.** Red-brown matrix comprising angular, poorly sorted quartz and fine-grained illite/muscovite and hematite cement (PPL, RD2751, 855.0 m). **d.** Part of the red-brown matrix with a hematite-poor halo around a sandstone fragment (off image) (PPL, RD1628, 386 m). **e-f.** Pandurra Formation. **e.** Poorly sorted quartz-rich Pandurra Formation sandstone from above the Oak Dam prospect (PPL, AD3, 548.4 m). **f.** Syntaxial quartz overgrowths on detrital quartz (PPL, AD3, 774.1 m). **g-h.** Whyalla Sandstone **g.** Poorly sorted/ bimodal, quartz-rich Whyalla Sandstone from above the Emmie Bluff prospect (PPL, SAE6, 376.8 m). **h.** Carbonate cement between detrital quartz in Whyalla Sandstone (CPL, SAE6, 376.8 m).

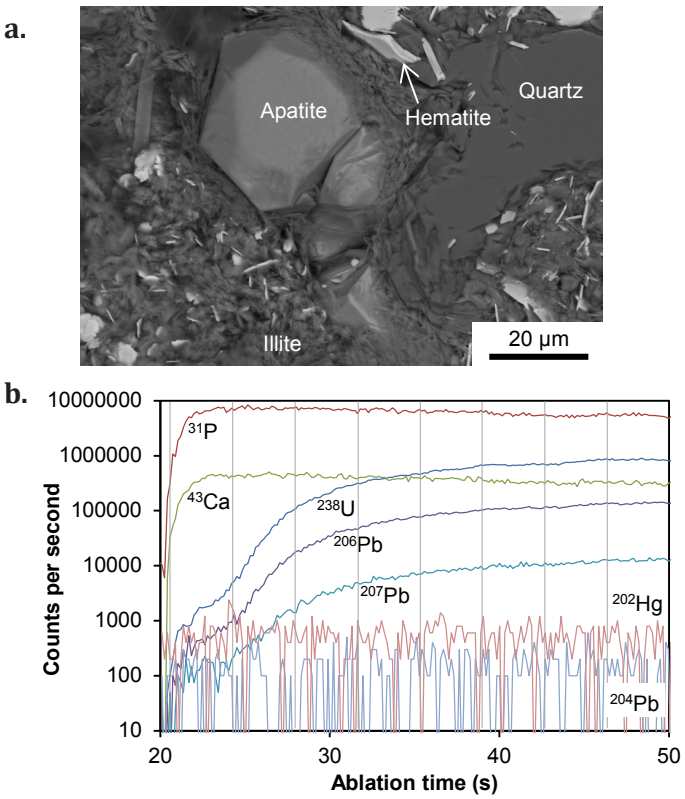

Figure 3.6 a. Back-scattered electron image of euhedral apatite interstitial to detrital quartz and intergrown with illite and hematite cement, RD2751, 919.6 m. **b.** Downhole/time-resolved laser ablation analysis profile of apatite grain showing consistent ^{43}Ca, ^{31}P, ^{202}Hg and ^{204}Pb but low initial ^{238}U and radiogenic Pb. Values are in counts per second (cps). Vertical lines represent the 8 splits of the laser ablation profile; the first three splits produced discordant ages with low apparent $^{238}U/^{206}Pb$ and high $^{207}Pb/^{206}Pb$ ratios.

3.5 Zircon and apatite geochronology

In order to constrain the regional affinities of the quartz-rich sandstone in the ODBC, we examined the age profile of detrital zircons within the sandstone fragments and determined the age of authigenic apatite in the sandstone matrix.

3.5.1 Methods

3.5.1.1 Zircon

Sandstone samples were crushed, sieved and panned to produce a heavy mineral concentrate. After removal of the magnetic fraction with an NdFeB hand magnet, zircons were handpicked and mounted on 1-inch epoxy resin disks and polished. The potential introduction of bias to the detrital zircon age populations through either heavy liquid- or water-based techniques was determined by Sláma and Košler (2012) to mostly occur as preferential loss of smaller zircon grains for both techniques. Mitigation of the tendency to favour larger grains during handpicking was attempted

through use of a very fine titanium needle to pick grains (instead of tweezers) (e.g. Sláma and Košler, 2012).

Zircons were analysed using Laser Ablation-Inductively Coupled Plasma Mass Spectrometry (LA-ICPMS) at the University of Tasmania (see Appendix 3.6 for details of instrument configuration). Age calculations and probability density plots were derived using the program ISOPLOT (Ludwig, 2008). The reference zircon 91500 (Wiedenbeck et al., 1995) was used as a primary standard for all analyses, and additional verification involved the secondary zircon standards Temora 2 (Black et al., 2003), Mud Tank (Black and Gulson, 1978), Plešovice (Sláma et al., 2008) and occasionally JG1 (Jackson et al., 2004) and Qinghu (Li et al., 2013).

The quartz-rich sandstone detrital zircon analyses presented here build on the dataset of McPhie et al. (2016), which was exclusively on samples from drill hole RD2751. In this study, additional samples from drill holes RD2751 as well as RD1628 were analysed (see Appendices 3.1 and 3.7). The detrital zircon analyses for samples of the other bedded clastic facies are the same as those presented in McPhie et al. (2016). Detrital zircons from two quartz-rich sandstone successions in the vicinity of OD, the Pandurra Formation and the Whyalla Sandstone, were also analysed for comparison. The Pandurra Formation and Whyalla Sandstone samples were obtained from exploration drill holes near OD. The Pandurra Formation samples came from drill holes at the Acropolis (ACD1, ACD15, ACD18), Emmie Bluff (SAE6), Oak Dam (AD1, AD3) and Wirrda Well IOCG prospects (WRD21, WRD31) (Fig. 3.1b). Samples were taken at intervals throughout the Pandurra Formation to also track any stratigraphic variation in detrital zircon age populations. The Whyalla Sandstone samples were collected from the Emmie Bluff prospect (SAE6) (Fig. 3.1b). Single spot analyses were recorded on zircon grains. Only those zircon analyses with a discordance of less than 10% were used for population interpretation on probability density plots. The Th/U ratios of zircon analyses were calculated for further comparison of zircon age populations (see Appendix 3.4 and 3.7).

3.5.1.2 Apatite

Due to the small size of the apatite grains (<100 μm), U-Pb analyses were conducted *in situ*, on polished mounts, using the same instrument and interpretation software as was used for the analyses of the detrital zircons (see Appendix 3.8 for additional details). The reference apatite OD306

(Thompson et al., 2016) was used as a primary standard. The analyses were further verified using secondary apatite standards 401 (Thompson et al., 2016), Kovdor (Amelin and Zaitsev, 2002) and McClure Mountain (Schoene and Bowring, 2006).

Apatite grains in the sample OD977 (RD2751, 919.6 m) were analysed. The ablation profiles of the apatite grains are variably heterogeneous; some zones (particularly rims) contain very low U and Pb (Fig. 3.6b, data in Appendix 3.10). The ablation profiles of the analyses were split into eight segments (of equal duration) to compensate for the heterogeneity and to improve age calculation statistics (e.g. Davidson et al., 2007; Kamenetsky et al., 2016).

3.5.2 Results

3.5.2.1 Zircon

Of the 630 detrital zircon grains analysed from the quartz-rich sandstone fragments, 289 had a discordance of less than 10%. The detrital zircon age distribution of the quartz-rich sandstone fragments shows three main populations at ca. 2.55-2.35 Ga, ca. 1.7 Ga and ca. 1.59 Ga, and a minor population at ca. 1.85 Ga (Fig. 3.7a). Identical populations of zircons are present in the red-brown matrix. The similarity in zircon age distribution of the quartz-rich sandstone fragments and enclosing red-brown sandy matrix is consistent with both being derived from brecciation of a single quartz-rich sandstone protolith.

The other bedded clastic facies in the ODBC have a single population of ca. 1.59 Ga detrital zircons (McPhie et al., 2016) (Fig. 3.7a). Detrital zircon grains in the Pandurra Formation samples from the Acropolis, Emmie Bluff, Oak Dam and Wirrda Well prospects (2416 grains analysed of which 1024 were <10% discordant) show the same overall distribution of ages as the quartz-rich sandstone in the ODBC (Fig. 3.7a); most single samples also have the same overall distribution of zircon ages as the quartz-rich sandstone. The similar age distribution is reflected in the variation in Th/U ratios of the quartz-rich sandstone and Pandurra Formation (see Appendix 3.4 and 3.7). Five of the analysed samples of Pandurra Formation from drill hole AD3 (Fig. 3.8) show that the distributions of zircon ages vary uphole: age distributions in lower samples are dominated by a Mesoproterozoic population whereas higher samples have larger Palaeoproterozoic and Archaean populations (including the appearance of the ca. 1.85 Ga population in the upper samples) (Fig. 3.8). The Whyalla Sandstone

at Emmie Bluff (171 grains analysed of which 81 were <10% discordant) has the same zircon age populations identified in the quartz-rich sandstone in the ODBC, but has additional age populations clustered at ca. 1.2 Ga and ca. 1.1 Ga (Fig. 3.7a).

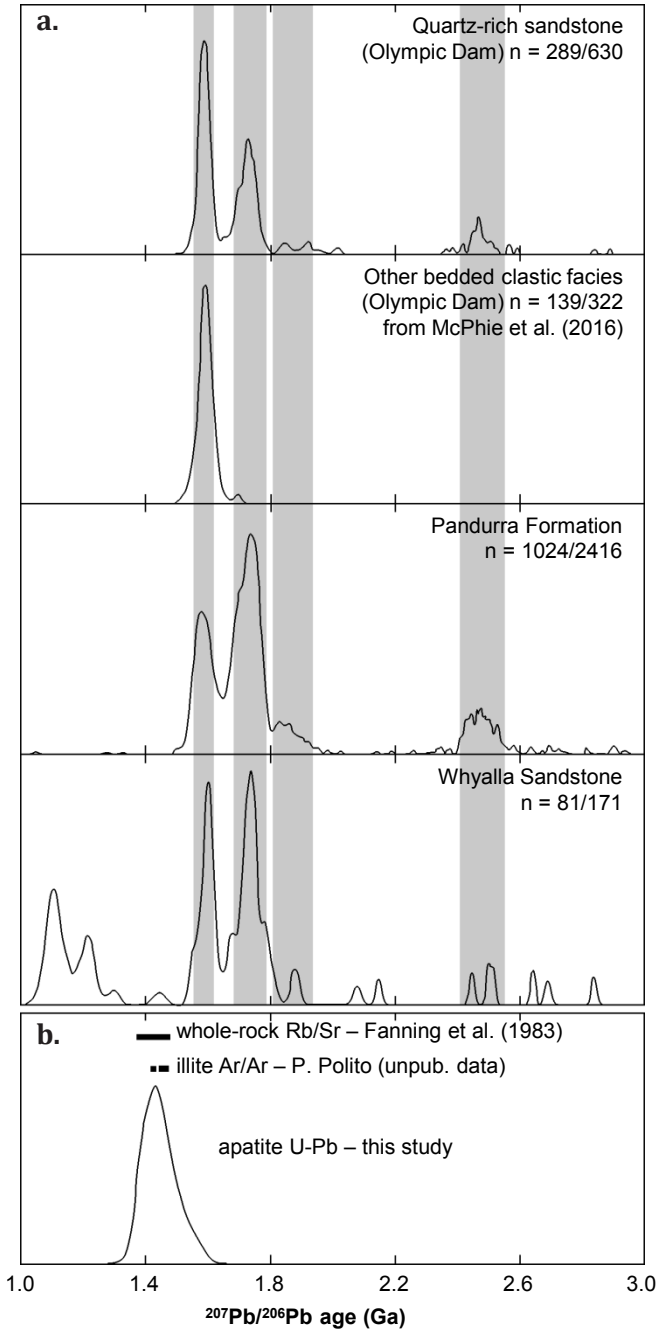

Figure 3.7 Probability density distributions of U-Pb age data (<10 % discordant) for **a.** Detrital zircons from the quartz-rich sandstone and other bedded clastic facies in the ODBC, the Pandurra Formation and Whyalla Sandstone. Gray bars highlight population correlation. Total analyses per sample and proportion of concordant analyses are shown (n). **b.** Authigenic apatite from the quartz-rich sandstone in OD, prior geochronology of the Pandurra Formation by Fanning et al. (1983) and P. Polito (pers. comm., 2016).

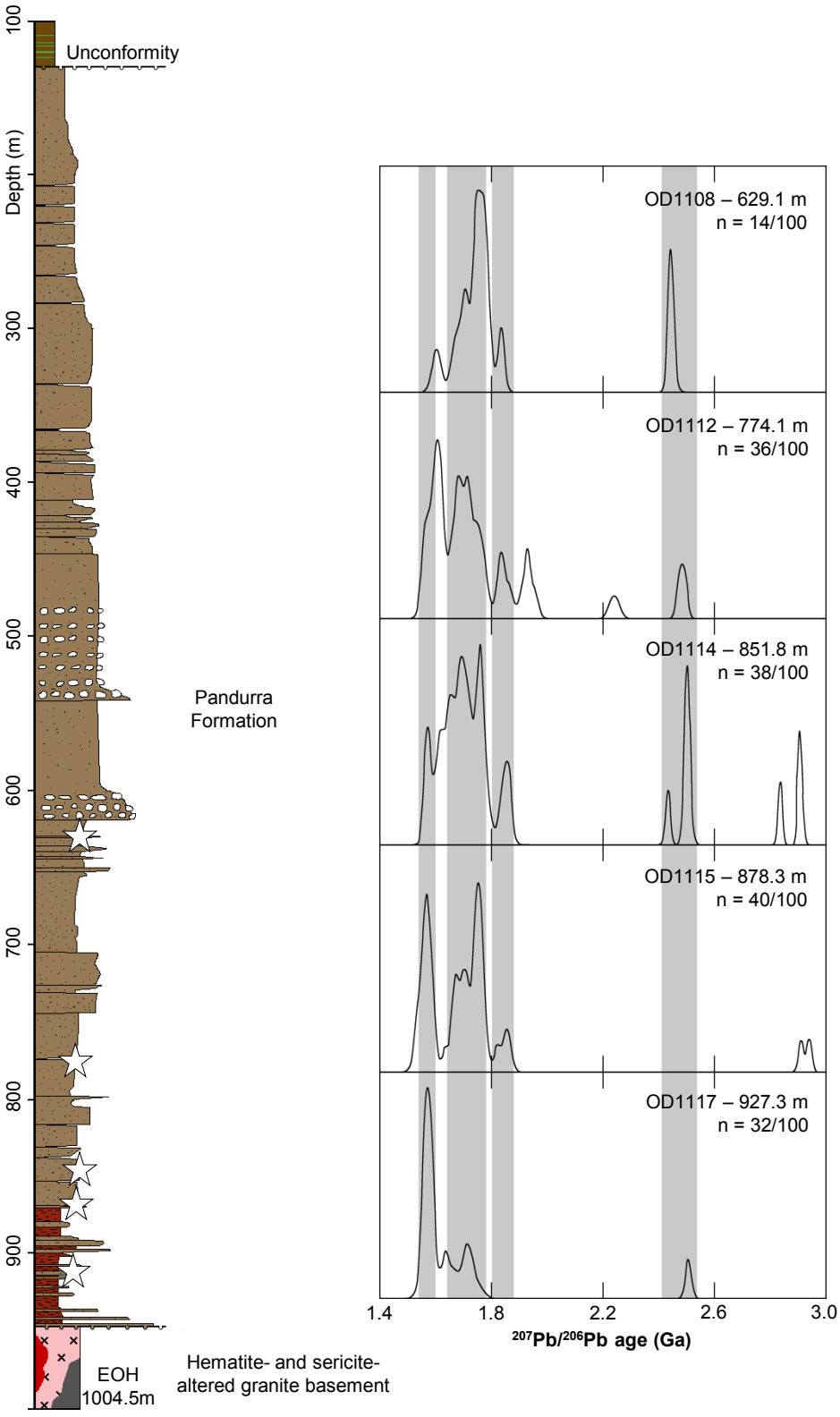

Figure 3.8 Log of drill hole AD3 intersecting Pandurra Formation above the Oak Dam IOCG prospect with probability density plots of U-Pb ages (<10 % discordant) of detrital zircons from five samples (depth recorded on plots). Total analyses per sample and proportion of concordant analyses are shown (n). Sample sites are indicated by stars.

3.5.2.2 Apatite

The most concordant apatite analyses (n = 19) also have the highest U concentrations (100-700 ppm) as well as Th, Ce and total Pb (see Appendix 3.9). The analyses that are more discordant and/or exhibited mixing with common Pb invariably have lower concentrations of U, Th, Ce and Pb. The apatite analyses have been split into multiple ablation segments and presented in a Tera-Wasserburg concordia plot (Fig. 3.9a, b). The majority of the split analyses cluster near concordia and form a single population which has a $^{207}Pb/^{206}Pb$ age peak at ca. 1.44 Ga (Fig. 3.7b). The remainder of the split analyses scatter out from the ca. 1.44 Ga population, representing mixing of radiogenic Pb with common Pb as well as analyses with very low $^{238}U/^{206}Pb$ ratios. The majority of the split analyses affected by common Pb and/or with very low $^{238}U/^{206}Pb$ ratios are of grain rims that have low counts of ^{238}U, ^{206}Pb and ^{207}Pb, but relatively constant ^{204}Pb (representing common Pb) (Fig. 3.6b). The low U and radiogenic Pb counts increase the influence of common Pb on $^{238}U/^{206}Pb$ and $^{207}Pb/^{206}Pb$ ratios. Split analyses containing elevated Fe (> 10 000 ppm) are interpreted to indicate mixing of apatite with fine-grained hematite and have also been excluded from the age interpretation. The final intercept age of the apatite is 1441 ± 15 Ma (MSWD = 3.3, n = 105) (Fig. 3.9b).

3.6 Discussion

3.6.1 Comparison of the quartz-rich sandstone with other bedded clastic facies in the ODBC

The quartz-rich sandstone and the other bedded clastic facies have the same maximum age of deposition of ca. 1.59 Ga, based on the youngest detrital zircon age population. This age reflects the involvement of the Mesoproterozoic Gawler SLIP in the provenance of all the bedded clastic facies. However, the quartz-rich sandstone contains additional zircon populations not present in the other bedded clastic facies, and indicating a significantly wider provenance that included Archaean and Palaeoproterozoic successions.

In sections through the bedded clastic facies, the facies associations other than the quartz-rich sandstone occur interbedded with each other and preserved contacts between them are gradational. In RD2751 and RD1628, the brecciated quartz-rich sandstone is separated from other bedded clastic facies by faults or by intervals of hematite-rich or volcanic breccia. Hence, the available data indicate that the quartz-rich sandstone was not originally interbedded with the other bedded clastic facies.

The quartz-rich sandstone is less hydrothermally altered than the other bedded clastic facies, despite juxtaposition with mineralized hematite-rich breccia in the ODBC; hydrothermal minerals are very rare, apart from pervasive, fine-grained hematite in the breccia matrix. The other bedded clastic facies have been variably affected by texturally destructive hydrothermal alteration (Ehrig et al., 2012) and contain the same hydrothermal mineral assemblage (e.g. hematite, sericite, chlorite, Cu sulfide, siderite, barite, fluorite) as the ore zones in the hematite-rich breccia. McPhie et al. (2016) therefore concluded that the altered and mineralized bedded clastic facies were present at the time of formation of the ODBC and the Cu mineralization event. However, the lower intensity of hydrothermal alteration in the brecciated quartz-rich sandstone suggests it was incorporated into the ODBC separately, at some time after the main mineralization and alteration events (Fig. 3.5c, d).

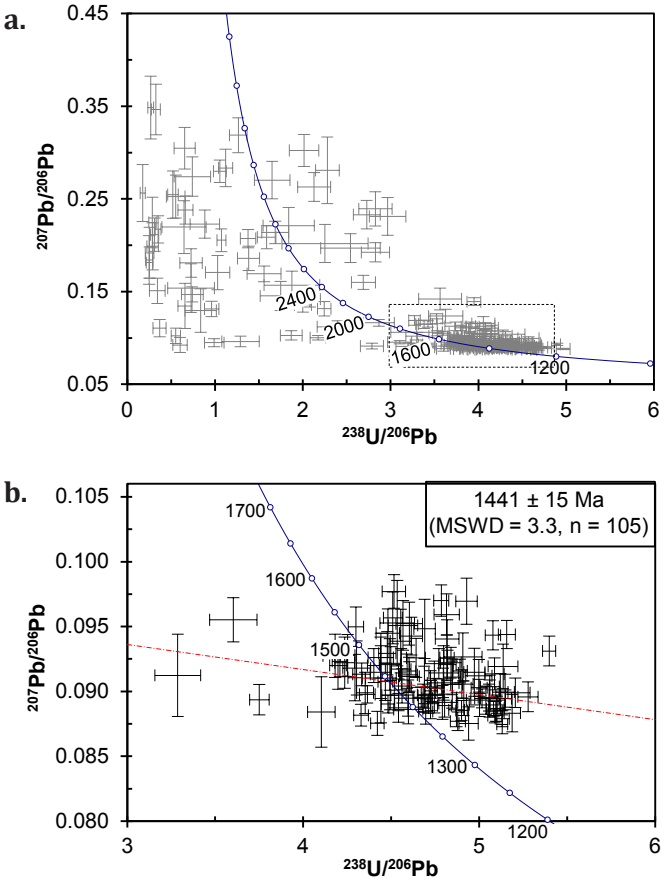

Figure 3.9 Authigenic apatite U-Pb geochronology **a.** Tera-Wasserburg concordia plot showing the fan of split analyses diverging from the ca. 1.44 Ga population due to low U and Pb grains. **b.** Tera-Wasserburg concordia plot of the filtered data used for age interpretation with a $^{207}Pb/^{206}Pb$ intercept of 1441 ± 15 Ma (MSWD = 3.3, n = 105).

3.6.2 Comparison of the quartz-rich sandstone in the ODBC with potential correlates

3.6.2.1 Pandurra Formation

The Pandurra Formation defines the known extent of the intracontinental Cariewerloo Basin (~42,500 km^2) (Cowley, 1993). The basin has a ~420 km northwesterly extent and is up to ~170 km wide; over 95% of the basin underlies Neoproterozoic and younger sedimentary rocks (Fig. 3.1). The Pandurra Formation consists of red-bed quartz sandstone that has a maximum thickness of ~1200 m recorded in drill holes from the northern portion of the basin (Keeling et al., 2012). The current margins of the Pandurra Formation in the area around OD have been interpreted to be faults, consistent with the Pandurra Formation having been present above OD originally but subsequently eroded from the top of an uplifted fault block (Cowley, 1993). Reconstructed sections through the Cariewerloo Basin indicate extensive post-depositional displacement of the Pandurra Formation on faults along the eastern basin margin (Cowley, 1993).

The Pandurra Formation sections examined in this study comprise internally massive or graded, well-defined sandstone beds that are commonly cross-stratified. The sandstone is typically poorly sorted and dominated by angular to subrounded fine- to very coarse-grained quartz. The quartz grains are mono- and poly-crystalline, show undulose extinction, and have numerous mineral and fluid inclusions. Syntaxial quartz overgrowths are common. Lithic fragments are variably abundant, comprising up to 50% of some sandstone samples. Minor detrital grains include muscovite, tourmaline, zircon, hematite, rutile and altered ilmenite. The diagenetic assemblage includes ubiquitous hematite coatings, quartz overgrowths and pore-filling dickite and illite cements, all of which have been reported in samples of the Pandurra Formation from other sections (Keeling et al., 2012). Spectral analyses of samples from >90 drill holes from across the Cariewerloo Basin indicate that only remnant patches of dickite remain; most dickite has been altered to illite/muscovite, due to deep burial and/or circulation of warm, acidic to neutral, saline fluids within the Cariewerloo Basin (Keeling et al., 2015). The detrital mineralogy and diagenetic cement of the Pandurra Formation are very similar to those in the brecciated quartz-rich sandstone in the ODBC (i.e. detrital angular to subrounded, mono- to polycrystalline quartz and lesser lithic fragments, and diagenetic quartz, illite and minor hematite). However, no apatite was observed in the Pandurra Formation samples examined in this study, and apatite has not been reported by other studies of the Pandurra Formation.

The zircon age populations in samples of the Pandurra Formation analysed in this study are also very similar to those of the quartz-rich sandstone in the ODBC (Fig. 3.7a), and the similar range of Th/U ratios for each age peak indicates a similar variety of source rocks contributed to both. A similar distribution of zircon ages has been reported for samples of the Pandurra Formation from drill holes farther to the northwest (Peeweena 1 – also known as Red Millers Creek 1) and south (CSR-PY1) Fanning and Link (2003) of OD, and from a drill hole to the south (Vanguard-1) (Rollison, 2016) of OD. The detrital zircon populations of drill hole AD3 reveals the appearance (or increasing proportion) of some Palaeoproterozoic and Archaean age populations in younger Pandurra Formation sandstones (Fig. 3.8) and suggests the fluvial drainage network was extended or modified over time and/or fluvial erosion exposed older basement beneath areas of thin volcanic cover in the Gawler SLIP (Fig. 3.8). Rollison (2016) offered a similar interpretation from the Vanguard-1 drill hole. However, the quantity of zircons analysed in this study limits the reliability of this interpretation (e.g. Andersen, 2005); a more systematic study involving greater numbers of grains is required to more effectively encapsulate the variation in detrital zircon age populations within and between members of the Pandurra Formation and throughout the Cariewerloo Basin.

The ca. 1.44 Ga age of interstitial authigenic apatite in the brecciated quartz-rich sandstone in the ODBC is interpreted to represent the timing of diagenesis and therefore the minimum depositional age for the quartz-rich sandstone. Authigenic apatite has been described in intracontinental sandstone from the Palaeoproterozoic Athabasca and Thelon basins and the Mesoproterozoic Hornby Bay Basin in Canada (Gall and Donaldson, 2006; Davis et al., 2008). The lack of recorded authigenic apatite in the Pandurra Formation and the observation of apatite in only a few fragments of the brecciated quartz-rich sandstone in the ODBC suggest apatite is a relatively rare phase in the Cariewerloo Basin. A whole rock Rb/Sr age of 1424 ± 51 Ma for Pandurra Formation siltstone beds in drill hole Peeweena 1 drilled in the northern Cariewerloo Basin, was interpreted as the minimum age of deposition (Fanning et al., 1983). This age is supported by unpublished authigenic illite/muscovite ages of 1426 ± 6 and 1458 ± 11 Ma ($^{40}Ar/^{39}Ar$; P. Polito, 2016, pers. comm.) for samples of basal Pandurra Formation in drill hole HHD1 (1071.6 m and 1046.0 m down hole, respectively), located ~40 km southwest of OD. Our result of ca. 1.44 Ga for the crystallization of euhedral, authigenic apatite in the quartz-rich sandstone cement is consistent with available data on the timing of deposition or early diagenesis/lithification of the Pandurra Formation (Fig. 3.7b). Coupled with the consistent detrital zircon age populations and mineralogy, the Pandurra Formation correlates very strongly with the brecciated quartz-rich sandstone in the ODBC.

3.6.2.2 Whyalla Sandstone

Another possible protolith for the brecciated quartz-rich sandstone in the ODBC is the Neoproterozoic Whyalla Sandstone. The Whyalla Sandstone extends ~25,000 km^2 across the Stuart Shelf; it has a ~470 km north to northwest extent and is up to ~170 km east to west (Fig. 3.1). This Neoproterozoic sandstone at one time may have extended across the ODBC and been removed later by erosion, as it is not preserved directly over the ODBC. The sandstone is predominantly medium to very coarse-grained, and composed of well-rounded quartz grains that are typically bimodal (Fig. 3.5g) (Williams, 1998). Whyalla Sandstone from drill hole SAE6 has a similar mineralogy to the quartz-rich sandstone in the ODBC, however, the bimodal grain size distribution, rounded grains and carbonate-dominated cement in the Whyalla Sandstone (Fig. 3.5g, h) are not characteristics of the quartz-rich sandstone. Also, the Whyalla Sandstone (Fig. 3.7a) contains 1.2-1.1 Ga zircons which are not present in the brecciated quartz-rich sandstone at OD.

3.6.2.3 Sedimentary successions related to the GRV

The GRV was present above the RDG at OD prior to formation of the ODBC (McPhie et al., 2011b; Ehrig et al., 2012). Regionally, sedimentary facies are very minor in the GRV (Blissett et al., 1993; Allen et al., 2008) though locally, they may be significant, for example, at Prominent Hill (Bull et al., 2015) and at Roopena (Fresh Well Formation; McAvaney and Wade, 2015). These successions comprise sandstone and conglomerate intercalated with GRV volcanic units, have sedimentary inputs from pre-Gawler SLIP lithologies and some contain zircons older than 1.59 Ga (e.g. Fresh Well Formation; Johnson, 1993). However, they are dominated by volcanic and metamorphic lithic clasts, distinct from the quartz-dominated mineralogy of the quartz-rich sandstone in the ODBC.

3.6.3 Probable protolith of the quartz-rich sandstone

We conclude that the brecciated quartz-rich sandstone in the ODBC is most probably part of the Pandurra Formation. In particular, the components and bedforms are identical to those in quartz sandstone of the Pandurra Formation; the timing of diagenesis determined for authigenic apatite in the cement of the sandstone fragments is consistent with the timeframe for deposition and diagenesis of the Pandurra Formation; the populations of detrital zircons match those in the Pandurra Formation and clearly distinguish the quartz-rich sandstone from other bedded clastic facies in the ODBC; and

the detrital and cement mineralogy are closely comparable with those of quartz sandstone in the Pandurra Formation.

Given that we have found remnants of the Pandurra Formation (ca. 1.44 Ga) within the ODBC (largely ca. 1.59 Ga), and that those remnants are relatively unaltered, the Cariewerloo Basin at one time must have covered the deposit and remained in place long enough for the Pandurra Formation to become lithified (i.e. after the diagenetic changes at ca. 1.44 Ga). If this conclusion is correct, then the Pandurra Formation was subsequently eroded from the uplifted fault block containing the ODBC, prior to deposition of the Nuccaleena Formation (ca. 635 Ma; Rose and Maloof, 2010), the oldest of the Neoproterozoic units directly overlying the ODBC (Roberts and Hudson, 1983). The complete erosion of the Pandurra Formation from above the ODBC implies that an unknown volume of the ODBC was also eroded at the same time.

3.6.4 Incorporation of the Pandurra Formation into the ODBC

The brecciated fragments of probable Pandurra Formation occur just below the unconformity surface at the top of the ODBC (RD1628), and over 400 m (RD2751) below the unconformity in faulted contact with hematite-rich breccia and bedded clastic facies. Tectonic activity is the most likely mechanism for incorporation of Pandurra Formation into the ODBC. The ODBC includes subvertical northwest-striking faults and northeast- to eastnortheast-striking faults that dip steeply northwest (Hayward and Skirrow, 2010; Ehrig et al., 2012). The brecciated Pandurra Formation within the ODBC is near the Jubilee Fault Zone (JFZ, also referred to locally as Masher's Fault) (Figs. 3.2, 3.10). The JFZ is a major subvertical, crustal-scale structure that has evidence of reactivation since the Neoproterozoic; other adjacent fault sets and splays in the ODBC also show evidence of localized reactivation (Hayward and Skirrow, 2010; Ehrig et al., 2012). It is noted that the majority of the preserved southern, steeply dipping portion of the bedded clastic facies are adjacent to the JFZ (Figs. 3.2, 3.10).

The position of the Pandurra Formation remnants and other bedded clastic facies adjacent to the JFZ suggests this fault zone and/or adjacent faults were involved in the incorporation of these lithologies into the ODBC. The southern preserved portion of the bedded clastic facies has an elongate, steeply-dipping geometry (McPhie et al., 2016). The two drill core intersections of the Pandurra Formation hint at a subvertical geometry (and may be connected, Fig. 3.10), potentially occupying a single fault. The thorough brecciation of the Pandurra Formation remnants and weak hydrothermal

alteration relative to the other bedded clastic facies imply the Pandurra Formation was incorporated separately from the other bedded clastic facies (Fig. 3.10). As the other bedded clastic facies are inferred to have been present at the time of formation of the ODBC (McPhie et al., 2016), they were probably incorporated prior to the deposition of the ca. 1.44 Ga Pandurra Formation.

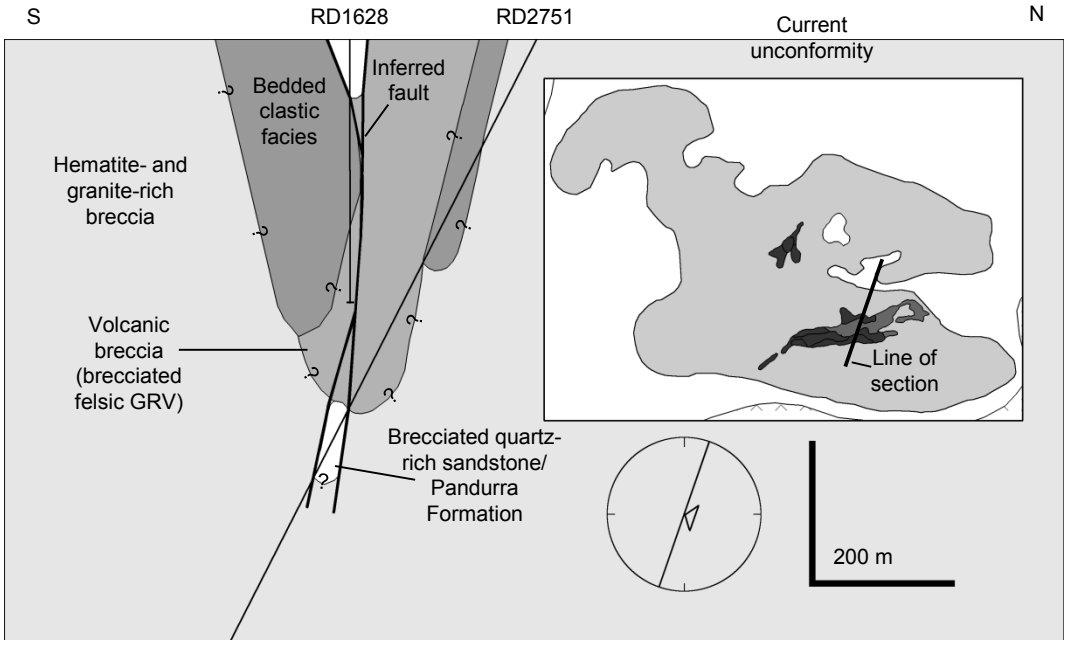

Figure 3.10 Cross-section of the ODBC showing the position of the incorporated remnants of the Pandurra Formation (brecciated quartz-rich sandstone) recorded in drill holes RD1628 and RD2751. Boundaries of lithologies (bedded clastic facies, volcanic breccia, brecciated quartz-rich sandstone) have been approximated with reference to Ehrig et al. (2012), McPhie et al. (2016) and unpublished reports by K. Orth. An inferred fault that may have been involved in incorporation of the Pandurra Formation remnants is shown. Inset shows the position of the cross-section relative to the breccia complex.

Incorporation of fragments of Pandurra Formation may have involved propagation of the JFZ, and associated reactivated faults, upwards into the overlying sandstone, causing brecciation and local entrainment of slices or fragments of sandstone along those faults. The faults bounding the remnants of Pandurra Formation lack dateable minerals and therefore the timing of tectonic movement leading to the entrainment of the sandstone fragments cannot be determined. As a result, constraints on the timing of incorporation are limited to maximum and minimum ages. The preservation of large fragments of the Pandurra Formation indicates incorporation occurred after lithification (inferred to be ca. 1.44 Ga), providing a maximum age. The late Neoproterozoic Stuart Shelf formations above the unconformity have not been faulted or otherwise incorporated into the ODBC, giving a minimum age of incorporation of ca. 635 Ma (e.g. Nuccaleena Formation; Rose and Maloof, 2010). The late Neoproterozoic Stuart Shelf formations also provide a minimum age for erosion of the Pandurra Formation from the top of the ODBC. Post-1.44 Ga faults in the vicinity of OD define much of the

eastern margin of the Pandurra Formation but do not affect the distribution of the overlying Stuart Shelf sedimentary formations (Cowley, 1993); the timing of movements on these faults, however, is presently unknown.

The Musgrave Orogeny (ca. 1.2 Ga; Major and Conor, 1993) and the Gairdner Dyke Swarm event (0.83 Ga; Wingate et al., 1998) are tectonic episodes that affected the Gawler Craton within the timeframe envisaged for incorporation of Pandurra Formation into the ODBC. The Musgrave Orogeny was centred on the Musgrave Province over 600 km away, but there is increasing evidence for an associated thermal pulse throughout much of the Gawler Craton (e.g. Reid et al., 2017), including fluid circulation in the Cariewerloo Basin (Keeling et al., 2015). However, no tectonic activity in the Gawler Craton has been correlated specifically with the Musgrave Orogeny. The intrusion of Gairdner Dyke Swarm was associated with significant extension (Wingate et al., 1998), including at OD (Huang et al., 2015). A spatial association between Gairdner dolerite dykes and the Pandurra Formation remnants in the ODBC would be expected if the extension associated with the dykes was responsible for incorporation of the Pandurra Formation. A probable Gairdner dolerite dyke is present 200 m uphole of the interval of brecciated Pandurra Formation in RD2751; however, there are no dykes in contact with the intervals of brecciated Pandurra Formation.

The Pandurra Formation may have been incorporated in much greater volumes than currently observed, the remnants having potentially been obliterated by brecciation and hematite alteration. Quartz is the only protolith relic in the most hematite-altered breccia zones. A search for pre-1.59 Ga zircons in the intensely altered hematite-rich breccia could reveal the presence of additional Pandurra Formation quartz-rich sandstone protolith.

3.6.5 Implications for modification of the U resource at Olympic Dam

Textural relationships among the copper sulfides and the uranium minerals, and geological constraints on the timing of precipitation of the copper sulfides have previously been interpreted to indicate that these minerals co-precipitated at ~1.59 Ma (Reeve et al., 1990; Johnson and Cross, 1995), even though the first attempt to date the U minerals gave younger ages (Trueman, 1986). Although there is now evidence of U having been present in OD at ca. 1.59 Ga (Ciobanu et al., 2013; Apukhtina et al., 2017), continuing studies of U minerals in the ODBC support the early results of Trueman (1986) and indicate the U resource has continued to be modified after ca. 1.59 Ga (Kirchenbaur et al., 2016;

Macmillan et al., 2016). The earliest identified uraninite generation in the ODBC has REE signatures consistent with derivation from a high-temperature magmatic fluid whereas the signatures of later generations are more consistent with precipitation from low-T (<250°C) fluids (Mercadier et al., 2011; Macmillan et al., 2016). Post-1.59 Ga ages of uraninite have generally been attributed to remobilization and reprecipitation of U minerals (Reeve et al., 1990; Johnson and Cross, 1995). Similarly, the deposit-wide deficit in Pb relative to the amount of U with an entirely ca. 1.59 Ga age (Trueman, 1986) has been attributed to episodic Pb loss from the deposit (Reeve et al., 1990). However, the Pb deficit only exists if the entire U resource is ca. 1.59 Ga in age and is also consistent with post-1.59 Ga addition of U to the deposit.

The Cariewerloo Basin is a potential source and conduit for post-1.59 Ga U, given that the Pandurra Formation is now known to have unconformably overlain the ODBC. The thick continental sandstone of the Pandurra Formation contained circulating oxygenated, saline, acidic fluids (Keeling et al., 2012). In addition to fluid movement associated with diagenesis at ca. 1.4 Ga, extensive fluid circulation in the Cariewerloo Basin at ca. 1.2 Ga and ca. 0.5 Ga has been inferred from the distribution and timing of crystallization of illite cements (Keeling et al., 2015). Such basin-derived fluids are widely implicated in the formation of unconformity-related U deposits associated with Proterozoic continental basins (Derome et al., 2005; Richard et al., 2012). The fluids are capable of liberating U from accessory U-bearing phases (e.g. volcanic glass, zircon, monazite, uranothorite) either in the basin succession or the underlying basement rocks (Kyser and Cuney, 2008). The source rocks and basement of the Pandurra Formation include lithologies with anomalous levels of U (e.g. Hiltaba Suite, and GRV to a lesser extent) (Neumann et al., 2000; Agangi et al., 2010). Hence, U sources (detrital grains or underlying basement) would have been available to the fluids circulating in the Cariewerloo Basin.

The geological setting, source rocks and interpreted fluid chemistry of the Cariewerloo Basin meet the requirements for mobilization of U by basin fluids (e.g. Kyser and Cuney, 2008). The faults that ruptured and re-located the Pandurra Formation from its original position above the ODBC could have also provided a pathway for fluids circulating within the Cariewerloo Basin into the ODBC (Fig. 3.11). These fluids may have upgraded or downgraded the deposit through precipitation or leaching of U minerals, respectively.

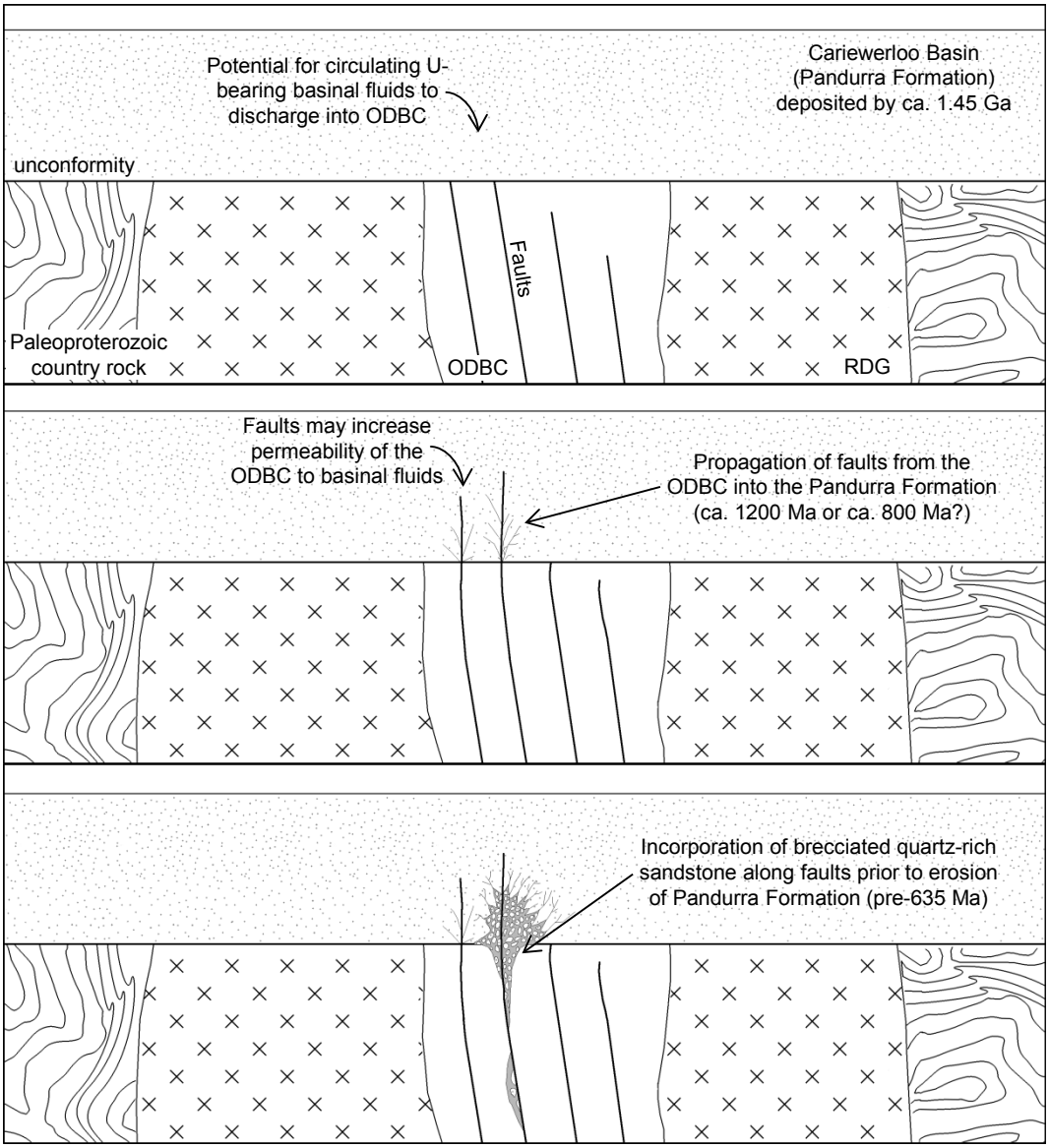

Figure 3.11 a. Schematic reconstruction of the Cariewerloo Basin overlying the ODBC and RDG. **b.** Propagation of faults from the ODBC into the Pandurra Formation may have facilitated discharge of circulating basinal fluids into the ODBC. **c.** Movement along these faults may have entrained fragments of quartz-rich sandstone into the ODBC from the overlying Pandurra Formation prior to its erosion.

Unconformity-related U deposits are associated with unconformities that juxtapose reducing basement rocks with oxidised fluids in overlying sedimentary basins (Kyser and Cuney, 2008). Reduction of mobile U^{6+} by Fe^{2+} is considered to be a plausible mechanism for the formation of unconformity-related U deposits (Yeo and Potter, 2010). Within the ODBC, siderite and magnetite are preserved mainly on the deposit margins and at depth (Ehrig et al., 2012). Both minerals are a potential source of Fe^{2+} ions capable of reducing U^{6+} to immobile U^{4+} and were likely more abundant throughout the ODBC (Reeve et al., 1990). Magnetite can transform to hematite in the presence of acidic fluids, releasing Fe^{2+} in the process (Otake et al., 2007) but Fe^{2+} in magnetite is also capable of directly reducing U^{6+} (Scott et al., 2005). Siderite has been experimentally shown to be capable of

reducing U^{6+} to U^{4+} in neutral and basic conditions (Ithurbide et al., 2010) but no data exist for acidic conditions.

3.7 Conclusions

We conclude that the brecciated quartz-rich sandstone in the ODBC is most probably part of the Pandurra Formation due to the positive comparison of texture, bedforms, detrital and cement mineralogy, detrital zircon age populations and diagenetic age. The presence of the Pandurra Formation within the ODBC requires that the Cariewerloo Basin at one time extended over the ODBC and that tectonic activity occurred on a scale large enough to brecciate and entrain the sandstone after ca. 1.44 Ga and before the Pandurra Formation was eroded from above OD. The potential for generation and circulation of oxidised, acidic fluids in the Cariewerloo Basin, capable of mobilizing U, raises the possibility that such fluids contributed to the development or modification of the world's largest U deposit. Addition of U from the Cariewerloo Basin is consistent with emerging evidence of post-1.59 Ga modification of the U resource in OD.

3.8 Acknowledgements

This paper represents part of the PhD project undertaken by A.R. Cherry while supported by an Australian Postgraduate Award scholarship. This project was funded by the Australian Research Council and BHP Billiton Olympic Dam with additional support from a student research grant awarded by the Society of Economic Geologists Foundation. Discussions with K. Cross, N. Chapman and M. Ferguson are gratefully acknowledged. This manuscript was greatly improved by the constructive comments of an anonymous reviewer. Geochronology and SWIR analyses were obtained with the help of J. Thompson and C. Harraden, respectively.

Appendix 3.1 Samples and locations

Table S3.1 List of samples used in this study, organised by sedimentary succession and drill hole. Samples in red (in RD2751) were the source of detrital zircon analyses from McPhie et al. (2016).

Pandurra Formation						
Oak Dam		Acropolis		Emmie Bluff	Wirrda Well	
AD1 (drill hole)		*ACD1*		*SAE6*	*WRD21*	
sample	m (depth)	sample	m	m	sample	m
OD0467	158.8	OD1118	412.8	402-404	OD446	468.1
OD0468	378.8	OD1119	425.8	404-406	WRD31	
OD0469	381.8	OD1120	470.1	407.6	OD455	486.7
OD0470	395.0	OD1121	495.2	413.4	OD456	493
OD0471	395.8	OD1122	533	436.4		
OD0472	398.5	OD1123	569.1	462.8		
OD0473	453.5	OD1124	588.1	482.9		
OD0474	463.0	OD1125	616.2	503.7		
OD0475	474.4	OD1126	651.3	546.4		
Quartz-rich sandstone (Olympic Dam)				Whyalla Sandstone (Emmie Bluff)		
RD1628		*RD2751*		*SAE6*		
sample	m	sample	m	m		
OD1052	362	OD0962	855	339.5		
OD1053	370	OD0963	909.3	356.7		
OD1054	386	OD0964	947.5	371.4		
OD1055	397	OD0970	849.3	376.6		
OD1169	350	OD0971	869.5	382		
OD1170	351.8	OD0972	874.5	385		
OD1171	380.1	OD0973	881.3			
OD1172	390.3	OD0974	899.6			
OD1173	415.5	OD0975	903.3			
		OD0976	914.2			
		OD0977	919.6			
		OD1061	900.7			

Table S3.2 Coordinates of sample drill holes. Easting and Northing coordinates are referenced to MGA94, zone 53.

Drill hole	Latitude	Longitude	Easting	Northing
RD1628	-30.4523	136.8936	681815.7	6629571.342
RD2751	-30.45	136.894	681858.4	6629825.642
AD1	-30.9798	137.246	714488.9	6570475.74
AD3	-30.9795	137.2297	712928.9	6570531.74
ACD1	-30.6212	136.7501	667748.9	6611071.78
ACD15	-30.626	136.7844	671026.5	6610488.022
ACD18	-30.6421	136.8121	673648.9	6608661.89
ACD19	-30.5906	136.7909	671711	6614398
SAE6	-31.1104	137.1494	704978.9	6556171.68
SAE15	-31.1048	137.1438	704458.9	6556811.68
WRD21	-30.6719	136.9368	685549	6605160
WRD31	-30.6718	136.9367	685535	6605173

Appendix 3.2 Clay Speciation methodology

Dry samples of drill core were analysed with a TerraSpec near-infrared and SWIR spectrometer (e.g. Harraden et al., 2013). Flat surfaces were used for analysis where available. Calibration was conducted with a Spectralon disk every half hour in the first hour and every hour thereafter. Reflectance spectra were analysed using The Spectral Geologist software package (AusSpec International Ltd). Speciation of clay minerals was assigned primarily on the position of AlOH absorption feature as well as best fit from reference library spectra (GMEX, 2008).

Dickite is characterised by a diagnostic doublet AlOH absorption feature at wavelengths of ~2178 and ~2206 nm. Illite, sericite and muscovite have similar spectra characterised by a single, sharp AlOH absorption at ~2180-2228 nm. Some success in distinguishing illite from sericite and muscovite may be achieved by considering the depth of the AlOH absorption relative to the depth of the H_2O absorption at ~1912 nm; muscovite tends to have ratios > 2 whereas illite-bearing samples have ratios closer to 1.

Around half of the Pandurra Formation samples were characterised by dickite and the rest characterised by illite ± sericite (on the basis of low $AlOH/H_2O$ ratios). Some samples revealed higher $AlOH/H_2O$ ratios, potentially due to the presence of detrital muscovite. The analysed quartz-rich sandstone samples contained illite ± sericite (again on the basis of low $AlOH/H_2O$ ratios), no dickite was observed.

Appendix 3.3 Clay speciation data [digital appendix]

Appendix 3.4 Additional images of apatite + bivariate plot of zircon Th/U ratios vs age

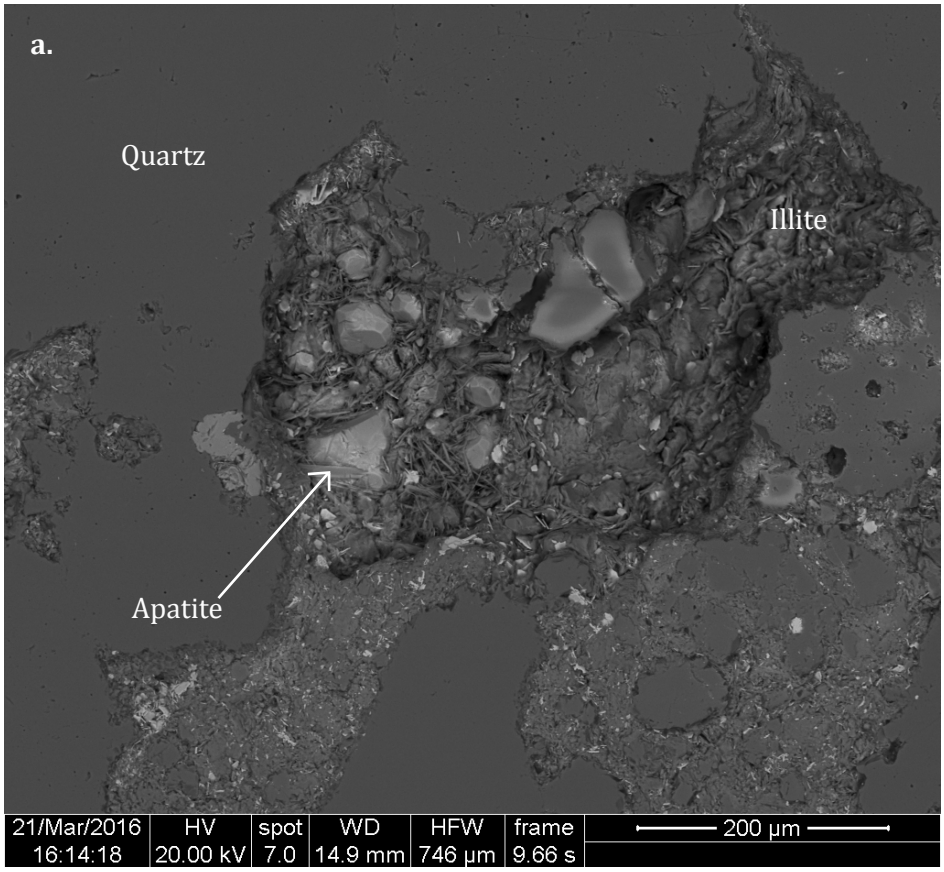

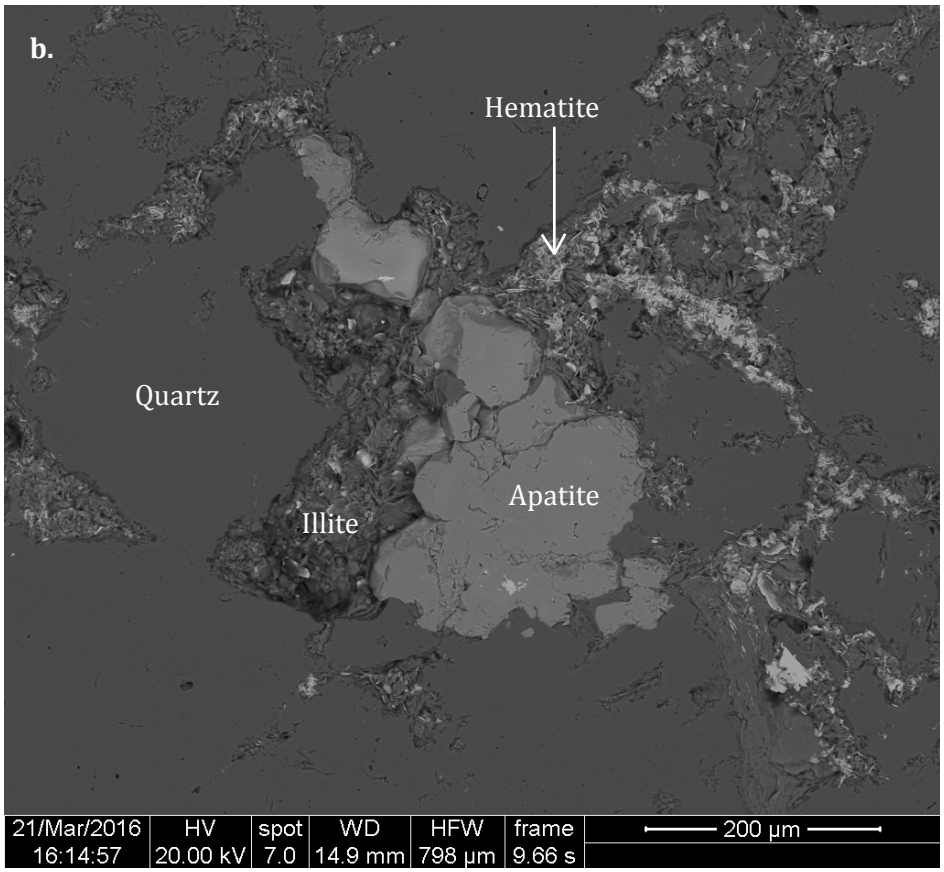

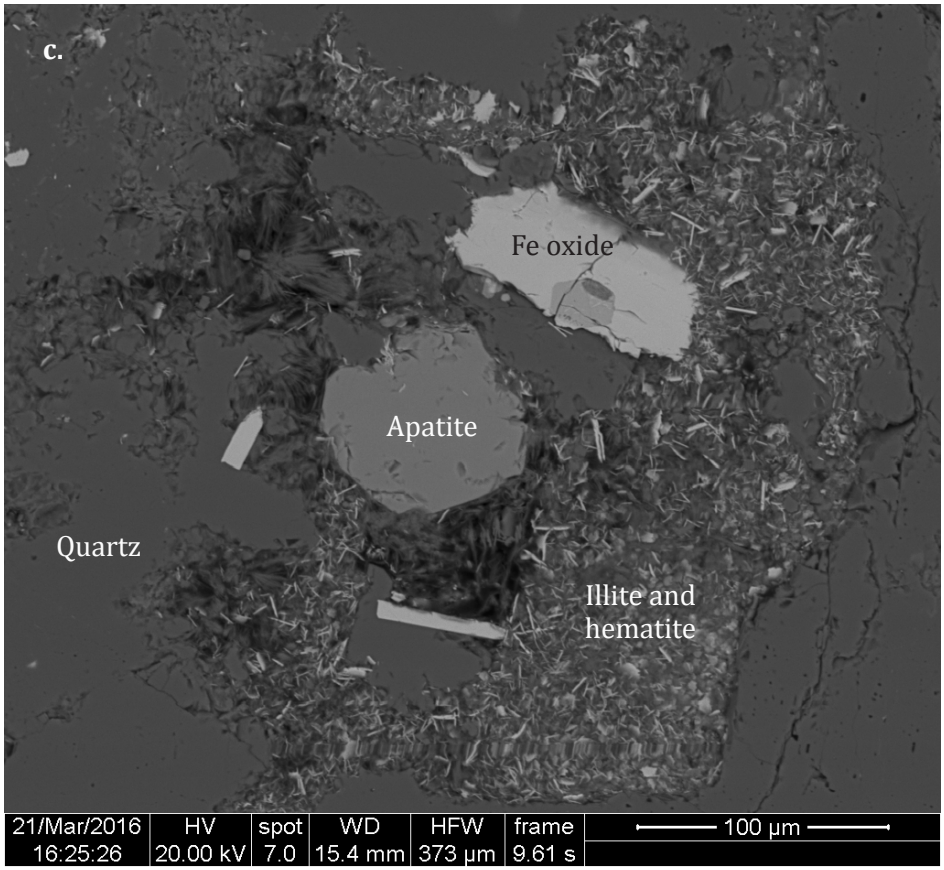

Figure S3.1 a. Cluster of euhedral apatite amongst illite and hematite interstitial to quartz grains. **b.** Cluster of subhedral apatite, intergrown with quartz overgrowths. Note the sparse hematite (brightest phase) enveloped by the apatite. **c.** Single subhedral apatite grain partially enveloping quartz, also note the very fine-grained, bladed hemaitte enveloped by the apatite.

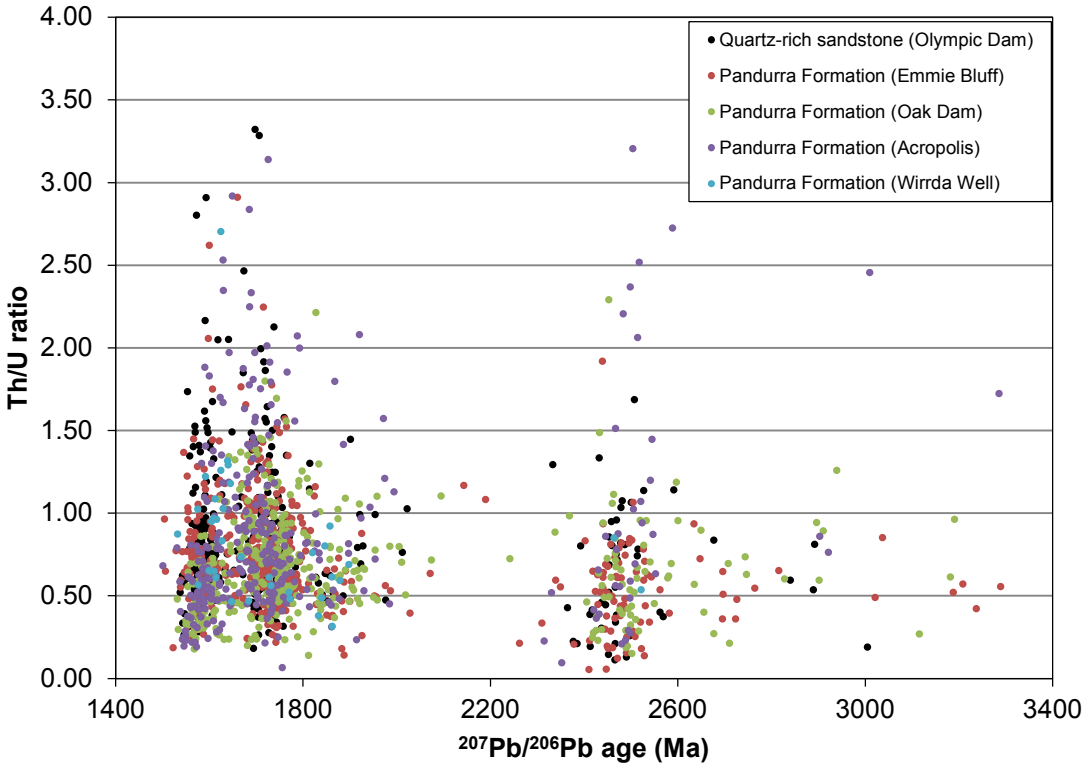

Figure S3.2 Bivariate plot of Th/U against 207Pb/206Pb the most concordant analyses. The quartz-rich sandstone in Olympic Dam has a similar Th/U range for each zircon age group.

Appendix 3.5 Drill hole assay methodology and data [digital appendix]

The drill holes RD1628 and RD2751 were assayed for U_3O_8 through lithium metaborate/ tetraborate fusion and inductively coupled plasma-mass spectroscopy by AMDEL-Bureau Veritas, Adelaide for BHP Billiton. The data is contained in the digital appendix.

Appendix 3.6 Zircon U-Pb geochronology methodology

The analyses in this study were performed on an Agilent 7900 quadrupole ICP-MS, coupled to a Coherent COMPex Pro 193nm ArF Excimer laser system equipped with a Laurin Technic (Resolution S155) constant geometry ablation cell. Downhole fractionation, instrument drift and mass bias correction factors for Pb/U ratios on zircons were calculated using 2 analyses of the primary zircon standard (91500) and checked on 1 analysis each of the secondary zircon standards (Temora 2, Mud Tank, Plešovice, JG1 and QingHu) analysed at the beginning of the session and 1 of each of the primary and secondary standards approximately every 15 unknown zircons (roughly every half hour) using the same spot size and analytical conditions as used on the samples. The correction factor for the $^{207}Pb/^{206}Pb$ ratio was calculated using large spots of the NIST610 reference glass analysed every 30 unknowns and corrected using the values recommended by Baker et al. (2004).

Each analysis of the zircon began with a 10-30 second analysis of the blank gas measurement followed by a further 20-30 seconds of analysis time when the laser was switched on. Zircons were sampled on 29-32µm spots using the laser at 5 Hz and a density of approximately 2 J/cm^2. The measurement time of the background and unknown as well as spot size were varied between analytical sessions over the several years of data collection but was consistent within sessions. A flow of He carrier gas at a rate of 0.35 litres/minute carried particles ablated by the laser out of the ablation cell to be mixed with Ar gas and carried to the plasma torch. Isotopes measured were ^{49}Ti, ^{56}Fe, ^{90}Zr, ^{178}Hf, ^{202}Hg, ^{204}Pb, ^{206}Pb, ^{207}Pb, ^{208}Pb, ^{232}Th, ^{235}U and ^{238}U with each isotope being measured every 0.17s with longer counting time on the Pb isotopes compared to the other isotopes. The data reduction used was based on the method outlined in Halpin et al. (2014) and is similar to that outlined in Black et al. (2004) and Paton et al. (2010).

Element abundances on zircons were calculated using the method outlined by Košler (2001) using Zr as the internal standard element, assuming stoichiometric proportions and using the NIST610 to standard correct for mass bias and drift.

Appendix 3.7 Zircon U-Pb geochronology data [digital appendix]

Appendix 3.8 Apatite U-Pb geochronology methodology

The analyses in this study were performed on an Agilent 7900 quadrupole ICP-MS, coupled to a Coherent COMPex Pro 193nm ArF Excimer laser system equipped with a Laurin Technic (Resolution S155) constant geometry ablation cell. Downhole fractionation, instrument drift and mass bias correction factors for Pb/U ratios on apatite were calculated with 2 analyses of the primary apatite standard (OD306) and 1 analysis each of the secondary apatite standards (401, Kovdor and McClure Mountain) at the beginning of the session and approximately every 12 unknown apatite analyses (roughly every half hour) using the same spot size and analytical conditions as used on the unknowns. The correction factor for the $^{207}Pb/^{206}Pb$ ratio was calculated using large spots of the NIST610 reference glass analysed every 30 unknowns and corrected using the values recommended by Baker et al. (2004). Element abundances on apatite were calculated using the method outlined by Košler (2001) using Ca as the internal standard element, assuming stoichiometric proportions and using the NIST610 abundances from Jochum et al. (2011) to correct for mass bias and drift.

Each apatite analysis began with a 30 second blank gas measurement followed by a further 30 seconds of analysis time when the laser was switched on. Apatite grains were sampled on 29μm spots using the laser at 5 Hz and a density of approximately 1.8 J/cm^2. The two apatite analytical sessions were conducted under the same operating conditions. A flow of He carrier gas at a rate of 0.35 litres/minute carried particles ablated by the laser out of the ablation cell to be to be mixed with Ar gas and carried to the plasma torch. Isotopes measured were ^{31}P, ^{43}Ca, ^{56}Fe, ^{140}Ce, ^{202}Hg, ^{204}Pb, ^{206}Pb, ^{207}Pb, ^{208}Pb, ^{232}Th, and ^{238}U with each isotope being measured every 0.18s with longer counting time on the Pb isotopes. The data reduction used was based on the method outlined in detail by Meffre et al. (2008) and Halpin et al. (2014) with an additional modification to help correct for the small amount of common Pb present in the primary standard using the ^{207}Pb-correction method of Chew et al. (2014).

Appendix 3.9 Apatite U-Pb geochronology data [digital appendix]

Appendix 3.10 Time resolved ablation data for Figure 3.6b [digital appendix]

Chapter 4 - Tectonothermal events in the Olympic IOCG Province constrained by apatite and REE-phosphate geochronology

Australian Journal of Earth Sciences, v. 65, p. 643-659

Alexander R. Cherry[1], Vadim S. Kamenetsky[1], Jocelyn McPhie[1], Jay M. Thompson[1], Kathy Ehrig[2], Sebastien Meffre[1], Maya B. Kamenetsky[1], and Sasha Krneta[3]

[1]ARC Centre of Excellence in Ore Deposits (CODES), School of Natural Sciences, University of Tasmania, Hobart, Tasmania 7001, Australia

[2]BHP Olympic Dam, 55 Grenfell Street, Adelaide, South Australia 5000, Australia

[3]School of Physical Sciences, University of Adelaide, Adelaide, South Australia 5000, Australia

4.0 Abstract

The Olympic iron oxide-copper-gold (IOCG) Province in South Australia contains numerous deposits and prospects, including the Olympic Dam Cu-U-Au-Ag deposit and the Acropolis prospect. The Acropolis prospect comprises massive, coarse-grained magnetite-apatite veins partly replaced by a hematite-stable assemblage. The apatite grains in the veins contain zones with abundant inclusions of other minerals (including monazite and xenotime) and low trace element concentrations relative to the inclusion-free zones. The inclusion-rich apatite zones are interpreted to be formed from the recrystallisation of the inclusion-free apatite and remobilisation of U, Th and REE from apatite into monazite and xenotime. Apatite, monazite and xenotime are all established U-Th-Pb geochronometers and offer the potential to constrain the alteration history of the Acropolis prospect. The LA-ICPMS U-Pb age of inclusion-free apatite is within error of the age of the host volcanic units (ca. 1.59 Ga). Inclusion-rich apatite yields both near concordant analyses that are within error of the inclusion-free apatite as well as highly disturbed (discordant) analyses. The most concordant analyses of monazite (Th-Pb) inclusions and xenotime (U-Pb) inclusions and rim grains indicate an alteration event occurred at ca. 1.37 Ga and possibly also at ca. 500 Ma. The disparity in age of the inclusion-rich apatite and the REE-phosphate inclusions (and rim grains) is suggested to be due to the apatite being initially recrystallised at ca. 1.59 Ga and modified again by a later event that also formed (or coarsened) most of the inclusions. Partial resetting of the majority of the monazite inclusions as well as the presence of significant amounts of common Pb has complicated the interpretation of the monazite results. In contrast, xenotime is a more robust geochronometer in this setting. The ages of the two post-1.59 Ga events that appear to have affected the Acropolis prospect do not correspond

to any events known to have occurred in the Gawler Craton. The earlier (ca. 1.37 Ga) age instead corresponds best with metamorphic-magmatic-hydrothermal activity in Laurentia, consistent with the proximity of Laurentia and the Gawler Craton inferred from palaeogeographic reconstructions. The later (ca. 500 Ma) event corresponds to the Delamerian Orogeny and has been shown by prior studies to have also affected the Olympic Dam deposit.

4.1 Introduction

The Olympic Cu-Au Province (also known as the Olympic IOCG Province) in the Gawler Craton of South Australia is a metallogenic province that contains significant iron oxide-copper-gold (IOCG) deposits, including the Olympic Dam Cu-U-Au-Ag, Prominent Hill and Carrapateena deposits (Skirrow et al., 2002; Fairclough, 2005; Belperio et al., 2007; Ehrig et al., 2012). Numerous subeconomic iron oxide-rich prospects also occur in the province (e.g. Acropolis, Wirrda Well, Titan; Bastrakov et al., 2007). The majority of these deposits and prospects contain an early magnetite-dominated assemblage and a later hematite-dominated assemblage (Oreskes and Einaudi, 1992; Bastrakov et al., 2007; Hayward and Skirrow, 2010; Ehrig et al., 2012). The Cu-Au-U mineralisation in the IOCG deposits in the Olympic Cu-Au Province is more strongly associated with the hematite assemblage than the magnetite assemblage (Bastrakov et al., 2007; Ehrig et al., 2012). The temporal evolution of a number of deposits and prospects in the Olympic Cu-Au Province have been suggested to have occurred over a geologically brief timeframe with both the magnetite and hematite assemblages formed between 1590 and 1570 Ma (Mortimer et al., 1988; Johnson and Cross, 1995; Skirrow et al., 2007; Ciobanu et al., 2013; Reid et al., 2013; Courtney-Davies et al., 2016; Apukhtina et al., 2017). However, younger ages have also been reported from many of these deposits and prospects, including Olympic Dam (Trueman, 1986; Davidson et al., 2007; McInnes et al., 2008; Meffre et al., 2010; Maas et al., 2011; Kamenetsky et al., 2015; Ehrig, 2016). The intense brecciation and hematite assemblage in the Olympic Dam deposit has obliterated much of the magnetite assemblage (Ehrig et al., 2012). In comparison, the nearby Acropolis prospect is much more structurally simple and a lesser proportion of the magnetite assemblage has been replaced by the hematite assemblage; this offers an opportunity to understand the temporal evolution of the hydrothermal assemblage at Acropolis and compare with the other deposits and prospects in the Olympic Cu-Au Province.

Recrystallisation of apatite and formation of rare earth element (REE) phosphate inclusions within apatite at Acropolis and other deposits/prospects in the Olympic Cu-Au Province was reported

by Krneta et al. (2016) to be spatially associated with replacement of the magnetite assemblage by the hematite assemblage. Determining the timing of recrystallisation of apatite and formation of REE-phosphate inclusions may help constrain the timing of the replacement of the magnetite-apatite assemblages with hematite and contribute to understanding of the overall temporal evolution of the Olympic Cu-Au Province. Here we report geochronological data for apatite and associated monazite and xenotime inclusions from the Acropolis prospect in order to constrain timing of their formation. Dating of REE-phosphate inclusions in apatite from iron oxide-apatite deposits has been attempted using various techniques such as electron microprobe (EPMA) (Torab and Lehmann, 2007), isotope dilution thermal ionisation mass spectrometry (ID-TIMS) (Stosch et al., 2011), sensitive high resolution ion microprobe (SHRIMP) and laser ablation (double focussing-single collector) inductively coupled plasma mass spectrometry (LA-ICPMS) (Neymark et al., 2016). These prior studies either suffered from poor spatial resolution or focussed on monazite as the only REE-phosphate inclusion. Our study utilises the spatial resolution of LA-quadrupole-ICPMS to date apatite formation and recrystallisation as well as formation of both monazite and xenotime inclusions. The U-Th-Pb systematics of apatite, monazite and xenotime are discussed. Furthermore, the new age data allow comparison with dated regional tectonothermal events, consideration of the effects of these events on the mobility of U, Th and REE in the Acropolis prospect and evaluation of palaeogeographic reconstructions.

4.2 Geologic setting

The Olympic Cu-Au Province is hosted by metamorphic and igneous basement rocks along the eastern margin of the Gawler Craton (Skirrow et al., 2007). The basement primarily comprises the Neoarchaean Sleaford and Mulgathing complexes (ca. 2.5 Ga), Palaeoproterozoic Donington Suite intrusions (ca. 1.85 Ga), Wallaroo Group volcanic and metasedimentary formations (ca. 1.75 Ga) and the Mesoproterozoic Gawler Silicic Large Igneous Province (Gawler SLIP, ca. 1.6 Ga), which comprises the Hiltaba Suite granitoids and contemporaneous Gawler Range Volcanics (Hand et al., 2007; Allen et al., 2008). The IOCG mineralisation of the Olympic Cu-Au Province has been temporally linked to the Gawler SLIP (Reeve et al., 1990; Skirrow et al., 2007). In the vicinity of the Olympic Dam deposit and Acropolis prospect, the Olympic Cu-Au Province is unconformably overlain by the Mesoproterozoic Pandurra Formation (ca. 1.44 Ga; Fanning et al., 1983; Cherry et al., 2017) as well as Neoproterozoic and younger sedimentary formations of the Stuart Shelf (Drexel et al., 1993) and is intruded by dykes of the Neoproterozoic Gairdner dyke swarm (Gairdner Dolerite) (0.83 Ga; Wingate et al., 1998).

The Acropolis prospect occurs approximately 20 km southwest of Olympic Dam (Fig. 4.1). The main host rock comprises felsic (and minor intermediate) lavas, minor ignimbrites and sills/dykes assigned to the Gawler Range Volcanics. Hiltaba Suite granite and brecciated Donington Suite granite and diorite are also present as minor host rocks (Paterson, 1986; Creaser, 1989; Cross, 1993; Jagodzinski, 2005; McPhie, 2016). The base of the overlying Pandurra Formation (or the top of the basement lithologies) is highly variable across the Acropolis area (from 360 m to 810 m downhole) which, along with the juxtaposition of different lithologies in adjacent drill holes and brecciation of lithologies in some drill holes, suggests significant faulting has occurred in the Acropolis area (McPhie, 2016). The Acropolis prospect is characterised by large coincident gravity and magnetic anomalies and comprises massive veins of iron oxide (magnetite replaced by hematite) associated with apatite, chlorite, quartz, siderite, K-feldspar, sericite, barite, fluorite, uraninite and sulfides (pyrite and chalcopyrite) (Paterson, 1986; Cross, 1993). Prior ID-TIMS geochronology of apatite (1602 ± 7 Ma; Mortimer et al., 1988) suggested that formation of the iron oxide-apatite assemblage was contemporaneous with the host Gawler Range Volcanics at Acropolis (ID-TIMS, 1591 ± 10 Ma; Creaser and Cooper, 1993).

4.3 Analytical methods

4.3.1 SEM and EPMA

Apatite-bearing samples were prepared as 1 inch epoxy discs (or polished thin section in the case of OD306). Samples were evaluated using back-scattered electron (BSE) imaging on a Hitachi SU-70 field emission scanning electron microscope (SEM). Electron microprobe (EPMA) analyses and additional BSE imaging of apatite, monazite and xenotime were obtained with a JEOL JXA-8530F Plus Hyper Probe field emission-EPMA equipped with 5 wavelength-dispersive X-ray spectrometers at the University of Tasmania. Operating conditions during apatite analyses included a beam energy of 16 keV and a beam current of 10 nA or 30 nA depending on the element measured. The beam diameter was 10 μm for all analysed elements and care was taken to avoid any inclusions or nearby zones with differing BSE brightness. Operating conditions during monazite and xenotime analyses included a beam energy of 16 keV, a beam current of 60 nA and a beam diameter of 1 μm. All analysed monazite and xenotime inclusions were at least 5 μm in size to take into account the larger diameter of the interaction volume. Elements analysed, X-ray lines, analysing crystals, standards, peak/off-peak counting times, detection limits and corrections are presented in Appendix 4.1. The apatite data are presented in Appendix 4.2 and the monazite and xenotime data are presented in Appendix 4.3.

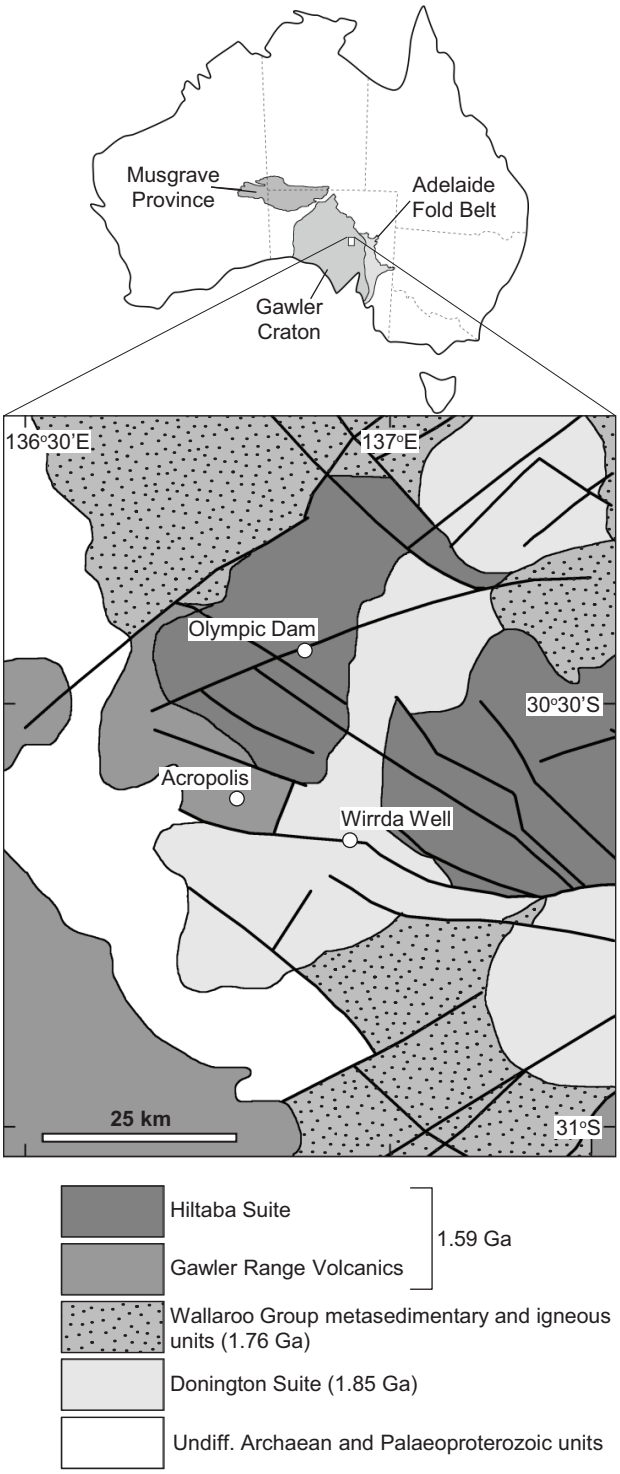

Figure 4.1 Location of the Gawler Craton, Musgrave Province and Adelaide Fold Belt in Australia. Inset shows the regional geology in the vicinity of the Olympic Dam deposit and Acropolis and Wirrda Well prospects. Heavy black lines represent inferred faults.

Monazite and xenotime inclusions were located for LA-ICPMS U-Pb analysis using the method of Sack et al. (2011). An FEI Quanta 600 SEM utilised an automated combination of BSE mapping to identify particles with high mean atomic number and energy-dispersive X-ray spectroscopy (EDS) to identify the mineralogy of the particles. The analysed mounts contain hundreds to thousands of

monazite and xenotime particles/inclusions (although xenotime is about an order of magnitude less abundant than monazite). Around 25-500 inclusions with a diameter greater than 10 μm were identified in each mount. Between 10 and 30 inclusions of monazite and xenotime each were selected from every mount for LA-ICPMS U-Pb analysis.

4.3.2 LA-ICPMS

Analyses of apatite, monazite and xenotime for U-Th-Pb geochronology and trace elements (apatite only) were conducted on an Agilent 7900 quadrupole ICPMS coupled to a Coherent COMPex Pro 110 utilising an ArF excimer laser operating at the 193 nm wavelength and a pulse width of ~20 ns. A RESOlution/Laurin Technic S155 constant geometry ablation cell was used. All apatite analyses with associated reference materials were ablated with a 29 μm spot size at 5Hz and ~2 J/cm^2 laser fluence and were completed in a single session (measured isotopes: ^{31}P, ^{43}Ca, ^{56}Fe, ^{89}Y, ^{140}Ce, ^{202}Hg, ^{204}Pb, ^{206}Pb, ^{207}Pb, ^{208}Pb, ^{232}Th and ^{238}U). The OD306 apatite (Thompson et al., 2016) was used as a primary in-house geochronology reference material for calibration of Pb/U ratios and to correct for instrument drift (e.g. Huang et al., 2015; Huang et al., 2016). Calibration of the ^{207}Pb/^{206}Pb ratio was done using analyses of the NIST610 reference glass analysed at the same conditions as the unknowns. The Durango (McDowell et al., 2005), Kovdor (Amelin and Zaitsev, 2002), McClure Mountain (Schoene and Bowring, 2006), Otter Lake (Barfod et al., 2005) and 401 (Thompson et al., 2016) apatites were employed as secondary geochronology reference materials and were treated as unknowns (published and measured ages of the secondary reference materials are reported in Table 4.1). The reference glasses GSD-1g and BCR-2g were used as reference materials in calibration and drift correction for most of the expanded suite of isotopes measured during trace element analysis (i.e. ^{23}Na, ^{24}Mg, ^{27}Al, ^{29}Si, ^{31}P, ^{43}Ca, ^{51}V, ^{55}Mn, ^{56}Fe, ^{57}Fe, ^{63}Cu, ^{66}Zn, ^{75}As, ^{88}Sr, ^{89}Y, ^{137}Ba, ^{139}La, ^{140}Ce, ^{141}Pr, ^{146}Nd, ^{147}Sm, ^{153}Eu, ^{157}Gd, ^{159}Tb, ^{163}Dy, ^{165}Ho, ^{166}Er, ^{169}Tm, ^{172}Yb, ^{175}Lu, ^{206}Pb, ^{207}Pb, ^{208}Pb, ^{232}Th and ^{238}U). ^{43}Ca was used as the internal standard element assuming stoichiometric proportions in apatite. The Durango apatite was used to calibrate measured values of ^{34}S and ^{35}Cl, which are not present in appreciable quantities in the above reference glasses.

Monazite and xenotime (and associated reference materials) were ablated with a 9 μm spot size except for the NIST610 reference glass which was ablated with a 29 μm spot size for better counting statistics on the calibration. All ablation was done at 5Hz and ~2 J/cm^2 laser fluence. Monazite and xenotime were analysed over two sessions with measured isotopes: ^{31}P, ^{43}Ca, ^{56}Fe, ^{89}Y, ^{140}Ce, ^{202}Hg,

^{204}Pb, ^{206}Pb, ^{207}Pb, ^{208}Pb, ^{232}Th and ^{238}U. The only difference between the sessions was that ^{43}Ca was not monitored in the first session and the ablation interval was decreased from 30 seconds to 20 seconds in the second session as longer ablation intervals were not found to be necessary due to the small size of the inclusions) An in-house monazite (14971 monazite, isotope dilution MC-ICPMS age = 909.0 ± 2.9 Ma [unpublished]) was employed as the primary reference material for calibration of Pb/U and Pb/Th ratios and to correct for instrument drift. The RGL-4B (Rubatto et al., 2001) and Bananeira (Gonçalves et al., 2016) monazites were employed as secondary reference materials and were treated as unknowns (published and measured ages of the secondary reference materials are reported in Table 4.1). A primary xenotime reference material was not available at the time of analysis due to difficulties in locating appropriate natural materials (e.g. Fletcher et al., 2004). Instead, the xenotime was calibrated using monazite and accuracy of the Pb/U and Pb/Th systems was assessed using an in-house secondary reference xenotime ('Brazil Xenotime') from Novo Horizonte in Brazil where xenotime from the same location were dated by ID-TIMS by Stern and Rayner (2003). The NIST610 reference glass was used in all sessions to calibrate the ^{207}Pb/^{206}Pb isotopic abundances as well as calibration and instrument drift correction of trace element concentrations. ^{140}Ce and ^{89}Y were used as the internal standard elements (assuming stoichiometric proportions) in monazite and xenotime, respectively. Additional details of the LA-ICPMS method are listed in Table S4.1 in the Appendix.

The time-resolved ablation signal for each analysis was examined in detail and the isotopic ratios used for age determination were calculated on intervals that passed specific criteria for each mineral phase. Intervals in analyses of apatite, monazite and xenotime were selected on the basis of high and consistent counts in ^{31}P, ^{238}U, ^{232}Th, and the radiogenic Pb isotopes, as well as the primary cation in each phase (^{43}Ca, ^{140}Ce and ^{89}Y, respectively). Elevated counts of ^{43}Ca, ^{140}Ce, ^{89}Y or ^{56}Fe in any analyses that were not of the target phase were taken to represent mixing with other phases and were avoided or the analysis was excluded altogether. Intervals with elevated ^{204}Pb and/or where the radiogenic Pb isotopes appeared decoupled from U and/or Th were taken to represent Pb inclusions and avoided where possible. Analyses with very short intervals (<3 s) that met the above criteria were excluded due to poor representivity of the target phase. The data were reduced using an in-house excel-based spreadsheet, with error propagation following the recommendations of Horstwood et al. (2016) (i.e. random uncertainties as well as total uncertainties including systematic uncertainties). The full results, including excluded analyses, are presented in Appendices 4.5-4.8. The concentrations of elements monitored during LA-ICPMS U-Pb geochronology were also calculated for monazite, xenotime and apatite.

Table 4.1 Summary of published and LA-ICPMS ages of reference materials. Published ages are derived from the following: [1] - Thompson et al. (2016), [2] - McDowell et al. (2005), [3] - Amelin and Zaitsev (2002), [4] - Schoene and Bowring (2006), [5] - Barfod et al. (2005), [6] - Rubatto et al. (2001), [7] - Gonçalves et al. (2016), and [8] - Stern and Rayner (2003). The age of the Brazil Xenotime reference material was obtained from the data for the xenotime sample 'z6414' by Stern and Rayner (2003). While heterogeneity is apparent in the data of Stern and Rayner (2003), a weighted average $^{206}Pb/^{238}U$ age was generated from the main age population (n = 6/8, MSWD = 33, p.o.f = 0.000) after exclusion of older outliers. The $^{207}Pb/^{206}Pb$ ages of the reference materials and unknowns were calibrated on the NIST610 reference glass. Reported uncertainties of all reference materials are at 95% confidence; systematic uncertainties of the reference material analyses are combined with random uncertainty as total uncertainty.

Reference material	Published age type	Published age ± 2s (Ma)	LA-ICPMS age type	n	Age ± random ± total (Ma)	MSWD (p.o.f)
Apatite						
OD306[1]	ID MC-ICPMS U-Pb concordia	1596.7 ± 7.1	U-Pb concordia	10	1596 ± 19 ± 26	0.33 (0.96)
Durango[2]	^{40}Ar-^{39}Ar	31.44 ± 0.18	^{207}Pb corr. $^{206}Pb/^{238}U$	5	29.6 ± 4.3 ± 4.3	1.4 (0.23)
Kovdor[3]	ID-TIMS U-Pb concordia	377.5 ± 3.5	U-Pb concordia	3 (1 excld)	376 ± 17 ± 17.5	1.9 (0.17)
McClure Mtn[4]	ID-TIMS $^{207}Pb/^{235}U$	523.98 ± 0.12	U-Pb concordia	5	534 ± 37 ± 37.5	0.27 (0.85)
Otter Lake[5]	MC-ICPMS Pb-Pb	913 ± 7	U-Pb concordia	3 (1 excld)	918 ± 89 ± 89.6	2.0 (0.16)
401[1]	ID MC-ICPMS U-Pb	530.3 ± 1.5	$^{206}Pb/^{238}U$	4	528.3 ± 9.9 ± 11.5	0.12 (0.95)
Monazite						
14971	ID MC-ICPMS U-Pb concordia	909.0 ± 2.0	$^{206}Pb/^{238}U$	20 (2 excld)	908.0 ± 4.3 ± 10.6	0.98 (0.48)
RGL-4B[6]	SHRIMP $^{207}Pb/^{206}Pb$	1566 ± 3	$^{207}Pb/^{206}Pb$	14	1576 ± 10 ± 19.5	1.17 (0.29)
Bananeira[7]	ID-TIMS $^{207}Pb/^{235}U$	507.7 ± 1.3	$^{206}Pb/^{238}U$	17	506.6 ± 4.0 ± 6.7	2.3 (0.002)
Xenotime						
Brazil Xenotime[8]	ID-TIMS $^{206}Pb/^{238}U$	498.9 ± 3.7	$^{206}Pb/^{238}U$	17	497.8 ± 7.9 ± 9.5	0.89 (0.58)

4.4 Apatite at Acropolis

Krneta et al. (2017) identified two main generations of apatite at Acropolis: early apatite enriched in REE + Y + Cl, and late apatite that is variably depleted in those elements (and consequently has a lower BSE brightness than the early apatite). The early (bright under BSE) apatite occurs within Ti-rich magnetite ± K-feldspar ± Mg-Mn-Fe-carbonate ± quartz (± biotite) veins. The late (dark under BSE) apatite is associated with partial replacement of the magnetite-apatite veins. In these veins the magnetite is replaced by hematite or siderite, K-feldspar is replaced by sericite and fine-grained hematite, and the bright, inclusion-poor apatite is replaced by the dark apatite (Fig. 4.2). The dark apatite occurs as zones within the bright apatite, and contains abundant inclusions of hematite + sericite + monazite ± barite ± chalcopyrite. Certain trace elements (e.g. REE + Y) in the dark, inclusion-rich apatite are depleted relative to the bright apatite depending on the late mineral assemblage (Krneta et al., 2017). Depletion of both light and heavy REE (LREE and HREE, respectively) as well as Y has occurred where hematite is the primary phase, whereas the presence of siderite is associated with even depletion of all REE + Y from the apatite. Additional generations of apatite associated with sericite and chalcopyrite were described (Krneta et al., 2017).

The samples used in this study were taken from the Olympic Dam sample collection at the University of Tasmania. The samples are of veins (up to 10 cm thick) that are hosted within Gawler Range Volcanics (Table 4.2). Apatite samples OD1068, OD743 and OD742 are very coarse grains (up to 1 cm, e.g. Fig. 4.3a-c) that are generally reddish but can have pale, translucent patches. These samples come from veins that include magnetite that is partially or completely replaced by hematite. Minor phases that occur interstitial to the apatite and iron oxide include Fe- and Mg-rich chlorite, rutile, quartz and xenotime. Barite, chalcopyrite, monazite, xenotime, $ThSiO_4$ (thorite or huttonite) and hematite occur as inclusions in the apatite. Chalcopyrite also occurs in sample OD1068 as veinlets crosscutting apatite and hematite. Siderite and barite are also present in sample OD742 rimming and crosscutting apatite grains. The OD306 apatite is distinct; the grains are colourless and translucent rather than reddish (Fig. 4.3d) and contain very few inclusions. OD306 comes from a vein composed almost entirely of apatite and only minor magnetite (partially replaced by hematite), in addition to fluorite and chlorite. The OD306 apatite was introduced as a potential U-Pb LA-ICPMS reference material by Thompson et al. (2016) and is further characterised for that reason.

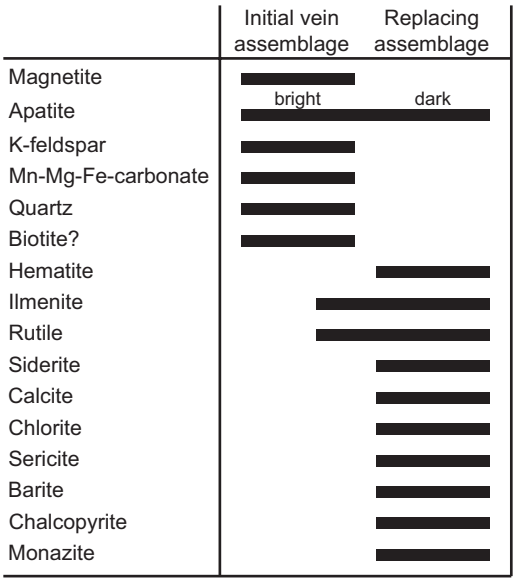

Figure 4.2 Two-stage paragenesis of the hydrothermal assemblage in the Acropolis prospect according to the observations of Krneta et al. (2017). Early, bright apatite was described to be part of the initial hydrothermal assemblage and late, dark apatite was observed to be spatially associated with the replacing assemblage. Hematite, chalcopyrite, monazite and barite were noted to also occur as inclusions in the late apatite.

Table 4.2 Samples and corresponding drill holes and depth. Sample coordinates are referenced to MGA94, zone 53.

Sample ID	Drill hole	Depth (m)	Easting	Northing	Elevation (m)
OD1068	ACD21	447.5	672751.8	6608273.0	-347.7
OD743	ACD9	827	669514.5	611280.0	-728.0
OD742	ACD9	780	669514.5	611280.0	-681.0
OD306	ACD19	897	671723.5	6614542.5	-781.2

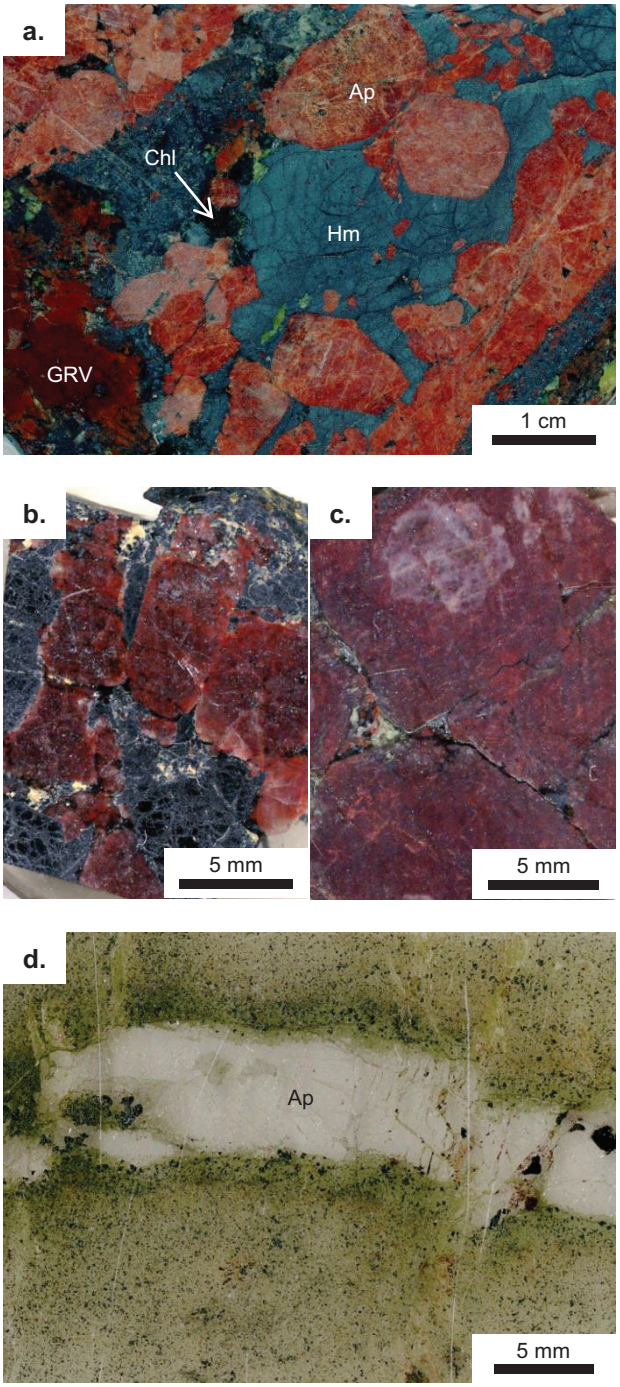

Figure 4.3 Apatite from the Acropolis prospect. **a.** Coarse-grained, red apatite (Ap) with Fe oxide (hematite; Hm) and minor chlorite (Chl) in a vein hosted by Gawler Range Volcanics (GRV) (OD1068, ACD21, 447.5 m). **b.** Coarse-grained red apatite with Fe oxide (magnetite + hematite). Rims of the apatite grains are paler and also contain fewer inclusions. (OD743, ACD9, 827 m). **c.** Coarse-grained red apatite with pale zones that contain few inclusions. Barite, siderite and chlorite occur interstitial to the apatite (OD742, ACD9, 780 m). **d.** Veinlet of coarse-grained, clear apatite with minor fluorite and pyrite (OD306, ACD19, 897 m).

4.5 Results

4.5.1 Mineral compositions

4.5.1.1 Apatite

The apatite grains contain zones that are distinguished by differing BSE brightness (Fig. 4.4) that also correspond to differences in trace element concentration. Bright zones have elevated concentrations of trace elements (e.g. REE, Y, U, Th, Na, Si) relative to the dark zones (Fig. 4.5, see Appendix 4.2). More than two shades of different BSE brightness are present in some samples (Fig. 4.4c). The dark zones are commonly distributed as a fine network through the apatite grains (Fig. 4.4d), as well as patches throughout or projecting inwards from the rims of apatite grains (Fig. 4.4e). In contrast, the cores of some apatite grains in one sample (OD743) almost entirely comprise dark apatite surrounded by a rim of mostly bright apatite (Fig. 4.4f). The dark zones contain abundant fine inclusions (< 50 μm, e.g. monazite, xenotime, iron oxide, barite, florencite, chalcopyrite, pyrite) (Fig. 4.6) and the darkest BSE zone is associated with the majority of the inclusions. Some dark zones have abundant fine pores (< 10 μm) apparent under SEM. In contrast, the bright areas contain little-to-no inclusions and are texturally homogeneous. The dark zones of samples OD742 and OD743 appear to contain the highest abundance of inclusions whereas dark zones in OD306 have the lowest abundance of inclusions (e.g. Fig. 4.4a-d)

Concentrations of the LREE (La + Ce + Nd) are over 1 wt. % in the bright zones but are commonly below detection (of the EPMA) in the dark zones (Fig. 4.5a). Concentrations of Na, Si, S and Cl are also elevated in the bright zones relative to the dark zones (e.g. Fig. 4.5a). The two samples OD742 and OD743 contain higher trace element concentrations in the bright zones than the other samples; those two samples (OD742 and OD743) also contain higher concentrations of trace elements in bright zones in cores than in the bright zones in the rims (see Appendix 4.2). The lower concentrations of the LREE, Na, Si, S and Cl in the dark zones are accompanied by relatively higher concentrations of both Ca and P (see Appendix 4.2). The concentration of F appears to be higher in some dark zones, however, the measured concentration of F is higher than is stoichiometrically possible and is attributed to unsuccessful correction of the increase in F concentration over time during EPMA analysis (Stormer et al., 1993). In addition to the LREE, Na, Si, S, and Cl depletion observed in EPMA analyses (in the dark zones relative to the bright zones), LA-ICPMS analyses record depletion of Mg, V, Mn, Fe, As, Th, U, Pb, Y and the rest of the REE (Fig. 4.5b, see Appendix 4.5). The chondrite-normalised REE + Y patterns of

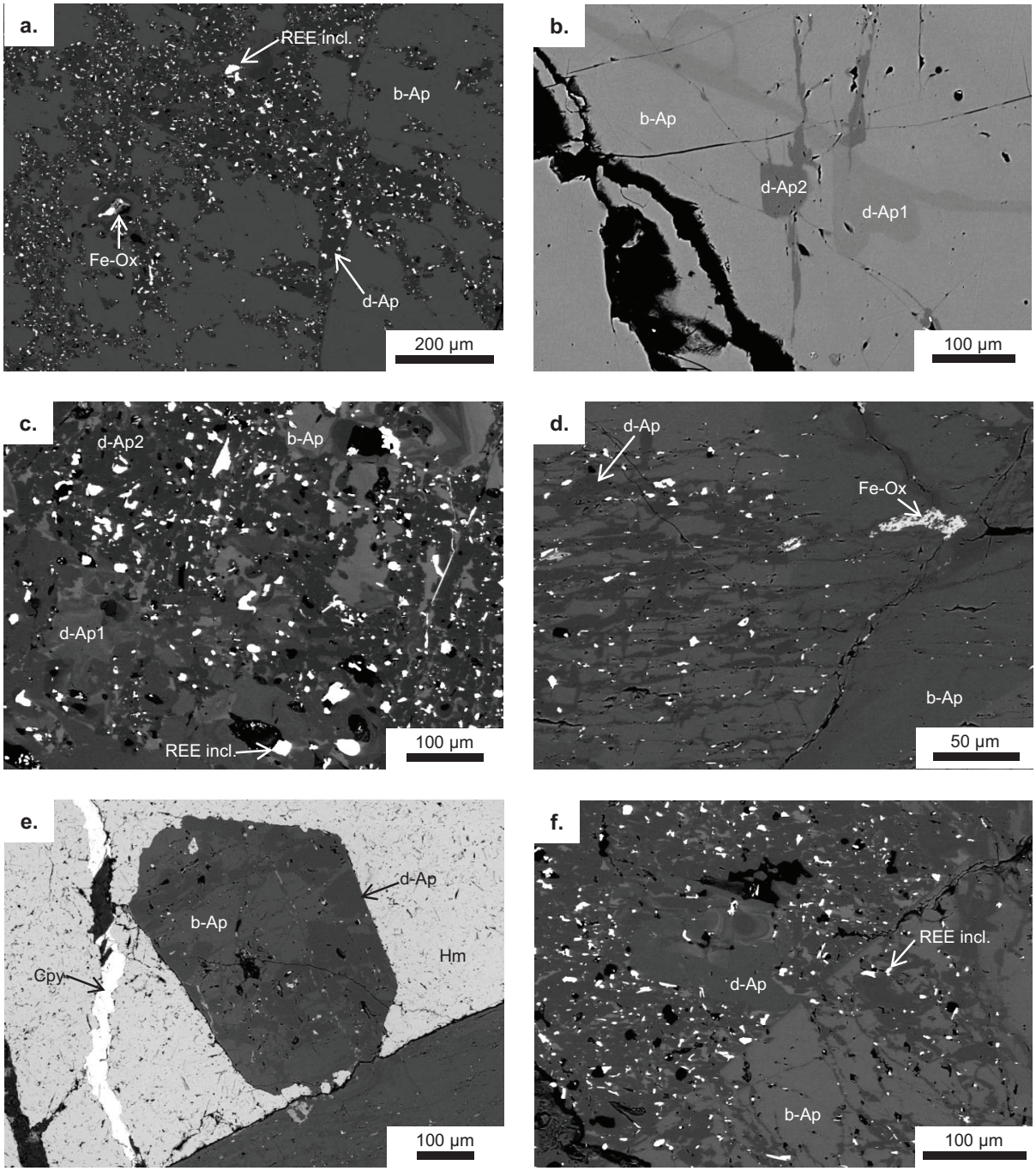

Figure 4.4 Back scattered electron (BSE) images of apatite. **a.** Apatite with bright- and dark-BSE zones (b-Ap and d-Ap respectively). Very bright REE-phosphate inclusions (REE-incl.) primarily occur within the dark-BSE zones (OD742). **b.** Primarily BSE-bright apatite with a narrow band of darker apatite (d-Ap1) apparently crosscut by an even darker zone of apatite (d-Ap2) (OD306). **c.** Multiple BSE shades in apatite. The majority of the very bright REE-phosphate inclusions occur within the darkest apatite (OD742). **d.** Network of dark apatite with associated very bright REE-phosphate inclusions in bright apatite. Iron oxide inclusions (Fe-Ox) also occur (OD1068). **e.** Small, euhedral apatite grain on the margin of a larger apatite grain and surrounded by Fe oxide. The dark zones are mainly around the grain margin. A chalcopyrite (Cpy) veinlet cuts through the Fe oxide next to the apatite (OD1068). **f.** An apatite grain in which the core (upper left) consists almost entirely of dark apatite and associated inclusions. The rim (lower right) mainly consists of bright apatite; REE-phosphate inclusions occur in the minor domains of dark apatite (OD743).

the bright apatite and dark apatite zones are consistent with those of Krneta et al. (2017), showing trends of depletion of mainly the LREE and HREE as well as negative Y anomalies in the dark zones relative to the bright zones (Fig. 4.5b). One dark apatite zone analysis has concentrations of HREE + Y that are elevated relative to the bright zone analyses of the same sample and may indicate the presence of an HREE + Y-bearing inclusion (e.g. xenotime) within the ablated volume. No consistent variation was observed in Sr, Al, Cu, Zn and Ba aside from elevated values in the dark zones of some samples. The core-rim zonation observed in the EPMA analyses of two of the samples were not replicated in the LA-ICPMS dataset due to the absence of bright areas of sufficient size for LA-ICPMS spots.

4.5.1.2 Xenotime and monazite

The REE-phosphate minerals primarily occur as irregular to euhedral inclusions within the dark apatite zones (Fig. 4.6). Monazite inclusions range from sub-μm to rarely over 100 μm (Fig. 4.6a, b) and commonly occur along fractures in the apatite. Xenotime inclusions (e.g. Fig. 4.6a) are rarely larger than 20-30 μm and are approximately an order of magnitude less abundant than monazite. Xenotime also occurs as rim grains around the margins of apatite; their morphology includes euhedral grains that are not in direct contact with apatite and are instead surrounded by rutile and Fe- or Mg-rich chlorite, and anhedral fine-grained aggregates in contact with (typically embayed) apatite margins (Fig. 4.6c, d). Monazite and xenotime can be intergrown with each other and with chalcopyrite, iron oxide and $ThSiO_4$ (Fig. 4.6a, b). Due to the small size of most inclusions, zonation is rarely observed in either monazite or xenotime but is apparent in high contrast BSE images in some grains (Fig. 4.6e, f). Electron microprobe analyses show the characteristic partitioning of LREE into monazite and HREE + Y into xenotime (see Appendix 4.3). The concentration of Th in monazite ranges from 0.07 to 1.99 wt. % whereas U is generally below EPMA detection. In contrast, Th in xenotime ranges from below detection to 0.24 wt. % but concentrations of U are between 0.18 and 0.60 wt. %. The Pb content of monazite is lower than in xenotime (from below detection to 0.11 wt. % and 0.06-0.17 wt. %, respectively).

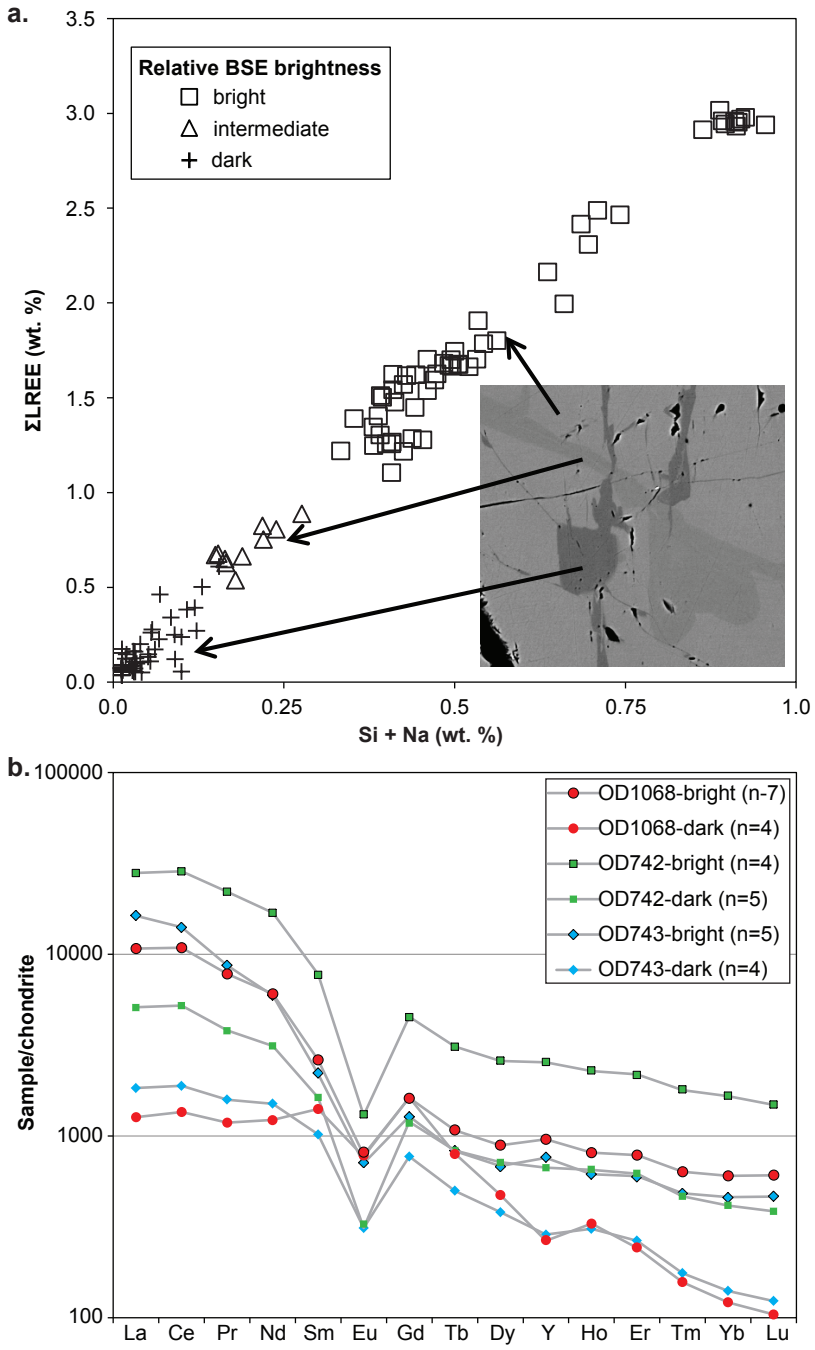

Figure 4.5 Electron microprobe trace/minor element plots of apatite zones. **a.** Bivariate plot of LREE (La + Ce+ Nd) vs. Si and Na concentration across the different apatite zones (□ = bright, Δ = intermediate and + = dark), showing a strong positive correlation. The concentration of LREE, Si and Na in many of the dark zone analyses are below detection (and have been substituted with half of the detection limit). An outlier (not shown) with high LREE concentration relative to Na and Si is inferred to be due to a monazite inclusion. Inset image is part of Figure 4.4b. **b.** Chondrite-normalised (Sun & McDonough, 1989) REE + Y spider plots of bright and dark apatite zones (LA-ICPMS, means of multiple analyses). The dark zones of the samples OD1068 (red) and OD743 (blue) are depleted in the L- and HREE +Y relative to the MREE whereas the OD742 dark zones (green) appear to have uniform depletion of all REE + Y.

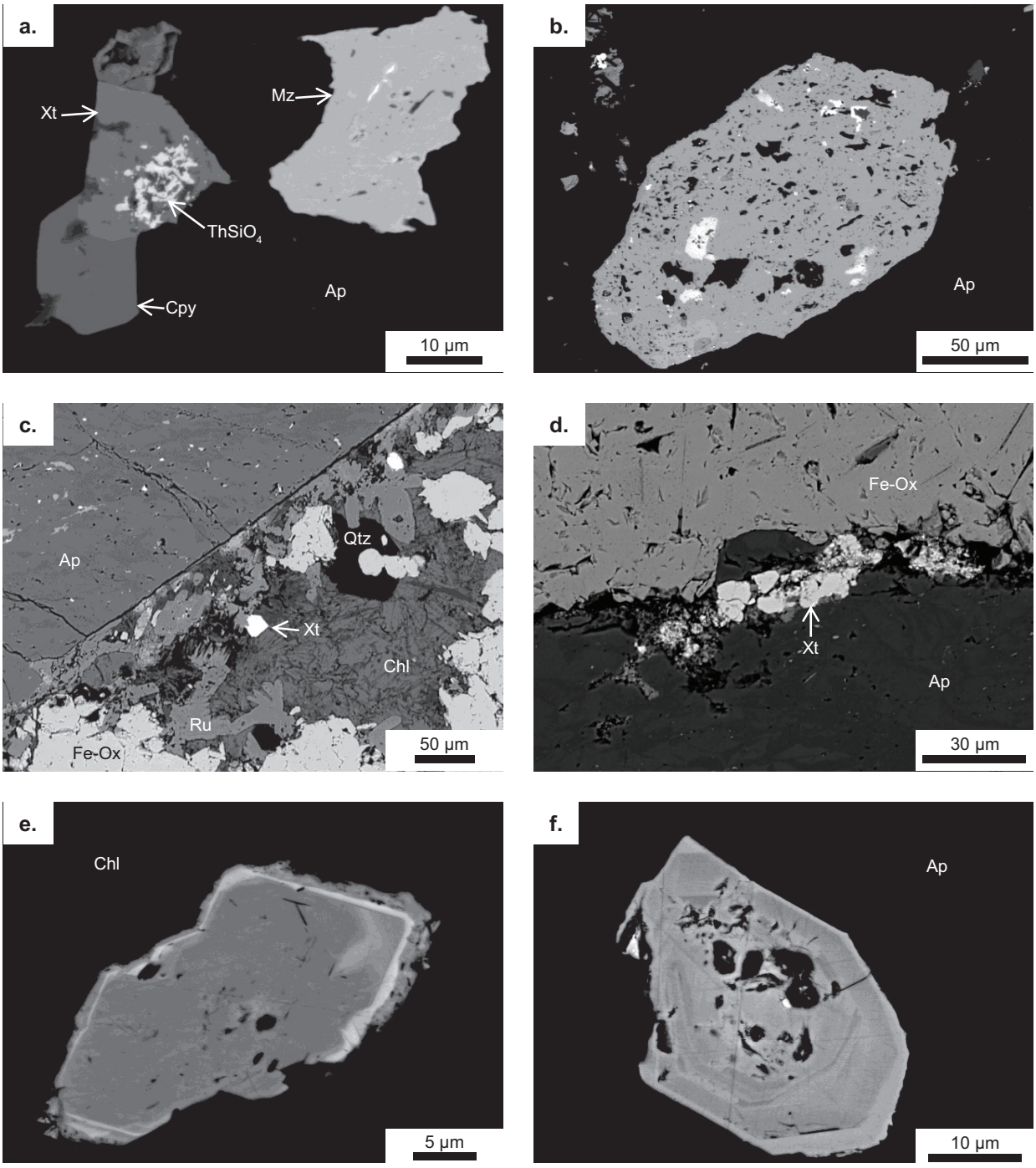

Figure 4.6 Monazite and xenotime inclusions in apatite and rim grains. **a.** Monazite (Mz), xenotime (Xt) and chalcopyrite inclusions in apatite (Ap). The xenotime inclusions contain even smaller inclusions of $ThSiO_4$ (OD743). **b.** Very large monazite inclusion in apatite with bright Th- and Si-rich zones (OD742). **c.** Euhedral xenotime rim grains associated with rutile (Ru), quartz (Qtz), Fe oxide (Fe-Ox) and Fe-Mg-rich chlorite (Chl) adjacent to a large apatite grain (OD1068). **d.** Anhedral xenotime rim grains on the margin of a large apatite grain in contact with Fe oxide (OD1068). **e.** Euhedral xenotime rim grain with bright rim in chlorite (OD1068). **f.** Zoned, euhedral monazite inclusion (OD1068).

4.5.2 Geochronology

4.5.2.1 Apatite

The majority of analyses of the bright apatite zones (including the OD306 apatite) plot as a near-concordant cluster, reflecting minimal mixing with common Pb. The measured intercept age of the OD306 apatite as a reference material is 1596 ± 19 ± 26 Ma (n = 10, MSWD = 0.33, p.o.f = 0.96, uncertainties reported at 95% confidence as ± internal/random and ± total, including systematic, Table 4.1). The analysed bright zones of the three different samples overlap strongly and give a combined concordia intercept age of 1579 ± 9 ± 20 Ma (n = 32, MSWD = 0.60, p.o.f = 0.96, ± 95% conf.) (Fig. 4.7a) which overlaps with the measured age of the OD306 apatite but is younger than the isotope dilution age of the OD306 apatite (1596.7 ± 7.1; Thompson et al., 2016). The combined intercept age of the three apatite samples is similar to the ages of titanite (SHRIMP U-Pb ages; 1574 ± 6.2 and 1580.1 ± 9.3 Ma) and muscovite (^{40}Ar-^{39}Ar age; 1575 ± 11 Ma) reported by Skirrow et al. (2007) from prospects in the Olympic Cu-Au Province. However, the young intercept age of the bright apatite is attributed to the additional weight given to analyses of the sample OD742 by the interpretation software Isoplot (Ludwig, 2008); analyses of this sample have the smallest error and are tightly clustered but are slightly discordant, suggesting either some disturbance relative to the other two samples or that the OD742 apatite might be younger. The combined concordia intercept age of OD743 and OD1068 is 1590 ± 16 ± 24 Ma (n = 21, MSWD = 0.41, p.o.f = 0.99, ± 95% conf.), which overlaps with the isotope dilution age of OD306.

The majority of analyses of the dark apatite zones have higher error than those of the bright apatite zones and most are more discordant along a mixing trend with common Pb (Fig. 4.7b). The greater degree of mixing with common Pb in the dark apatite is attributed to greater depletion of U relative to Pb such that less radiogenic Pb is subsequently produced, which leads to higher relative proportions of common Pb. The fact that many of the dark apatite analyses, which are discordant through mixing with common Pb occur along the same common Pb mixing trend as the bright apatite analyses indicates they are around the same age as the bright apatite (i.e. the dark apatite formed before significant radiogenic Pb was generated). A subset of the dark apatite analyses produces a lower intercept age of 1599 ± 25 ± 31 Ma (n = 20, MSWD = 2.9, p.o.f = 0.00, ± 95% conf., see Appendix 4.6), which overlaps with the measured ages of the bright apatite. The increased scatter of the analyses of the dark apatite relative to those of the bright apatite is attributed to the lower precision associated

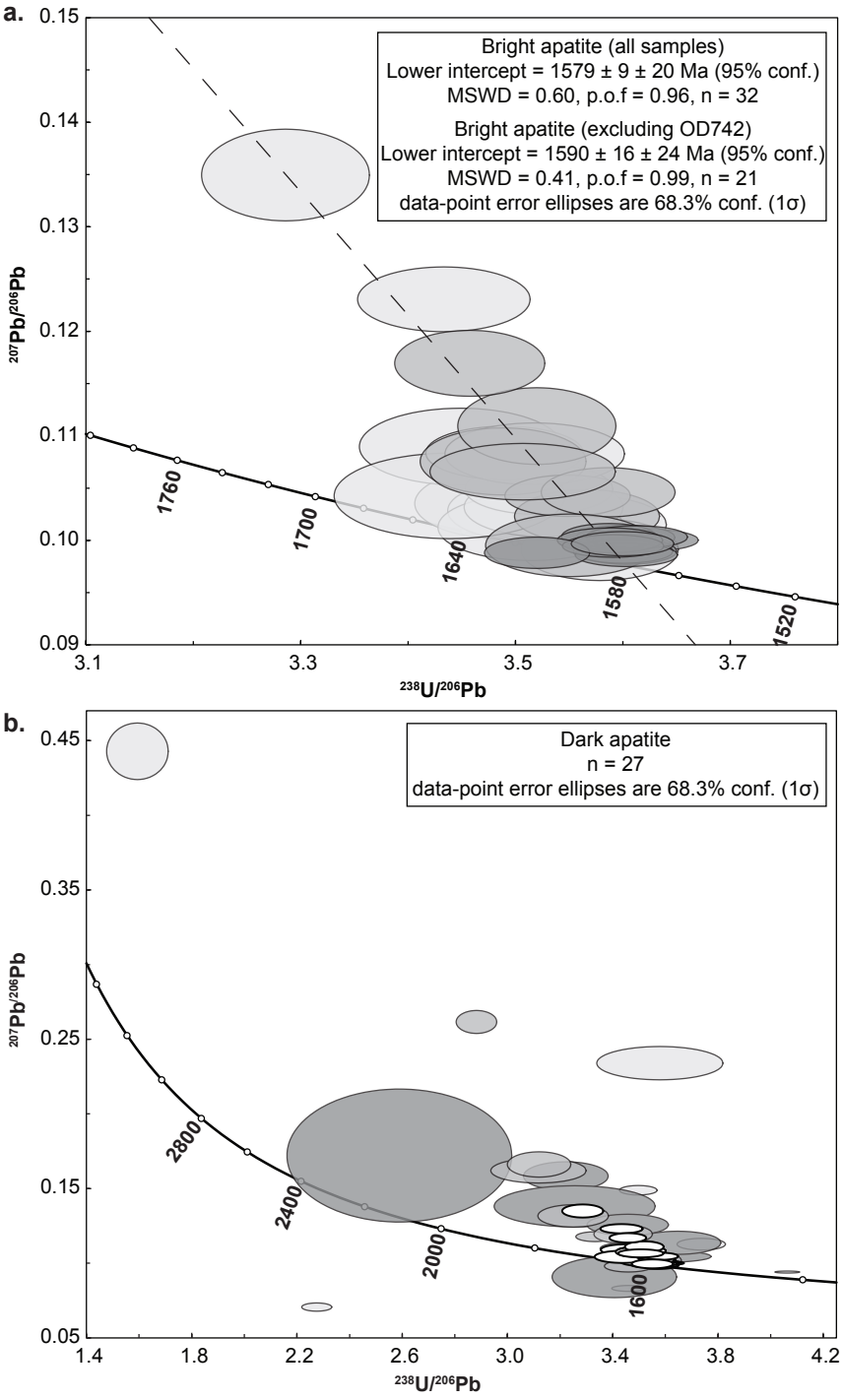

Figure 4.7 Apatite U-Pb Tera-Wasserburg concordia plots. **a.** Bright, early apatite zones. Number of analyses - OD1068 (light grey) = 13, OD743 (medium grey) = 8, OD742 (dark grey) = 11. Reported uncertainties here and in Fig. 4.8a are given as 95% confidence and reported as ± internal/random and ± total, including systematic. **b.** Dark, late apatite zones; the analyses of the bright early apatite from Figure 6A are plotted as opaque ellipses with heavy outlines. Number of analyses OD1068 (light grey) = 7, OD743 (medium grey) = 10, OD742 (dark grey) = 10. The majority of the OD742 and OD743 analyses follow the same common Pb mixing trend as the bright, early apatite (indicating a ca. 1590 Ma age) whereas most of the OD1068 analyses appear disturbed.

with significantly lower concentrations of U and Pb. The high MSWD of the subset of dark apatite analyses suggests there is additional open system behaviour with respect to U and Pb beyond mixing with common Pb. Reverse discordance and Pb loss are apparent in some analyses. Some of the dark apatite zone analyses are near concordant and overlap with those of the bright apatite zones; these analyses commonly have concentrations of U, Th, Pb, Ce and/or Y intermediate to those of the bright apatite and the strongly discordant analyses of dark apatite (see Appendix 4.6). Those dark apatite zones with intermediate trace element concentrations also have a BSE brightness intermediate to the bright apatite and the dark apatite that is most strongly associated with the REE-phosphate inclusions.

4.5.2.2 Xenotime

Around 100 spots in total (from all of the samples) were analysed on xenotime inclusions within apatite and grains along apatite rims. Analyses that exhibited mixing with other mineral phases and/or were of very small grains were excluded, producing a dataset of around 70 viable analyses (see Appendix 4.7). The majority of retained analyses are concordant or near-concordant and define a weighted average $^{207}Pb/^{206}Pb$ age of 1379 ± 7 ± 16 Ma (analyses >90% concordant, n = 39/43, MSWD = 0.98, p.o.f = 0.51, ± 95% conf.) (Fig. 4.8) as well as trends dominated by Pb loss and minor common Pb. An apparent trend of non-t_0 Pb loss is evident in a few analyses (Fig. 4.8a). Concordant outliers have apparent ages of ca. 1600 and 1180 Ma.

4.5.2.3 Monazite

Around 185 monazite inclusions in the dark apatite were analysed. Analyses that exhibited mixing with other phases, were of very small grains, had low Th concentrations and/or were dominated by common Pb were excluded, resulting in a dataset of around 100 analyses (see Appendix 4.8). Examination of the time-resolved signal for each laser ablation analysis of monazite revealed that the Th and U in most of the monazite analyses are decoupled; Th has high and consistent count-rates whereas the count-rate of U is lower and heterogeneous (e.g. Fig. 4.9a). The radiogenic Pb isotopes mimic the behaviour of their parent U and Th, except where affected by common Pb inclusions.

The majority of the U-Pb data is discordant, has large errors when plotted on a Tera-Wasserburg concordia diagram and shows strong evidence of Pb loss and mixing with common Pb (Fig. 4.9b). The

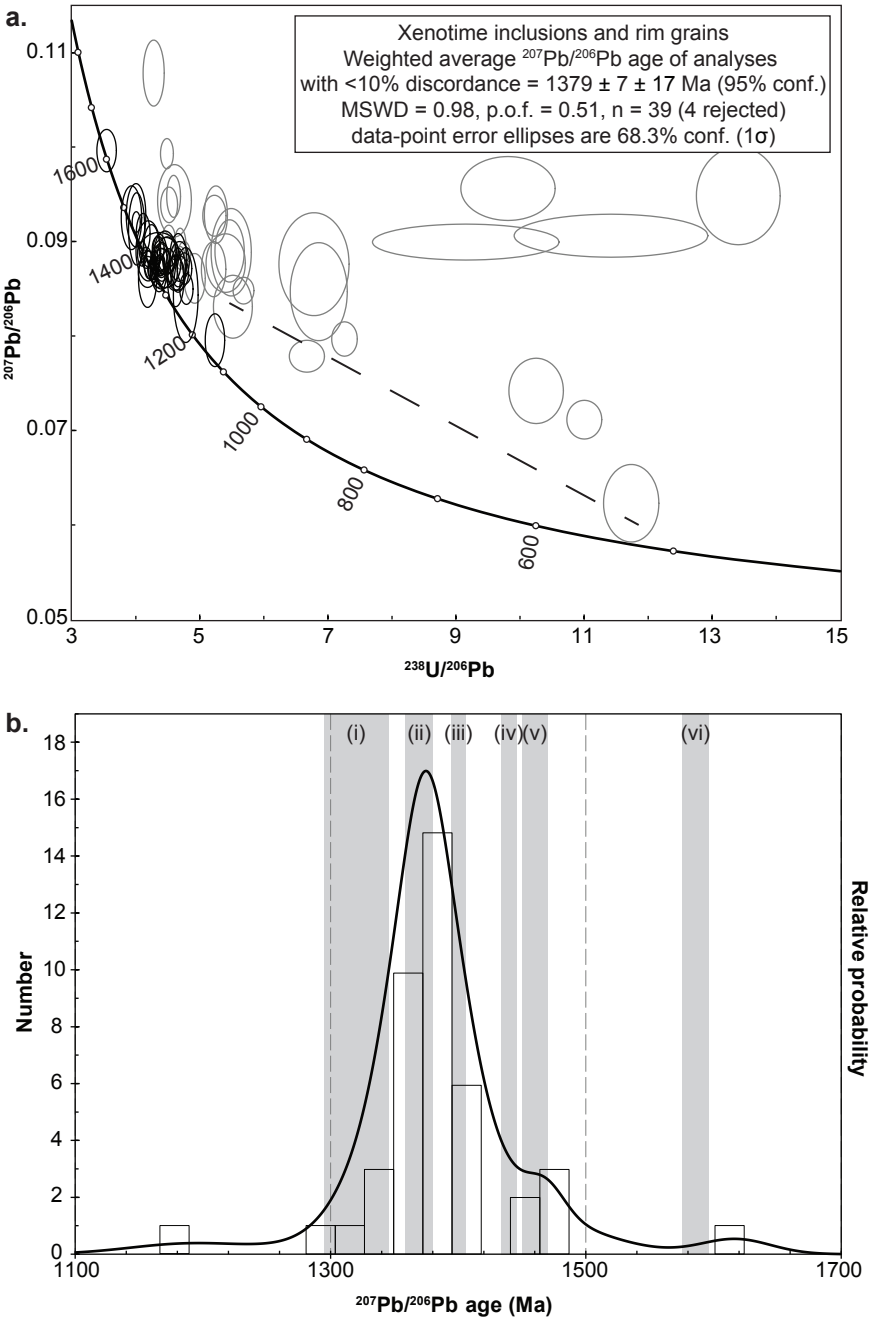

Figure 4.8 Xenotime U-Pb geochronology. **a.** Tera-Wasserburg concordia plot of analyses of xenotime inclusions and rim grains. Analyses with less than 10% discordance are black ellipses; those with greater than 10% discordance are in grey. Potential non-t_0 Pb loss is apparent (trend marked with a line) in the form of a few analyses approaching a lower intercept at around 500 Ma. **b.** Probability density plot ($^{207}Pb/^{206}Pb$ age) of xenotime analyses with less than 10% discordance (black ellipses in Figure 4.8a). Timing of regional tectonothermal events are overlain (see text for references): i = Wankanki Supersuite (Musgrave Province), ii = East Kootenay Orogeny (Laurentia), iii = Papulankutja Supersuite (Musgrave Province), iv = Pandurra Formation diagenesis (Gawler Craton), v = Coorabie Orogeny (Gawler Craton), vi = Gawler Silicic Large Igneous Province.

main cluster of near-concordant analyses and the main common Pb mixing trend approach concordia at ca. 1400 Ma, which is broadly coincident with the xenotime $^{207}Pb/^{206}Pb$ ages. The typically high Th/U ratios in the analysed monazite make Th-Pb ages less affected by common Pb than U-Pb ages, as reflected in measured $^{208}Pb/^{232}Th$ ages that are mostly younger than corresponding $^{206}Pb/^{238}U$ and $^{207}Pb/^{206}Pb$ ages (see Appendix 4.8).

Three main methods exist to correct measured $^{206}Pb/^{238}U$ and $^{208}Pb/^{232}Th$ ages for common Pb. Correction through the ^{204}Pb method uses Stacey and Kramers (1975) ratios of ^{206}Pb, ^{207}Pb and ^{208}Pb and measured values of ^{204}Pb (Chew et al., 2011). However, this method requires accuracy beyond the capacity of the LA-ICPMS used in this study; in particular, a significant proportion of the ^{204}Pb signal is due to interference of ^{204}Hg in the gas supply that delivers ablated material to the ICPMS (Chew et al., 2011). Correction through the ^{208}Pb method relies on the assumption that the ratio of Th to U has not been disturbed since closure of the respective isotopic systems and is also only suitable for analyses/grains with low Th/U ratios (i.e. not monazite) (Chew et al., 2011). The ^{207}Pb method was therefore used to correct for the effect of common Pb on the $^{206}Pb/^{238}U$ and $^{208}Pb/^{232}Th$ ages of monazite, although this method relies on the composition of the common Pb component being based on the Stacey and Kramers (1975) Pb evolution model. The workflow for ^{207}Pb correction and full error propagation of the $^{206}Pb/^{238}U$ and $^{208}Pb/^{232}Th$ ages of monazite is that developed by Berry et al. (2016) and is included in Appendix 4.8. An iterative approach in which the ^{207}Pb-corrected ages are used to update the initial Stacey and Kramers (1975) estimate of common Pb was applied to further refine the corrected age of the monazite grains (Chew et al., 2011). The $^{208}Pb/^{232}Th$ ages were used to iteratively update the Stacey and Kramers (1975) estimate of common Pb (updating the common Pb estimate with the $^{206}Pb/^{238}U$ age results in final ages differing by <2%, on average). The corrected $^{208}Pb/^{232}Th$ ages range from ca. 1500 to 430 Ma (e.g. Fig. 4.9c) whereas the corrected $^{206}Pb/^{238}U$ ages have a much greater range (from around 1590 Ma to 300 Ma) as well as several geologically implausible ages (older than the host apatite or host rock) (see Appendix 4.8). The monazite analyses where Th and U appear decoupled have younger corrected $^{208}Pb/^{232}Th$ ages than those where Th and U appear to be coupled (Fig. 4.9c).

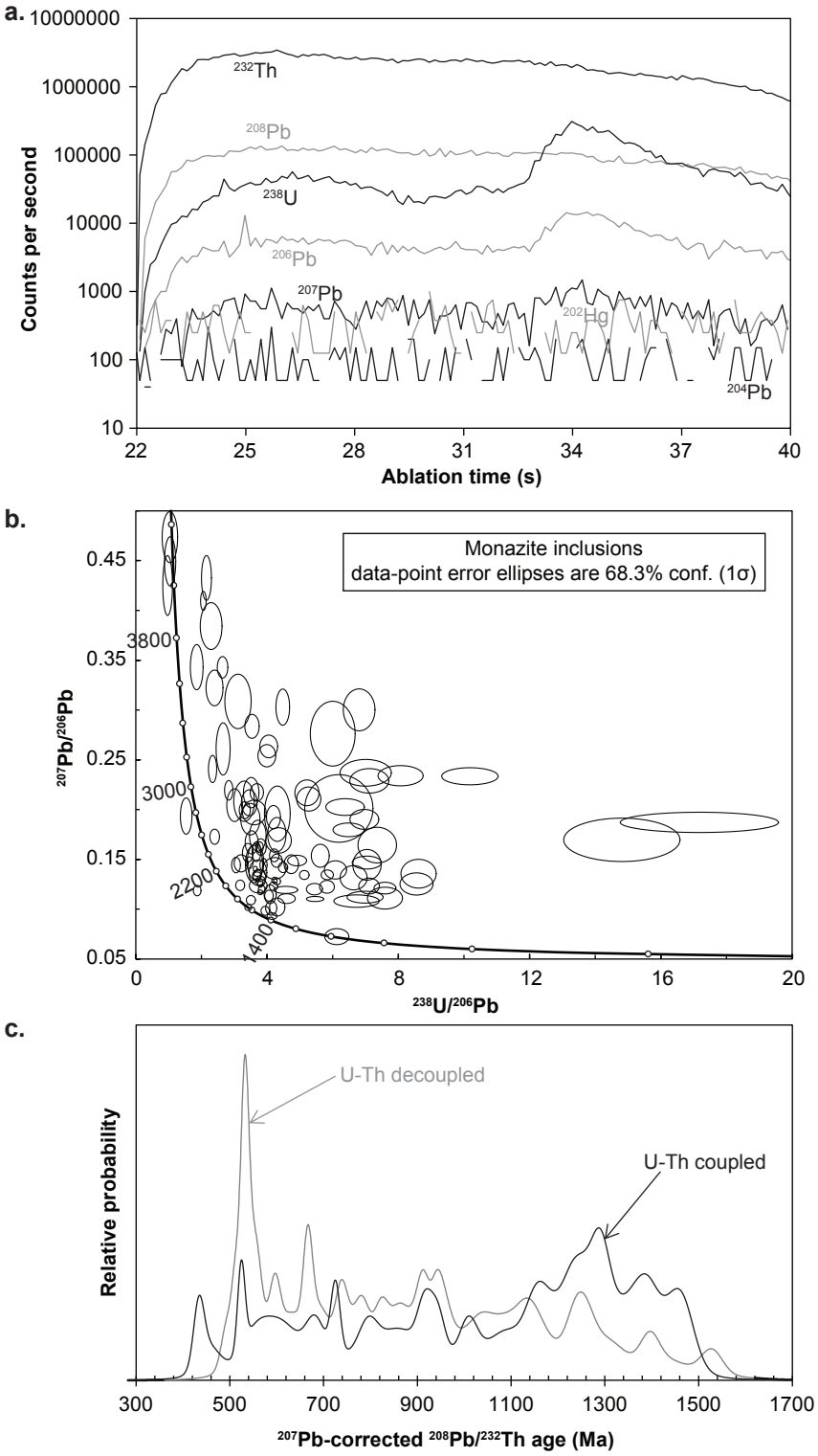

Figure 4.9 Monazite U-Th-Pb geochronology. **a.** Time-resolved ablation plot of monazite analysis (MY30A0013) with decoupled U and Th (raw data in Table S9 of the supplement). Note that counts of the uranogenic and thorogenic Pb mimic those of their respective parents, and that counts of U (as well as ^{206}Pb and ^{207}Pb) are significantly lower than those of Th (and ^{208}Pb). **b.** Tera-Wasserburg concordia plot showing significant Pb loss and common Pb in the monazite U-Pb data. **c.** Probability density plots of ^{207}Pb-corrected ^{208}Pb-^{232}Th ages of monazite. Analyses with decoupled U and Th (grey line) are plotted separately from those where U and Th do not appear decoupled (black line).

4.6 Discussion

4.6.1 Apatite and REE-phosphate textures and chemistry

The apatite grains examined in this study have distinct zones where BSE brightness corresponds to trace element content (i.e. dark zones have low trace element abundances). The abundance of inclusions (particularly REE-phosphates) in the apatite is inversely related to the trace element content and BSE brightness. Numerous natural and experimental studies (e.g. Harlov et al., 2002a; Harlov and Förster, 2002; Harlov et al., 2002b; Harlov and Förster, 2003; Harlov et al., 2005; Bonyadi et al., 2011; Harlov, 2011, 2015; Harlov et al., 2016; Krneta et al., 2016; Krneta et al., 2017; Lupulescu et al., 2017) observed the same correlations between BSE brightness, trace element concentration and REE-phosphate inclusion abundance; they invoked a mechanism of coupled dissolution and reprecipitation as a result of interaction with a fluid (e.g. Putnis, 2002, 2009) to explain the formation of REE-phosphate inclusions in apatite. The trivalent REE + Y (when substituting for Ca^{2+}) are charge-compensated in apatite by coupled-substitution with Na^{+} and Si^{4+} (Rønsbo, 1989; Pan and Fleet, 2002); destabilisation of this coupled-substitution by removal of Na and Si from the apatite (due to interaction with a fluid depleted in those elements) causes liberation of the REE + Y and nucleation of monazite and xenotime. This interpretation implies the bright apatite is early relative to the dark apatite. The degree of depletion of certain trace elements from the bright (early) apatite was noted by Krneta et al. (2017) to vary with the assemblage that replaced the original magnetite assemblage; in particular, hematite is associated with depletion of LREE, HREE + Y in the associated apatite, whereas siderite is associated with uniform depletion of all REE + Y in the associated apatite. We follow this interpretation and attribute the patterns in trace element abundance in Acropolis apatite (e.g. Fig. 4.5a) to recrystallisation of the bright, trace element-rich apatite and associated mobilisation of the majority of the trace elements (including the REE, Y, U and Th) either into nucleating inclusions or out of the apatite grains. The distribution of many of the dark zones in the apatite grains (defining fracture networks as well as patches along rims) is also consistent with the above interpretation of interaction of the apatite with an external fluid.

The greater abundance of REE-phosphate inclusions and higher proportion of dark apatite (relative to bright apatite) in the cores of some apatite grains correspond with the higher concentration of REE + Y (and other associated trace elements) in the remaining early apatite in the core relative to the rim. The replacement by dark apatite of most of the core zone of an apatite grain in sample OD743 has revealed an apparent core-rim boundary (parallel to the grain margin) that suggests that

the core was preferentially recrystallised relative to the rim (Fig. 4.4f). This apparent preferential replacement may be due to the higher trace element concentration of the core rendering it more easily recrystallised.

The relative abundance and compositions of the REE-phosphate inclusions reflect the trace element composition of the original, bright apatite. The higher concentration of LREE relative to HREE + Y in the bright apatite corresponds to a significantly greater observed abundance of monazite than xenotime inclusions in the dark apatite zones. The depletion in HREE + Y in the dark, later apatite generation(s) observed by Krneta et al. (2017) and in this study is now better understood given the recognition of xenotime inclusions and rim grains. The relatively low concentrations of Th and U in the REE-phosphate inclusions (0.07-2.27 wt. % ThO_2 in monazite and 0.20-0.68 wt. % UO_2 in xenotime, Appendix 4.3) are likely to be a function of the temperature of formation (Williams et al., 2011 and references therein) and/or the low concentrations present in the apatite (60-580 ppm ThO_2 and 16-110 ppm UO_2, Appendix 4.5) from which they were derived. Partial resetting associated with later events may have also led to loss of U and Th from monazite (e.g. Williams et al., 2011) and potentially also from xenotime. The enrichment of Th and U in monazite and xenotime relative to apatite indicates the REE-phosphate minerals preferentially partition those elements relative to apatite. The partitioning of U, Th, and the REE into inclusions, particularly into xenotime rim grains outside the apatite, indicates that the fluids associated with the formation of these REE-phosphates were capable of mobilising U, Th and REE.

Apparent cross-cutting and overprinting of BSE zones within apatite grains (Fig. 4.4b, c) could indicate the occurrence of multiple events; apatite zones of intermediate BSE brightness may represent earlier event(s) and apatite with the darkest BSE shade may represent the last event. The association of the majority of, and the largest, REE-phosphate inclusions with the darkest apatite zones suggests that either most of the REE-phosphate inclusions formed during a more recent event or formed earlier and were subsequently recrystallised (and coarsened).

The reddish colour of the apatite grains is attributed to the numerous inclusions (including hematite) in the dark zones distributed throughout the apatite grains. Pale, translucent zones in the apatite grains (including all of OD306) correspond to the inclusion-free bright zones (Fig. 4.3b, c). The non-REE-phosphate inclusions (e.g. iron oxide, pyrite and chalcopyrite) may have been derived from

the trace Fe, Cu and S contained in the host apatite (see Appendix 4.5). Alternatively (or additionally) Fe, Cu and S may have been derived from an external source such as hematite and chalcopyrite associated with the hematite assemblage. The formation of iron oxide and sulfide inclusions in the dark apatite may have been facilitated by the porosity that is commonly induced by coupled dissolution-reprecipitation reactions (Putnis, 2002, 2009). The paucity of iron oxide and sulfide inclusions in dark zones in OD306 apatite could reflect not only the low concentrations of Fe, Cu and S in the bright zones but also the lack of iron oxide and copper sulfide in the OD306 vein assemblage.

4.6.2 U-Th-Pb systematics of apatite, monazite and xenotime

4.6.2.1 Apatite

The age of the bright apatite is consistent with its crystallisation at around the same time as (or shortly after) the deposition of the Gawler Range Volcanics hosting the Acropolis prospect (e.g. Mortimer et al., 1988). As with the OD306 apatite reference material, the bright apatite at Acropolis contains relatively little common Pb, particularly when compared with other apatite reference materials (e.g. Chew et al., 2011; Thompson et al., 2016).

Thorium and U partition into monazite and xenotime relative to apatite whereas Pb partitions into apatite relative to monazite and xenotime (Harrison et al., 2002). The formation of REE-phosphate inclusions would then be expected to disturb the U-Th-Pb systematics of the host apatite (Stosch et al., 2011); the loss of U and Th and retention of Pb in apatite would lead to discordant analyses. The observation that many of the dark apatite analyses overlap with and are coincident with the common Pb trends of the bright apatite is therefore surprising (although there are several analyses that are disturbed, e.g. dark apatite from sample OD1068, Fig. 4.7b). Furthermore, the ages of the majority of the xenotime (1370 Ma) and monazite (ca. 1400 Ma) inclusions (and rim grains) are significantly younger than the apparently undisturbed dark apatite. The difference in age of the REE-phosphate inclusions and dark apatite is at odds with the inference that the formation of the inclusions coincided with the modification of the bright apatite to dark apatite.

An explanation of the difference in age of the dark apatite and the REE-phosphate inclusions is that the bright apatite was initially modified to dark apatite at ca. 1590 Ma and was modified again by a later event during which most of the REE-phosphate inclusions formed. Disturbance of the U-Th-Pb

systematics of the apatite at ca. 1590 Ma would not be readily apparent because significant quantities of radiogenic Pb would not have been generated in the short time available. Any apatite that was modified by the later event (at ca. 1400-1370 Ma) would exhibit more significant disturbance of the U-Th-Pb systematics (e.g. OD1068 analyses; Fig. 4.7b). This disturbed apatite was presumed to have been missed in most analysed spots in part because it has no inclusion-free zones large enough for a 29 μm spot to be placed. If REE-phosphate inclusions were formed at ca. 1590 Ma, they may have been less abundant, too small to be analysed (i.e. < 10 μm) and/or were recrystallised during the later event into larger REE-phosphate inclusions (e.g. Ostwald ripening; Harlov, 2015).

4.6.2.2 Xenotime

The consistency of the $^{207}Pb/^{206}Pb$ (calibrated by the NIST610 reference glass) and $^{238}U/^{206}Pb$ ratios (calibrated by the 14971 monazite primary reference material) of the majority of the xenotime analyses (i.e. they are concordant) indicates that the use of monazite as calibration for Pb/U ratios is suitable for LA-ICPMS analysis of xenotime (e.g. Thompson et al., 2017) (also demonstrated by the concordance of the monazite and xenotime secondary reference materials, see Appendix 4.9). The clustering of the majority of concordant xenotime analyses around a single $^{207}Pb/^{206}Pb$ age of ca. 1370 Ma indicates that most of xenotime inclusions formed or were completely reset at around this time, and that the xenotime rim grains are contemporaneous with the inclusions. Very few analyses show minor mixing with common Pb and relatively few analyses show significant Pb loss, both of which indicate negligible Pb was initially incorporated into the xenotime and that xenotime is a robust U-Pb geochronometer, particularly when compared with the significant effect of Pb loss and common Pb on the monazite analysed in this study. The few concordant analyses with higher $^{207}Pb/^{206}Pb$ ratios than the main population (including a single ca. 1600 Ma xenotime analysis) is consistent with some xenotime inclusions having formed at ca. 1590 Ma (at the same time as the ca. 1590 Ma late dark apatite). Alternatively, these analyses with higher $^{207}Pb/^{206}Pb$ ratios than the main population may be due to mixing with minor Pb inherited from the apatite (which would also contain Pb generated in the apatite since ca. 1590 Ma).

4.6.2.3 Monazite

Interpretation of the monazite data is not straightforward. The Pb loss evident in many of the monazite analyses may have been caused by diffusion of Pb from the monazite or by a fluid/thermal event that caused partial or complete resetting of the monazite. Volume diffusion of Pb in monazite has been determined to be very low and monazite has an effective closure temperature of at least 900°C for 10 μm-sized grains (Cherniak et al., 2004). The inclusions analysed in this study were at least that size (to accommodate the 9 μm laser spot) and so diffusion is considered an unlikely cause of Pb loss. Fluid-mediated recrystallisation in monazite at temperatures well below that of the closure for Pb diffusion has been invoked as the cause of disturbance (partial or complete resetting) of the monazite U-Th-Pb system in several studies (e.g. Hawkins and Bowring, 1997; Townsend et al., 2001; Williams et al., 2011; Seydoux-Guillaume et al., 2012; Grand'Homme et al., 2016). The decoupling of U and Th evident in the time-resolved signal of most of the laser ablation analyses of monazite (e.g. Fig. 4.9a) suggests that U was disturbed relative to Th. The potentially greater mobility of U relative to Th may be due to its higher solubility in the fluid that mediated recrystallisation of the monazite, particularly if the fluid was oxidising (e.g. Williams et al., 2011).

The oldest Th-Pb age peaks are ca. 1440 and 1370 Ma (Fig. 4.9c), which suggest the analysed monazite inclusions probably first formed at around this time, broadly consistent with the main xenotime U-Pb population. The continuum of Th-Pb ages from ca. 1440 Ma to 530-430 Ma indicates most of the inclusions subsequently experienced partial resetting. Although the formation of monazite inclusions after ca. 1440-1370 Ma cannot be discounted, the main, concordant xenotime population suggests that a younger event of REE-phosphate inclusion formation (than 1370 Ma) is less likely. The youngest significant age population (ca. 530 or 430 Ma) constrains the timing of the most recent thermal/fluid event responsible for monazite resetting/Pb loss. Any additional events between the most recent event and initial formation cannot be distinguished. Despite the attempt to correct for common Pb, the continuum in Th-Pb ages suggests the effectiveness of this technique is limited in this setting. The limitations of this technique are attributed to the presence of common Pb that is more radiogenic than the modelled Stacey and Kramers (1975) Pb isotopic composition used for correction or when there is partial Pb loss. Such instances lead to underestimates of ^{206}Pb, ^{207}Pb and ^{208}Pb in the common Pb in the monazite and result in ages that are older than the formation or resetting of the monazite inclusions (e.g. Stosch et al., 2011). Thus the apparent Th-Pb ages can be interpreted only as maximum ages of formation or resetting.

The changes in relative concentrations of Th, U, Ce, and Y expected to result from alteration of monazite (i.e. loss of U and HREE + Y relative to Th and LREE) (e.g. Read et al., 2002; Williams et al., 2011; Seydoux-Guillaume et al., 2012; Grand'Homme et al., 2016) are not well correlated with the Th-Pb ages of the analysed inclusions (Fig. 4.10). This relationship suggests that nearly all of the inclusions have been affected by alteration/Pb loss to varying degrees. Partial resetting at a time close to the initial age of the monazite and/or minimal Pb loss could result in retention of old Th-Pb ages but relative concentrations of the above elements (e.g. high Th/U and Ce/Y ratios; Fig. 4.10) would still be modified. The few older monazite analyses for which Th and U do not appear to be decoupled and that have higher U/Th and Y/Ce ratios could be the least altered and closest to representative of the monazite inclusions that originally formed at ca. 1400 Ma (Fig. 4.10).

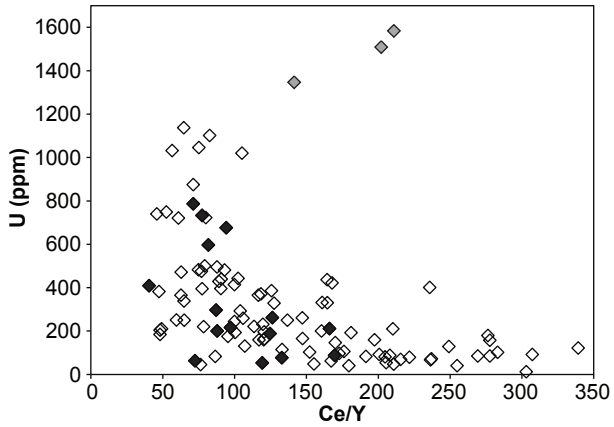

Figure 4.10 Bivariate plot showing the relationship of U concentration and REE fractionation (Ce/Y) in the monazite LA-ICPMS U-Pb analyses. Analyses with corrected Th-Pb ages older than 1200 Ma and apparently coupled U and Th are plotted as black symbols. Unfilled symbols represent analyses that have decoupled U and Th and/or have apparent Th-Pb ages younger than 1200 Ma. High U outliers with decoupled Th-U are marked by filled grey symbols.

4.6.3 Significance of apatite, monazite and xenotime ages

4.6.3.1 Mesoproterozoic

The coincidence of the ages of bright apatite and dark apatite (with undisturbed U-Th-Pb systematics) indicates that not only did the apatite form at ca. 1590 Ma (e.g. Mortimer et al., 1988), but the bright apatite was altered to form the first(?) dark apatite generation at around the same time. Multiple magmatic events have occurred in the Acropolis area; the main Gawler Range Volcanics host units have been intruded by Hiltaba Suite granite (described as syenite in Paterson, 1986) and sills/dykes that are also assigned to the ca. 1590 Ma Gawler Range Volcanics (McPhie, 2016). These events could have been related to the initial alteration of the apatite at Acropolis.

The age of the majority of the xenotime inclusions (and rim grains; ca. 1370 Ma) is approximately coincident with the oldest monazite inclusions and ca. 200 myr younger than the apatite with undisturbed systematics. This younger age is interpreted as the time when the inclusions were formed and/or altered by a distinct thermal/fluid event. Other dates around this age have been encountered in the vicinity of Acropolis (1370 ± 54 Ma monazite at Oak Dam East prospect; Davidson et al., 2007), which suggests this age represents a previously unrecognised thermal/fluid event in the Olympic Cu-Au Province. The ca. 1370 Ma age from Acropolis does not appear to correspond with any Mesoproterozoic thermal events that have been recorded regionally in the Gawler Craton (e.g. 1470-1450 Ma Coorabie Orogeny and the ca. 1440 Pandurra Formation diagenesis; Fanning et al., 1983; Hand et al., 2007; Cherry et al., 2017) or the Musgrave Province (e.g. ca. 1400 Ma Papulankutja and 1345-1293 Ma Wankanki Supersuites; Howard et al., 2015). Palaeogeographic reconstructions have suggested the Gawler Craton was connected (or in proximity) to Laurentia (the North America Craton) during the Mesoproterozoic (e.g. Moores, 1991; Goodge et al., 2008; Pisarevsky et al., 2014; Schmidt, 2014); these reconstructions are based on correlations in provenance, age and palaeomagnetic position between the Pandurra Formation (Gawler Craton) and the lower Belt-Purcell Supergroup (Laurentia) (Ross et al., 1992; Fanning and Link, 2003; Link et al., 2007; Schmidt and Williams, 2011; Schmidt, 2014). This raises the potential thermal events in Laurentia are also recorded in the Gawler Craton. A potential correlated event in Laurentia is the East Kootenay Orogeny, a period of metamorphism, bimodal magmatism and hydrothermal activity in the Belt-Purcell Supergroup at ca. 1370 Ma (Evans and Zartman, 1990; Doughty and Chamberlain, 1996; Aleinikoff et al., 2012; McFarlane, 2015).

4.6.3.2 Cambrian

The non-t_0 Pb loss trend evident in the xenotime U-Pb analyses indicates an apparent lower intercept of ca. 500 Ma, coincident with the youngest population(s) in the monazite Th-Pb analyses. The ca. 500 Ma Delamerian Orogeny affected much of southeastern Australia, including the Adelaide Fold Belt immediately to the east of the Gawler Craton (Preiss, 1993a) and Delamerian ages have been recorded by a number of isotopic systems at Olympic Dam (Maas et al., 2011; Kamenetsky et al., 2015; Clark et al., 2016; Ehrig, 2016). The Cambrian Pb loss/resetting that affected the xenotime and monazite at Acropolis is suggested to have been caused by this event.

4.6.3.3 Relationship to the hematite assemblage

The dark apatite and REE-phosphate inclusions in apatite at the Acropolis prospect were suggested to be hydrothermal textures coeval with the replacement of the magnetite-rich assemblage by hematite-stable (and other) assemblages (Krneta et al., 2017). However, further work is required to resolve which of the dark apatite generations identified in this study (the dark apatite that formed at ca. 1590 Ma, or the later dark apatite associated with the majority of the REE-phosphate inclusions, ca. 1370 Ma), is associated with the hematite assemblage.

4.7 Conclusion

This study of the U-Th-Pb geochronology of apatite and contained REE-phosphate inclusions (and rim grains) has provided temporal constraints on the mineralisation and post-mineralisation history of the Acropolis prospect within the Olympic Province. The bright (BSE), inclusion-poor apatite is close in age (i.e. ca. 1590 Ma) to the host Gawler Range Volcanics, indicating the iron oxide-apatite assemblages at Acropolis formed shortly after deposition of the host volcanic units. Dark (BSE), inclusion-rich apatite that replaces bright apatite has the same age, which suggests modification of the bright apatite shortly after the initial formation of the iron oxide-apatite assemblage, potentially by one or more of the multiple magmatic events that occurred at Acropolis. Some analyses of the dark apatite reflect disturbed U-Th-Pb systematics. The dark apatite is associated with REE-phosphate (monazite, xenotime) inclusions. The main U-Pb age of the most concordant xenotime inclusion (and rim grain) analyses is ca. 1370 Ma and is coincident with the oldest Th-Pb ages of the monazite inclusions. This result indicates another event affected the Acropolis prospect ca. 200 myr after initial formation. The significance of the ca. 1370 Ma age requires additional data but it is possible that the age reflects an orogenic event recognised in once contiguous Laurentia. The Pb loss/partial resetting of monazite and, to a lesser extent, xenotime inclusions at ca. 500 Ma, is evidence of another thermal event affecting the Acropolis Prospect, suggested to have been the Delamerian Orogeny. The two events that appear to have been associated with REE-phosphate formation/modification at Acropolis appear to have been capable of mobilisation of U, Th and the REE. Xenotime is found to be a more robust geochronometer than monazite in the current setting, mainly because it is more resistant to Pb loss and is more effective in excluding common Pb.

4.8 Acknowledgements

This paper represents part of the PhD project undertaken by A.R. Cherry while supported by an Australian Research Council Postgraduate Award. This work was funded by the Australian Research Council and BHP Olympic Dam. K. Goemann and S. Feig of the Central Science Laboratory at the University of Tasmania assisted with the EPMA analyses and automated mineralogy function of the SEM. C. Harraden assisted with execution of the Pb correction workflow. Discussions with M. Ferguson and N. Chapman greatly improved the quality of this work and are gratefully acknowledged. E. Jagodzinski and Y. Uvarova provided constructive reviews, which improved the quality of this manuscript.

Appendix 4.1 Metadata for EPMA analyses of apatite, monazite and xenotime [digital appendix]

Appendix 4.2 Apatite EPMA data [digital appendix]

Appendix 4.3 Monazite and xenotime EPMA data [digital appendix]

Appendix 4.4 Metadata for LA-ICPMS analyses of apatite, xenotime and monazite

Table S4.1 Instrument configuration of LA-ICPMS geochronology analyses. Template from Horstwood et al. (2016)/www.plasmage.org

Laboratory and Sample Preparation	
Laboratory name	Department of Earth Sciences, University of Tasmania
Sample type/mineral	In-situ, hydrothermal apatite and inclusions of monazite and xenotime
Sample preparation	Conventional 1-inch rock mounts, 0.3 micron diamond polish. Cleaned in DI H_2O. Degassed in vacuum.
Imaging	BSE: JEOL JXA-8530 plus, Hitachi SU-70, FEI Quanta 600
Laser ablation system	
Make, Model and type	Coherent COMPex Pro 110, RESOlution/Laurin Technic S155
Ablation cell and volume	Two volume laser cell with a volume 8.8 cm^3 small 2nd volume fixed cup
Laser wavelength (nm)	193 nm
Pulse width (ns)	ca. 20 ns
Fluence (J cm^{-2})	ca. 2 J/cm^2
Repetition rate (Hz)	5 Hz
Ablation duration (s)	30 s (apatite + one session of monazite+xenotime), 20 s (second session of monazite+xenotime)
Ablation pit depth / ablation rate	n.m.
Spot diameter nominal/ actual	29µm (apatite + NIST610 SRM) 9µm (monazite+xenotime)
Sampling mode / pattern	Static spot ablation
Carrier gas	100% He in the cell set to 0.35 l/min, Ar carrier gas combined in 2nd volume of laser cell and was set to 1.05 l/min.
ICP-MS Instrument	
Make, Model and type	Agilent 7900 quadrupole ICPMS
Sample introduction	Ablation aerosol mixed with Ar and sent into ICP-MS
RF power (W)	1350 W
Make-up gas flow (l min^{-1})	0.0
Detection system	Electron multiplier with Pb and U in pulse counting mode
Masses measured	For geochronology: 31, 43, 56, 89, 140, 202, 204, 206, 207, 208, 232, 238. For trace element analysis: 23, 24, 27, 29, 31, 43, 51, 55, 56, 57, 63, 66, 75, 88, 89, 137, 139-141, 146, 147, 153, 157, 159, 163, 165, 166, 169, 172, 175, 206, 207, 208, 232, 238
Integration time per peak/ dwell times (ms)	31P, 43Ca, 56Fe, 89Y, 140Ce = 2ms; 202Hg = 8 ms; 204Pb, 206Pb = 20 ms; 207Pb = 25 ms; 208Pb, 232Th = 10 ms; 238U = 15 ms

Total integration time per output data point (s)	~180 ms for geochronology method
'Sensitivity' as useful yield (%, element)	2,200 cps / ppm on ^{238}U in 91500 zircon using a 29 μm spot at 5Hz, 2J/cm2 and assuming ~80 ppm U in 91500.
IC Dead time (ns)	37
Data Processing	
Gas blank	30 s on-peak zero subtracted
Calibration strategy	Apatite: OD306 used as primary reference material, Durango, Kovdor, McClure Mountain, Otter Lake and 401 used as secondary reference materials. Xenotime-Monazite: 14971 (in-house monazite) used as primary reference material, RGL-4B, Bananeira and an in-house xenotime used as secondary reference materials.
Reference Material info	OD306 apatite (Thompson et al., 2016) Durango apatite (McDowell et al., 2005) Kovdor apatite (Amelin and Zaitsev, 2002) McClure Mountain apatite (Schoene and Bowring, 2006) Otter Lake apatite (Barfod et al., 2005) 401 apatite(Thompson et al., 2016) 14971 Monazite (in-house reference material) RGL-4B monazite (Rubatto et al., 2001) Bananeira monazite (Gonçalves et al., 2016) Brazil Xenotime (in-house referencematerial, age after "z6414" in Stern and Rayner, 2003)
Data processing package used / Correction for LIEF	In-house macro-based Excel workbooks "apcalc" and "moncalc"
Mass discrimination	Corrected using standard - sample bracketing
Common-Pb correction, composition and uncertainty	Common Pb correction applied to OD306 apatite. No common-Pb correction applied to apatite or xenotime data. ^{207}Pb correction applied to monazite data.
Uncertainty level and propagation	Ages are quotes at 2s absolute, propagation is by quadratic addition of components of random error from unknowns and reference material, uncertainty in drift corrections, etc. as described by Horstwood et al. (2016).
Quality control / Validation	See Table 4.1 in text for validation of secondary reference materials.

Appendix 4.5 Apatite LA-ICPMS trace element data [digital appendix]

Appendix 4.6 Apatite LA-ICPMS U-Pb geochronology [digital appendix]

Appendix 4.7 Xenotime LA-ICPMS U-Pb geochronology [digital appendix]

Appendix 4.8 Monazite LA-ICPMS U-Th-Pb geochronology [digital appendix]

Appendix 4.9 Tera-Wasserburg concordia plots of primary and secondary reference materials used for xenotime and monazite geochronology

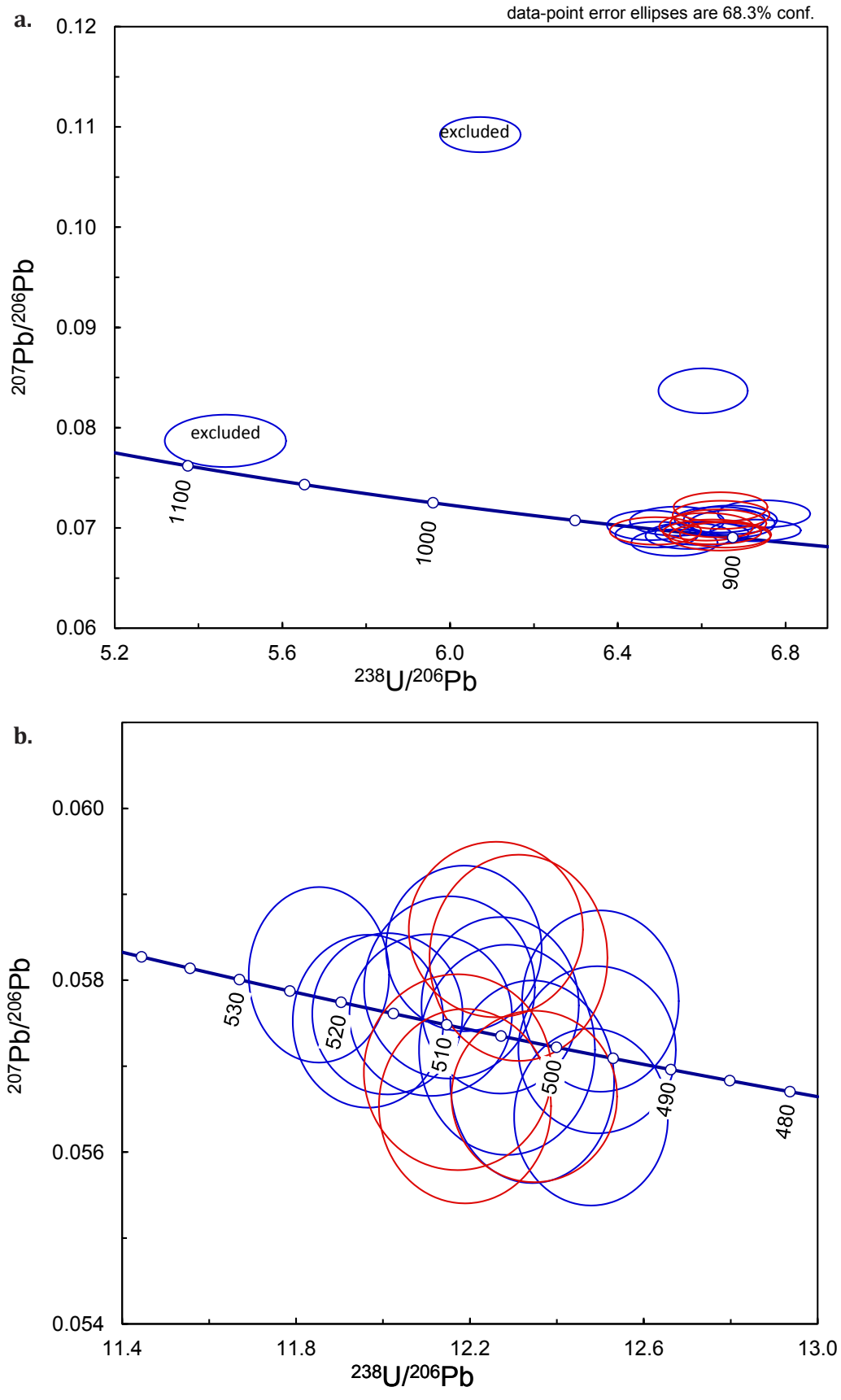

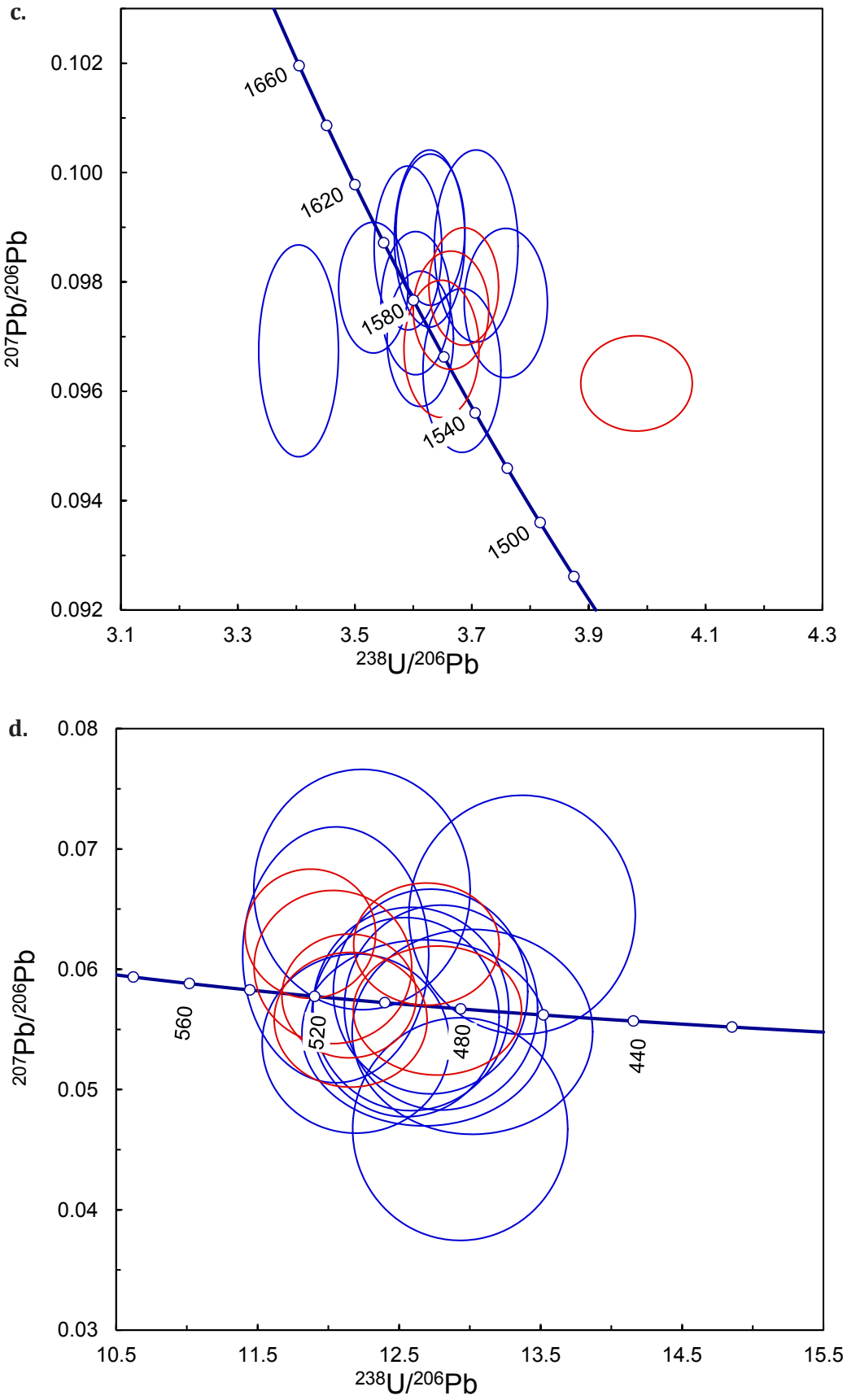

Figure S4.1 Tera-Wasserburg concordia plots of the primary and secondary reference materials used for monazite and xenotime geochronology demonstrating the consistency of $^{207}Pb/^{206}Pb$ and $^{206}Pb/^{238}U$ ratios. Red and blue ellipses are of session 1 (AP13) and 2 (MY30), respectively. **a.** 14971 monazite (primary). **b.** Bananeira monazite (secondary). **c.** RGL-4B monazite (secondary). **d.** Brazil xenotime (secondary).

Appendix 4.10 Time resolved ablation data for Figure 4.8a [digital appendix]

Chapter 5 - Synthesis

5.1 Introduction

This study aims to contribute to understanding of the evolution of the Olympic Dam deposit and the wider Olympic Province. This chapter summarises the findings and significance of the preceding research chapters and, where appropriate, discusses further implications or reviews prior work in the context of the findings of this study. Opportunities for future research that have arisen throughout the course of this study are outlined at the end of this chapter.

5.2 Summary of findings and further implications

5.2.1 Chapter 2: Precise geochronological constraints on the origin, setting and incorporation of ca. 1.59 Ga surficial facies into the Olympic Dam Breccia Complex, South Australia

This chapter used high precision CA-TIMS geochronology of host rocks of the Olympic Dam deposit to constrain the early setting and maximum timing of tectonic and hydrothermal activity at Olympic Dam. A deposition and incorporation model was proposed to account for the distribution of the domains of surficial facies in the breccia complex.

Summary

The precise CA-TIMS geochronology has resolved the age of the host Roxby Downs Granite as ca. 1 myr younger than felsic volcanic rocks present as brecciated domains in the ODBC and as clasts in the bedded clastic facies. The observation of shallow emplacement textures in the Roxby Downs Granite (Creaser, 1989) and the absence of evidence (thus far) of any precursor country rock in the ODBC indicates the Roxby Downs Granite intruded felsic volcanic rocks that were initially present.

Detrital zircon populations indicate that the bedded clastic facies were being deposited ca. 3 myr after the emplacement of the Roxby Downs Granite; the incorporation, brecciation and hydrothermal alteration of the bedded clastic facies indicate the ODBC and hydrothermal system were active after their deposition. The distribution of the bedded clastic facies associations in the ODBC have been used to infer a stratigraphy, even though the majority of contacts between facies associations are faulted. The inferred stratigraphy is suggested to reflect a transition in provenance as

Gawler Range Volcanics lavas are eroded to expose underlying Hiltaba Suite granite in the vicinity of the ODBC. The combination of the above age constraints and inferred stratigraphy with the structural interpretations of Hayward and Skirrow (2010), Ehrig et al. (2012) and McPhie et al. (2016) have enabled the proposal of an incorporation model where the bedded clastic facies were deposited in a basin overlying felsic volcanic lava(s) and were segmented, brecciated and entrained into the ODBC primarily through movement along northeast-striking faults.

Depth of emplacement of the RDG

Geobarometry of the Roxby Downs Granite by Kontonikas-Charos et al. (2017) suggested a crystallisation depth of 6-8 km which would indicate a significant volume of country rock was present above the Roxby Downs Granite. However, the geobarometer used by Kontonikas-Charos et al. (2017) is very sensitive to calculated temperature (where underestimates of temperature can lead to significant overestimates of pressure/crystallisation depth). The compositional data used by Kontonikas-Charos et al. (2017) was applied to the thermobarometric formulations of Ridolfi et al. (2010) and returned significantly higher temperatures and lower pressures that are more consistent with shallow emplacement (~1 kbar or 3-4 km) of the Roxby Downs Granite (see Appendix 5.1). A shallow emplacement is also supported by textural evidence such as miarolitic cavities, aplitic dykes, granophyric zones (Creaser, 1989).

The maar-diatreme model and prior age constraints on the ODBC and deposit

The maar-diatreme model used to explain the presence of bedded clastic facies and brecciated mafic dykes in the ODBC (Reeve et al., 1990) has influenced interpretations of the timing of formation of the deposit and ODBC (e.g. Johnson and Cross, 1995; Johnson and McCulloch, 1995; Hayward and Skirrow, 2010). The spatial association of mafic dykes with the bedded clastic facies, particularly towards the base of the package of bedded clastic facies, were interpreted to be equivalent to feeder dykes to a diatreme structure (Reeve et al., 1990). A number of cross-cutting relationships were observed by Reeve et al. (1990): the diatreme-fill faices (bedded clastic facies) were observed in at least one case to apparently truncate mineralised breccia, and felsic peperite dykes were observed to intrude bedded clastic facies rocks interpreted as ‘epiclastic rocks derived from major hydrothermal breccias’ (p. 1033). As a result, subsequent geochronological work focussed on constraining the

timing of mineralisation within the framework of the maar-diatreme setting of Olympic Dam and led to the conclusion that the ODBC and deposit formed entirely within a single, geologically brief magmatic-hydrothermal event at ca. 1590 Ma (Johnson, 1993; Johnson and Cross, 1995). This conclusion was largely predicated on interpretation of a 'minimum age constraint' on mineralisation and maar-diatreme activity utilising geochronology of the lithologies associated with the cross-cutting relationships identified by Reeve et al. (1990). Geochronology (SHRIMP U-Pb in zircon) of the felsic dykes and diatreme-fill tuff produced ca. 1590 Ma ages overlapping with that of the Roxby Downs Granite (Johnson and Cross, 1995). However, the features used by Johnson and Cross (1995) to argue an intrusive origin for the 'felsic dykes' are also consistent with fault zones intercalating brecciated felsic volcanic rocks with bedded clastic facies and/or hematite-rich breccia (e.g. disruption of bedded clastic facies immediately adjacent to the interval of felsic volcanic breccia). One of the 'felsic dyke' samples examined by Johnson and Cross (1995) occurs within what is now known as a large domain of felsic volcanic breccia within the ODBC(Ehrig et al., 2012). This is the same domain from which sample OD1207 was collected for CA-TIMS analysis and found to be older than the Roxby Downs Granite and the bedded clastic facies. This indicates that the 'felsic dykes' cannot be part of an intrusive phase. Delicate or ragged shapes of felsic volcanic clasts argued by Johnson and Cross (1995) to indicate they were molten and part of a peperitic intrusive facies have since been interpreted to be the result of corrosion by F-rich hydrothermal fluids (McPhie et al., 2011a). Furthermore, the drill hole assays presented by Johnson and Cross (1995) do not show consistent depletion of Cu, U or Au across the 'felsic dyke' intervals.

The CA-TIMS age of the tuffaceous mudstone obtained in this study refined the initial SHRIMP U-Pb zircon age of the 'diatreme-fill tuff' by Johnson and Cross (1995) and demonstrated it was significantly younger than the host Roxby Downs Granite and the felsic volcanic rocks. The apparent cross-cutting relationship of the bedded clastic facies truncating mineralised breccia was utilised by Reeve et al. (1990) and Johnson and Cross (1995) as a potential minimum constraint on mineralisation. However, the tuffaceous mudstone was observed in this study to be hydrothermally altered/mineralised. This indicates the Olympic Dam hydrothermal system was active after deposition of the bedded clastic facies and the ca. 1590 Ma minimum age constraint of Johnson and Cross (1995) is no longer valid.

It is unclear whether the bedded clastic facies were altered by the Olympic Dam hydrothermal system before or after entrainment into the ODBC. The zonation of Cu-Fe sulfides in the ODBC appears

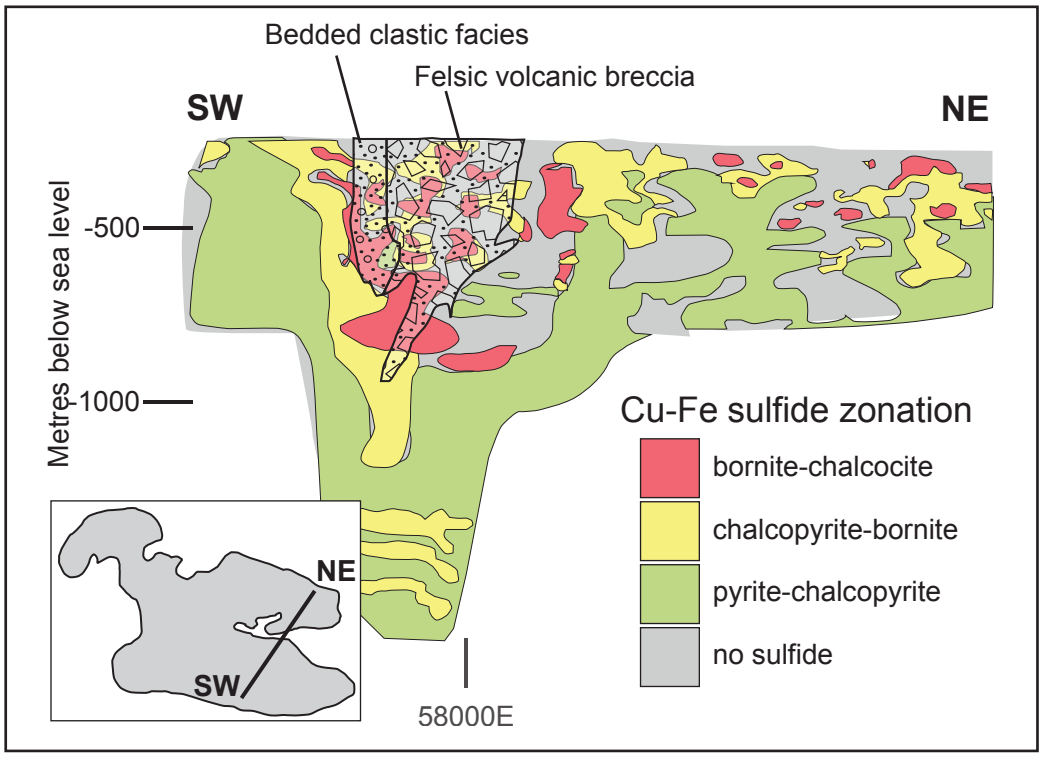

Figure 5.1 Cross-section of the Olympic Dam Breccia Complex showing Cu-Fe sulfide zonation as well as the distribution of the domains of bedded clastic facies and felsic volcanic breccia, after Ehrig et al. (2012) and Ciobanu et al. (2017). The inset shows the location of the cross-section relative to the 5% Fe outline of the ODBC.

to correspond with the shape of the southern domain of bedded clastic facies (Fig. 5.1) which may be due to deposition of the sulfides prior to the entrainment of the bedded clastic facies or may be due to movement of the large southern fault (see Hayward and Skirrow, 2010) truncating the distribution of sulfides in the ODBC.

5.2.2 Chapter 3: Linking Olympic Dam and the Cariewerloo Basin: Was a sedimentary basin involved in formation of the world's largest uranium deposit?

The focus of this chapter was on the characterisation of a distinct quartz-rich sandstone facies association within the Olympic Dam Breccia Complex and correlation with similar successions that are present regionally.

Comparison of detrital and secondary mineralogy, sedimentary textures and detrital zircon geochronology of the quartz-rich sandstone facies association with two similar and regionally significant sedimentary successions found a close match with sandstones of the Pandurra Formation. Authigenic apatite in the quartz-rich sandstone in the ODBC also closely matches known minimum

depositional ages of the Pandurra Formation (1441 ± 15 Ma vs 1424 ± 51 Ma; this study, Fanning et al., 1983). The correlation with the Pandurra Formation indicates the Cariewerloo Basin (in which the Pandurra Formation was deposited) once extended over Olympic Dam. The presence of the Cariewerloo Basin above Olympic Dam raises the possibility that circulating fluids from the Cariewerloo Basin had access to the deposit. The Cariewerloo Basin was briefly considered by Johnson and McCulloch (1995) to be a potential source of metals for the Olympic Dam deposit. However, the Cariewerloo Basin was ultimately considered too young to have been a source as the deposit was, at the time, regarded to have formed entirely at ca. 1590 Ma (Johnson and McCulloch, 1995). Geochronology of uraninite in the deposit has recorded numerous post-1590 Ma U-Pb ages which suggest repeated remobilisation of U in the deposit (Trueman, 1986; Johnson, 1993; Ehrig, 2016). The apparent deficit of Pb (relative to all U being introduced at 1590 Ma; Reeve et al., 1990) suggest a portion of the U resource was added post-1590 Ma. Circulation of oxidised, potentially U-bearing fluids has been recorded in the Cariewerloo Basin at ca. 1200 Ma (Keeling et al., 2016), which raises the possibility the Cariewerloo Basin had a role in development of the Olympic Dam U resource. The entrainment of fragments of Pandurra Formation into the ODBC indicates tectonic activity (faulting) occurring after ca. 1440 Ma and also represents the generation of porosity or pathways/conduits for fluids to more easily penetrate the breccia complex.

5.2.3 Chapter 4: Tectonothermal events in the Olympic IOCG Province constrained by apatite and REE-phosphate geochronology

This chapter recognised that at least two tectonothermal events have affected the Acropolis prospect within the Olympic Province since its initial formation at ca. 1590 Ma and explored correlations with known local and regional events.

Apatite grains in veins in the Acropolis prospect have been partially recrystallised; the recrystallised zones are depleted in trace elements (including U, Th and REE) and contain numerous inclusions of monazite and xenotime. In situ geochronology of the apatite zones as well as the associated xenotime and monazite inclusions and rim grains from veins in the Acropolis prospect returned a range of ages. The inclusion-free, bright (in BSE) apatite formed at ca. 1590 Ma, as did the recrystallised zones of apatite (that had few enough inclusions to place LA-ICPMS spots). These ages indicate the apatite was partially recrystallised shortly after it initially formed. In contrast, the majority of the xenotime inclusions are significantly younger at ca. 1370 Ma and also show evidence of partial resetting at ca. 500 Ma (monazite inclusions have a similar trend, though with poorer

resolution), which indicates at least two more events recrystallised apatite, formed or reworked xenotime and monazite, and mobilised REE, U, Th and Pb. Multiple BSE shades (i.e. at least 3) are evident in recrystallised apatite zones, and are consistent with multiple additional events having reset the apatite.

The ca. 500 Ma Delamerian Orogeny affected the Adelaide Fold Belt adjacent to the Gawler Craton; the thermal gradient, tranferral of stress and/or expulsion of fluids from this orogenic event are suggested to have been the cause of the partial resetting of the REE-phosphate inclusions in the Acropolis prospect at ca. 500 Ma. Similar ages have also been recorded by a number of different isotopic systems in the Olympic Dam deposit (Maas et al., 2011; Kamenetsky et al., 2015; Clark et al., 2016; Ehrig, 2016).

The ca. 1370 Ma age recorded by the xenotime inclusions and rim grains has only been rarely encountered in the Olympic Province, most likely due to prior geochronological attempts being focussed on constraining the primary ca. 1590 Ma mineralising event (e.g. Skirrow et al., 2007). Geochronology of monazite in the nearby Oak Dam prospect (Davidson et al., 2007) and uraninite in the Olympic Dam deposit (Trueman, 1986; Joohnson 1993) produced ages overlapping with ca. 1370 Ma. However, the high uncertainties of these ages (e.g. Oak Dam monazite: 1370 ± 54 Ma, Olympic Dam uraninite: 1390 ± 100 and 1342 ± 35 Ma) limits the confidence with which these ages can be attributed to the same event that caused the ca. 1370 Ma age in Acropolis. The tectonothermal event that could have caused this modification to the Acropolis and Oak Dam prospects has not yet been recorded in the Gawler Craton or in any adjacent terranes (such as the Adelaide Fold Belt or the Musgrave Province) in Australia. The ca. 1370 Ma age instead corresponds best with an episode of metamorphic, igneous and hydrothermal activity in Laurentia (the East Kootenay Orogeny; McMechan and Price, 1982). Metamorphism associated with the East Kootenay Orogeny is imposed on the Belt-Purcell Supergroup (on the margin of Laurentia) where high-temperature metamorphic rocks (migmatites and sillimanite-metapelites) have ages of ca. 1370 Ma (Doughty and Chamberlain, 1996; McFarlane, 2015). Bimodal magmatism associated with the East Kootenay Orogeny produced intrusions into the Belt-Purcell Supergroup at ca. 1370 Ma (Evans and Zartman, 1990; Doughty and Chamberlain, 1996; Aleinikoff et al., 2012; McFarlane, 2015). Hydrothermal mineralisation associated with the Blackbird Co-Cu district (also hosted by Belt-Purcell Supergroup) also has U-Pb ages of ca. 1370 Ma (early stage hydrothermal xenotime, Aleinikoff et al., 2012).

A number of palaeogeographic reconstructions have suggested the Gawler Craton (the South Australia Craton) was in proximity, or even connected, to Laurentia (North American craton) during the Mesoproterozoic (e.g. Moores, 1991; Goodge et al., 2008; Pisarevsky et al., 2014; Schmidt, 2014). These reconstructions are based on the presence of early Mesoproterozoic detrital zircons (e.g. 1650-1590 Ma) in lower successions of the Belt-Purcell Supergroup that have no known source in Laurentia but have abundant sources in the Gawler Craton (Ross et al., 1992; Ross and Villeneuve, 2003; Link et al., 2007). Later workers (Fanning and Link, 2003; Goodge et al., 2008) compared the Pandurra Formation of the Gawler Craton and lower successions of the Belt-Purcell Supergroup as proximal and distal correlates with a common provenance and similar depositional ages. Furthermore, the palaeopoles of the Pandurra Formation (Schmidt and Williams, 2011) and the lower Belt-Purcell Supergroup (Elston et al., 2002) are consistent with the two successions (and therefore the Gawler Craton and Laurentia) being in close proximity at ca. 1400 Ma (Schmidt and Williams, 2011; Schmidt, 2014).

5.3 Implications for the supergiant size of Olympic Dam

The Olympic Dam deposit is one of the largest economic accumulations of metals in the world and its genesis has been the subject of study since its discovery. Early studies interpreted the deposit as having formed entirely at ca. 1590 Ma as a result of a geologically brief magmatic-hydrothermal event (Reeve et al., 1990; Johnson and Cross, 1995; Johnson and McCulloch, 1995; McInnes et al., 2008). However, more recent studies have suggested that mineralisation and alteration at Olympic Dam developed episodically and may potentially be polygenetic (Maas et al., 2011; Kamenetsky et al., 2015; Ehrig, 2016; Kirchenbaur et al., 2016; Macmillan et al., 2016). The genesis of Olympic Dam is likely the result of ore-forming conditions that were particularly optimal relative to the other deposits and prospects in the Olympic IOCG Province (Hayward and Skirrow, 2010), which is consistent with how other giant deposits form (Richards, 2013; Laznicka, 2014; Meffre et al., 2016).

The size of Olympic Dam and the abundance of U are the main characteristics that distinguish it from the other IOCG deposits and prospects in the Olympic Province and elsewhere around the world. Olympic Dam's size is likely a consequence of the maintenance of a high fluid-rock ratio facilitated by prolonged, episodic brecciation of a large volume of rock due to repeated tectonic and hydrothermal activity (Oreskes and Einaudi, 1990; McPhie et al., 2011a). The near-surface setting (<4 km) and the presence of a sedimentary basin immediately above the ODBC at ca. 1590 Ma suggests there was a

plentiful supply of meteoric or basinal fluids, which have been suggested to have been a significant potential source of metals and/or were responsible for leaching/upgrading an initially subeconomic magnetite body (Haynes et al., 1995; Hayward and Skirrow, 2010). The exposure of Olympic Dam to a second sedimentary basin (Cariewerloo Basin), along with coincident tectonic activity generating new permeability in the ODBC, raises the potential for additional influx of fluids and metals such as U. In contrast, the lack of significant brecciation and consequent low fluid-rock ratios in subeconomic prospects (such as Acropolis) likely accounts for their small size and low grades. Many of the other prospects in the Olympic Province are also overlain by the Cariewerloo Basin but it is unknown whether they had access to basinal fluids through additional permeability generated by post-1590 Ma tectonic activity (the Oak Dam prospect is a potential exception, Davidson et al., 2007).

Determining whether the presence of multiple ages in mineral deposits is indicative of accumulation of metals through time or just remobilisation of a pre-existing resource is challenging. The direct dating of different generations of U minerals (Trueman, 1986; Johnson, 1993; Ehrig, 2016) has been used to argue for both post-1590 Ma addition of U as well as remobilisation and upgrading of an existing resource. Studies that identified distinct chemistries of different generations of U minerals (Macmillan et al., 2016) and the absence of evidence of natural fission reactions (à la Oklo; Gauthier-Lafaye et al., 1996) expected from an ancient high-grade U resource (Kirchenbaur et al., 2016) have favoured multi-stage addition of U to Olympic Dam. However, by far the most compelling evidence of multi-stage addition of U is the deficit of radiogenic Pb in the deposit (relative to the entire U resource being emplaced at ca. 1590 Ma) which was first noted by Trueman (1986) and Reeve et al. (1990). The various generations of U minerals in the deposit are commonly intergrown with Cu-Fe sulfides (Macmillan et al., 2016), which indicates that Cu has been remobilised within the deposit in a similar manner to U. The only attempt to directly date Cu mineralisation was through Re-Os geochronology of Cu-Fe sulfides from a variety of ore types (McInnes et al., 2008); the most meaningful age extracted from the data was 1258 ± 28 Ma, derived from a subset of chalcopyrite-pyrite ore. The initial interpretation of this age by McInnes et al. (2008) was resetting of the Re-Os isotope systematics of the sulfides as a result of a regional tectonothermal event, largely because of the age constraints imposed by Johnson and Cross (1995). Even though the minimum age constraints of Johnson and Cross (1995) are now known to be invalid, the Re-Os ca. 1250 Ma age of chalcopyrite-pyrite ore remains equivocal (i.e. it could represent the timing of mineralisation or of remobilisation/resetting). A similar age (ca. 1300 Ma) was obtained from attempts to directly date REE mineralisation in Olympic Dam (Maas et al., 2011).

Exploration for IOCG deposits has commonly invoked the potential of finding another 'Olympic Dam-type' deposit (i.e. similar size and polymetallic assemblage). However, despite being one of the founding deposits of the IOCG class, the size and polymetallic tenor of Olympic Dam sets it apart from other IOCG deposits. The evidence of a prolonged history of tectonic and hydrothermal modification of the deposit, as well as evidence of exposure to a variety of fluid sources (including two sedimentary basins), suggests Olympic Dam may be more than a 'typical' IOCG deposit. This, in turn, suggests that areas that meet those additional criteria may be required to facilitate the discovery of another deposit approaching the size and tenor of Olympic Dam.

5.4 Future research

In the course of this study, a number of potential avenues for further work have become apparent:

1. Resolve the stratigraphy of the bedded clastic facies within the northern and southern domains in the ODBC.

The stratigraphic relationship of the various bedded clastic facies associations has been suggested at in Chapter 2 but has not been unequivocally resolved. Soft sediment deformation has contorted the bedded clastic facies and the majority of contacts between facies associations are faulted (McPhie et al., 2016), which has impeded determination of the stratigraphy. A detailed study of younging textures and contacts between facies associations would offer the opportunity to test the stratigraphic succession that is suggested in this study. Furthermore, as the Olympic Dam operations extend drives into the southern mine area of the ODBC, new drilling will become available.

2. Was the Pandurra Formation (Cariewerloo Basin) truly a source or conduit for U-bearing fluids?

One of the significant implications of the findings of Chapter 3 is that the Cariewerloo Basin was a significant source of U-bearing fluids that may have contributed to the U resource of Olympic Dam. Recent work by Keeling et al. (2012) and (2016) has identified that fluid circulation occurred within the Cariewerloo Basin at ca. 1200 Ma and that it may have been of sufficient temperature to mobilise U from resistate phases (e.g. zircon) in the sandstone. However, it is not known whether mobile U was ever present within the Cariewerloo Basin.

Identification and potential quantification of radiation effects in detrital phases in Pandurra Formation sandstone which appear to have experienced later fluid flow could resolve this question. The premise behind this study is that mobile U in the Pandurra Formation sandstone would be present in pore fluids interstitial to detrital grains and that resident U that was being circulated through the sandstones for a long period of time at potentially significant concentrations would lead to radiation effects (damage) to the margins of detrital grains. A number of tools are suggested to help resolve this question:

- The potential of quartz thermoluminescence as a tool to identify the effect of and/or the prior presence of U has been demonstrated in two different sedimentary successions in South Australia alone (i.e. the Namba or Eyre Formations and the Corunna Conglomerate; Hochman and Ypma, 1984; Ypma and Hochman, 1987).

- Detrital zircon geochronology conducted on Pandurra Formation sandstones as part of Chapter 3 was accompanied by the observation that a large percentage of the analysed detrital zircons were metamict (i.e. destruction of crystal structure through radiation damage). The degree of metamictisation of a population of zircon grains is due to the amount of radiation that they receive (i.e. those zircon grains with high U concentrations and/or older grains are more likely to be metamict). It was speculated (by S. Meffre, CODES, UTas) that prolonged exposure to U present outside the zircon grains (i.e. in circulating U-bearing fluids) would increase the radiation dose of those zircon grains and lead to a greater proportion becoming metamict. Comparison of the proportion of metamict zircon grains (relative to grain age and internal U concentration) from sandstone samples that did and did not experience fluid flow could be used to indicate the prior presence of U.

- Cathodoluminescence is another tool that has the potential to identify (and image) the effects of radiation on detrital grains and could be used to supplement the detrital zircon study.

Context for this study could be provided by first examining the characteristics of zircon and quartz grains in U-rich deposits (e.g. Roxby Downs Granite zircons in the ODBC, sediment-hosted U deposits such as Beverly, South Australia) and in sedimentary basins that host large unconformity-

related U deposits (e.g. the Athabasca and McArthur Basins of Canada and northern Australia, respectively). Leaching of U from detrital zircon grains (or total dissolution) has been suggested to be a primary source of U for the unconformity-related U deposits of the Athabasca Basin (Fayek and Kyser, 1997; Kyser et al., 2000); identification of similar leached zircon (or zircon-poor) zones in the Cariewerloo Basin could be a potentially significant vector for U-mobilising fluids.

3. Constraining the timing of entrainment of the brecciated quartz-rich sandstone facies association (Pandurra Formation) into the ODBC.

The brecciated quartz-rich sandstone facies association occurs in the ODBC as fragments of sandstone suspended in a matrix of disaggregated sandstone that has been relithified. The sandstone fragments indicate brecciation and entrainment occurred after initial lithification of the Pandurra Formation sandstone (i.e. post-1440 Ma). The minimum timing of entrainment is constrained by the maximum age of the undisturbed cover sequence above the ODBC (i.e. ca. 625 Ma for the Nuccaleena Dolomite immediately above the unconformity). These age constraints leave a time gap of approximately 800 myr during which faults propagated up into, brecciated and entrained fragments of overlying Pandurra Formation sandstone. Tightening this ca. 800 myr time gap may improve correlation with the fluid circulation observed in the Pandurra Formation (Keeling et al., 2016) and/or provide further correlation with tectonic activity that has been observed regionally (e.g. Musgrave Orogeny).

One method to further constrain the minimum timing of entrainment of the Pandurra Formation sandstone is determining the timing of relitihification of the matrix in which the sandstone fragments are suspended. Phyllosilicate clays (illite?) comprise a significant component of the matrix, the authigenic crystallisation of which is suggested to have contributed to the relithification of the matrix. Such authigenic clays may be dated through K-Ar geochronology. Techniques such as gentle disaggregation (such as freeze thaw) and rigorous size separation can help mitigate the main challenge of this dating technique, i.e. contamination with detrital phases (e.g. Zwingmann and Hatcher, 2002). Alternatively, further petrographic study could identify additional dateable secondary phases (e.g. xenotime) in the matrix that may constrain lithification or other fluid events.

4. Are the post-1590 Ma ages recorded in REE-phosphate inclusions in apatite in the Acropolis prospect present in other deposits and prospects in the Olympic Province?

The post-1590 Ma ages revealed from geochronology of REE-phosphates (particularly xenotime) associated with fluid-aided recrystallisation of apatite in the Acropolis prospect have implications for whether the entire Olympic Province was similarly affected by the events represented by these ages. Some prior work (using the same or different isotopic systems) in the Olympic Dam deposit and Oak Dam prospect suggested the post-1590 Ma events identified in Chapter 4 are more widespread in the Olympic Province (Davidson et al., 2007; Maas et al., 2011; Kamenetsky et al., 2015), but further work is required.

Further study is proposed where the approach employed in Chapter 4 (i.e. description of texture and LA-ICPMS geochronology of apatite and associated xenotime and monazite) is extended to more deposits and prospects in the Olympic Province. Apatite has been observed as part of the hydrothermal assemblage of numerous deposits and prospects (including Olympic Dam, Carrapateena, Prominent Hill, Wirrda Well, Oak Dam, Emmie Bluff, Torrens, Titan, Murdie Murdie, and Vulcan; Gow et al., 1994; Bastrakov et al., 2007; Davidson et al., 2007; Ehrig et al., 2012). Extending the study to other deposits would enable the validity of the implications of Chapter 4 to be tested and enable additional questions to be answered: 1) whether certain deposits/prospects were affected by fewer or even more events, and 2) what are the implications of their distribution, if there is variation in the number and ages of events affecting certain deposits.

Appendix 5.1 Roxby Downs Granite geobarometry reformulation after Ridolfi et al. (2010) [digital appendix]

References

Agangi, A., 2011. Magmatic and volcanic evolution of a silicic large igneous province (SLIP): the Gawler Range Volcanics and Hiltaba Suite, South Australia. University of Tasmania.

Agangi, A., Kamenetsky, V.S., McPhie, J., 2010. The role of fluorine in the concentration and transport of lithophile trace elements in felsic magmas: Insights from the Gawler Range Volcanics, South Australia. Chem Geol 273, 314-325.

Aleinikoff, J.N., Slack, J.F., Lund, K., Evans, K.V., Fanning, C.M., Mazdab, F.K., Wooden, J.L., Pillers, R.M., 2012. Constraints on the timing of Co-Cu ± Au mineralization in the Blackbird District, Idaho, using SHRIMP U-Pb ages of monazite and xenotime plus zircon ages of related Mesoproterozoic orthogneisses and metasedimentary rocks. Econ Geol 107, 1143-1175.

Allen, S.R., McPhie, J., Ferris, G., Simpson, C., 2008. Evolution and architecture of a large felsic Igneous Province in western Laurentia: The 1.6 Ga Gawler Range Volcanics, South Australia. J Volcanol Geoth Res 172, 132-147.

Amelin, Y., Zaitsev, A.N., 2002. Precise geochronology of phoscorites and carbonatites: The critical role of U-series disequilibrium in age interpretations. Geochim Cosmochim Ac 66, 2399-2419.

Andersen, T., 2005. Detrital zircons as tracers of sedimentary provenance: limiting conditions from statistics and numerical simulation. Chem Geol 216, 249-270.

Anderson, J.L., Smith, D.R., 1995. The effects of temperature and fO2 on the Al-in-hornblende barometer. Am Mineral 80, 549-559.

Apukhtina, O.B., Kamenetsky, V.S., Ehrig, K., Kamenetsky, M.B., Maas, R., Thompson, J., McPhie, J., Ciobanu, C.L., Cook, N.J., 2017. Early, deep magnetite-fluorapatite mineralization at the Olympic Dam Cu-U-Au-Ag deposit, South Australia. Econ Geol 112, 1531-1542.

Armstrong, J.T., 1988. Quantitative analysis of silicate and oxide materials: comparison of Monte Carlo, ZAF, and phi-rho-z procedures. Microbeam Analysis, 239-246.

Baker, J., Peate, D., Waight, T., Meyzen, C., 2004. Pb isotopic analysis of standards and samples using a 207Pb–204Pb double spike and thallium to correct for mass bias with a double-focusing MC-ICP-MS. Chem Geol 211, 275-303.

Barfod, G.H., Krogstad, E.J., Frei, R., Albarède, F., 2005. Lu-Hf and PbSL geochronology of apatites from Proterozoic terranes: A first look at Lu-Hf isotopic closure in metamorphic apatite. Geochim Cosmochim Ac 69, 1847-1859.

Bastrakov, E.N., Skirrow, R.G., Didson, G.J., 2007. Fluid evolution and origins of iron oxide Cu-Au prospects in the Olympic Dam district, Gawler Craton, south Australia. Econ Geol 102, 1415-1440.

Belperio, A., Flint, R., Freeman, H., 2007. Prominent Hill: A hematite-dominated, iron oxide copper-gold system. Econ Geol 102, 1499-1510.

Berry, R., Thompson, J., Meffre, S., Goemann, K., 2016. U-Th-Pb monazite dating and the timing of arc-continent collision in East Timor. Australian Journal of Earth Sciences 63, 367-377.

BHP, 2017. Annual Report 2017, p. 296.

BHP Billiton, 2016. Annual Report 2016, p. 296.

Black, L.P., Gulson, B.L., 1978. The age of the Mud Tank Carbonatite, Strangways Range, Northern Territory. BMR Journal of Australian Geology and Geophysics 3, 227-232.

Black, L.P., Kamo, S.L., Allen, C.M., Aleinikoff, J.N., Davis, D.W., Korsch, R.J., Foudoulis, C., 2003. TEMORA 1: a new zircon standard for Phanerozoic U–Pb geochronology. Chem Geol 200, 155-170.

Black, L.P., Kamo, S.L., Allen, C.M., Davis, D.W., Aleinikoff, J.N., Valley, J.W., Mundil, R., Campbell, I.H., Korsch, R.J., Williams, I.S., Foudoulis, C., 2004. Improved 206Pb/238U microprobe geochronology by the monitoring of a trace-element-related matrix effect; SHRIMP, ID–TIMS, ELA–ICP–MS and oxygen

isotope documentation for a series of zircon standards. Chem Geol 205, 115-140.

Blissett, A.H., Creaser, R.A., Daly, S.J., Flint, R.B., Parker, A.J., 1993. Gawler Range Volcanics, in: Drexel, J.F., Preiss, W.V., Parker A.J. (Eds.), The Geology of South Australia. Vol. 1, The Precambrian, Geological Survey of South Australia, pp. 107-131.

Blundy, J.D., Holland, T.J.B., 1990. Calcic amphibole equilibria and a new amphibole-plagioclase geothermometer. Contrib Mineral Petr 104, 208-224.

Bonyadi, Z., Davidson, G.J., Mehrabi, B., Meffre, S., Ghazban, F., 2011. Significance of apatite REE depletion and monazite inclusions in the brecciated Se Chahun iron oxide-apatite deposit, Bafq district, Iran: insights from paragenesis and geochemistry. Chem Geol 281, 253-289.

Bradbury, J., 1988. The volcanic and shallow sub-volcanic component of the breccia hosted Olympic Dam U-Cu-Au deposit: Implications for breccia pipe development. Monash University.

Bull, S., Meffre, S., Allen, M., Freeman, H., Tomkinson, M., Williams, P., 2015. Volcanosedimentary and chronostratigraphic architecture of the host rock succession at Prominent Hill, South Australia, SEG 2015: World-Class Ore Deposits: Discovery to Recovery. Society of Economic Geologists, Hobart, Tasmania, Australia, p. 1.

Candela, P.A., 1997. A review of shallow, ore-related granites: textures, volatiles and ore metals. J Petrol 38, 1619-1633.

Cherniak, D.J., Watson, E.B., Grove, M., Harrison, T.M., 2004. Pb diffusion in monazite: a combined RBS/SIMS study. Geochim Cosmochim Ac 68, 829-840.

Cherry, A.R., McPhie, J., Kamenetsky, V.S., Ehrig, K., Keeling, J.L., Kamenetsky, M.B., Meffre, S., Apukhtina, O.B., 2017. Linking Olympic Dam and the Cariewerloo Basin: Was a sedimentary basin involved in formation of the world's largest uranium deposit? Precambrian Research 300, 168-180.

Chew, D.M., Petrus, J.A., Kamber, B.S., 2014. U–Pb LA–ICPMS dating using accessory mineral standards with variable common Pb. Chem Geol 363, 185-199.

Chew, D.M., Sylvester, P.J., Tubrett, M.N., 2011. U-Pb and Th-Pb dating of apatite by LA-ICPMS. Chem Geol 280, 200-216.

Ciobanu, C.L., Wade, B.P., Cook, N.J., Mumm, A.S., Giles, D., 2013. Uranium-bearing hematite from the Olympic Dam Cu-U-Au deposit, South Australia: A geochemical tracer and reconnaissance Pb-Pb geochronometer. Precambrian Research 238, 129-147.

Clark, J., Poznik, N., Ehrig, K., 2016. Unravelling the giant: Evidence for post-mineralisation modification of the Olympic Dam Cu-Au-U-Ag deposit, Gawler Craton, South Australia, Australian Earth Sciences Convention. Geological Society of Australia Abstracts, Adelaide, Australia, p. 494.

Courtney-Davies, L., Zhu, Z., Ciobanu, C.L., Wade, B.P., Cook, N.J., Ehrig, K., Cabral, A.R., Kennedy, A., 2016. Matrix-matched iron-oxide laser ablation ICP-MS U-Pb geochronology using mixed solution standards. Minerals 6, 1-18.

Cowley, W.M., 1991. The Pandurra Formation. Department of Mines and Energy, South Australia, open file Report Book 91/7, p. 45.

Cowley, W.M., 1993. Pandurra Formation, in: Drexel, J.F., Preiss, W.V., Park, J.K. (Eds.), The Geology of South Australia. Vol. 1, The Precambrian, Geological Survey of South Australia, pp. 139-142.

Creaser, R.A., 1989. The geology and petrology of Middle Proterozoic felsic magmatism of the Stuart Shelf, South Australia. La Trobe University.

Creaser, R.A., 1996. Petrogenesis of a Mesoproterozoic quartz latite-granitoid suite from the Roxby Downs area, South Australia. Precambrian Research 79, 371-394.

Creaser, R.A., Cooper, J.A., 1993. U-Pb Geochronology of Middle Proterozoic Felsic Magmatism Surrounding the Olympic Dam Cu-U-Au-Ag and Moonta Cu-Au-Ag Deposits, South Australia. Econ Geol 88, 186-197.

Cross, K.C., 1993. Acropolis and Wirrda Well prospects, in: Drexel, J.F., Preiss, W.V., A.J., P. (Eds.), The geology of South Australia, Volume 1, the Precambrian. Geological Survey of South Australia Bulletin, South Australia.

Crowley, J.L., Schoene, B., Bowring, S.A., 2007. U-Pb dating of zircon in the Bishop Tuff at the millennial scale. Geology 35, 1123-1126.

Curtis, S., Wade, C., Reid, A., 2018. Sedimentary basin formation associated with a silicic large igneous province: stratigraphy and provenance of the Mesoproterozoic Roopena Basin, Gawler Range Volcanics. Australian Journal of Earth Sciences 65, 447-463.

Davidson, G.J., Paterson, H., Meffre, S., Berry, R.F., 2007. Characteristics and origin of the Oak Dam East breccia-hosted, iron oxide Cu-U-(Au) deposit: Olympic Dam region, Gawler craton, South Australia. Econ Geol 102, 1471-1498.

Derome, D., Cathelineau, M., Cuney, M., Fabre, C., Lhomme, T., Banks, D.A., 2005. Mixing of sodic and calcic brines and uranium deposition at McArthur River, Saskatchewan, Canada: A Raman and laser-induced breakdown spectroscopic study of fluid inclusions. Econ Geol 100, 1529-1545.

Doughty, P.T., Chamberlain, K.R., 1996. Salmon River Arch revisited: new evidence for 1370 Ma rifting near the end of deposition in the Middle Proterozoic Belt basin. Canadian Journal of Earth Sciences 33, 1037-1052.

Drexel, J.F., Preiss, W.V., Parker, A.J., 1993. The Geology of South Australia, Volume 1, The Precambrian. Geological Survey of South Australia Bulletin 54, 242p.

Ehrig, K., 2016. The Olympic Dam Fe-oxide Cu-U-Au-Ag deposit: 40 years since discovery, Australian Earth Sciences Convention. Geological Society of Australia, Adelaide.

Ehrig, K., McPhie, J., Kamenetsky, V.S., 2012. Geology and mineralogical zonation of the Olympic Dam Iron Oxide Cu-U-Au-Ag Deposit, South Australia, in: Hedenquist, J.W., Harris, M., Camus, F. (Eds.), Economic Geology Special Publication 16, pp. 237-267.

Elston, D.P., Enkin, R.J., Baker, J., Kisilevsky, D.K., 2002. Tightening the Belt: Paleomagnetic-stratigraphic constraints on deposition, correlation, and deformation of the Middle Proterozoic (ca. 1.4 Ga) Belt-Purcell Supergroup, United States and Canada. Geological Society of America Bulletin 114, 619-638.

Evans, K.V., Zartman, R.E., 1990. U-Th-Pb and Rb-Sr geochronology of middle Proterozoic granite and augen gneiss, Salmon River Mountains, east-central Idaho. Geological Society of America Bulletin 102, 63-73.

Fairclough, M., 2005. Geological and metallogenic setting of the Carrapateena FeO-Cu-Au prospect - a PACE success story. Minerals and Energy South Australia Journal 38, 4-7.

Fanning, C.M., Flint, R.B., Parker, A.J., Ludwig, K.R., Blissett, A.H., 1988. Refined Proterozoic evolution of the Gawler Craton, South Australia, through U-Pb zircon geochronology. Precambrian Research 40, 363-386.

Fanning, C.M., Flint, R.B., Preiss, W.V., 1983. Geochronology of the Pandurra Formation. Geological Survey of South Australia Quarterly Geological Notes 88, 11-16.

Fanning, C.M., Link, P.K., 2003. Detrital zircon provenance of the Mesoproterozoic Pandurra Formation, South Australia: Gawler Craton - zircon population and implications for the Belt Supergroup, Geological Society of America 2003 Annual Meeting Geologial Society of America, Seattle, p. 465.

Fayek, M., Kyser, T.K., 1997. Characterization of multiple fluid-flow events and rare-earth-element mobility associated with formation of unconformity-type uranium deposits in the Athabasca Basin, Saskatchewan. Can Mineral 35, 627-658.

Fisher, R.V., Schmincke, H.-U., 1984. Pyroclastic Rocks. Springer-Verlag, Berlin.

Fletcher, I.R., McNaughton, N.J., Aleinikoff, J.A., Rasmussen, B., Kamo, S.L., 2004. Improved calibration

procedures and new standards for U-Pb and Th-Pb dating of Phanerozoic xenotime by ion microprobe. Chem Geol 209, 295-314.

Flint, R.B., 1993. Hiltaba Suite, in: Drexel, J.F., Preiss, W.V., A.J., P. (Eds.), The Geology of South Australia, Volume 1 The Precambrian. Geological Survey Bulletin, South Australia.

Gauthier-Lafaye, F., Holliger, P., and Blanc, P.-L., 1996, Natural fission reactoors in the Franceville basin, Gabon: A review of the conditions and results of a “critical event” in a geologic system. Geochim Cosmochim Ac 60, 4831-4852.

Gerstenberger, H., Haase, G., 1997. A highly effective emitter substance for mass spectrometric Pb isotope ratio determinations. Chem Geol 136, 309-312.

GMEX, 2008. Spectral interpretation field manual, edition 3. AusSpec International Ltd.

Gonçalves, G.O., Lana, C., Scholz, R., Buick, I.S., Gerdes, A., Kamo, S.L., Corfu, F., Marinho, M.M., Chaves, A.O., Valeriano, C., Nalini Jr, H.A., 2016. An assessment of monazite from the Itambé pegmatite district for use U-Pb isotope reference material for microanalysis and implications for the origin of the "Moacyr" monazite. Chem Geol 424, 30-50.

Goodge, J.W., Vervoort, J.D., Fanning, C.M., Brecke, D.M., Farmer, G.L., Williams, I.S., Myrow, P.M., DePaolo, D.J., 2008. A positive test of East Antarctica-Laurentia juxtaposition within the Rodinia supercontinent. Science 321, 235-240.

Gow, P.A., Wall, V.J., Oliver, N.H.S., Valenta, R.K., 1994. Proterozoic iron oxide (Cu-U-Au-REE) deposits: Further evidence of hydrothermal origins. Geology 22, 633-636.

Grand'Homme, A., Janots, E., Seydoux-Guillaume, A.M., Guillaume, D., Bosse, V., Magnin, V., 2016. Partial resetting of the U-Th-Pb systems in experimentally altered monazite: Nanoscale evidence of incomplete replacement. Geology 44, 431-434.

Halpin, J.A., Jensen, T., McGoldrick, P., Meffre, S., Berry, R.F., Everard, J.L., Calver, C.R., Thompson, J., Goemann, K., Whittaker, J.M., 2014. Authigenic monazite and detrital zircon dating from the Proterozoic Rocky Cape Group, Tasmania: Links to the Belt-Purcell Supergroup, North America. Precambrian Research 250, 50-67.

Hand, M., Reid, A., Jagodzinski, L., 2007. Tectonic framework and evolution of the Gawler Craton, southern Australia. Econ Geol 102, 1377-1395.

Harlov, D.E., 2011. Formation of monazite and xenotime inclusions in fluorapatite megacrysts, Gloserheia Granite Pegmatite, Froland, Bamble Sector, southern Norway. Miner Petrol 102, 77-86.

Harlov, D.E., 2015. Apatite: a fingerprint for metasomatic processes. Elements 11, 171-176.

Harlov, D.E., Andersson, U.B., Förster, H.-J., Nyström, J.O., Dulski, P., Broman, C., 2002a. Apatite-monazite relations in the Kirrunavaara magnetite-apatite ore, northern Sweden. Chem Geol 191, 47-72.

Harlov, D.E., Förster, H.-J., 2002. High-grade fluid metasomatism on both a local and a regional scale: the Seward Peninsula, Alaska, and the Val Strona di Omegna, Ivrea-Verbano Zone, northern Italy. Part II: phosphate mineral chemistry. J Petrol 43, 801-824.

Harlov, D.E., Förster, H.-J., 2003. Fluid-induced nucleation of (Y+REE)-phosphate minerals within apatite: nature and experiment. Part II. fluorapatite. Am Mineral 88, 1209-1229.

Harlov, D.E., Förster, H.-J., Nijland, T.G., 2002b. Fluid-induced nucleation of (Y + REE)-phosphate minerals within apatite: Nature and experiment. Part 1. Chlorapatite. Am Mineral 87, 245-261.

Harlov, D.E., Meighan, C.J., Kerr, I.D., Samson, I.M., 2016. Mineralogy, chemistry and fluid-aided evolution of the Pea Ridge Fe oxide-(Y + REE) deposit, southeast Missouri, USA. Econ Geol 111, 1963-1984.

Harlov, D.E., Wirth, R., Förster, H.-J., 2005. An experimental study of dissolution-reprecipitation in fluorapatite: fluid infiltration and formation of monazite. Contrib Mineral Petr 150, 268-286.

Harraden, C.L., McNulty, B.A., Gregory, M.J., Lang, J.R., 2013. Shortwave infrared spectral analysis of hydrothermal alteration associated with the Pebble porphyry copper-gold-molybdenum deposit, Iliamna, Alaska. Econ Geol 108, 483-494.

Harrison, T.M., Catlos, E.J., Montel, J.M., 2002. U-Th-Pb dating of phosphate minerals. Reviews in Mineralogy and Geochemistry 48, 523-558.

Hawkins, D.P., Bowring, S.A., 1997. U-Pb systematics of monazite and xenotime: case studies from the Paleoproterozoic of the Grand Canyon, Arizona. Contrib Mineral Petr 127, 87-103.

Haynes, D.W., Cross, K.C., Bills, R.T., Reed, M.H., 1995. Olympic Dam ore genesis: a fluid-mixing model. Econ Geol 90, 281-307.

Hayward, N., Skirrow, R., 2010. Geodynamic setting and controls on iron oxide Cu-Au (±U) ore in the Gawler Craton, South Australia. Hydrothermal iron oxide copper-gold and related deposits: A global perspective 3, 105-131.

Hiess, J., Condon, D.J., McLean, N., Noble, S.R., 2012. $^{238}U/^{235}U$ systematics in terrestrial uranium-bearing minerals. Science 335, 1610-1614.

Hitzman, M.W., Oreskes, N., Einaudi, M.T., 1992. Geological characteristics and tectonic setting of Proterozoic Iron-Oxide (Cu-U-Au-REE) Deposits. Precambrian Research 58, 241-287.

Hitzman, M.W., Valenta, R.K., 2005. Uranium in iron oxide-copper-gold (IOCG) systems. Econ Geol 100, 1657-1661.

Hochman, M.B.M., Ypma, P.J.M., 1984. Thermoluminescence as a tool in uranium exploration. Journal of Geochemical Exploration 22, 315-331.

Horstwood, M.S.A., Košler, J., Gehrels, G., Jackson, S.E., McLean, N.M., Paton, C., Pearson, N.J., Sircombe, K., Sylvester, P., Vermeesch, P., Bowring, J.F., Condon, D.J., Schoene, B., 2016. Community-derived standards for LA-ICP-MS U-(Th-)Pb geochronology - uncertainty propagation, age interpretation and data reporting. Geostandards and Geoanalytical Research 20, 311-332.

Howard, H.M., Smithies, R.H., Kirkland, C.L., Kelsey, D.E., Aitken, A., Wingate, M.T.D., Quentin de Gromard, R., Spaggiari, C.V., Maier, W.D., 2015. The burning heart - The Proterozoic geology and geological evolution of the west Musgrave Region, central Australia. Gondwana Research 27, 64-94.

Huang, Q., Kamenetsky, V.S., Ehrig, K., McPhie, J., Kamenetsky, M., Cross, K., Meffre, S., Agangi, A., Chambefort, I., Direen, N.G., Maas, R., Apukhtina, O., 2016. Olivine-phyric basalt in the Mesoproterozoic Gawler silicic large igneous province, South Australia: Examples at the Olympic Dam Cu-U-Au-Ag deposit and other localities. Precambrian Research 281, 185-199.

Huang, Q., Kamenetsky, V.S., McPhie, J., Ehrig, K., Meffre, S., Maas, R., Thompson, J., Kamenetsky, M., Chambefort, I., Apukhtina, O., Hu, Y., 2015. Neoproterozoic (ca. 820-830 Ma) mafic dykes at Olympic Dam, South Australia: Links with the Gairdner Large Igneous Province. Precambrian Research 271, 160-172.

Ithurbide, A., Peulon, S., Miserque, F., Beaucaire, C., Chausse, A., 2010. Retention and redox behaviour of uranium(VI) by siderite (FeCO3). Radiochimica Acta 98, 563-568.

Jackson, S.E., Pearson, N.J., Griffin, W.L., Belousova, E.A., 2004. The application of laser ablation-inductively coupled plasma-mass spectrometry to in situ U–Pb zircon geochronology. Chem Geol 211, 47-69.

Jaffey, A.H., Flynn, K.F., Glendenin, L.E., Bentley, W.C., Essling, A.M., 1971. Precision measurements of half-lives and specific activities of ^{235}U and ^{238}U. Physical Review C, 1889-1906.

Jagodzinski, E.A., 2005. Compilation of SHRIMP U-Pb geochronological data - Olympic Domain, Gawler Craton, South Australia, 2001-2003, in: Australia, G. (Ed.), p. 197 pp.

Jagodzinski, E.A., 2014. The age of magmatic and hydrothermal zircon at Olympic Dam, Australian Earth Sciences Convention. Geological Society of Australia Abstracts, Newcastle, Australia, p. 260.

Jagodzinski, E.A., Reid, A., Crowley, J., McAvaney, S.O., Wade, C., 2016. Precise zircon U-Pb dating of a Mesoproterozoic silicic large igneous province: the Gawler Range Volcanics and Benageric Volcanic Suite, South Australia, Australian Earth Sciences Convention. Geological Society of Australia, Adelaide, Australia, p. 494.

Jagodzinski, E.A., Reid, A.J., Crowley, J.L., McAvaney, S., Wade, C.E., submitted. Precise zircon U-Pb dating of a Mesoproterozoic silicic large igneous province: the Gawler Range Volcanics and Benagerie Volcanic Suite, South Australia. Journal of the Geological Society.

Jochum, K.P., Weis, U., Stoll, B., Kuzmin, D., Yang, Q., Raczek, I., Jacob, D.E., Stracke, A., Birbaum, K., Frick, D.A., D., G., Enzweiler, J., 2011. Determination of reference values for NIST SRM 610-617 glasses following ISO guidelines. Geostandards and Geoanalytical Research 35, 397-429.

Johnson, J.P., 1993. The geochronology and radiogenic isotope syetematics of the Olympic Dam copper-uranium-gold-silver deposit, South Australia. The Australian National University, p. 318.

Johnson, J.P., Cross, K.C., 1995. U-Pb geochronological constraints on the genesis of the Olympic Dam Cu-U-Au-Ag deposit, South Australia. Econ Geol 90, 1046-1063.

Johnson, J.P., McCulloch, M.T., 1995. Sources of mineralising fluids for the Olympic Dam deposit (South Australia) - Sm-Nd isotopic constraints. Chem Geol 121, 177-199.

Kamenetsky, V., Clocchiatti, R., 1996. Primitive magmatism of Mt Etna: insights from mineralogy and melt inclusions. Earth and Planetary Science Letters 142, 553-572.

Kamenetsky, V., Ehrig, K., Maas, R., Meffre, S., Kamenetsky, M., McPhie, J., Apukhtina, O., Huang, Q., Thompson, J., Ciobanu, C., Cook, N., 2015. The supergiant Olympic Dam Cu-U-Au-Ag ore deposit: toward a new genetic model, SEG-CODES 2015. Society of Economic Geologists, Hobart, Australia.

Kamenetsky, V.S., Crawford, A.J., Meffre, S., 2001. Factors Controlling Chemistry of Magmatic Spinel: an Empirical Study of Associated Olivine, Cr-spinel and Melt Inclusions from Primitive Rocks. J Petrol 42, 655-671.

Kamenetsky, V.S., Lygin, A.V., Foster, J.G., Meffre, S., Maas, R., Kamenetsky, M.B., Goemann, K., Beresford, S.W., 2016. A story of olivine from the McIvor Hill complex (Tasmania, Australia): Clues to the origin of the Avebury metasomatic Ni sulfide deposit. Am Mineral 101, 1321-1331.

Keeling, J., Wilson, T., Zwingmann, H., van der Wielen, S., Mauger, A., 2016. Mesoproterozoic Cariewerloo Basin, South Australia: spectral approach to mapping mineral diagenesis as a guide to fluid flow and unconformity uranium potential, Australian Earth Sciences Convention. Geological Society of Australia, Adelaide.

Keeling, J.L., Mauger, A.J., Wilson, T., Raven, M.D., 2012, 2012. Diagenetic clay mineral distribution in Mesoproterozoic sandstones of the Cariewerloo Basin, South Australia - implications for uranium mobilisation, in: Churchman, G.J., Creswell, R., Singh, B. (Eds.), Australian Regolith Geoscientists Association and Australian Clay Minerals Society Conference, Mildura, Victoria, pp. 17-21.

Keeling, J.L., Wilson, T., Mauger, A., 2015. Gawler Craton: potential for unconformity-related uranium - spectral insights. South Australian Resources & Energy Investment Conference Abstracts, Department of State Development, South Australia, Report Book 2015/00006, 35-37.

Kirchenbaur, M., Maas, R., Ehrig, K., Kamenetsky, V.S., Strub, E., Ballhaus, C., Munker, C., 2016. Uranium and Sm isotope studies of the supergiant Olympic Dam Cu-Au-U-Ag deposit, South Australia. Geochim Cosmochim Ac 180, 15-32.

Kontonikas-Charos, A., Ciobanu, C.L., Cook, N.J., Ehrig, K., Krneta, S., Kamenetsky, V.S., 2017. Feldspar evolution in the Roxby Downs Granite, host to Fe-oxide Cu-Au-(U) mineralisation at Olympic Dam, South Australia. Ore Geology Reviews 80, 838-859.

Košler, J., 2001. Laser-ablation ICPMS study of metamorphic minerals and processes, in: Sylvester, P.J. (Ed.), Laser-ablation-ICPMS in the earth sciences; principles and applications. Mineralogical Association of Canada Short Course Handbook, pp. 185-202.

Krneta, S., Ciobanu, C.L., Cook, N.J., Ehrig, K., Kontonikas-Charos, A., 2016. Apatite at Olympic Dam,

South Australia: A petrogenetic tool. Lithos 262, 470-485.

Krneta, S., Cook, N.J., Ciobanu, C.L., Ehrig, K., Kontonikas-Charos, A., 2017. The Wirrda Well and Acropolis prospects, Gawler Craton, South Australia: insights into evolving fluid conditions through apatite chemistry. Journal of Geochemical Exploration 181, 276-291.

Krogh, T.E., 1973. A low contamination method for hydrothermal decomposition of zircon and extraction of U and Pb for isotopic age determination. Geochim Cosmochim Ac 37, 485-494.

Kyser, K., Cuney, M., 2008. Chapter 8: Unconformity-related uranium deposits, in: Cuney, M., Kyser, K. (Eds.), Recent and not-so-recent developments in uranium deposits and implications for exploration. Mineralogical Association of Canada Short Course Series, Quebec City.

Kyser, K., Hiatt, E., Renac, C., Durocher, K., Holk, G., Deckart, K., 2000. Chapter 10. Diagenetic fluids in Paleo- and Meso-Proterozoic sedimentary basins and their implications for long protracted fluid histories, in: Kyser, K. (Ed.), Fluids and basin evolution, Short Course Series. Mineralogical Association of Canada, pp. 225-262.

Laznicka, P., 2014. Giant metallic deposits-a century of progress. Ore Geology Reviews 62, 259-314.

Li, X.H., Tang, G.Q., Gong, B., Yang, Y.H., Hou, K.J., Hu, Z.C., Li, Q.L., Liu, Y., Li, W.X., 2013. Qinghu zircon: A working reference for microbeam analysis of U-Pb age and Hf and O isotopes. Chinese Science Bulletin 58, 4647-4654.

Link, P.K., Fanning, C.M., Lund, K.I., Aleinikoff, J.N., 2007. Detrital-zircon populations and provenance of Mesoproterozoic strata of East-central Idaho, U.S.A.: correlation with Belt Supergroup of Southwest Montana, in: Link, P.K., Lewis, R.S. (Eds.), Proterozoic geology of Western North American and Siberia. SEPM (Society for Sedimentary Geology), pp. 101-128.

Ludwig, K.R., 2008. User's manual for Isoplot 3.70: A geochronological toolkit for Microsoft Excel. Berkeley Geochronological Center Special Publication 4.

Lupulescu, M.V., Hughes, J.M., Chiarenzelli, J.R., Bailey, D.G., 2017. Texture, crystal structure, and composition of fluorapatites from iron oxide-apatite (IOA) deposits, eastern Adirondack Mountains, New York. Can Mineral 55, 399-417.

Maas, R., Kamenetsky, V.S., Ehrig, K., Meffre, S., McPhie, J., Diemar, G., 2011. Olympic Dam Cu-U-Au deposit, Australia: new age constraints. Mineralogical Magazine 75, 1375.

Macmillan, E., Cook, N.J., Ehrig, K., Ciobanu, C.L., Pring, A., 2016. Uraninite from the Olympic Dam IOCG-U-Ag deposit: Linking textural and compositional variation to temporal evolution. Am Mineral 101, 1295-1320.

Major, R.B., Conor, C.H.H., 1993. Musgrave Block, in: Drexel, J.F., Preiss, W.V., A.J., P. (Eds.), The geology of South Australia. Vol. 1, The Precambrian. Geological Survey of South Australia, South Australia, pp. 156-167.

Mattinson, J.M., 2005. Zircon U-Pb chemical abrasion ("CA-TIMS") method: combined annealing and multi-step partial dissolution analysis for improved precision and accuracy of zircon ages. Chem Geol 220, 47-66.

McAvaney, S.O., Wade, C.E., 2015. Stratigraphy of the Lower Gawler Range Volcanics in the Roopena area, northeastern Eyre Peninsula. Department of State Development, South Australia.

McDowell, F.W., McIntosh, W.C., Farley, K.A., 2005. A precise 40Ar-39Ar reference age for the Durango apatite (U-Th)/He and fission track dating standard. Chem Geol 214, 249-263.

McFarlane, C.R.M., 2015. A geochronological framework for sedimentation and Mesoproterozoic tectono-magmatic activity in lower Belt-Purcell rocks exposed west of Kimberley, British Columbia. Canadian Journal of Earth Sciences 52, 444-465.

McInnes, B.I.A., Keays, R.R., Lambert, D.D., Hellstrom, J., Allwood, J.S., 2008. Re-Os geochronology and isotope systematics of the Tanami, Tennant Creek and Olympic Dam Cu-Au deposits. Australian Journal of Earth Sciences 55, 967-981.

McMechan, M.E., Price, R.A., 1982. Superimposed low-grade metamorphism in the Mount Fisher area, southeastern British Columbia-implications for the East Kootenay orogeny. Canadian Journal of Earth Sciences 19, 476-489.

McPhie, J., 2016. Geology of the Acropolis prospect, McPhie Volcanology, report for K. Ehrig BHP Olympic Dam, July 2016, 46 p, p. 46p.

McPhie, J., DellaPasqua, F., Allen, S.R., Lackie, M.A., 2008. Extreme effusive eruptions: Palaeoflow data on an extensive felsic lava in the Mesoproterozoic Gawler Range Volcanics. J Volcanol Geoth Res 172, 148-161.

McPhie, J., Kamenetsky, V.S., Allen, S., Ehrig, K., Agangi, A., Bath, A., 2011a. The fluorine link between a supergiant ore deposit and a silicic large igneous province Geology 39, 1003-1006.

McPhie, J., Kamenetsky, V.S., Chambefort, I., Ehrig, K., Green, N., 2011b. Origin of the supergiant Olympic Dam Cu-U-Au-Ag deposit, South Australia: Was a sedimentary basin involved? Geology 39, 795-798.

McPhie, J., Orth, K., Kamenetsky, V., Kamenetsky, M., Ehrig, K., 2016. Characteristics, origin and significance of Mesoproterozoic bedded clastic facies at the Olympic Dam Cu-U-Au-Ag deposit, South Australia. Precambrian Research 276, 85-100.

Meffre, S., Ehrig, K., Kamenetsky, V.S., Chambefort, I., Maas, R., McPhie, J., 2010. Pb isotopes at Olympic Dam: Constraining sulphide growth, 13th Quadrennial IAGOD Symposium Abstracts, Adelaide, International Association on the Genesis of Ore Deposits. International Association on the Genesis of Ore Deposits, Adelaide, South Australia, p. 78.

Meffre, S., Large, R.R., Scott, R., Woodhead, J., Chang, Z., Gilbert, S.E., Danyushevsky, L.V., Maslennikov, V., Hergt, J.M., 2008. Age and pyrite Pb-isotopic composition of the giant Sukhoi Log sediment-hosted gold deposit, Russia. Geochim Cosmochim Ac 72, 2377-2391.

Meffre, S., Large, R.R., Steadman, J.A., Gregory, D.D., Stepanov, A.S., Kamenetsky, V.S., Ehrig, K., Scott, R.J., 2016. Multi-stage enrichment processes for large gold-bearing ore deposits. Ore Geology Reviews 76, 268-279.

Mercadier, J., Cuney, M., Lach, P., Boiron, M.-C., Bonhoure, J., Richard, A., Liesen, M., Kister, P., 2011. Origin of uranium deposits revealed by their rare earth element signature. Terra Nova 23, 264-269.

Moores, E.M., 1991. Southwest U.S.-East Antarctic (SWEAT) connection: A hypothesis. Geology 19, 425-428.

Mortimer, G.E., Cooper, J.A., Paterson, H.L., Cross, K., Hudson, G.R.T., Uppill, R.K., 1988. Zircon U-Pb Dating in the Vicinity of the Olympic Dam Cu-U-Au Deposit, Roxby Downs, South-Australia. Econ Geol 83, 694-709.

Neumann, N., Sandiford, M., Foden, J., 2000. Regional geochemistry and continental heat flow: implications for the origin of the South Australian heat flow anomaly. Earth and Planetary Science Letters 183, 107-120.

Neymark, L.A., Holm-Demona, C.S., Pietruszka, A.J., Aleinikoff, J.N., Fanning, C.M., Pillers, R.M., Moscati, R.J., 2016. High spatial resolution U-Pb geochronology and Pb isotope geochemistry of the magnetite-apatite ore from the Pea Ridge iron oxide-apatite deposit, St Francois Mountains, southeat Missouri, USA. Econ Geol 111, 1915-1933.

Oreskes, N., Einaudi, M.T., 1990. Origin of rare-earth element-enriched hematite breccias at the Olympic-Dam Cu-U-Au-Ag Deposit, Roxby Downs, South Australia. Econ Geol 85, 1-28.

Oreskes, N., Einaudi, M.T., 1992. Origin of Hydrothermal Fluids at Olympic Dam: Preliminary Results from Fluid Inclusions and Stable Isotopes. Econ Geol 87, 64-90.

Otake, T., Wesolowski, D.J., Anovitz, L.M., Allard, L.F., Ohmoto, H., 2007. Experimental evidence for non-redox transformations between magnetite and hematite under H2-rich hydrothermal conditions. Earth and Planetary Science Letters 257, 60-70.

Pan, Y., Fleet, M.E., 2002. Compositions of the apatite-group minerals: Substitution mechanisms and controlling factors. Reviews in Mineralogy and Geochemistry 48, 13-49.

Paterson, H.L., 1986. The Acropolis prospect, in: Paterson, H.L.C. (Ed.), Basement geology of the Stuart Shelf region, South Australia. 8th Australian Geological Convention, 1986, Adelaide, pp. 17-18.

Paton, C., Woodhead, J.D., Hellstrom, J.C., Hergt, J.M., Greig, A., Mass, R., 2010. Improved laser ablation U-Pb zircon geochronology through robust down-hole fractionation correction. Geochemistry Geophysics Geosystems 11, 1525-2027.

Pisarevsky, S.A., Elming, S.-Å., Pesonen, L.J., Li, Z.-X., 2014. Mesoproterozoic paleogeography: supercontinent and beyond. Precambrian Research 244, 207-255.

Preiss, W.V., 1987a. The Adelaide Geosyncline. Late Proterozoic stratigraphy, sedimentation, palaeontology and tectonics Geological Survey of South Australia, Bulletin 53, 438.

Preiss, W.V., 1987b. Basement to the Adelaide Geosyncline, in: Preiss, W.V. (Ed.), The Adelaide Geosyncline, late Proterozoic stratigraphy, sedimentation, palaeontology and tectonics. Geological Survey of South Australia Bulletin, South Australia, pp. 35-41.

Preiss, W.V., 1993a. Delamerian Orogeny, in: Drexel, J.F., Preiss, W.V. (Eds.), The Geology of South Australia. Vol. 2, The Phanerozoic, Geological Survey of South Australia, pp. 45-60.

Preiss, W.V., 1993b. Neoproterozoic, in: Drexel, J.F., Preiss, W.V., A.J., P. (Eds.), The geology of South Australia, Volume 1, the Precambrian. Geological Survey of South Australia Bulletin, South Australia, pp. 170-203.

Preiss, W.V., 2000. The Adelaide Geosyncline of South Australia and its significance in Neoproterozic continental reconstruction. Precambrian Research 100, 21-63.

Putnis, A., 2002. Mineral replacement reactions: from macroscopic observations to micrscopic mechanisms. Mineralogical Magazine 66, 689-708.

Putnis, A., 2009. Mineral replacement reactions. Reviews in Mineralogy and Geochemistry 70, 87-124.

Read, D., Andreoli, M.A.G., Knoper, M., WIlliams, C.T., Jarvis, N., 2002. The degradation of monazite: implications for the mobility of rare-earth and actinide elements during low-temperature alteration. Eur J Mineral 14, 487-498.

Reeve, J.S., Cross, K.C., Smith, R.N., Oreskes, N., 1990. Olympic Dam copper-uranium-gold-silver deposit, in: Hughes, F.E. (Ed.), Geology of the mineral deposits of Australia and Papua New Guinea. Australasian Institute of Mining and Metallurgy, Melbourne, Monograph 14, pp. 1009-1035.

Reid, A.J., Jourdan, F., Jagodzinski, E., 2017. Mesoproterozoic fluid events affect Archean crust in the northern Olympic Cu-Au Province, Gawler Craton: insights from 40Ar/39Ar thermochronology. Australian Journal of Earth Sciences 64, 103-119.

Reid, A., Smith, R.N., Baker, T., Jagodzinski, E.A., Selby, D., Gregory, C.J., Skirrow, R.G., 2013. Re-Os dating of molybdenite within hematite breccias from the Vulcan Cu-Au prospect, Olympic Cu-Au Province, South Australia. Econ Geol 108, 883-894.

Richard, A., Rozsypal, C., Mercadier, J., Banks, D.A., Cuney, M., Boiron, M.-C., Cathelineau, M., 2012. Giant uranium deposits formed from exceptionally uranium-rich acidic brines. Nature Geoscience 5, 142-146.

Richards, J.P., 2013. Giant ore deposits formed by optimal alignments and combinations of geological processes. Nature Geoscience 6, 911-916.

Ridolfi, F., Renzulli, A., Puerini, M., 2010. Stability and chemical equilibrium of amphibole in calc-alkaline magmas: an overview, new thermobarometric formulations and application to subduction-related volcanoes. Contrib Mineral Petr 160, 45-66.

Roberts, D.E., Hudson, G.R.T., 1983. The Olympic Dam copper-uranium-gold deposit, Roxby Downs,

South Australia. Econ Geol 78, 799-822.

Rollison, L., 2016. Stratigraphy, sedimentology and geochemistry of the Pandurra Formation. Univeristy of Adelaide, p. 157.

Rønsbo, J.G., 1989. Coupled susbtitutions involving REEs and Na and Si in apatites in alkaline rocks from the Ilímaussaq intrusion, South Greenland, and the petrological implications. Am Mineral 74, 896-901.

Rose, C.V., Maloof, A.C., 2010. Testing models for post-glacial 'cap dolostone' deposition: Nuccaleena Formation, South Australia. Earth and Planetary Science Letters 296, 165-180.

Ross, G.M., Parrish, R.R., Winston, D., 1992. Provenance and U-Pb geochronology of the Mesoproterozoic Belt Supergroup (northwestern United States): implications for age of deposition and pre-Panthalassa plate reconstructions. Earth and Planetary Science Letters 113, 57-76.

Ross, G.M., Villeneuve, M., 2003. Provenance of the Mesoproterozoic (1.45 Ga) Belt basin (western North America): Another piece in the pre-Rodinia paleogeographic puzzle. GSA Bulletin 115, 1191-1127.

Rubatto, D., Williams, I.S., Buick, I.S., 2001. Zircon and monazite response to prograde metamorphism in the Reynolds Range, central Australia. Contrib Mineral Petr 140, 458-468.

Sack, P.J., Berry, R.F., Meffre, S., Falloon, T.J., Gemmell, J.B., Friedman, R.M., 2011. In situ location and U-Pb dating of small zircon grains in igneous rocks using laser ablation-inductively coupled plasma-quadrupole mass spectrometry. Geochemistry, Geophysics, Geosystems 12, 1-23.

Schmidt, P.W., 2014. A review of Precambrian palaeomagnetism of Australia: Palaeogeography, supercontinents, glaciations and true polar wander. Gondwana Research 25, 1164-1185.

Schmidt, P.W., Williams, G.E., 2011. Paleomagnetism of the Pandurra Formation and Blue Range Beds, Gawler Craton, South Australia, and the Australian Mesoproterozoic apparent polar wander path. Australian Journal of Earth Sciences 58, 347-360.

Schmitz, M.D., Schoene, B., 2007. Derivation of isotope ratios, errors and error correlations for U-Pb geochronology using ^{205}Pb-^{235}U-(^{233}U)-spiked isotope dilution thermal ionization mass spectrometric data. Geochemistry, Geophysics, Geosystems 8, Q08006.

Schoene, B., Bowring, S.A., 2006. U-Pb systematics of the McClure Mountain syenite: thermochronological constraints on the age of the 40Ar/39Ar standard MMhb. Contrib Mineral Petr 151, 615-630.

Scott, T.B., Allen, G.C., Heard, P.J., Randell, M.G., 2005. Reduction of U(VI) to U(IV) on the surface of magnetite. Geochim Cosmochim Ac 69, 5639-5646.

Seydoux-Guillaume, A.M., Montel, J.M., Bingen, B., Bosse, V., de Parseval, P., Paquetter, J.L., Janots, E., Wirth, R., 2012. Low-temperature alteration of monazite: Fluid mediated coupled dissolution-precipitation, irradiation damage, and disurbance of the U-Pb and Th-Pb chronometers. Chem Geol 330-331, 140-158.

Skirrow, R.G., Bastrakov, E., Davidson, G., Raymond, O.L., Heithersay, P., 2002, The geological framework, distribution and controls of Fe-oxide Cu-Au mineralisation in the Gawler Craton, South Australia: Part II: Alteration and mineralisation Hydrothermal iron oxide copper-gold and related deposits: A global perspective 2, 33-47.

Skirrow, R.G., Bastrakov, E.N., Baroncii, K., Fraser, G.L., Creaser, R.A., Fanning, C.M., Raymond, O.L., Davidson, G.J., 2007. Timing of iron oxide Cu-Au-(U) hydrothermal activity and Nd isotope constraints on metal sources in the Gawler craton, South Australia. Econ Geol 102, 1441-1470.

Sláma, J., Košler, J., 2012. Effects of sampling and mineral separation on accuracy of detrital zircon studies. Geochemistry Geophysics Geosystems 13, 17.

Sláma, J., Košler, J., Condon, D.J., Crowley, J.L., Gerdes, A., Hanchar, J.M., Horstwood, M.S.A., Morris, G.A., Nasdala, L., Norberg, N., Schaltegger, U., Schoene, B., Tubrett, M.N., Whitehouse, M.J., 2008.

Plešovice zircon - a new natural reference material for U-Pb and Hf isotopic microanalysis. Chem Geol 249, 1-35.

Stacey, J.S., Kramers, J.D., 1975. Approximation of terrestrial lead isotope evolution by a two-stage model. Earth and Planetary Science Letters 26, 207-221.

Steiger, R.H., Jager, E., 1977. Subcomission on geochronology: Convention on the use of decay constants in geo- and cosmochronology. Earth and Planetary Science Letters 36, 359-362.

Stern, R.A., Rayner, N., 2003. Ages of several xenotime megacrysts by ID-TIMS: potential reference materials for ion microprobe U-Pb geochronology, Radiogenic Age and Isotopic Studies: Report 16. Geological Survey of Canada, p. 7.

Stormer, J.C., Pierson, M.L., Tacker, R.C., 1993. Variation of F and Cl X-ray intensity due to anisotropic diffusion in apatite during electron microprobe analysis. Am Mineral 78, 641-648.

Stosch, H.-G., Romer, R.L., Daliran, F., Rhede, D., 2011. Uranium-lead ages of apatite from iron oxide ores of the Bafq District, east-central Iran. Miner Deposita 46, 9-21.

Thompson, J., Meffre, S., Danyushevsky, L., 2017. Monazite and xenotime Pb/U dating by LA-ICP-MS: importance of operating conditions for accurate analysis, North American Workshop on Laser Ablation, Austin, United States of America, p. p. 77.

Thompson, J., Meffre, S., Maas, R., Kamenetsky, V., Kamenetsky, M., Goemann, K., Ehrig, K., Danyushevsky, L., 2016. Matrix effects in Pb/U measurements during LA-ICP-MS analysis of the mineral apatite. Journal of Analytical Atomic Spectroscopy 31, 1206-1215.

Torab, F.M., Lehmann, B., 2007. Magnetite-apatite deposits of the Bafq district, central Iran: apatite geochemistry and monazite geochronology. Mineralogical Magazine 71, 347-363.

Townsend, K.J., Miller, C.F., D'Andrea, J.L., Ayers, J.C., Harrison, T.M., Coath, C.D., 2001. Low temperature replacement of monazite in the Ireteba granite, Southern Nevada: geochronological implications. Chemical Geology 172, 95-112.

Trueman, N.A., 1986. Lead-uranium systematics of the Olympic Dam deposit and Stuart Shelf mineralization: Summary report of U-REE mineralization, Adelaide, Australia, Western Mining Corp., internal memo, XPSA86/1, 13 January 1986, 7 p.

Wade, C.E., Reid, A.J., Wingate, M.T.D., Jagodzinski, E.A., Barovich, K., 2012. Geochemistry and geochronology of the c. 1585 Ma Benagerie Volcanic Suite, southern Australia: Relationship to the Gawler Range Volcanics and implications for the petrogenesis of a Mesoproterozoic silicic large igneous province. Precambrian Research 206-207, 17-35.

Wiedenbeck, M., Alle, P., Corfu, F., Griffin, W.L., Meier, M., Oberli, F., Von Quadt, A., Roddick, J.C., Spiegel, W., 1995. Three natural zircon standards for U-Th-Pb, Lu-Hf, trace element and REE analysis. Geostandards Newsletter 19, 1-23.

Williams, G.E., 1979. Sedimentology, stable-isotope geochemistry and palaeoenvironment of dolostones capping late Precambrian glacial sequences in Australia. Journal of the Geological Society of Australia 26, 377-386.

Williams, G.E., 1998. Late Neoproterozoic periglacial aeolian sand sheet, Stuart Shelf, South Australia. Australian Journal of Earth Sciences 45, 733-741.

Williams, M.L., Jercinovic, M.J., Harlov, D.E., Budzyń, B., Hetherington, C.J., 2011. Resetting monazite ages during fluid-related alteration. Chem Geol 283, 218-225.

Wingate, M.T.D., Campbell, I.H., Compston, W., Gibson, G.M., 1998. Ion microprobe U–Pb ages for Neoproterozoic basaltic magmatism in south-central Australia and implications for the breakup of Rodinia. Precambrian Research 87, 135-159.

Yeo, G.M., Potter, E.G., 2010. Review of reducing mechanisms potentially involved in the formation unconformity-type uranium deposits and their relevance to exploration, Summary of investigations 2010. Saskatchewan Geological Survey, Sask. Ministry of Energy and Resources, p. 13.

Ypma, P.J., Hochman, M.B.M., 1987. A thermoluminescence study of the role of a Middle Proterozoic unconformity in controlling uranium mineralization, as shown at Eyre Peninsula, South Australia. Bulletin de Mineralogie 110, 173-186.

Zwingmann, H., Hatcher, B., 2002. Application of K/Ar and Rb/Sr geochronology to constrain the timing of sedimentary deposition and diagenesis: preliminary results from Western Australian basins, in: Keep, M., Moss, S.J. (Eds.), The sedimentary basins of Western Australia 3. Petroleum Exploration Society of Australia, Perth, Western Australia, p. 966.